Fluid Mechanics of Polymer Melt Filtration

Joseph Daniel Bennett

Submitted in accordance with the requirements for the degree of
Doctor of Philosophy

The University of Leeds

EPSRC Centre for Doctoral Training in Fluid Dynamics

September 2024

Intellectual Property and Publication Statements

The candidate confirms that the work submitted is his own, except where work which has formed part of jointly authored publications has been included. The contribution of the candidate and the other authors to this work has been explicitly indicated below. The candidate confirms that appropriate credit has been given within the thesis where reference has been made to the work of others.

Chapter 4 is based on work from the jointly authored publication:

J.D. Bennett, M.C.T. Wilson, N. Kapur, P.K. Jimack, R.P. Maltby and M.K. Looney, Computational Modelling and Experimental Validation of Pressure Drop through Multi-Layered Woven Screens for Polymer Melts. *Chemical Engineering Research and Design.* 209 (2024). `https://doi.org/10.1016/j.cherd.2024.08.002`

The candidate was responsible for the research work undertaken within the publication including all data processing and numerical simulations, as well as being the main author of the manuscript. Richard Maltby and Kieran Looney, along with site engineers from Mylar Specialty Films, helped with conceptualization and provided the resources and assistance for the experimental work. All co-authors are thesis supervisors and contributed towards conceptualization and the review and editing of the manuscript.

Acknowledgements

I would like to thank my academic supervisors, Dr Mark Wilson, Prof Peter Jimack and Prof Nikil Kapur, who guided me and provided me with support throughout my PhD. I would also like to thank my industrial supervisors, Dr Kieran Looney and Dr Richard Maltby, whose knowledge on the process was invaluable. This project would not have been possible without the expertise and enthusiasm of all my supervisors.

I would also like to thank the management board of the EPSRC Centre for Doctoral Training in Fluid Dynamics for giving me this opportunity and allowing me to complete this research. Thank you to Mylar Specialty Films for sponsoring this research. Thank you to Hugo Overturf and Mylar Specialty Films' staff for contributing to the smooth execution of pilot scale experimental work.

I would like to thank my cohort for all the help and all the memories made over the course of this project. Finally, I would like to thank my family: Mum, Dad, Nana Gill, Grandma Janet, Granddad Terry, Nana June, Libby, Lucas, Jim, Ella and my dog Sweetie. Thank you all for your support, belief and distractions.

Abstract

Polymer melt filtration is a crucial part of thermoplastic extrusion systems, including film casting, as the process removes contaminants from polymer melts which ensures product quality and process robustness. Millions of tonnes of plastic waste are generated every year. Ambitious goals have been proposed by leading organisations to reduce such waste through recycling. Melt filtration is crucial in processing with recycled material as it ensures that contaminants from recycled plastic have been removed and the final product is suitably clean.

There is little academic research tailored to melt filtration. Before computationally modelling melt filtration, it is crucial to determine the nature of the physical mechanisms driving particle transport, particle deposition and flow across a porous medium for potentially viscoelastic, non-Newtonian polymer melt flows in filter systems. An experiment is undertaken and clarifies that the most common polymer used in film production by Mylar obeys Darcy's law through an in-line screen filter.

Computational fluid dynamics modelling is used to investigate flow across the simple filter system; an experimental setup is used to test the validity of the porous media model in representing filters in polymer melt systems. Computational models of geometrically complex filter systems are created. These models are used to investigate and visualize initial flow patterns in each system.

Filter blocking models are fitted to experimental or production run data to investigate the blocking mechanisms taking place for each filter element. A novel filter blocking model is developed by modifying the blocking models to allow for permeability coupling with velocity. The model is implemented into the computational models of the filter systems created. The blocking model is shown to fit well to pressure drop evolution data from production runs with the filter systems. Results from the model offer insight into flow pattern alteration as filters block. Proposed design improvements to filter systems are suggested based on this model.

Contents

List of Figures

List of Tables

Nomenclature

Symbols

A	Area [m^2]
A_0	Initial area [m^2]
$\boldsymbol{B}$	Force due to Brownian motion [N]
C	Concentration of solid particles [kg/m^3]
C_F	Forchheimer coefficient [m^{-1}]
D	Diameter [m]
D_c	Diffusion coefficient [m^2/s]
d	Thickness [m]
d_D	Downstream support layer thickness [m]
d_F	Filter layer thickness [m]
d_U	Upstream support layer thickness [m]
d_p	Particle diameter [m]
d_s	Weft wire diameter [μm]
d_{total}	Total filter thickness [m]
d_w	Warp wire diameter [μm]
F	Force [N]
$\boldsymbol{F}$	Body force per unit volume [N/m^3]
G''	Loss modulus [Pa]
G'	Storage modulus [Pa]
h	Length [m]
K_I	Consistency index [Pa s^n]

K_b	Complete blocking constant [kg^{-1}]
K_c	Cake filtration constant [kg^{-1}]
K_i	Intermediate blocking constant [kg^{-1}]
K_s	Standard blocking constant [kg^{-1}]
k	Permeability [m^2]
k_0	Initial permeability [m^2]
k_b	Boltzmann constant [J/K]
L	Characteristic length [m]
L_p	Pipe length [m]
M	Concentration of deposited particles [kg/m^3]
m	Mass [kg]
m_x	Linear gradient [m^2/kg]
$\dot{m}$	Mass flow rate [kg/s]
n	Power-law exponent
$\boldsymbol{n}$	Normal vector [m]
$\hat{\boldsymbol{n}}$	Unit normal vector
P	Pressure [Pa]
ΔP	Pressure drop [Pa]
ΔP_0	Initial pressure drop [Pa]
ΔP^*	Non-dimensional pressure drop
Pe	Peclet number
Q	Volumetric flow rate [m^3/s]
q	Volumetric flow rate per unit area [m/s]
R	Resistance [m^{-1}]
R_0	Initial resistance [m^{-1}]
r	Radius/Radial coordinate [m]
r_c	Central radial coordinate [m]
r_o	Outer radial coordinate [m]
r_p	Particle radius [m]
$\dot{r}$	Radial velocity [m/s]
$\dot{r}_c$	Central radial velocity [m/s]

$\dot{r}_o$	Outer radial velocity [m/s]
$\dot{r}^*$	Non-dimensional radial velocity
$\dot{r}_c^*$	Non-dimensional central radial velocity
$\dot{r}_o^*$	Non-dimensional outer radial velocity
Re	Reynolds number
$\boldsymbol{S}$	Source term [N/m^3]
Stk	Stokes number
T	Temperature [°C]
t	Time [s]
$t_{\max}$	Maximum simulation time [s]
t_r	Particle relaxation time [s]
t_s	Time at which singularity occurs [s]
Δt	Time step size [s]
U	Plate velocity [m/s]
U_I	Averaged inlet velocity [m/s]
u	x-velocity component [m/s]
$\|u\|$	Velocity magnitude [m/s]
$\|u\|^*$	Non-dimensional velocity magnitude [m/s]
$\boldsymbol{u}$	Velocity vector [m/s]
v	y-velocity component [m/s]
$\boldsymbol{v}$	Particle velocity vector [m/s]
w	z-velocity component [m/s]
X_D	Flow redevelopment length [m]
x	Distance in the x direction [m]
x_o	Position of outer candle in x direction [m]
$\boldsymbol{x}$	Position vector [m]
y	Distance in the y direction [m]
z	Distance in the z direction [m]
z_o	Position of outer candle in z direction [m]

Greek letters

α	Intrinsic viscosity [dL g^{-1}]

γ	Shear strain
γ_0	Amplitude of shear strain
γ_f	Friction coefficient [kg/s]
$\dot{\gamma}$	Shear rate [1/s]
$\dot{\gamma}_0$	Amplitude of shear rate [1/s]
$\Delta\xi$	Corrected pressure drop [1/s]
η	Viscous resistance [m^{-2}]
η_0	Initial viscous resistance [m^{-2}]
η_o	Outer viscous resistance [m^{-2}]
η_c	Central viscous resistance [m^{-2}]
θ	Angular coordinate [degrees]
θ_c	Central angular coordinate [degrees]
θ_o	Outer angular coordinate [degrees]
$\dot{\theta}$	Tangential velocity [m/s]
λ	Time constant [s]
μ	Viscosity [Pa s]
μ_0	Zero shear viscosity [Pa s]
μ_∞	Infinite shear viscosity [Pa s]
ξ	Corrected pressure [1/s]
ρ	Density [kg/m^3]
ρ_p	Particle density [kg/m^3]
τ	Shear stress [Pa]
$\boldsymbol{\tau}$	Stress tensor [Pa]
Ω	Domain
Ω_f	Fluid domain
Ω_p	Porous domain
ω	Frequency [1/s]
$\partial\Omega$	Domain boundary
$\partial\Omega_{in}$	Inlet boundary
$\partial\Omega_{out}$	Outlet boundary
$\partial\Omega_s$	Wall boundary

μCT	X-ray computed tomography
2D	Two-dimensional
3D	Three-dimensional
BSA	Bovine serum albumin
CAD	Computer-aided design
CFD	Computational fluid dynamics
DF	Layer between downstream and filter layer
GUI	Graphical user interface
IV	Intrinsic viscosity
MD	Machine direction
Mylar	Mylar Specialty Films
PEN	Polyethylene naphthalate
PET	Polyethylene terephthalate
SEM	Scanning electron microscope
TD	Transverse direction
UDF	User-defined function
UDM	User-defined memory
UF	Layer between upstream and filter layer

Chapter 1

Introduction

This chapter presents the motivation and purpose behind this research, background on melt filtration at Mylar Specialty Films and discusses the aims and objectives of this research.

1.1 Motivation and purpose

Mylar Specialty Films (Mylar), formerly DuPont Tejin Films, is a world-leading global manufacturer of polyethylene terephthalate (PET) and polyethylene naphthalate (PEN) film. The film produced by Mylar has a range of applications in sectors including healthcare, electronics, packaging and electrical insulation. In the United Kingdom, Mylar have a European manufacturing site in Dumfries and a Global Innovation Centre in Teesside.

Mylar produce film through a process known as sequentially stretched film casting. The process is shown in Figure 1.1. Polymer chip is fed through a hopper into an extruder, where melting takes place due to frictional and conductive heating [1]. For PET film, around 40% of the material is made from recycled polymer [2]. A steady flow of polymer is required after leaving the extruder as variations in throughput lead to thickness fluctuations in the machine

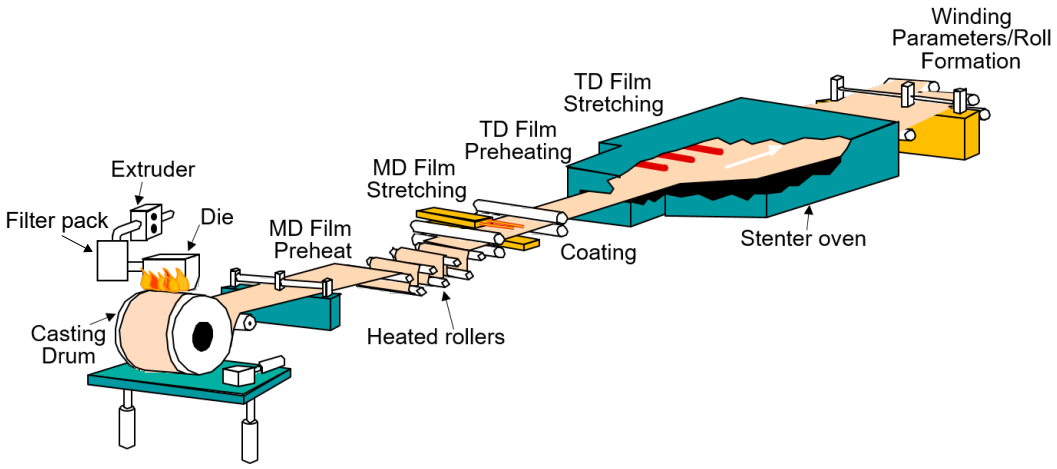

Figure 1.1: The sequentially stretched film casting process. Image adapted from [3].

direction (MD). A gear pump is therefore employed downstream of the extruder. Typical throughputs range from 100 to 3500 kg/hr. The melt then enters a filter pack, which removes any contaminants. A die then generates a uniformly thick melt curtain, which falls onto a casting drum, where it is rapidly cooled to a temperature below its glass transition.

The cast film then travels over a series of heated rollers, which rotate at different speeds. This stretches the film, aligning polymer chains in the MD [2]. This improves the film's tensile properties in the MD [3]. The film is again cooled below its glass transition temperature and aqueous based coatings can be applied to either side to add functionality to the final film. The film is then gripped by clips which run along each side of a stenter oven. The oven heats the film, where it is then stretched in the transverse direction (TD); some of the chains are oriented in the transverse direction by this process [2]. This improves the film's tensile properties in the TD [3]. The orientation is locked in by crystallising the film at high temperatures in the stenter oven post-draw. The film is then cooled and travels on winders where it is slit and wound onto rolls.

Filtration is a key step in film casting as it excludes unwanted solid particles from the polymer melt. Unwanted solid particles include catalyst residues, contaminants and filler or additive agglomerates [4]. Furthermore, filter packs remove unmelted or degraded material [5]. Such

particles and material can damage and deform the final product or cause costly process interruptions. For example, during stretching, unwanted particles will not draw. The film must then stretch more to compensate. This can cause the film to exceed its breaking stress, causing a split and an interruption to the process. A key benefit of using a filter is that it can maximize the amount of recycled content in the polymer while maintaining the integrity of the film as recycled material is likely to have high contaminant levels [4]. Filter packs also serve to homogenise the melt with regards to temperature and composition [6].

The thermoplastic industry is expected to be valued at more than 500 billion dollars by 2033 [7]. PET is the most commonly used thermoplastic polymer resin, with a global demand of 42 million metric tons expected by 2030 [8]. PET accounts for 7% of the total plastic market [7]. PET processing is used for manufacturing in industries such as packaging, textiles, electrical and electronics, the automotive industry and many more [9]. As PET is a thermoplastic, it is easily processed by extrusion and is generally used to produce film and sheets [9].

Around 25.8 million tons of plastic waste was generated in the EU in 2019, and the European Strategy for Plastics in a Circular Economy proposed the goal that 75% of packaging waste would be recycled by 2030 [6]. Recycled polymer contains high levels of contaminants, which, if not removed, can downgrade the quality of the final product in processing [6]. As industry tries to maximise the amount of recycled polymer used in processing to achieve ambitious recycling goals, melt filtration is crucial as it ensures the final product is suitably clean and free of contaminants [5].

There has been a growing demand for the use of computational methods, such as computational fluid dynamics (CFD), to aid in the innovation and understanding of filtration methods in industry [10]. As such, Mylar have shown interest in formulating a computational model of the flow of unfiltered polymer melt through candle and disc filter packs, with the goal of understanding the flow behaviour within the packs. This understanding could lead to the improvement of the current filter pack designs by homogenizing flow distributions around the filters, decreasing mean melt residence time and residence time distribution, eliminating dead

spots and ultimately improving filter lifetime.

1.2 Melt filtration background

Mylar employ two main types of filter packs: candle packs and disc packs. Figure 1.2a shows a cross-sectional drawing of a candle filter pack. Figure 1.2b shows a cross-sectional drawing of a multiple disc filter pack. In both cases, polymer melt enters the pack through the bottom inlet pipe at a constant flow rate. To escape the pack, the melt must travel through candle or disc shaped structures which house the filter medium. This ensures that only filtered polymer melt may move onto the next stage of production.

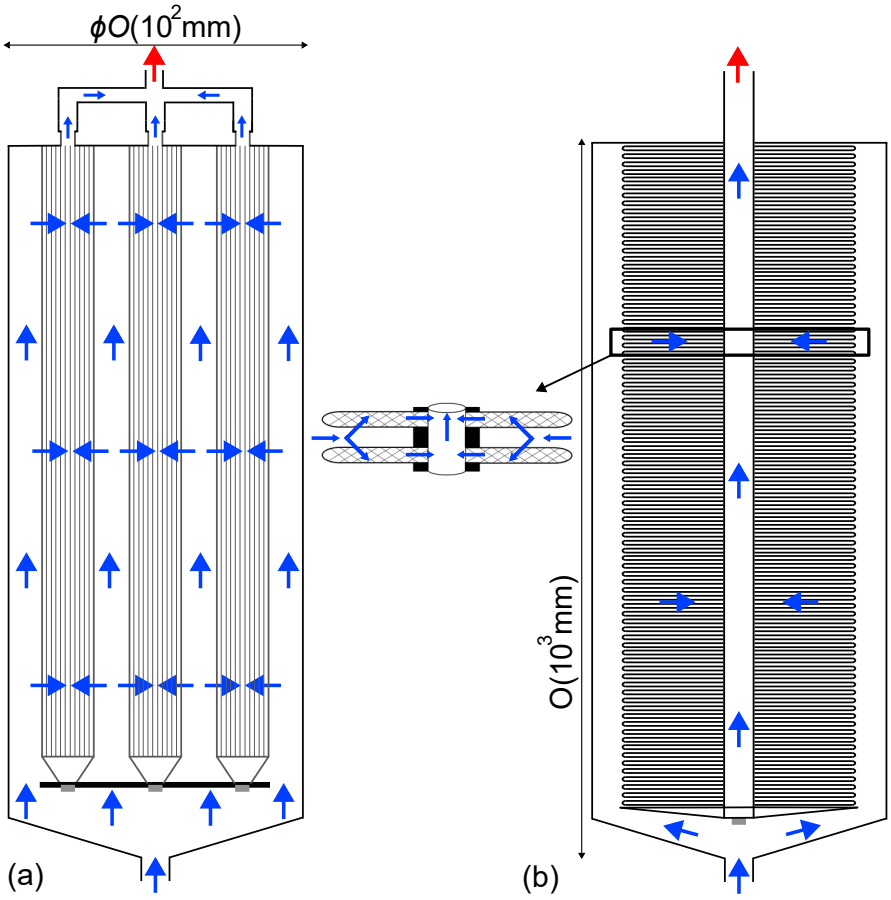

Figure 1.2: Sketch of (a) a candle filter pack and (b) a disc filter pack with arrows indicating the direction of melt flow.

The structure of a candle filter and a disc filter can be seen in Figure 1.3a and Figure 1.3b respectively. For a candle filter, melt must travel past the guard cage and through the pleated structure, which houses the filter medium. The filter medium is supported upstream and downstream by support mesh and a Dutch twill support layer. The melt must then travel through a heavy duty central core. This core, along with the layers surrounding the filter medium, are designed to support the filter medium and withstand high pressure gradients [11]. For a disc filter, two annular discs of filter medium are stacked either side of one or more supporting structures [11]. A layer of support mesh then surrounds the filter medium. Discs stack on a central mandrel. The melt must travel through the discs, out through the melt exit and into the mandrel. Mylar employ a range of candle filter pack designs, including a single and a seven candle pack.

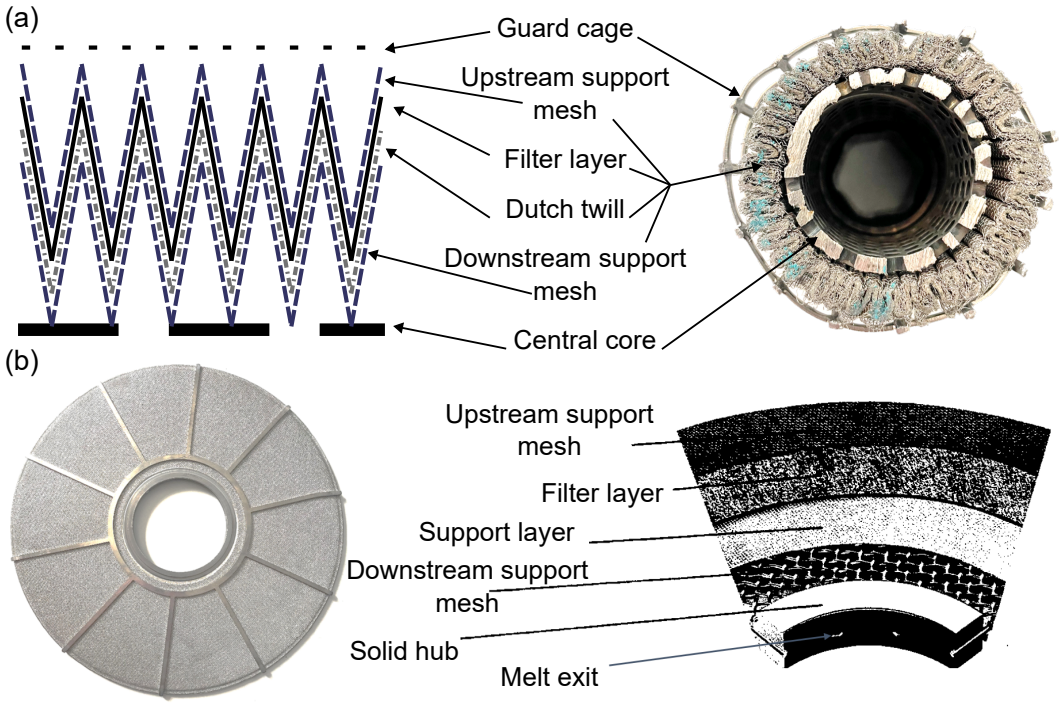

Figure 1.3: Structure of (a) a candle filter and (b) a disc filter. Image of disc filter structure from [12].

Mylar also utilize a pilot scale film line at the Global Innovation Centre. This line is known as the Semi-Tech, and is used for a variety of functions, including research and innovation. The

pilot scale line does not employ candle or disc filter packs. Instead, screen filters are used. A screen filter is a circular structure where filter medium is sandwiched between support mesh. The machine which holds a screen filter is designed so that each screen filter can be efficiently replaced mid run. The screen filter is inserted into a circular pipe so that the flow passes through its flat surface and the filter is supported by a filter holder. Figure 1.4 shows a sketch of the machine that houses screen filters, a cross section of the filter system surrounding the screen filter and a screen filter. The structure of a screen filter is relatively simple compared to the structure of a candle or disc filter element. The geometry of the filter system in which the screen filter is housed is also relatively simple. The structure of screen filters and the geometry of the filter system supporting them is discussed in detail in Chapter 4.

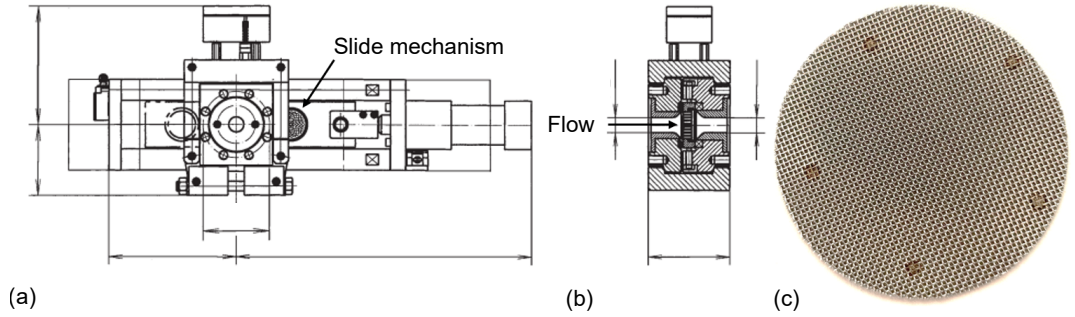

Figure 1.4: The device used by Mylar in the pilot scale line which houses the screen filter. (a) The view from the extruder. (b) A cross-section of the device. (c) A screen filter. Drawings from [13].

As more polymer melt is filtered, the filter medium collects more contaminants. These block pores, which decreases the porosity and permeability of the filter medium. This increases resistance to the flow, which leads to an increase in pressure drop through the filter pack over time. Figure 1.5 shows pressure evolution upstream of a screen filter in the pilot scale line. After an initial start-up jump, the pressure increases steadily. The rate of increase of pressure grows as time advances. A high pressure plateau implies that the process has been stopped due to a high pressure trip. Such a profile is typical of pressure drop over time for all filter designs in the sequentially stretched film casting process. This increase in pressure will eventually exceed pressure limits for the line and require a lengthy process interruption for

the filter to be changed. If the run is not stopped, this can lead to the final product failing quality checks as high pressures can force unwanted particles through the filter medium. At present, Mylar do not know what mechanisms of flow and filtration in the filter pack lead to observed pressure drop evolution curves.

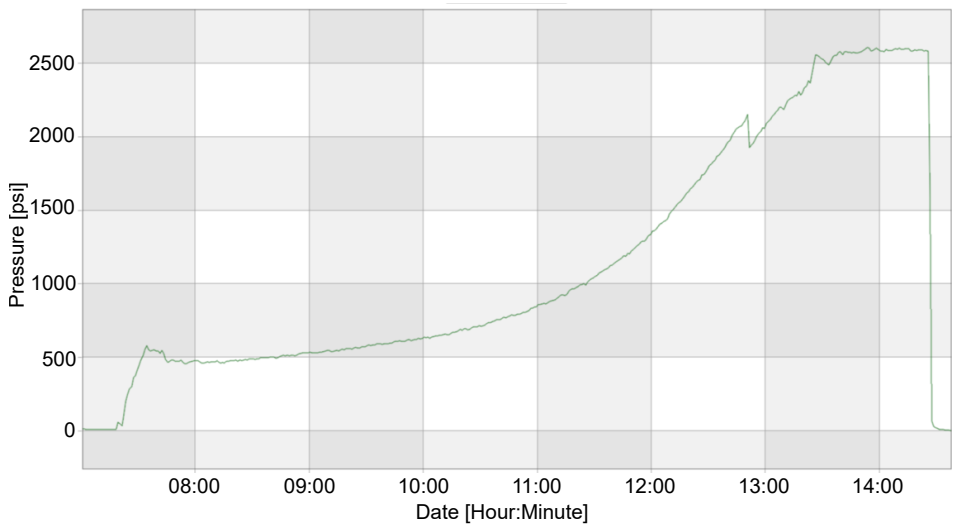

Figure 1.5: An example of pressure evolution due to filter blocking. Pressure recorded upstream of a screen filter on the pilot scale line.

1.3 Aims and objectives

The key aim of this research is to better understand how the blocking of filter elements in filter packs over time affects performance. To this end, novel CFD models of the flow of a polymer melt through, and the degradation of, single and seven candle filter packs are developed in ANSYS Fluent [14]. These models are used to understand how flow patterns alter as the filter medium blocks and to provide suggestions on how to enhance the current filter pack performance, efficiency and longevity. Objectives include:

- Establish a macroscopic CFD model of flow evolution through two candle filter packs which couples properties such as flow rates and filter medium permeability.
- Validate the model through comparison with pressure drop data from Mylar's sequen-

tially stretched film casting line.

- Analyse results from the model to inform understanding on the pressure drop evolution and flow behaviour of a polymer melt through candle filter packs.
- Establish how flow patterns alter as the filter medium blocks.

These are the overarching aims and objectives of the project. The following subsections give a breakdown of intermediate aims and objectives.

1.3.1 Clean candle filter pack modelling

Prior to the inclusion of filtration, it is necessary to develop viable models for flow through clean candle filter packs. To achieve this, virtual geometries are built from computer-aided design (CAD) engineering drawings of the packs provided by Mylar. The aims of this modelling are to have viable, validated macroscale models ready for the implementation of filtration modelling and to understand and compare flow distribution through different clean candle filter packs. The objectives of these models are:

- Establish and examine computational models of candle filter packs, identifying any symmetries in the flow distribution which could lead to simplifications in modelling.
- Create simplified macroscopic CFD models of flow through each clean filter pack.
- Calibrate models through comparison to pressure drop data from Mylar's sequentially stretched film casting line.

1.3.2 Screen filter modelling

Due to the complexity of the design of the candle filter packs, the screen filter is the initial subject of computational modelling. The aims of this model are therefore to develop the skills and tools necessary to model filtration through candle filter packs, and to understand

the mechanisms that lead to observed pressure drop evolution profiles, such as the pressure evolution profile observed in Figure 1.5. The objectives of this modelling are:

- Establish a macroscopic computational model of flow through a screen filter.
- Execute several experiments on the pilot scale line designed to investigate the physical behaviour of melts in a filter medium and the mechanisms that drive filtration.
- Validate the computational model through comparison with experimental data from the pilot scale line.
- Use the tools and insight derived from the screen filter model to assist in modelling candle filter packs.

Chapter 2

Literature Review

This chapter contains a discussion on the fundamental principles behind the mechanisms that drive polymer melt filtration. This includes polymer melt rheology, flow across a porous medium, and filtration principles. It also contains a review of previous published work on computationally modelling the flow of fluids across a porous medium and filtration. The literature surrounding polymer melt filtration is discussed.

2.1 Polymer melt rheology

Polymers are large molecules made up of many repeating elementary units, known as monomers [15]. The majority of polymers produced are thermoplastics. Thermoplastics are melted in processing, which allows moulding and can influence the mechanical properties of the final product [16]. Polymers have the widest range of flow and deformation behaviors compared to any other material [17]. They are viscoelastic materials and are classified as non-Newtonian fluids [1, 15, 16, 18, 19].

Polymer melts are incompressible fluids; their dynamics can thus be described by a coupling

of a simplified continuity equation and the Cauchy momentum equation. That is

$$\begin{aligned} \nabla \cdot \boldsymbol{u} &= 0, \\ \rho\left(\frac{\partial \boldsymbol{u}}{\partial t} + \boldsymbol{u} \cdot \nabla \boldsymbol{u}\right) &= -\nabla P + \boldsymbol{F} + \nabla \cdot \boldsymbol{\tau}, \end{aligned} \tag{2.1}$$

where ρ, $\boldsymbol{u}$, P, $\boldsymbol{F}$ and $\boldsymbol{\tau}$ are the fluid's density, the fluid's velocity vector, the pressure, body forces acting on the fluid and the stress tensor respectively. Fluids have the property that under deformation, rate of strain is proportional to shear stress. Viscosity describes a fluids resistance to shearing. Figure 2.1 shows a simple way of visualising viscosity. Consider a fluid trapped between two parallel plates of area A, with a gap h between them, where some force on the upper plate causes it to move at a velocity U relative to the lower plate. Viscosity is given by the ratio of the shear stress and the shear rate [16]. Shear stress is defined as the force per unit area and shear rate by the velocity divided by the gap, that is

$$\mu = \frac{F/A}{U/h} = \frac{\tau}{\dot{\gamma}}, \tag{2.2}$$

where $\dot{\gamma}$ is the shear rate. Rearranging gives

$$\tau = \mu\dot{\gamma}. \tag{2.3}$$

Equation 2.3 is Newton's law of viscosity. Viscosity is a material function that is a general property of a fluid [1]. A fluid is Newtonian if the viscosity is independent of shear rate. Conversely, a fluid is non-Newtonian if its viscosity is dependent on shear rate. The majority of polymer melts are shear-thinning non-Newtonian fluids. That is, as the shear rate applied to a polymer melt increases, its viscosity decreases. This is because as the shear rate imposed on a polymer melt increases, individual polymer chains disentangle and align, allowing easier movement relative to one another [16]. Typical melt viscosity varies from 150-300 Pa s for PET melt used for film applications [18].

The viscosity of a polymer melt can be described by several models. The most common model

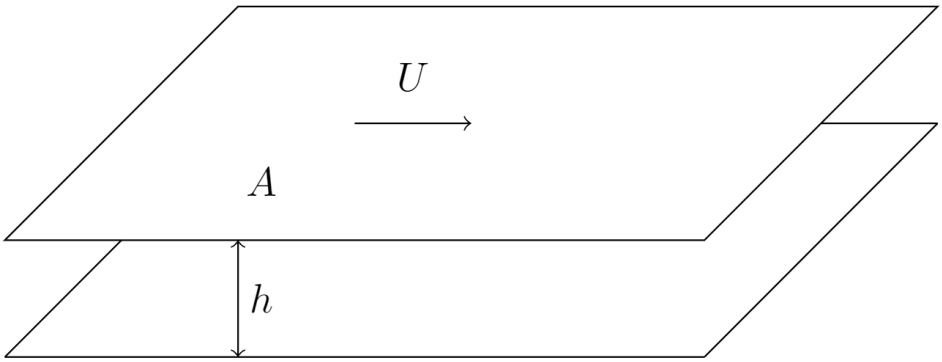

Figure 2.1: A drawing of a fluid trapped between two parallel plates, where the top plate moves at a velocity U relative to the bottom plate.

is the power-law model [1, 18, 19], given by

$$\mu = K_I \dot{\gamma}^{n-1}, \tag{2.4}$$

where n is the fluid's power-law exponent and K_I is the consistency index. For $n = 1$, the power-law model reduces to the Newtonian description. For $n > 1$, the fluid exhibits shear-thickening behaviour. For $0 < n < 1$, the fluid exhibits shear thinning behaviour, putting the value of n for polymer melts in this bracket.

The power-law model only holds for polymer melts over a certain range of shear rates. The viscosity of most polymer melts converges to some constant value in the limits of very small and very large shear rates. These constant values are known as the zero shear viscosity and the infinity shear viscosity [18]. The power-law model predicts viscosity to approach infinity at low shear rates. A widely used model which accounts for this is the Carreau-Yasuda model [20], which is given by

$$\mu = \mu_\infty + (\mu_0 - \mu_\infty) \left[1 + (\lambda \dot{\gamma})^2\right]^{\frac{n-1}{2}}, \tag{2.5}$$

where μ_0 is the zero shear viscosity, μ_∞ is the infinity shear viscosity and λ is a time constant.

Another common model is the Cross model [21], which is given by

$$\mu = \mu_\infty + \frac{\mu_0 - \mu_\infty}{1 + (\lambda\dot{\gamma})^{1-n}}. \tag{2.6}$$

Both models have been successfully correlated with experimental data, with the Cross model giving a better fit for commercial applications using polymers. [22].

Despite being classified as non-Newtonian fluids, polymer melts have constant viscosity and behave as Newtonian fluids in their zero shear viscosity range. The Newtonian assumption allows for simpler modelling as shear thinning can be omitted. This Newtonian assumption transforms the coupling of the continuity equation and the Cauchy momentum equation (2.1) into the incompressible Navier-Stokes equations:

$$\begin{aligned} \nabla \cdot \boldsymbol{u} &= 0, \\ \rho\left(\frac{\partial \boldsymbol{u}}{\partial t} + \boldsymbol{u} \cdot \nabla \boldsymbol{u}\right) &= -\nabla P + \mu \nabla^2 \boldsymbol{u}. \end{aligned} \tag{2.7}$$

2.1.1 Viscoelasticity in polymer melt flows

An inelastic fluid has no memory; the stress in the fluid depends only on the instantaneous strain rate. Entangled polymers should have memory; the response to deformation depends on the reorganisation of entangled chains. If a stress is applied to some polymer molecules in the entangled network, over a short timescale, other molecules will not have time to respond and disentangle, and the melt will act like an elastic solid [1]. If the applied stress is maintained, the network will have sufficient time to respond, and the polymer chains will disentangle and move like a viscous fluid [1]. Polymer melts are therefore classified as viscoelastic materials.

Viscoelastic materials can be classified by oscillatory rheology. Oscillatory rheology involves placing a fluid between two plates. One of the plates is oscillated sinusoidally relative to the other, at a frequency ω. That is, a shear strain $\gamma = \gamma_0 \sin(\omega t)$ is applied to a plate, giving a shear rate $\dot{\gamma} = \dot{\gamma}_0 \cos(\omega t)$. The fluid's linear shear stress response is then recorded as a

superposition of the forms of the shear strain and shear rate:

$$\tau = G'(\omega)\sin(\omega t) + G''(\omega)\cos(\omega t), \tag{2.8}$$

where G' is the storage modulus and G'' is the loss modulus. For viscous fluids, shear stress is proportional to shear rate. Therefore the linear stress response (2.8) would be in phase with shear rate, implying $G' = 0$. Similarly, for an elastic solid, shear stress is proportional to shear strain [1]. Therefore the linear stress response (2.8) would be in phase with shear strain, implying $G'' = 0$. The storage modulus and the loss modulus therefore measure the magnitude of an elastic and viscous response to deformation respectively. For a viscoelastic material, both G' and G'' would be non-zero.

For PET used at shear rates associated with the film casting process by Mylar, it is found that the loss modulus dominates the storage modulus [18]. This can be seen from a rheometer test on a 0.61 IV PET melt, a typical polymer used in processing. Figure 2.2 shows that for a 0.61 IV PET melt over a range of shear rates, the loss modulus is shown to be at least an order of magnitude larger than the storage modulus, suggesting it is the dominant factor in the melt's linear shear stress response.

Note that the term IV denotes the intrinsic viscosity of a polymer, with units of dL/g. IV is described as a measure of the ability of a polymer in solution to increase the viscosity of that solution and is measured either directly using solution IV techniques or is inferred from the melt viscosity measured via a capillary or parallel plate melt rheometer. IV is a function of molecular weight; an increase in molecular weight causes an increase in IV.

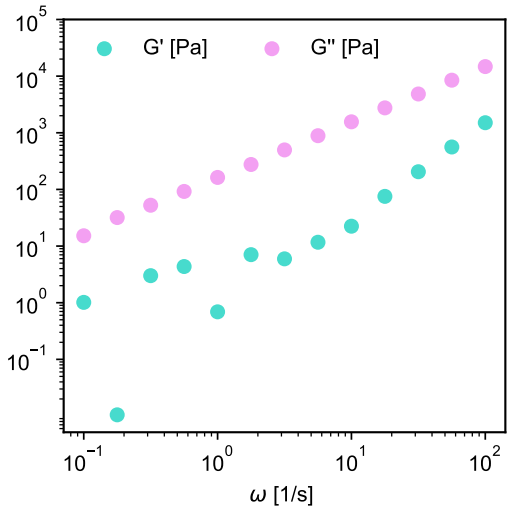

Figure 2.2: Storage modulus and loss modulus against frequency for a 0.61 IV PET melt at 280°C. From a rheometer test using a TA DHR-1 parallel plate rheometer with an oscillation sweep method. Data provided by Mylar.

2.1.2 Temperature and other effects

The viscosity of polymer melts does not just depend on shear rate. In fact, melt viscosity depends on factors such as temperature, pressure, the use of a filler or an additive and the molecular weight [18]. The transition from zero shear viscosity to shear thinning is gradual for polymer melts with a large molecular weight distribution. In industrial processes, polymers are likely to contain a large molecular weight distribution [1]. Fillers are often added to the melts. Fillers are used to modify surface or bulk properties [3], for example, particulate fillers may be used to create surface roughness. This is typically to reduce the blocking or sticking of the film during winding [3]. An increase in temperature leads to a decrease in polymer melt viscosity. Figure 2.3 shows how melt viscosity changes with temperature for the 0.61 IV PET melt. PET melt is usually maintained between 280-310°C, above its melting temperature [3]. It can be seen that melt viscosity is strongly influenced by temperature; a 40°C decrease leads to over a 250% increase in melt viscosity. It is therefore critical to carefully maintain the temperature of the melt throughout processing.

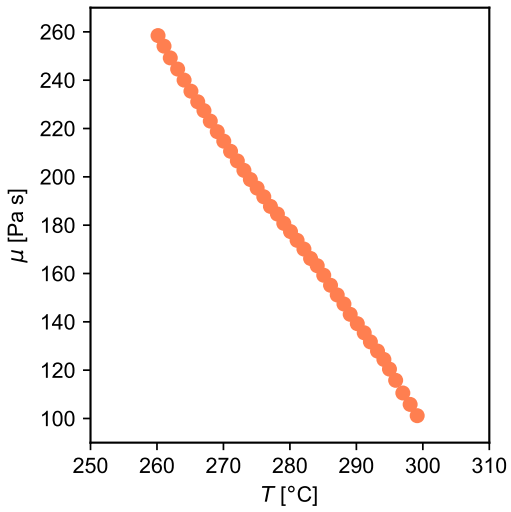

Figure 2.3: Melt viscosity against temperature for a 0.61 IV PET melt. From a parallel plate rheometer test at Mylar.

The viscosity of polymer melts varies with temperature in an exponential manner [23]. Within Mylar, a model developed in-house is used to represent the viscosity-temperature relationship:

$$\mu = 0.1 \left[10^{\left(\frac{5 \ln \alpha}{2.30259} + \frac{2953}{T} - 0.9508 \right)} \right], \tag{2.9}$$

where T is the melt temperature in Kelvin and α is the IV of the polymer. The Vogel-Fulcher-Tammann equation, which uses a similar exponential form as (2.9), is frequently used to describe the temperature dependence on viscosity for polymer melts [24]. Wang et al. [25] also highlight two of the most commonly used equations for expressing viscosity-temperature behaviour of polymer melts. One is an Arrhenius type equation and the second is the WLF equation [25], both express the relationship as an exponential decay in viscosity with increasing temperature. The in-house model has been found internally within Mylar to give an excellent correlation to PET rheology for modelling purposes.

In order to maintain the molten state of the polymer through the film casting process, the temperature of the melt must be maintained. To this end, pipes are heated through either

electric elements attached to the outside of the pipe or the pipes are encased in a jacket charged with a thermal transfer fluid.

A combination of high temperatures and long processing times leads to the thermal degradation of polymer melts. Thermal degradation is the molecular deterioration of polymer chains as a result of heating, and leads to the separation and reaction of chains [26]. It occurs due to the instability of macromolecules under heat treatment and may affect either the main chain linkages or substituent atoms and side chains [27]. Main chain linkages may break or crosslink; the former leading to a molecular weight decrease and the latter leading to gel formation and a molecular weight increase. Reactions at the side chains or substituent atoms may lead to their elimination or cyclization, and the release of free radicals; the former resulting in the main chain reactions described above. Gels lead to a variety of visual defects in the finished product [28]. It is desirable for filters to remove gels from the process. Gels are deformable and can be broken up by the filter medium [11]. High molecular weight molecules and free radicals may change the physical and optical properties of the melt, affecting the final product.

2.2 Flow through a porous medium

A porous medium is a solid structure which contains interconnected pores. The pores often form a large network of interconnected voids, allowing a fluid to pass through the medium. Porous media are found in natural systems and are used for engineering processes. Examples in natural systems range from transport through river sediments to extra-cellular transport in brain tissue [29]. Examples in engineering process include hydrocarbon recovery to filtration systems [29]. A porous medium may be categorized by pore location, shape and size, as well as the extent of pore interconnectedness [30]. A porous medium has an associated porosity. Porosity describes the fraction of void space in a medium [31].

A porous medium may be described on the macroscale or at the pore scale [31]. At the pore scale, porosity, permeability, tortuosity and connectivity describe the structure of the mate-

rial [32]. Permeability describes the ability of a medium to allow fluids to pass through it. Due to the scales of size between a porous medium and the pore structure, the descriptors at the pore scale vary enormously throughout the medium [31]. As such, a statistical distribution or averaging methods are often used to represent porosity, permeability, tortuosity and connectivity across a medium [10, 33–35].

At the macroscale, the description of a porous medium is determined by bulk properties that have been averaged at larger scales compared to the pore size. A microscopic description is important for the study of transport behaviour of flow passing through a porous medium [36]. The macroscopic approach may be sufficient for process design where fluid flow and mass transfer are the focus of an investigation [37].

Flow through a porous medium may be described by Darcy's law. It is given by

$$\Delta P = \frac{q\mu d}{k}, \tag{2.10}$$

where ΔP is the pressure drop through the porous medium, q is the volumetric flow rate per unit area, d is the thickness of the porous medium and k is the permeability of the medium. Permeability is a function of only the pore structure [30]. Darcy's law is observational and applies for Stokes flows; higher order corrections exist for higher Reynolds number flows [38]. This is because Darcy's law does not account for inertial effects, which are insignificant in low Reynolds number flows. For Darcy's law to be valid, it is therefore necessary that $\mathrm{Re} < 1$, where Re is the Reynolds number; it measures the ratio between viscous and inertial forces [39] and is given by

$$\mathrm{Re} = \frac{\rho u L}{\mu}, \tag{2.11}$$

where L is a characteristic length scale of the geometry. In a porous medium, this is often defined as the typical diameter of a pore in the medium.

Permeability of a porous medium is usually determined using Darcy's law. For example, experimentally, a volumetric flow rate through a porous medium may be varied and the

pressure drop output measured. If the relationship is linear, Darcy's law applies, and the slope of the line can be used to calculate the permeability if the density and viscosity of the fluid is known [40].

The Darcy-Forchheimer equation accounts for inertial effects in porous media [38]. It can be expressed as

$$\Delta P = \frac{q\mu d}{k} + \frac{C_F \rho d q^2}{\sqrt{k}}, \tag{2.12}$$

where C_F is a Forchheimer coefficient. The first term represents Darcy's law, accounting for the viscous effects. The second term is a second order correction to Darcy's law, representing the inertial effects [41]. Finding the Forchheimer coefficient is often determined experimentally [42].

The flow of a non-Newtonian fluid through a porous medium requires further consideration. Non-Newtonian rheology has a major impact on flow characteristics in porous media [43]. There has been little progress in the theoretical understanding of what occurs during non-Newtonian flow in porous media [43]. Furthermore, viscoelastic flow through porous media is far from being understood [44]. For the flow of viscoelastic fluids in porous media, shear, rotational and elastic effects can arise [44]. Sochi et al. [45] review non-Newtonian flow in porous media and conclude that no general methodology can deal with all cases of non-Newtonian flow through porous media and only modest success has been achieved by the state of the art methodologies for modelling this phenomena. A viscoelastic fluid may not exhibit any elastic behaviour in a porous medium due to plateaus in the rate of strain-viscosity relationship [45].

At typical film casting processing shear rates ($\dot{\gamma} \ll 150\text{s}^{-1}$), the viscosity of polyester melts is constant at constant temperatures and the flow is considered Newtonian in the extrusion system. Champion [18] confirms the Newtonian assumption at typical processing shear rates for a range of different PET IV grades. However, this Newtonian behaviour has not been investigated through filter media, where the microstructure of a porous medium can lead to a broad range of flow velocities and shear rates [46]. An experiment is therefore undertaken

to investigate the behaviour of a typical PET melt in screen filters in Chapter 4.

2.3 Filtration

The process of separating solid particles and fluid from a suspension using a filter medium is known as filtration. Both solid-liquid and solid-gas separation are common; the filtration of polymer melt flows is of the solid-liquid type. In industrial applications, the performance of a filter can be assessed by the pressure drop through the filter, the filtration efficiency and the particle holding capacity. The solid-liquid suspension fed into a filter system is often referred to as the feed. After passing through the filter, the suspension is then referred to as the filtrate.

A filter medium must be impermeable to some components of a suspension, but permeable to the other components [47]. Many different structures and materials can be used as a filter medium. Examples include woven, non-woven and sintered structures. The performance of a filter medium can be influenced by the microstructure of the media, the material used, deformations of the media under operating conditions, etc. [10]. It is not realistic to expect every single solid particle to be filtered out when passing through a filter medium. As such, a filter medium may be defined by a cut off size. For example, a manufacturer may specify that a significant percentage of all particles larger than a certain size will be filtered under certain operating conditions for a given filter medium [48].

There are many different types of filter media employed in industry. Candle filters exclusively use sintered metal fibres. Fibres are around 20 mm long and have diameters of a few microns. This leads to a voidage of over 60%. The filter material is often made by sintering together two or more grades of media, with the outer layer being made coarser through thicker fibres. The filter medium of disc filters may be sintered fibre or sintered powder. The voidage in sintered powder is around 30%. The size of individual particles that make up sintered powder used by Mylar vary from 40 to 200 microns. The larger voidage of sintered fibre gives a lower

pressure drop through the medium, and a greater dirt holding capacity. However, this also leads to worse solid particle and gel retention. On the pilot scale line, screen filters comprise of multiple layers of woven wire mesh.

There are two main types of solid-liquid filtration: depth filtration (deep bed filtration) and surface filtration. Surface filtration occurs when the average size of solid particles in the suspension is comparable to the average pore size of the filter medium. Solid particles are then captured on the surface of the filter medium. As more of the suspension passes through the filter, more particles are captured and pile up on the filter medium surface, forming a filter cake [49]. The filter cake acts as a filter itself, and is typically more effective at filtering out solid particles from the suspension than the filter medium [50]. Depth filtration occurs when the average size of solid particles in the suspension is a lot smaller than the average pore size of the filter medium. Particles then easily penetrate the top layer of the filter medium, and are instead captured inside the medium [51]. Figure 2.4 visualizes both surface and depth filtration. In reality, there will be a distribution of particle sizes present in the suspension. It is therefore common for both types of filtration to occur for any given filtration process [52].

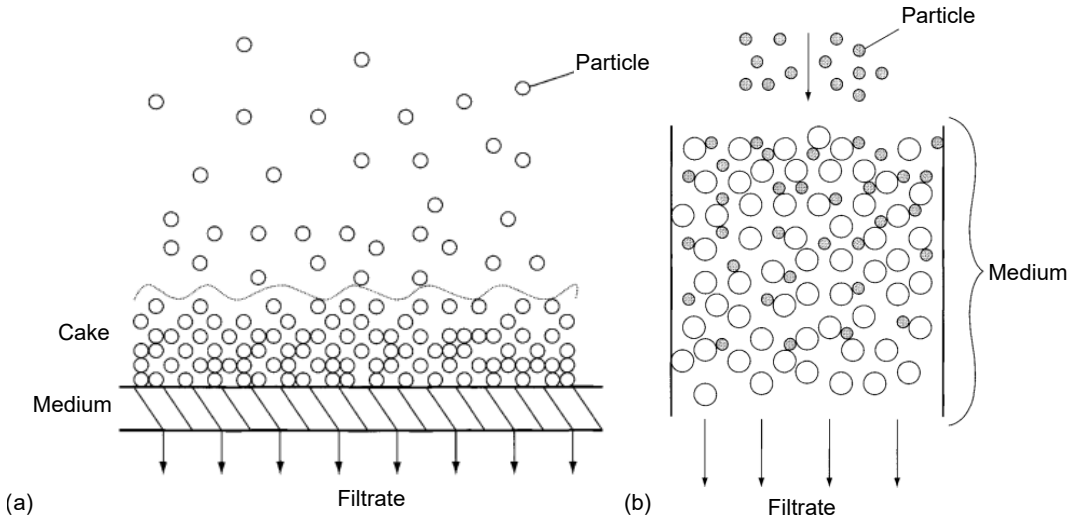

Figure 2.4: Illustration of (a) surface filtration and (b) depth filtration. Diagram obtained from [53].

Particles may be deposited inside a filter medium through several different mechanisms. In-

ertial impaction, interception, electrostatic forces and Brownian diffusion lead to particle deposition in depth filtration; straining leads to deposition in surface filtration [54]. Inertial impaction occurs when solid particle trajectories intersect with the filter medium surface. Interception occurs when a solid particle comes within its own radius of the filtering medium's solid surface. If solid particles are charged, or the filtering medium is charged, electrostatic forces can influence particle deposition. If solid particles are small enough, the Brownian diffusion force leads to particle deposition. Straining is the mechanism behind cake filtration; it occurs when solid particle sizes are larger than pore constriction sizes. After deposition, it is possible for particles to detach and be re-entrained by the flow [54]. Particles may be detached by the lift force imposed on them by the flow. The drag force imposed by the flow may cause rolling or sliding along the filter medium's surface.

Solid-liquid filtration processes are often configured under constant rate or constant pressure filtration. The constant rate condition maintains a constant throughput throughout the filtration process. This leads to a pressure drop rise across the filter over time. Conversely, the constant pressure condition leads to flux decline. In most cases, laboratory testing of filter systems is performed with the constant pressure condition [55]. Constant rate filtration is more common in industrial processes [55]. Constant rate filtration is used throughout the film casting process.

Two types of solid-liquid filtration are commonly used in industrial processes; dead-end and cross-flow filtration. In dead-end filtration, all of the flow is forced through the filter medium [56]. In cross-flow filtration, the feed flow and the filtration flow direction are at a 90° angle [57]. Figure 2.5 illustrates the differences between dead-end and cross-flow filtration. In cross-flow filtration, not all of the feed is filtered; anything that does not pass through the filter is retained and referred to as the retentate. Cross-flow filtration increases the length of time for which a filter can be operational as the filter cake is washed away with the retentate. Dead-end filtration is simpler to operate and has a high filtrate recovery. All filter packs used by Mylar result in dead-end filtration. All of the melt must pass through filters in the pack before moving onto the next stage of production.

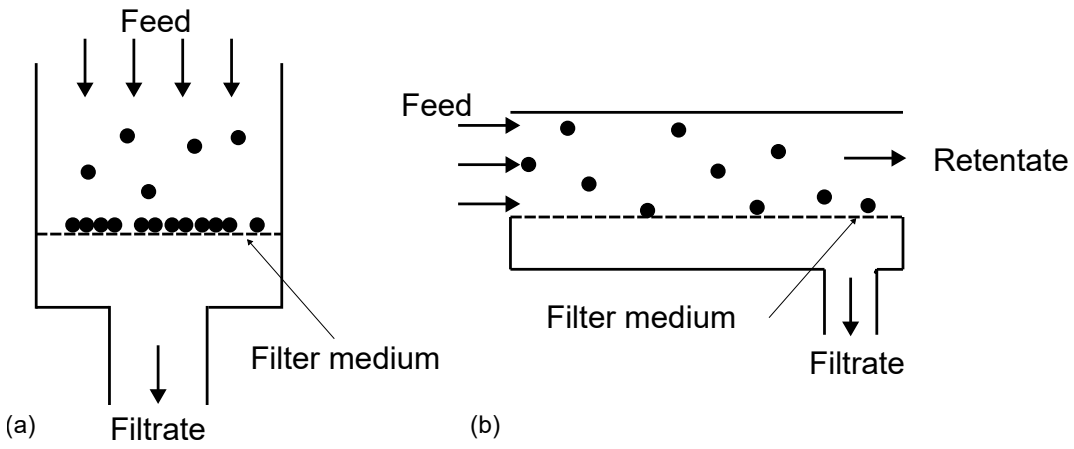

Figure 2.5: Illustration of (a) dead-end filtration and (b) cross-flow filtration.

In industrial applications, it is important to consider filter element design. For example, a filter medium may be encased with support mesh. This mesh may influence the flow field, and even block off some of the filter medium, reducing the filtration area. The shape and size of a filter element will influence the filtration process. For example, pleated filter panels have a larger filtration area to volume ratio and are more compact than a flat sheet filter medium [58]. The housing of a filter element may be restricted depending on the application. Such restrictions will affect how the flow distributes around the filter medium and, in turn, the pressure drop through the element.

2.3.1 Filter blocking models

Several mechanistic models have been developed to describe how a filter blocks with particles over time for both pore blocking (depth filtration) and cake filtration [59]. Among them, four standard mechanistic models are used to describe how filters block with particle deposition [60]. There is the complete blocking model, the intermediate blocking model, the standard blocking model and cake filtration. These models were initially proposed in the context of constant pressure filtration, but have since been reworked to suit constant rate filtration [61]. As constant rate is utilized for film production as a constant flow rate must be maintained to

ensure film consistency, the models are considered in this context. The models are all derived from Darcy's law [60]. In terms of mass flow rate, Darcy's law (2.10) may be written as

$$\dot{m} = \frac{\Delta P \rho A}{R\mu}, \tag{2.13}$$

where R is the resistance of the filter imposed on the flow and $\dot{m}$ is the mass flow rate. Initially, when no filtration has taken place, $R_0 = d/k$.

The complete model assumes that particles are intercepted at a pore surface, sealing it off. The intermediate model additionally assumes that particles can then accumulate on top of previously deposited particles. The standard model describes pore constriction as particles deposit on the surfaces of pore walls. Cake filtration describes the accumulation of particles on the surface of the filter medium; the cake formed from this accumulation increases in thickness as more particles accumulate. Iritani and Katagiri [59] reviewed the developments of these models. The models provide a powerful tool to reasonably evaluate the behaviour of filtration resistance [59]. Figure 2.6 shows an illustration on the filtration mechanisms represented by each model. The mathematical expressions describing each constant rate blocking model are presented below. The rigorous theory of each constant rate blocking model is given in detail in [61].

The complete blocking model describes the available filter medium area as decreasing with time according to

$$\frac{A}{A_0} = 1 - K_b \dot{m} t \tag{2.14}$$

where A_0 is the initial filter media frontal area, K_b is the complete blocking constant and the mass flow rate is constant [59]. Substituting (2.14) into Darcy's law (2.13) gives pressure drop across the filter medium as a function of time:

$$\Delta P = \frac{\Delta P_0}{1 - K_b \dot{m} t}, \tag{2.15}$$

where ΔP_0 is the initial pressure drop across the filter, before any fouling has taken place.

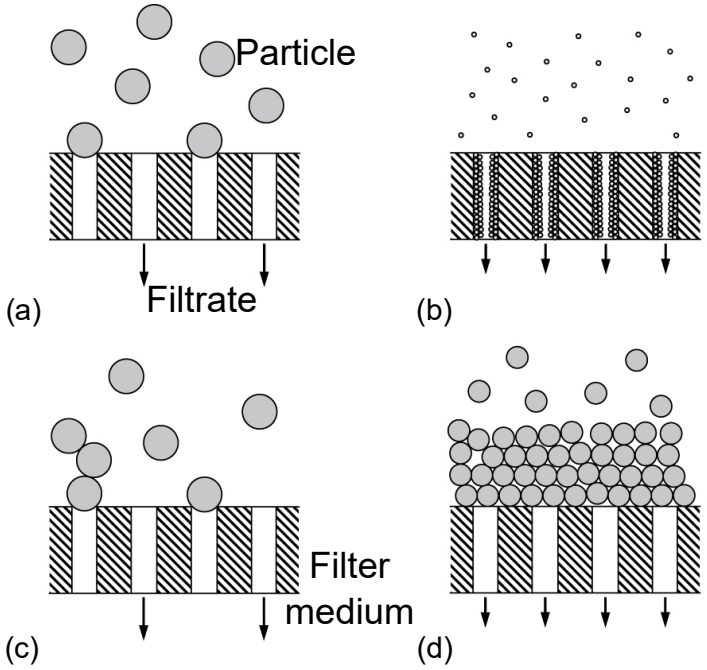

Figure 2.6: Schematic view of fouling patterns represented by (a) complete blocking (b) standard blocking (c) intermediate blocking and (d) cake filtration. Diagram obtained from [59].

The intermediate blocking model describes the available filter medium area as decreasing with time according to

$$\frac{A}{A_0} = \exp(-K_i \dot{m} t), \tag{2.16}$$

where K_i is the intermediate blocking constant [59]. Substituting (2.16) into Darcy's law (2.13) gives

$$\Delta P = \Delta P_0 \exp(K_i \dot{m} t). \tag{2.17}$$

The standard blocking model describes the resistance of the filter medium as a function of time, where pores in the filter are assumed to be straight and cylindrical which decline in radius [59]. The resistance evolution is given as

$$R = R_0 \left(1 - \frac{K_s \dot{m} t}{2}\right)^{-2}, \tag{2.18}$$

where K_s is the standard blocking constant. Substituting (2.18) into Darcy's law (2.13) gives

$$\Delta P = \frac{\Delta P_0}{\left(1 - \frac{K_s \dot{m} t}{2}\right)^2}. \tag{2.19}$$

For cake filtration, the total resistance is the sum of filter medium resistance and cake layer resistance [59]. The resistance evolution is given as

$$R = R_0(1 + K_c \dot{m} t), \tag{2.20}$$

where K_c is the cake filtration constant. Substituting (2.20) into Darcy's law (2.13) gives

$$\Delta P = \Delta P_0(1 + K_c \dot{m} t). \tag{2.21}$$

These models can be used individually to explain experimental observations [60]. Hlavacek and Bouchet [61] fitted the models to experimental pressure drop evolution curves for constant flow rate filtration of bovine serum albumin (BSA) solutions and found that the intermediate model gave the best fit. Scanning electron micrographs showed the fouling was mainly due to particle surface deposits, showing that the intermediate model was an appropriate choice. Ito et al. [62] fitted the models to dead-end filtration in bio-process applications. It was found that filtration behaviours differ for different bio-processes and types of filter, hence the suitability of each model changes on a case by case basis. Bowen and Gan [63] found that BSA fouled microporous aluminum oxide internally due to the exceptional fit of the standard model to experimental data.

Several mechanisms may combine to simultaneously or consecutively foul a filter [62]. Combinations of filter blocking models have been described to evaluate situations where several fouling mechanisms occur simultaneously or consecutively, which is frequently observed [59]. Tracey and Davis [64] found that filter fouling by BSA could be fitted initially by either the complete model or standard model (depending on filter choice) and subsequently by cake

filtration. This is because pores eventually became so constricted that a cake layer began to form on the filter medium surface. Taghavijeloudar et al. [65] detailed a model that combined the complete model and cake filtration which gave good agreement to experimental data for the filtration of wastewater sludge. Kirschner et al. [66] extended blocking models' utility to constant flux crossflow filtration and found a combined model of intermediate blocking and cake filtration gave a good fit to experimental data of the filtration of a latex bead suspension. Many combinations of the blocking models have been proposed and are detailed in [59]. Cheng et al. [67] developed a general blocking equation based on the Hagen-Poisseuille equation, which summarises the blocking models which have been proposed in the literature.

Ito et al. [62] stated that combining models generally gives a superior fit to experimental data due to the increased flexibility of an increased number of fitting parameters. This presents an issue with combining models; it is possible that combined models show improved fit not due to an improved physical representation, but rather an increased flexibility due to an increase in number of fitting parameters. Cheng et al. [67] concluded that simply fitting blocking models to data does not suffice to justify the observed blocking behaviour without assessing the structure of the filter itself. As such, the simpler models should be fitted to experimental data first and the fouling mechanism that each model represents should be considered before any conclusions are drawn. If a simpler model gives a good fit to experimental data and the filtration mechanism they represent is appropriate for the specific application, then it is sufficient in representing the experimental data. If the simpler models all give a poor fit, then combined models should be considered for fitting, as long as the combination of filtration mechanisms represented is logical for the specific application.

Blocking models have also been modified for non-Newtonian flows. The blocking models have been modified specifically for the power-law model representation of non-Newtonian fluids. The theory for using the power-law model to modify blocking models for power-law non-Newtonian flows is detailed in [59]. These models incorporate the fluid's power law exponent and reduce to the Newtonian formulations if $n = 1$. Iritani et al. [68] tested these models by filtering a suspension of diatomaceous earth in non-Newtonian fluids. It was shown that

the intermediate non-Newtonian blocking model fitted well to the data when particle size was larger than pore size; the standard model gave the superior fit in the case where the particle size was smaller than the pore size [68].

2.4 CFD modelling of flow through a porous medium

Modelling flow through a porous medium can be separated into two distinct categories. Modelling may be microscopic, where pore-scale simulations are undertaken to directly solve transport processes in realistic porous structures [69]. Pore-scale models aim to capture all the features of the microscopic structure of a porous medium and predict fluid flow and transport behaviour within the porous medium. Pore-scale modelling can provide deep understanding of the relationship between structures, processes and performance [69].

On the other hand, modelling may be macroscopic, where the porous medium is treated as a continuum and averaged representations of microscale properties, such as permeability, are used. Then, a continuum equation such as Darcy's law can be used to predict the behaviour of fluids in the porous medium. This approach simplifies the complexity of the pore scale and allows for the study of larger systems. Macroscopic models are computationally efficient [70]. Macroscale models are often chosen for industrial system assessment [70].

Figure 2.7 shows an example of a pore-scale geometry and a macroscopic filter system geometry. Pore-scale models require very fine spatial resolution to capture details of a pore structure. It would require a vast number of computational cells to model large elements that are resolved at the pore scale. Furthermore, pore-scale details are often unnecessary for understanding macroscopic behaviour. Macroscopic models have made great progress at the scale of engineering interest [69]. However, microscale heterogeneity of a porous medium structure can greatly affect system performance [69]. It is therefore important to carefully consider the scale of the computational model when modelling flow through a porous medium depending on the aims and objectives of the research.

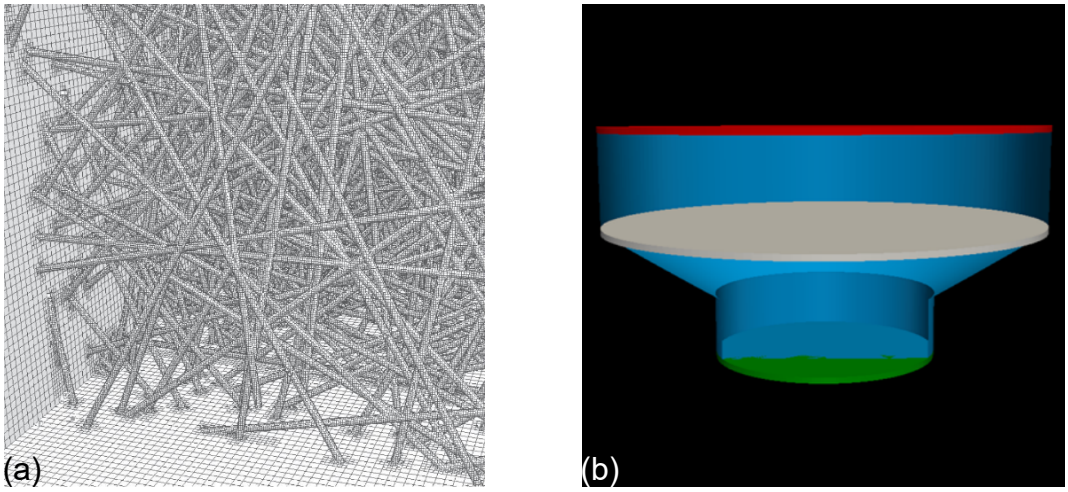

Figure 2.7: (a) An example of a virtual pore-scale geometry of a sintered fibre structure. Image adapted from [71]. (b) An example of a virtual macroscopic geometry of a filter element, where the green and red surfaces are the outlet and inlet respectively. The blue volume is the fluid domain and the grey volume is the macroscopic representation of the filter medium. Image from [10].

2.4.1 CFD modelling of flow through a porous medium at the microscale

The first challenge of modelling at the microscale is creating a virtual geometry that accurately represents the desired porous medium at the pore scale. Simply using virtual idealized geometries which fail to capture variations in the medium, such as changes in the diameter of fibres, may not sufficiently represent their real counterparts, which could impact the accuracy of results [72]. Previously, Sambaer et al. [72] used a scanning electron microscope (SEM) to capture the pore scale geometry of a nanofiber based nonwoven filter. Images were then converted into a three-dimensional (3D) structure model. More recently, Abishek et al. [71] proposed modern methods in generating virtual geometries and argued that pore-scale geometries could be accurately represented through virtual generation. Pressure drop results obtained from CFD simulations run with both the virtually generated geometries and geometries generated through conversion from SEM images showed good agreement.

For the generation of virtual sintered structures, micro X-ray computed tomography (μCT) is often employed. μCT is nondestructive and can give detailed images of the structure of

a porous medium down to a few hundred nanometres [73]. Georgiadis et al. [74] created a virtual sintered glass-bead sample using μCT images. Jung et al. [75] used μCT to acquire images of slices of a sintered titanium porous medium. Images were filtered by removing noise and artifacts. Images were then segmented and edges from the segmented image were overlaid onto the filtered images. A pore network was then extracted with an open source porous media image analysis toolkit.

To simulate at the pore scale, it is necessary to solve for fluid flow. A Newtonian, steady, incompressible, viscous flow is described by the Navier-Stokes equations (2.7). The no-slip condition applies at solid boundaries. Typical inlet conditions involve prescribing a known velocity or flow rate normal to the boundary. A prescribed pressure is a typical outlet condition.

Meshing presents a significant challenge for the completion of a successful pore-scale simulation. To resolve the fine details of a pore structure, the mesh must be extremely fine and adaptable. The high resolution required results in a significant computational cost to generate and numerically solve for fluid flow across the mesh [76].

Aminpour et al. [77] conducted lattice Boltzmann simulations to explore pore-scale flow behaviour for flows that obey Darcy's law. A static porous medium composed of fixed spherical particles was created. A dynamic porous medium was also tested, where particles constantly spin with different angular velocities around fixed axes. Pore-scale flow structures were observed to remain dynamically similar in the static case over a range of different Re where Darcy's law is applicable. Darcy's law was proved to be applicable in both cases.

Yang et al. [78] modelled laminar flow and heat transfer through a woven wire mesh at the pore scale. The model was validated with comparison to experimental data. A Dutch twill weave was modelled, where weft wires alternatively pass under and over warp wires. As the Reynolds number increased, increased inertial forces resulted in flow reversal in the wake of weft wires and convective heat transfer occurred mainly at the impinging surface of the weft wires [78].

2.4.2 CFD modelling of flow through a porous medium at the macroscale

Modelling at the macroscale does not depend on the pore scale geometry of a porous medium. Instead, the porous medium is defined as a porous zone [10, 52, 79, 80]. Consider a porous element on the domain Ω. The domain may be categorized by two subdomains, the fluid region and the porous region. Then

$$\Omega = \Omega_f \cup \Omega_p,$$

where Ω_f is the fluid region and Ω_p is the porous region. Note that there is no overlap between regions. Boundaries of the domain, $\partial\Omega$, may be subcategorized by inlets, outlets and solid boundaries. That is

$$\partial\Omega = \partial\Omega_{in} \cup \partial\Omega_{out} \cup \partial\Omega_s,$$

where $\partial\Omega_{in}$ represents inlet boundaries, $\partial\Omega_{out}$ represents outlet boundaries and $\partial\Omega_s$ represents solid boundaries. Inlet and outlet conditions are specified based on each problem. The no-slip condition applies at solid boundaries. Figure 2.8 shows a simple illustration of a two-dimensional (2D) porous element domain.

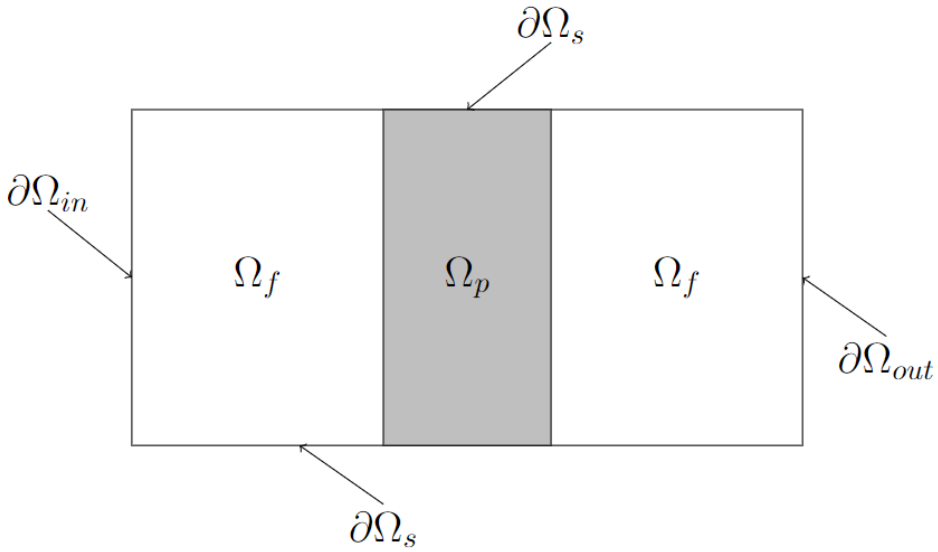

Figure 2.8: An example domain Ω for a simple 2D filter element.

The porous medium is assumed to be a homogenized continuum. Again, assuming a Newtonian, incompressible, viscous flow, the flow field is computed by the Navier-Stokes equations (2.7) outside of the porous zone. A popular model used in CFD to macroscopically model flow in the porous zone is the porous media model [14], which prescribes some properties to a cell zone in the computational geometry, the porous zone, imposing a pressure penalty through it.

The porous media model assigns an additional source term in any cell zone where it is enabled, such that

$$\rho\left(\frac{\partial \boldsymbol{u}}{\partial t}+\boldsymbol{u}\cdot\nabla\boldsymbol{u}\right)=-\nabla P+\mu\nabla^2\boldsymbol{u}+\boldsymbol{S}. \tag{2.22}$$

This source term accounts for the additional pressure drop due to the resistance imposed on the flow by the porous medium and is given by

$$\boldsymbol{S}=-\left((\mu/k)\boldsymbol{u}+0.5C_F\rho|u|\boldsymbol{u}\right). \tag{2.23}$$

Note that the source term is in the form of the Forchheimer equation (2.12). The Forchheimer coefficient is usually determined through empirical relations and $C_F = 0$ if Darcy's law applies.

The porous media model has been used to predict pressure drop through porous media in a range of flow applications. Pashchenko et al. [81] determined the pressure drop characteristics for fixed bed reactors filled with porous particles using a porous zone with an average error of less than 10%. Cornejo et al. [82] computationally modelled the pressure drop through a monolith using a multi-zone model. Multiple porous zones were employed to account for entering, passing through and leaving the substrate. This was seen to improve accuracy of the total pressure drop across the monolith compared to prior models.

Teitel [83] found that the pressure drop through a screen can be determined by the porous media model, reducing computational time significantly as there was no need to refine the mesh to resolve flow near screen wires. Teitel [84] used a porous zone to represent a woven screen to investigate if the Forchheimer coefficient is constant over a wide range of Reynolds numbers.

Garg et al. [85] modelled a stacked woven wire mesh with a porous zone in a miniature Stirling cryocooler, with the goal of capturing accurate heat transfer characteristics. A local thermal equilibrium model and local thermal non-equilibrium model were used to model the energy equation in the porous zone; the non-equilibrium model was shown to give better understanding of the heat transfer characteristics in the stacked wire mesh. Trilok et al. [86] used a porous zone to model the pressure drop across stacked woven wire mesh for heat exchanger applications. Pressure drop across the stacked mesh was in good agreement with an experiment, with an average discrepancy of less than 8%.

2.4.3 CFD modelling of non-Newtonian flow through a porous medium

Simulations modelling non-Newtonian flows through a porous medium have been undertaken. De et al. [44] used CFD to model creeping flow of a viscoelastic fluid through a 3D random porous medium. The continuity and momentum equations were coupled with a constitutive equation for the non-Newtonian stress components and it was found that energy in porous media is mainly dissipated in shear dominated regimes, even at high viscoelasticity [44].

Hauswirth et al. [87] computationally modelled non-Newtonian flow through a 3D packing of non-overlapping spheres. The Cross model (2.6) was used to include shear rate dependent dynamic viscosity in the numerical simulations, which used the lattice Boltzmann method. The methodology developed was found to capture the behaviour of non-Newtonian flow in porous media through validation with experiments and alternate numerical approaches.

Rath and Terzis [88] investigated the transport of non-Newtonian fluids through a porous medium consisting of an array of uniformly arranged square pillars. The power-law model was used to include viscosity-shear rate dependence in this case. Simulations ran over a large range of Reynolds numbers and power-law exponent values. Two main microscopic flow features were identified; stream-wise momentum and flow leakage. These characteristics of the flow were found to be highly influenced by Reynolds number and power-law exponent.

Macroscopic models for computationally modelling non-Newtonian flow through a porous medium have had little development. Models are usually based on Darcy's law, with a constant effective viscosity term used to represent the shear-dependent viscosity of a non-Newtonian fluid. There is no consensus on what this effective viscosity represents physically [43]. Typically, the effective viscosity is calculated from a porous medium shear rate [89–91], which is the average shear rate that the fluid experiences when moving through a porous medium. Alternatively, analytical models of non-Newtonian flow through capillary tubes are used to obtain a definition of effective viscosity [92, 93].

2.5 CFD modelling of filtration processes

To computationally model a filtration process in its entirety, a model needs to capture the interaction between the fluid and the filter medium, the transport of solid particles in the fluid, the capture and deposition of solid particles and the interaction between particles in the suspension [10]. An added difficulty comes from the fact all these processes are coupled. Deposited particles in a filter medium act as part of the filter medium itself, changing the geometry at the pore scale. This results in a change in the flow field and the pressure distribution across the filter medium, which in turn influences the transport and deposition of solid particles. The filter medium may also be deformed by the flow field [94]. For example, an increased pressure may lead to warping of the filter medium, influencing particle deposition and potentially forcing through already captured particles. The computational cost of simulating such a complicated process over an entire filter element or system is unrealistic at present [95].

In order to keep computational costs down, simulations of filtration processes have been considered on different scales. At the microscale, simulations consider flow and particle deposition at the pore scale [72, 96], neglecting filter element design. At the macroscale, the filter medium is treated as a black box [97], with global values of porosity and permeability assigned. Multiscale modelling, which couples the microscale and macroscale, is the state-of-art in filtration

modelling at present [98].

2.5.1 CFD modelling of filtration processes at the microscale

At the microscale, pore-scale modelling is again utilized, and the workflow follows the same structure as described in Subsection 2.4.1. That is, a virtual representation of the microstructure of the porous medium is needed. To simulate at the pore scale, it is necessary to solve for fluid flow and particle transport. Clearly, fluid flow and particle transport are coupled, so an iterative algorithm may be employed to capture the evolution of the filtration process [99].

At the pore scale, the path of each individual particle is simulated. Based on a Lagrangian approach, a Langevin equation, a type of stochastic differential equation, is used to solve Newton's second law [100]. A solid particle moves in a flow field as a result of its inertia, friction, Brownian motion and, in some cases, an electrostatic force [101]. An example of a Langevin equation which describes the motion of a particle in a flow field is given by

$$m\frac{\mathrm{d}\boldsymbol{v}}{\mathrm{d}t} = -\gamma_f(\boldsymbol{v} - \boldsymbol{u}) + \boldsymbol{B}(t), \tag{2.24}$$

where m is the mass of the particle, $\boldsymbol{v}$ is the velocity of the particle and γ_f is a friction coefficient. The first term on the right-hand side represents the drag force acting on the particle as a result of its motion relative to the fluid (whose velocity is denoted by $\boldsymbol{u}$) and the second term represents a force characteristic of Brownian motion [100]. Other forces, such as an electrostatic force, can be represented by the addition of terms on the right-hand side [99].

Deposited particles cause a change in the pore-scale geometry of a filter medium. Such changes in geometry eventually lead to a significant change in the flow field. It is therefore necessary to periodically recompute the flow field [10]. Armed with the equations for describing the flow field and particle transport, an evolving pore-scale simulation can be described by the following process:

1. Compute the flow field and track individual particles.

2. Once the influence of the deposited particles on the flow field cannot be ignored, recompute the flow field.

To capture the evolution of the pressure drop, it is critical for a simulation to register the deposition of particles in the pore-scale geometry. There are two methods for updating the geometry: solid deposition mode and porous deposition mode [101]. If solid particles are of similar size to each voxel, solid deposition mode is utilized. A voxel defines an element on a regularly spaced three-dimensional mesh. After a particle is deposited, the voxel is marked as solid. If solid particles are of a size smaller than each voxel, porous deposition mode is utilized. After a particle is deposited, a permeability value is assigned to the voxel. The Navier-Stokes-Brinkman equations are then solved in the voxel at the next flow field update. The Navier-Stokes-Brinkman equations are modified Navier-Stokes equations which can be used to solve fluid flow in a porous medium [10]; they are of a similar form to the porous media model.

Wiegmann et al. [101] and Schmidt et al. [99] simulated soot filtration at the microscale. A solid particle was assumed to stick to any surface it touched. Schmidt et al. [99] found good agreement with experimental results for the pressure drop evolution, deposition rate and soot distribution in the microstructure at sufficiently resolved meshes. Such a mesh resolution led to excessive computational costs. This could be reduced by coarsening the mesh away from the porous geometry. Sambaer et al. [72] took a different approach in modelling the interaction between solid particles and the filter medium. The filter medium modelled was a nanofibre mat. A solid particle was not assumed to stick to the surface of any fibre it touched. Instead, the particle could slip along the surface of a fibre, then detach. An experimental rig, measuring the filtration efficiency of the capture of aerosol particles in a nanofibre mat, was undertaken. Good agreement between the simulation and experimental filtration efficiency was found. Particle detachment due to sliding will occur if the drag force imposed by the flow is greater than the friction force imposed by the surface. If these conditions are not met, the particle will not slide, and that type of detachment does not need to be considered.

Hoppach et al. [102] used a pore-scale filtration model to obtain additional information on

the filtration process of metal melt with aluminium oxide particles in ceramic foam filters. The lattice Boltzmann method was chosen to solve the fluid flow. Particle transport includes the influence of drag and buoyancy, has no influence on the flow field and a particle was considered captured when it approached a wall by a distance shorter than its radius. This model was created to support experimental work and was used to understand flow patterns inside the filter medium. The model was also used to examine the distribution of particle deposition inside the filter medium. There was some discrepancy between simulation particle deposition and the particle distribution observed with μCT scanning of experimental samples. The simulation predicted that nearly all of the particles were captured on the front face of the filter medium, which was not the case from μCT scanning. This is likely due to the simple requirement used for particle deposition which neglects detachment or sliding after deposition.

2.5.2 CFD modelling of filtration processes at the macroscale

At the macroscale, the filter medium is defined as a porous zone and solid particles may be defined by a concentration in the suspension [10, 52, 79, 80]. However, it is still common to model each particle individually through a Lagrangian approach [95, 103, 104].

Figure 2.8 shows an example of a macroscopic description of a filter element domain. For depth filtration, the interface between the fluid and porous region, $\partial\Omega_p$, is static and the continuity of velocity and the normal component of the stress tensor is required [10]. For cake filtration, $\partial\Omega_p$ changes as the cake grows, a moving boundary problem [79].

Assuming the concentration of particles in the suspension can be described by a mass per unit volume, and that particles move with the flow field, particle transport can be described by a convection-diffusion-reaction equation [79]. The reaction term is a sink term designed to represent the deposition of solid particles. The convection-diffusion-reaction equation is given

by

$$\frac{\partial C}{\partial t} + \boldsymbol{u} \cdot \nabla C - D_c \nabla^2 C = \begin{cases} 0, & \boldsymbol{x} \in \Omega_f, \\ -\frac{\partial M}{\partial t}, & \boldsymbol{x} \in \Omega_p, \end{cases} \tag{2.25}$$

where $C(\boldsymbol{x}, t)$ is the concentration of solid particles, $M(\boldsymbol{x}, t)$ is the concentration of deposited particles and D_c is a diffusion constant. The diffusion constant quantifies the rate of deposition; a larger diffusion constant implies a larger rate of particle deposition. The term on the RHS in Ω_p represents the deposition of solid particles. Boundary conditions on the concentration are usually of the form $C(\boldsymbol{x}, t) = C_{in}(t)$ for $\boldsymbol{x} \in \partial\Omega_{in}$ and $\frac{\partial C}{\partial \boldsymbol{n}} = 0$ for $\boldsymbol{x} \in \partial\Omega_s \cup \partial\Omega_{out}$, where $\boldsymbol{n}$ is the normal to the boundary at $\boldsymbol{x}$ [79].

A model for the rate of deposition must be chosen. This choice is usually based on comparisons with experimental data [79]. A permeability model is also required to simulate using a macroscopic approach. An example of such a model is the The Kozeny-Carman model [105]. It is commonly used for calculating the permeability in granular porous media. In order to successfully simulate a filtration process at the macroscale, appropriate models and parameter values must be selected for the rate of deposition and permeability. In general, such choices should be determined from comparisons with experiments [80].

Armed with the Navier-Stokes equations, a porous media model, the convection-diffusion-reaction equation, and appropriate models for the rate of deposition and permeability for describing the flow field and particle transport, a macroscale simulation can be described by the following process [10]:

1. Compute the flow field.
2. Find the captured solid particle mass.
3. Update the porosity and calculate the permeability.
4. Repeat 2 and 3 until the permeability of the filter changes to such a degree that its influence on the flow field cannot be ignored. Begin from 1.

Osterroth [79] extended the macroscopic approach to simulate combined depth and cake

filtration in one dimension using a moving boundary. Iliev et al. [52] were able to model the combined process for pleated structures by coupling a two-dimensional flow solver with a one-dimensional combined depth and filtration model.

Alternatively to the concentration approach, the path of individual particles can be simulated on the macroscale using a Langevin equation of the form (2.24). Fotovati et al. [103] developed a computational model designed to capture the filtration process through pleated filters over time. To save computational cost, particles were released from the inlet in clusters; it was then assumed that clusters deposit fractions of their mass as they travel through the porous medium. Saleh et al. [104] extended the model to consider polydispersed solid particle loading. Hrouda et al. [95] developed a novel macroscopic model designed to model filtration processes over time based on a statistical approach using escape probability. The statistical model relates particle diameters to the pore size distribution, which allowed simulations to track if pore spaces are partially or fully blocked as solid particles are filtered.

Basha et al. [106] used the porous media model and discrete phase modelling to investigate air-oil separation in cartridge filters. As oil droplets deposited over time, the decline in permeability was addressed by updating the inertial and viscous resistances in the porous zone. Computational results showed non-uniform deposition, which was confirmed by experimental observation.

Liu et al. [107] simulated dust removal by and deposition on ceramic candle filters. The filter medium was again represented by a porous zone and to keep computational costs reasonable, particles were grouped into spherical clusters. Particle motion was simulated by considering the drag force on the spherical clusters. Through the CFD model, they were able to find that deposition started at the bottom of the filters before moving upwards. This was verified through comparisons with used filters.

2.5.3 Multiscale modelling of filtration processes

In filtration processes, the microscale and macroscale are coupled. The macroscopic flow field influences particle transport and deposition, which in turn changes the pore-scale geometry, leading to a change in local permeability, which influences the flow field. Here, a multiscale filtration workflow detailed by Iliev et al. [10] is summarised.

To save computational expense, the process solves the problem on a coarse mesh, but accounts for unresolved geometrical features by solving local auxiliary problems on an underlying finer grid in selected locations [10]. To save time, the microscale simulations at selected locations may be run in parallel.

Armed with a macroscopic geometry of a filter element and pore-scale geometry of selected representative locations within the filter element, a multiscale simulation can be described by the following process at each time step [10]:

1. At the pore scale, within the selected locations, compute the flow field then simulate particle transport and deposition.

2. Update the permeability using the appropriate model at the selected locations then interpolate to find the permeability throughout the filter medium.

3. Find the flow field using a macroscopic model in the filter element.

4. Compute concentration of the particles in the filter element and use as an input for step 1 at the next time step.

Steps 1 and 2 describe the microscale modelling in each time step. Steps 3 and 4 describe the macroscale modelling in each time step. Selected locations are chosen based on capturing filtration behaviour in different regions. For example, locations near the inlet, outlet, near any solid structures and in the middle of a filter medium may be chosen for a representative set of filtration behaviour in the filter medium.

Recently, Lee et al. [108] modelled the filtration of solid particles from air through a face mask using sequential modelling. A virtual pore-scale model was constructed from μCT images of a mask sample. A virtual face mask was generated through three-dimensional scanning. The permeability profile found from the pore scale was used as a property of the virtual face mask. Gong and Rutland [109] developed a heterogeneous multiscale filtration model based on probability density functions. The model integrates local filtration efficiencies, which are upscaled to cover the entire filter element. This was later extended to model gasoline particulate filters [98].

Li et al. [110] coupled a pore-scale filter model with a macroscopic scale sedimentation-filtration model to create a tool for examining particle filtration in radial cartridge filtration. Pore-scale simulations were used to find a filtration coefficient needed for the macroscale CFD model. This coupling showed that filtration mechanisms were dictated by particle size; Brownian diffusion dominated for small particles whereas gravitational forces began to dominate as particles increased in diameter and density.

Lee et al. [111] used a variety of CFD modelling techniques to model air filtration across filter webs of various scales. A pore-scale model, a parametric model and a porous media model were tested. The parametric model acted as a bridge between the two scales, where the model simplifies the fibrous morphology based on geometrical properties of the fibre material. Modelling methods all suitably predicted the characteristics of filter media tested and were agreeable with experimental data [111].

2.6 Polymer melt filtration

Despite the common use of melt filtration in industry, there is little scientific research in the field [112]. Pachner et al. [5] created a CFD model of a double-cavity piston screen filter used for processing recycled polymer. The filter was not directly modelled. Instead, a pressure drop penalty was imposed on the flow based on analytical calculations. The melt

was assumed to act as a Newtonian fluid. Pachner et al. [6] then went on to develop generally valid analytic equations for predicting the initial pressure drop across woven screens by using heuristic optimisation algorithms. The analytical models developed incorporate the power-law exponent for the consideration of non-Newtonian melts.

Koller et al. [113] investigated the mechanisms underlying melt filtration at the outlet of an extruder to determine how effective the process is depending on the type of contamination. Experiments were performed with polypropylene melt filled with glass beads or ground PET particles. The melt passed through multi-layered woven screen filters. Screen filters were recovered after use and examined through magnification. Contaminants which were larger than the mesh size were filtered successfully. This was more effective for glass beads; it was beneficial to use smaller screen mesh sizes for softer PET particles. This was due to screen deformation, which was minimised using an additional backup plate for support. It was concluded that the amount of contaminants, particle size and rigidity must be considered when choosing an appropriate screen filter [113].

Liedl and Burgstaller [112] investigated the influence of typical impurities that arise in recycled melt on the mechanical and rheological properties of acrylonitrile-butadiene-styrene, which is a copolymer of polystyrene–polyacrylonitrile and polybutadiene. From experimental results, low amounts of contaminants, which consisted of wood and rubber, were found to lower key properties of the melt and this was not resolved with a finer screen filter.

Schöppner and Meilwes [114] carried out experimental investigations on the pressure drop evolution of disc filters. In industry processes, filter lifetime is commonly hours to weeks; this had to be reduced for laboratory experiments so a PET melt was artificially contaminated with calcium carbonate. An analytical model was developed which is designed to be fitted to experimental pressure drop evolution data. The analytical model was then used to calculate the pressure drop evolution as a function of starting pressure, filter fineness, contaminant particle size and the permissible pressure limit. As a necessary step, existing calculation models, such as Darcy's law, should be validated for their applicability to polymer melt

filtration [114].

2.7 Summary

Polymer melt filtration incorporates complex mechanisms such as non-Newtonian and viscoelastic flow, flow through porous media and filtration. It has been shown that there is very little theoretical understanding of non-Newtonian flow through porous media, before even considering the additional complexity of filtration. There is even less research available on polymer melt filtration. It is therefore imperative to this research that the physical mechanisms dictating the filtration of polymer melts are either classified based on experimental work or informed assumptions, before any CFD modelling takes place.

Literature has shown that CFD modelling of filtration is possible and helps to understand and visualise the physical mechanisms of filtration, offering insights into how filters block and flow patterns inside filter systems alter as filtration advances. At this point, a macroscopic approach to capture global characteristics is appropriate to develop our understanding. The key goal of this project is to better understand how the degradation of filter packs over time affects performance, for which macroscopic models have been shown to be sufficient if they are applied appropriately based on the physical mechanisms driving filtration and if they are calibrated based upon suitable experimental data.

The next chapter outlines the physical mechanisms that are assumed throughout this thesis for modelling polymer melt filtration. The choice of each physical mechanism is based on experimental work, where the behaviour of a PET melt through a screen filter is investigated, or is assumed based on the calculation of prominent non-dimensional numbers which are commonly used to inform on the mechanisms driving various physical phenomena.

Chapter 3

Methodology

This chapter outlines the physical mechanisms driving various aspects of polymer melt filtration. These physical mechanisms are based on either experimental work or prominent non-dimensional quantities. The CFD methodology employed throughout this project is also outlined. Experimental set-ups and a comprehensive experimental methodology are not discussed in detail here, with such discussions occurring in subsequent chapters.

3.1 Modelling assumptions

Assumptions on the mechanisms driving melt flow, melt flow through a porous medium, particle transport and filtration are outlined here. The reasons for such assumptions are given.

3.1.1 Melt behaviour

Polymer melts are classified as non-Newtonian, shear-thinning, viscoelastic materials. However, Champion [18] determines that at shear rates found throughout processing ($\dot{\gamma} \leq 150\text{s}^{-1}$)

polyester melt flows are considered Newtonian. Chapter 4 verifies that PET melt can be considered Newtonian through filter media. All flows considered in this project will therefore be considered Newtonian.

3.1.2 Flow regime

Darcy's law applies when viscous forces dominate inertial forces (Re < 1). An upper limit can be calculated for the Reynolds number of each filter system. For example, through the seven candle filter pack, upper limits on throughputs at the inlet are 3000 kg/hr, which is the largest of all filter systems modelled. The inlet pipe diameter, D, is 0.03 m for a seven candle filter pack. Polymer melts with density above 2000 kg/m^3 and viscosity below 100 Pa s will not be considered throughout this thesis. Therefore, the Reynolds number through filter systems in this thesis has an upper limit such that

$$\mathrm{Re} < \frac{4\dot{m}}{\pi\mu D} < \frac{4 \times 3000/3600}{100\pi \times 0.03} = 0.36.$$

Viscous forces dominate inertial forces throughout each filter system and Stokes flow holds. For a steady flow, this simplifies the Navier-Stokes equations further as the inertial term can be neglected:

$$\begin{aligned} \nabla \cdot \boldsymbol{u} &= 0, \\ -\nabla p + \boldsymbol{F} + \nabla^2 \boldsymbol{u} &= 0. \end{aligned} \tag{3.1}$$

3.1.3 Particle transport

The Péclet number (Pe) is the ratio of the rate of advection to the rate of diffusion of a physical property [115], and, for mass transfer, is given by

$$\mathrm{Pe} = \frac{L|u|}{D_c}, \tag{3.2}$$

where L is a characteristic length scale, $|u|$ is the velocity magnitude and D_c is the diffusion coefficient. The Stokes-Einstein equation may be used to find D_c for spherical particles through a low Reynolds number liquid [116]; it is given by

$$D_c = \frac{k_b T}{6\pi\mu r_p}, \tag{3.3}$$

where k_b is Boltzmann's constant, T is the absolute temperature and r_p is the radius of the particle. The filter media modelled in this work is graded between 23 and 80 microns. Therefore, particles with diameters of the order 10 microns are targeted for filtration. A beyond cautious minimum estimate for filtered particle size is therefore 1 micron in radius. Temperatures in the filter will never exceed, or even approach, 1000K since such a temperature exceeds operating ranges for the filters [11]. An upper bound on D_c is therefore

$$D_c < \frac{k_b \times 1000}{6\pi \times 100 \times 1 \times 10^{-6}} < 1 \times 10^{-17}.$$

A lower bound on pore diameter, which is often chosen as the characteristic length of a filter medium, is 1 micron. This is a cautious estimate as the lowest grade of filter material in this considered here is 23 microns and pore diameter would have to be of the same order to capture particles through surface filtration. Therefore, at velocities near the filter medium, $\mathrm{Pe} \gg 1$, and Brownian motion is negligible.

Furthermore, the Stokes number is a dimensionless number corresponding to the behaviour of particles suspended in a fluid flow [117]. It is the ratio of characteristic time of a particle

to a characteristic time of the flow and is given by

$$\text{Stk} = \frac{t_r|u|}{L}, \tag{3.4}$$

where t_r is the particle relaxation time. For $\text{Stk} \ll 1$, particles will follow streamlines closely [117]. The particle relaxation time is given by

$$t_r = \frac{\rho_p d_p^2}{18\mu}, \tag{3.5}$$

where ρ_p is particle density and d_p is particle diameter [118]. Typical contaminant particle density is not known, but typical contaminants may include degraded polymer or metal catalyst residues. An overcautious maximum particle density is chosen as $\rho_p = 10000$ kg/m^3, which is larger than most metals. An overcautious maximum particle diameter is chosen as $d_p = 1$ mm, which is two orders of magnitude larger than the largest filter grade. Hence, a pessimistic upper bound for the particle relaxation time is

$$t_r = \frac{10000 \times 0.001^2}{18 \times 100} < 1 \times 10^{-5}.$$

The largest throughput through any filter pack is 3000 kg/hr through the seven candle filter pack. The seven candle filter pack has an inlet pipe diameter of $D = 0.03$ m. Hence,

$$\text{Stk} < \frac{1 \times 10^{-5} \times 0.6}{0.03} < 1 \times 10^{-3}$$

and particles follow streamlines in polymer melt flow.

3.1.4 Filtration mechanisms

Screen filters are made up of several layers of woven screen, where the filter medium is sandwiched between support meshes. The mechanism of filtration for screen filters is therefore

surface filtration. The screen captures particles larger than the mesh openings, preventing them from moving onto the next stage of production. This is verified in [113], where captured particles are seen on the surface of used screen filters after polymer melt filtration. For candle filters, the filter medium consists of sintered metal fibres with a voidage of 60% and a thickness of approximately 1 mm. The sintered metal fibre used in candle filters is a depth filtration medium [119]. The sintered fibre structure is a less organised structure than a weave, hence pore diameter will vary and openings will be larger than particles. A thickness of 1 mm is therefore required as particles will be deposited within the porous structure.

3.2 Computational fluid dynamics methods

All computational models used throughout the project will rely on CFD methods. CFD is a numerical approach to solving the equations which govern fluid flow problems, such as the Navier-Stokes equations. Systems such as the Navier-Stokes equations are nonlinear and, for a given problem, rarely have a known analytical solution. Experiments are therefore the most reliable technique for fluid flow analysis, but experiments are expensive and measurements may only be obtainable at isolated points. CFD is therefore used to give detailed approximate solutions at a lower cost than experiments. CFD models of three filter systems are created for this research: a screen filter model, a single candle filter pack model and a seven candle filter pack model.

CFD is limited by the standard errors associated with numerical modelling on a computer, such as round-off and discretization errors. As such, CFD models should be validated by comparisons with the literature or experimental work.

Computational modelling in this thesis will follow the usual stages of a CFD simulation:

1. Creation of a geometry that captures the real geometry of interest.

2. Mesh the geometry and implement boundary conditions.

3. Specify the physics of the problem and choose the appropriate solvers.

4. Run the simulation and ensure convergence of any iterative solution steps.

5. Refine the mesh and repeat the simulation to ensure mesh independence. If the problem is unsteady, ensure time-step independence.

6. Post-process results.

Appropriate results are then processed and extracted. ANSYS Fluent has been identified as the software used to model CFD problems in this project [14]. ANSYS Fluent is a commercial software and is supported by other ANSYS software. ANSYS DesignModeler [120] is used to import a geometry from SolidWorks [121]. ANSYS Meshing is used to mesh the geometry [120]. Fluent is used to set up the physics and solvers, and to run the CFD simulation. Results are post-processed through a mixture of Fluent and CFD-Post. ANSYS was selected due to its intuitive graphical user interface (GUI), making it ideal for efficiently running problems with relatively simple physics, such as flow problems for highly viscous, Newtonian flows. It was also selected as it may be customised through user-defined functions and named expressions can be used to create custom variables. It was also selected for its in-built macroscopic porous media model.

3.2.1 Geometry construction

Geometrical measurements for each filter design considered are provided in CAD drawings provided by Mylar. From measurements, SolidWorks parts are created and combined in an assembly. As the interest is in the flow of polymer melts through the geometry, the final geometry created is of the space in which the fluid occupies. After creation of the full geometry, .STEP files are imported into DesignModeler, where the geometry is broken into different parts to help with meshing.

3.2.2 Boundary conditions

Mass flow inlets are chosen as inlets for every model as melt pumps are employed to maintain a constant flow rate upstream of filter packs in each extrusion system. A mass flow rate is selected with a direction specified as normal to the boundary. Due to the viscous nature of polymer melt flows, a no-slip boundary condition is chosen on each wall of the geometry. No-slip specifies that a fluid has no velocity at the boundary of a wall. A pressure outlet is chosen at the outlet boundary of each simulation. The pressure is fixed at atmospheric pressure at the outlet. A die is found downstream of the filter in an extrusion system. Here, fluid flows out of the die into open channel flow, into atmospheric pressure. The die and the pipe system between the filter and die is not modelled in CFD simulations. However, as the pressure drop across the filter pack is of interest, with information on pressure upstream and downstream of the filter, pressure drop across the pack can be found by taking the difference of the two. Symmetrical boundary conditions are also employed, which exploit the symmetry of each filter pack. Symmetrical boundary conditions assume that the flow entering the domain on one side of the symmetry plane is mirrored on the other side, and no fluid flows across the symmetry plane. Any identified plane of symmetry allows the geometry to be reduced, reducing the computational domain size and, consequently, the computational expense of a simulation.

3.2.3 Meshing

After creation of a geometry, the domain must be meshed so discretised differential equations can be solved. ANSYS Meshing was chosen to mesh the geometry. All meshes are detailed in relevant chapters but were generally generated with tetrahedra cell shapes, with mesh defeaturing, curvature capture and capture proximity specified. Sweep meshing generates a mesh by sweeping a 2D mesh along a path to create a 3D mesh. Sweep meshing was utilized in the inlet and outlet pipe section of every 3D geometry. It was also utilized in specific sections of axial symmetry inside the filter packs, for example along the central cylinder of a candle

filter. It creates an ordered structure to the mesh, which can improve accuracy in results and efficiency in mesh generation.

In Fluent, it is possible to further refine the mesh in regions of high pressure gradients with mesh adaptation. When using adaptive meshing, pressure hessian indicator refinement is chosen as the refinement criterion. That is, the mesh is adapted based on the second derivatives of pressure, refining it in regions of rapid pressure changes, such as regions of high pressure gradients. Refining the mesh in regions of high pressure gradients improves the reliability of results, while allowing the mesh to remain coarser in other regions, where a fine mesh has less influence on reducing numerical error. This balances the need to save computational expense while not compromising the reliability of the model. This is particularly useful in this research, where mesh needs to be finer in the vicinity of porous zones and coarser elsewhere to save computational cost.

3.2.4 Mesh independence

It is crucial that each CFD model is mesh independent. Mesh resolution directly impacts the accuracy of CFD results. A coarse mesh may fail to capture important flow features and gradients. Mesh independence ensures that observed results are not affected by artifacts of the mesh. To ensure mesh independence, at least two parameters will be monitored for at least three meshes of different sizes. As this research is particularly interested in pressure drop across filter packs, pressure at a plane near the inlet for each model will be ensured to be independent with increasing mesh size. Furthermore, since changes to flow patterns are of interest, flow development length will be compared to the analytical relationship developed by Durst et al. [122]. This particular correlation is chosen as it accounts for the role diffusion plays in flow redevelopment in the creeping flow limit [123]. The relationship is given by

$$X_D/D = \left[0.619^{1.6} + (0.0567\mathrm{Re})^{1.6}\right]^{0.625}, \tag{3.6}$$

where Re is the Reynolds number in the pipe, D is the pipe diameter and X_D is the development length. Flow development length is the distance over which a flow evolves into a fully developed state. Further mesh independence checks will take place for candle filter packs, which will be discussed in the subsequent chapters.

3.2.5 Physics and solvers

A steady, pressure-based solver is specified and a viscous, incompressible laminar model is used for every CFD model. That is, the Navier-Stokes equations are discretised and solved using the finite volume method. The Navier-Stokes equations for a viscous, Newtonian fluid are given by

$$\begin{aligned} \nabla \cdot \boldsymbol{u} &= 0, \\ \rho \boldsymbol{u} \cdot \nabla \boldsymbol{u} &= -\nabla P + \mu \nabla^2 \boldsymbol{u}. \end{aligned} \tag{3.7}$$

A coupled pressure-velocity scheme is used, with least squares cell based gradient discretization. Second order pressure and second order upwind momentum discretization are also specified. A hybrid initialization method is used. That is, initial values are assigned to each cell based on the solution to a Laplace equation which determines an initial non-uniform guess for the velocity and pressure fields.

3.2.6 The porous media model

The porous media model [124] is used to represent the filter in each model. The porous media model is built into Fluent and accounts for the additional pressure drop due to filter resistance and was detailed in Subsection 2.4.2. A cell zone representing filters in each geometry is created for each CFD model, and the porous media model is enabled in these porous zones. Viscous resistance is required as an input for porous zones. Viscous resistance is simply defined as the inverse of permeability. From experimental data of pressure drop against flow

rate, if Darcy's law holds, a permeability may be determined for each filter. This permeability will then decrease as particles block pores in a filter, increasing the viscous resistance.

3.2.7 Convergence

Convergence in CFD refers to the state where the numerical solution stabilizes, and further iterations of the simulation do not significantly change the computed results. Residuals are monitored for each iteration. Residuals are a measure of the numerical error in a simulation representing the discrepancies between the computed values at a particular iteration and the values from the previous iteration. The convergence criterion is set for a maximum scaled residuals of the order 10^{-5}. Furthermore, pressure drop across each geometry and mass imbalance between the inlet and outlet are ensured to vary by less than 0.001% per iteration.

3.2.8 Post-processing

Post-processing in CFD refers to the analysis and interpretation of simulation results after simulations have converged and ensured to be mesh independent. Post-processing is performed in Fluent and CFD-post, and data is exported into Excel and Python 3.9 for comparisons with experiments, different models and plotting. Visualizations of the flow are created in Fluent, including contour plots and streamlines. Sensitivity analysis is also performed, where model parameters are varied to understand how they influence the flow.

Chapter 4

Modelling Polymer Melt Flow Through Screen Filters

This chapter focuses on screen filters, the filters employed on the pilot scale line of the film casting process. The structure of screen filters is examined and the geometry and set-up of the pilot scale line in which they are employed is shown. An experiment, designed to capture the relationship between pressure drop and throughput across varying grades of screen filter is detailed. A computational model of the filter system that includes the screen filter is created and calibrated to match experimental results. By considering the influence of multiple layers on flow behavior, the developed computational model aims to provide accurate predictions of pressure drop across the multi-layered screen filters and flow patterns in the filter system.

4.1 Screen filter geometry

In-line screen filters are employed on a pilot scale film line. An in-line screen filter is shown in Figure 4.1b; they are circular structures where a filter medium is sandwiched between coarse upstream and downstream support mesh. The filter is inserted into the circular pipe,

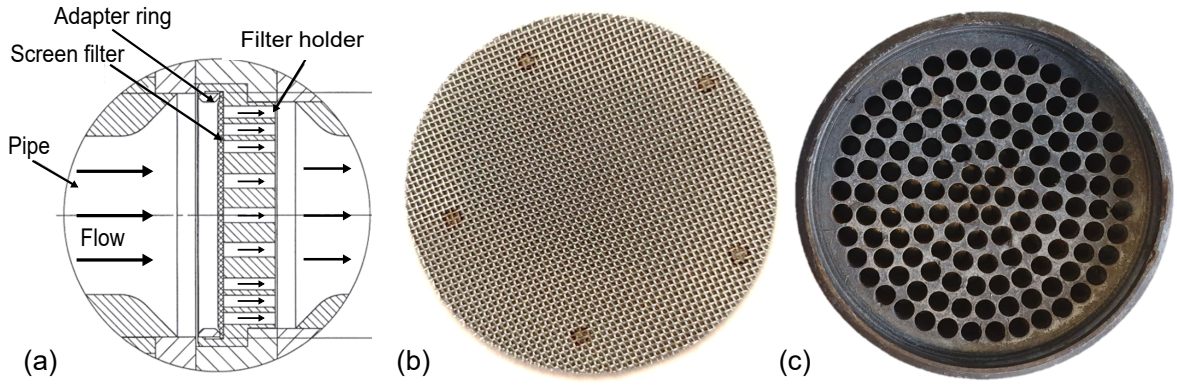

Figure 4.1: (a) A cross-section of the geometry around the filter. The adapter ring was not used in the experiment. (b) An in-line screen filter. (c) A filter holder.

supported by a filter holder, so that melt passes through its flat surface. After passing through the filter, the melt passes through the holder, shown in Figure 4.1c, via the circular holes in it.

This geometrical set-up is shown in Figure 4.1a. Melt enters through a circular pipe, which widens in the upstream section prior to encountering the filter. It then traverses the filter and the holder, then, downstream of the holder, the pipe channel constricts to its original diameter. Note that Figure 4.1a shows only the geometry in the vicinity of the filter and holder. The pipes in and out of this section extend and remain straight with constant diameter for at least a metre in both directions away from the filter and holder. This ensures fully developed pipe flow upstream and downstream of the filter system.

The filter holder is used to keep the in-line filter in place and support it against the high pressures in the extrusion system. The filter sits in the holder, against the surface shown in Figure 4.1c. The holder is the only part of the geometry which cannot be modelled as axisymmetric, due to the holes in it.

To understand how permeability influences pressure drop, four grades of filters are utilised during this work: three-layered 80, 60 and 40 micron filters and a five-layered 23 micron filter. An 80 micron filter captures 99% of particles with diameter larger than 80 microns.

The three-layered filters are made up of a downstream support layer, a filter layer and an upstream support layer. The 23 micron filter is made up of five layers: a filter layer, two upstream support layers and two downstream support layers. Figure 4.2 shows different types of weaves. It also shows how the thickness of the weaves can be calculated. Thickness is calculated as some form of sum of warp and weft wires, given by d_w and d_s respectively in Figure 4.2. All support layers are plain weaves, with an example downstream support layer shown in Figure 4.3. A variety of weaves are employed for filter layers, listed in Table 4.1.

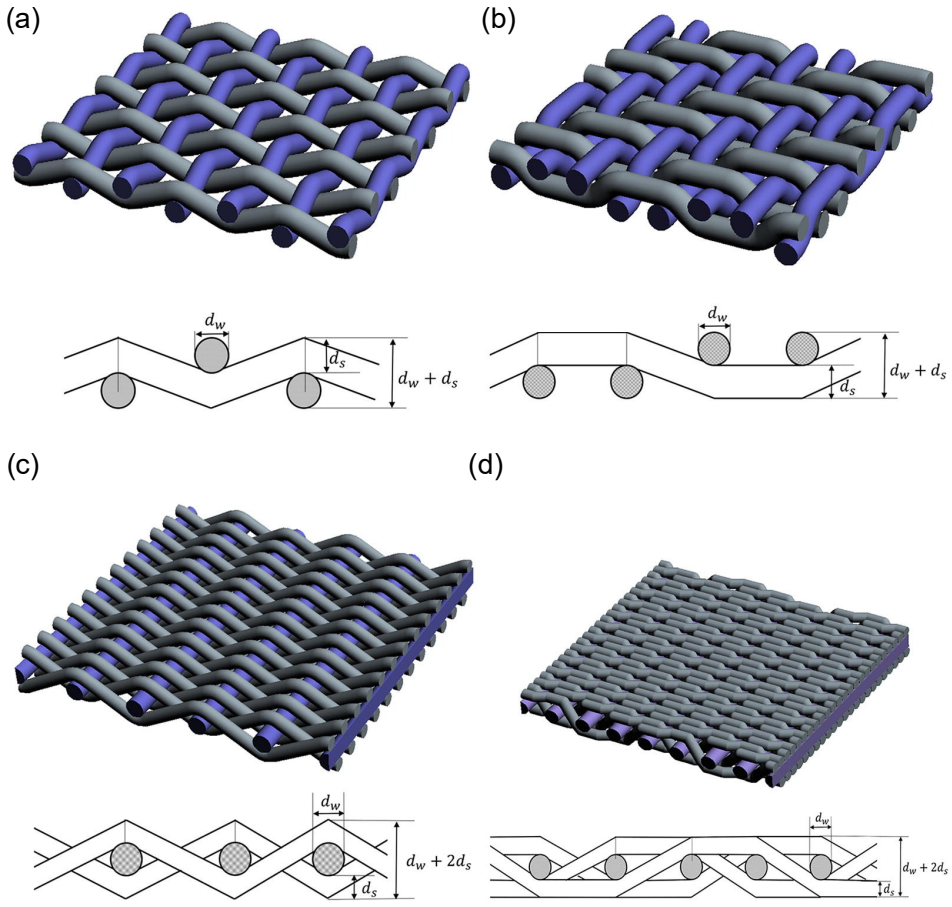

Figure 4.2: Schematics of (a) plain (b) twill (c) plain Dutch and (d) Dutch twill weaves. Figure from [41].

A Keyence VHX-6000 3D Optical Microscope with a 20x-200x magnification range was used to examine and categorise the structure of screen filter layers. The microscope has built

in image analysis software which was used to measure the thickness of metal wires used as weaves for screen filter layers. Screen filters consist of multiple layers of woven metal wires. Samples of each layer were prepared by separating the screen filter with pliers. Each sample was washed and cleaned with a brush to ensure any contaminants were removed.

The total thickness of each filter and each support layer was also measured using a caliper with precision of 10 microns. Each individual layer for each filter was measured three times, as well as the total thickness of each filter. For each filter, the sum of the average measurements of each layer were found to be the same as the average thickness of the filter. Multiple new filters of each grade were available for microscopic examination and measurements.

Table 4.1: Weaves of the filter layer for each screen filter.

Filter layer	80	60	40	23
Weave	Twill	Twill	Plain Dutch	Twill Dutch

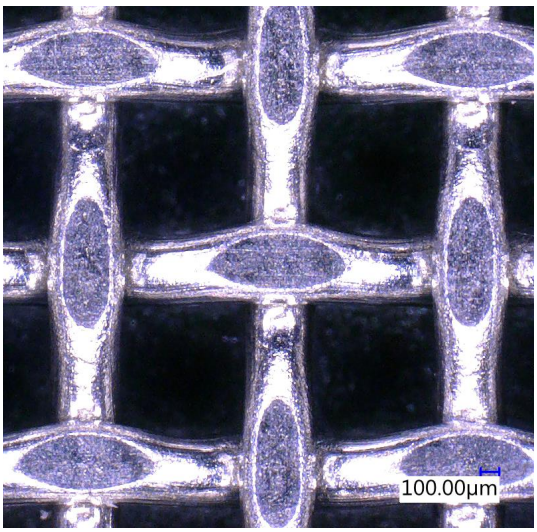

Figure 4.3: A x60 magnified image of a 40 micron screen filter downstream support mesh. The same downstream support mesh is employed for the 80 and 60 micron filters.

4.1.1 80 micron filter

Table 4.2 shows the measurements taken from the filter and each individual layer when using a caliper for the 80 micron filter. The final column shows a direct measurement of the whole filter. As expected, summing the average of each layer gives the same thickness as the average thickness of the filter itself. Figure 4.4 shows how the wire diameter of the filter layer was determined for the 80 micron filter. Using the microscope, a single wire diameter was determined from in-built measuring software. Another measurement was then taken, and the measurements were averaged. A third measurement was taken and averaged with the previous measurements, and so on, until the average was deemed to have varied insignificantly with subsequent measurements. This technique was repeated for the filter layers of the other filter grades. The diameter of wires that made up the filter layer was found to be 80 and 90 microns in the weft and warp direction respectively. Figure 4.4 shows the structure of the filter layer. For twill weaves, the thickness, d_F, of the weave is given by the sum of the diameters of the weft and warp wires. From microscope readings, this gives $d_F = 170$ μm. Similarly, from the caliper measurements, the thickness of the filter layer was found to be 170 μm.

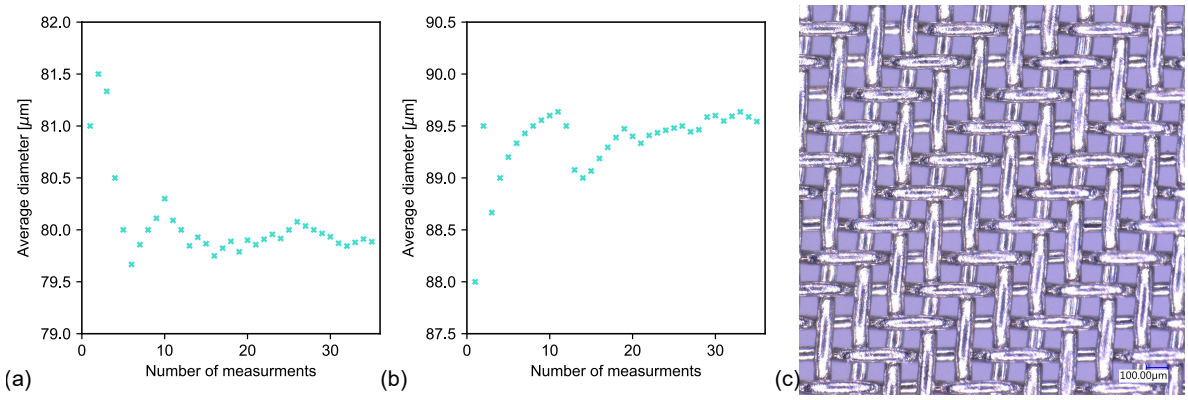

Figure 4.4: Determined (a) warp and (b) weft wire diameter for the filter layer of a 80 micron filter. The warp and weft wires were observed to have different diameters. (c) A x140 magnified image of the twill weave used for the filter layer.

Table 4.2: Caliper measurements taken from the 80 micron filter.

Layer	Upstream support	Filter layer	Downstream support	80
Thickness [μm]	250	170	550	970
Repeat 1 [μm]	250	170	550	970
Repeat 2 [μm]	250	170	550	970
Average [μm]	250	170	550	970

4.1.2 60 micron filter

Table 4.3 shows the measurements taken from the filter and each individual layer when using a caliper for the 60 micron filter. Measurements were taken multiple times to ensure accuracy. The sum of the average thickness of each layer is within 10 microns of the average thickness of the filter itself. The discrepancy can be attributed to error caused by caliper resolution. Figure 4.5 shows how the wire diameter of the filter layer was determined for the 60 micron filter. The diameter of wires that made up the filter layer was found to be 60 microns. As the filter layer of this screen filter is a twill weave, $d_F = 120$ μm. Similarly, from the caliper measurements, the thickness of the filter layer was found to be 120 μm.

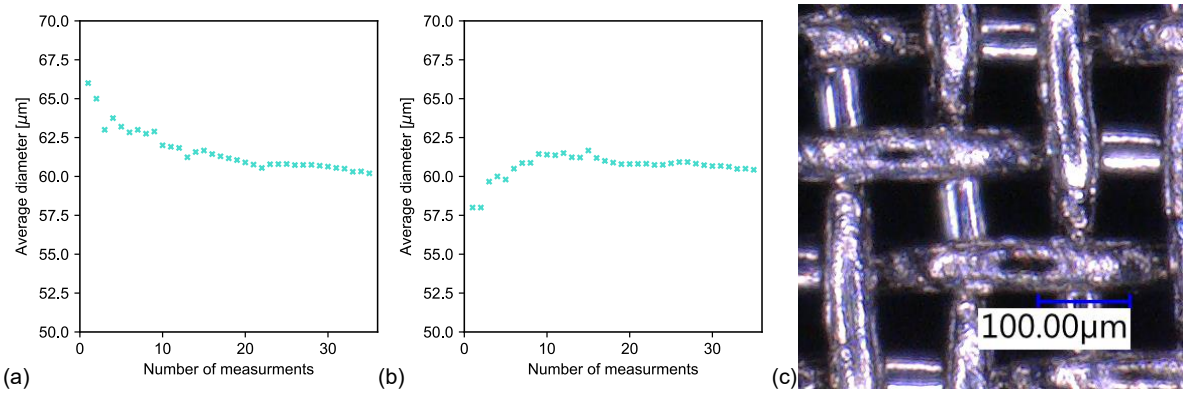

Figure 4.5: Determined (a) warp and (b) weft wire diameter for the filter layer of a 60 micron filter. (c) A x200 magnified image of the twill weave used for the filter layer.

Table 4.3: Caliper measurements taken from the 60 micron filter.

Filter	Upstream layer	Filter layer	Downstream layer	60
Thickness [μm]	240	120	550	900
Repeat 1 [μm]	240	120	540	900
Repeat 2 [μm]	240	120	550	900
Average [μm]	240	120	550	900

4.1.3 40 micron filter

Table 4.4 shows the measurements taken from the filter and each individual layer when using a caliper for the 40 micron filter. As expected, summing the average of each layer gives the same thickness as the average thickness of the filter itself. Figure 4.6 shows how the wire diameter of the filter layer was determined using the microscope for the 40 micron filter. The weft wire and warp wires are 100 μm and 150 μm respectively. As the filter layer is a plain Dutch weave, weft wires weave under and over warp wires, giving a total thickness of $d_F = 350$ μm. Similarly, for the caliper measurements, $d_F = 350$ μm.

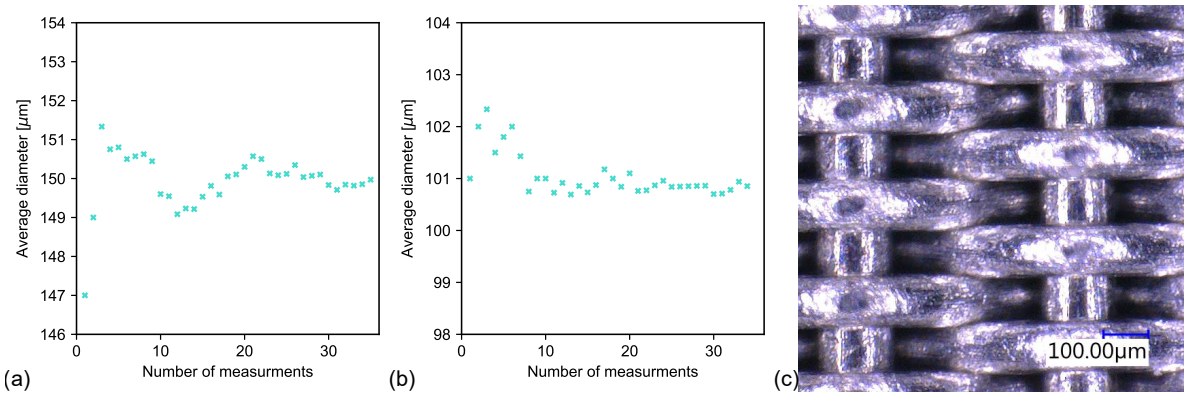

Figure 4.6: Determined (a) warp and (b) weft wire diameter for the filter layer of a 40 micron filter. The warp and weft wires were observed to have different diameters. (c) A x140 magnified image of the plain Dutch weave used for the filter layer.

Table 4.4: Caliper measurements taken from the 40 micron filter.

Filter	Upstream layer	Filter layer	Downstream layer	40
Thickness [μm]	250	350	550	1150
Repeat 1 [μm]	250	350	550	1150
Repeat 2 [μm]	250	350	550	1150
Average [μm]	250	350	550	1150

4.1.4 23 micron filter

Table 4.5 shows the measurements taken from the filter and each individual layer when using a caliper for the 23 micron filter. UF represents the layer between the filter layer and the upstream layer. DF represents the layer between the filter layer and the downstream layer. As expected, summing the average of each layer gives the same thickness as the average thickness of the filter itself. Figure 4.7 shows how the wire diameter of the filter layer was determined using the microscope for the 23 micron filter. The weft wire and warp wires are 40 μm and 50 μm respectively. As the filter layer is a twill Dutch weave, weft wires weave under and over warp wires, giving a total thickness of $d_F = 130$ μm. Similarly, for the caliper measurements, $d_F = 130$ μm.

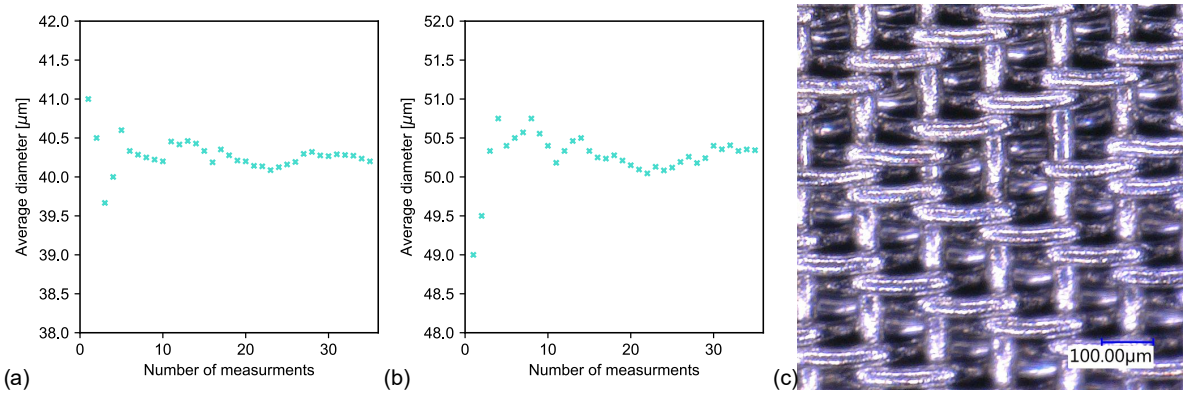

Figure 4.7: Determined (a) warp and (b) weft wire diameter for the filter layer of a 23 micron filter. The warp and weft wires were observed to have different diameters. (c) A x200 magnified image of the twill Dutch used for the filter layer.

Table 4.5: Caliper measurements taken from the 23 micron filter.

Filter	Upstream	Filter	downstream	UF	DF	23
Thickness [μm]	380	130	380	110	210	1210
Repeat 1 [μm]	370	130	370	110	210	1210
Repeat 2 [μm]	380	130	380	110	210	1220
Average [μm]	380	130	380	110	210	1210

4.2 Experimental set-up

The objective of the experiment presented in this chapter was to investigate how pressure drop across an in-line screen filter is influenced by varying throughput and filter permeability. To this end, polymer melt was extruded and pumped through an in-line filter. The throughput and filter were varied throughout and pressure upstream of the filter was recorded. Figure 4.8 shows the geometry of the pilot scale extrusion system used for this experiment. PET chip was fed into the extruder via a cold feedstock where it was extruded and maintained at 275°C by a series of heaters along the extruder, melt system and die. The extrusion system is heated to control viscosity and prevent solidification. A full vacuum was used on the extruder to remove moisture and minimise trapped air in the melt. The polymer melt then passed through the filter holder and then the die.

Initially, no filter was placed within the screen filter holder. The process then began, where the throughput was gradually increased to flush out any debris from previous use with no filter in the system. The experiment proceeded as follows:

1. With no filter, the throughput was maintained for at least 15 minutes at 40, 60, 80, 120 and 160 kg/hr.

2. The throughput was then reduced to 0 kg/hr, the system shut down and an 80 micron screen filter was inserted.

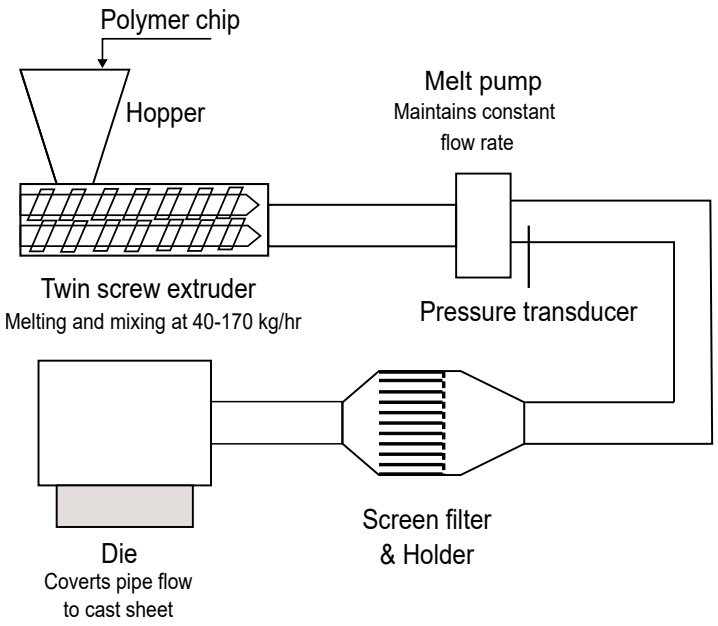

Figure 4.8: Sketch of the pilot scale extrusion system.

3. The system restarted, and the throughput was maintained at 40, 60 and 80 kg/hr with the 80 micron filter inserted.

4. Steps 2-3 were then repeated with a 60 micron filter.

5. Step 2 was then repeated with a 40 micron filter. The throughput was maintained at 40, 60, 80, 100, 120 and 140 kg/hr in this case.

6. Steps 2-3 were then repeated with a 23 micron filter. The experiment was then concluded and the system was shut down.

Table 4.6 summarizes the filters used and range of mass flow rates tested. Figure 4.9 shows the mass flow rate and pressure at the transducer, recorded every minute over the course of the experiment. Throughputs were targeted by specifying the rpm of the melt pump. This led to some fluctuations from targeted throughputs. To minimise the impact of any fluctuations, targeted throughputs were maintained for 15 minutes, and the actual throughput and pressure data was averaged over the final 10 minutes. Throughputs were maintained in increments of

at least 20 kg/hr to maximise the range of data covered. Different throughputs for each filter were chosen to maximise the amount of data recovered over the limited time allowed.

Table 4.6: Screen filters and flow rates used in the experiment.

Filter [μm]	-	80	60	40	23
$\dot{m}$ [kg/hr]	40-160	40-80	40-80	40-140	40-80

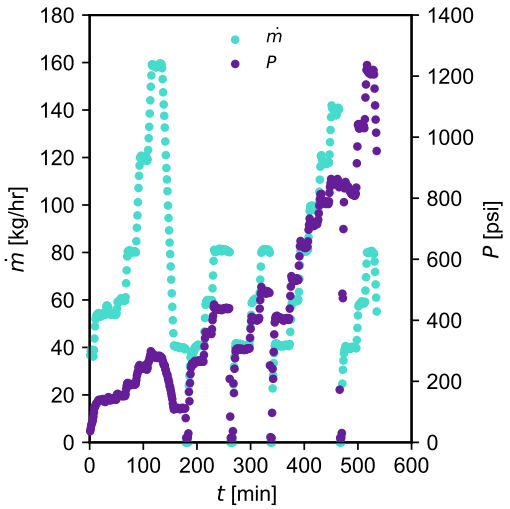

Figure 4.9: Mass flow rate at the melt pump and pressure at the transducer throughout the experiment.

A Minolta/Land Cyclops 79 pyrometer was used to record the temperature of the melt curtain as it exited the die. This was done for each filter at each maintained throughput to check the temperature of the melt.

4.3 Computational model

Figure 4.10 shows the model of the 3D geometry used for CFD simulations. It was created in SolidWorks 2019 using CAD drawings of the filter system employed on the pilot line. All simulations were implemented in ANSYS Fluent 2022 R1. At the inlet, a mass flow inlet

boundary condition was specified normal to the boundary with a throughput ranging from 40-160 kg/hr. A static pressure outlet boundary condition was chosen with 0 Pa gauge pressure; the inlet and outlet were chosen to be sufficiently far away from the filter and filter holder, as to have no influence on flow development near the filter. All other external boundaries are walls with the no-slip condition applied. An incompressible, Newtonian fluid with $\rho = 1225$ kg/m^3 and a viscosity ranging from 120-180 Pa s was modelled. This puts an upper limit of 0.01 on the Reynolds number, ensuring the laminar regime is maintained throughout.

A steady, pressure-based solver was specified and a viscous, incompressible laminar model was used. A coupled pressure-velocity scheme was used, with least squares cell-based gradient discretization. Second order pressure and second order upwind momentum discretization were also specified. A hybrid initialization method was used. The convergence criterion was set for maximum scaled residuals of the order 10^{-5}. Furthermore, pressure drop across the geometry and mass imbalance between the inlet and outlet were ensured to vary by less than 0.001% per iteration.

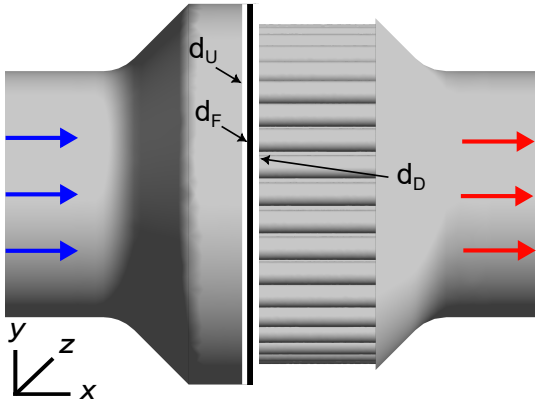

Figure 4.10: The virtual geometry used to model flow through a screen filter. The blue and red arrows indicate the flow upstream and downstream of the filter respectively. Note that the figure does not show the whole length of the inlet and outlet pipes.

The porous media model, detailed in Subsection 2.4.2, was used to represent different configurations of the screen filter in the computational model. In total, twelve variations of the virtual geometry in Figure 4.10 were generated, to account for varying filter thickness and porous zone position. Permeability inputted into the porous media model is determined based

on experimental results. Permeability therefore varied based on filter grade and porous media model configuration. The different porous media model configurations, and their associated permeability values, are discussed in Section 4.5.

A mesh independence study was performed on each mesh to ensure that mesh resolution did not have a significant effect on any of the CFD results. The mesh was refined systematically until a stable pressure drop across the filter was observed, and the redevelopment length from the inlet was compared to a correlation in the literature. An example of this process is described in Subsection 4.5.1.

4.4 Experimental results

Figure 4.11 shows pressure at the pressure transducer, shown in Figure 4.8, found at each throughput interval. Error was calculated by calculating standard deviation over the averaged pressure data, and was found to be universally under 2 psi, which would not be identifiable in Figure 4.11. As expected, pressure increases with increasing throughput and filter fineness. Pressure does not increase linearly with throughput.

This can be explained by Figure 4.12a, which shows the average temperature recorded using the pyrometer at the throughputs of interest. The temperature was found to vary by several degrees along the curtain, giving a range of 5°C from one end of the curtain to the other. As a result, temperature was measured in the middle of the curtain, and this variation was accounted for with a ±2.5°C error. The temperature increased by nearly 20°C over the range of throughputs. As throughput increases, the speed of the extruder screw increases, leading to an increase of shearing of the polymer melt, thus energy dissipates through heat. Increasing temperature leads to a decrease in viscosity, decreasing pressure drop.

Figure 4.12b shows that over the range of temperatures recorded, the viscosity of the polymer varies by 38%. The relationship between viscosity and temperature was determined using

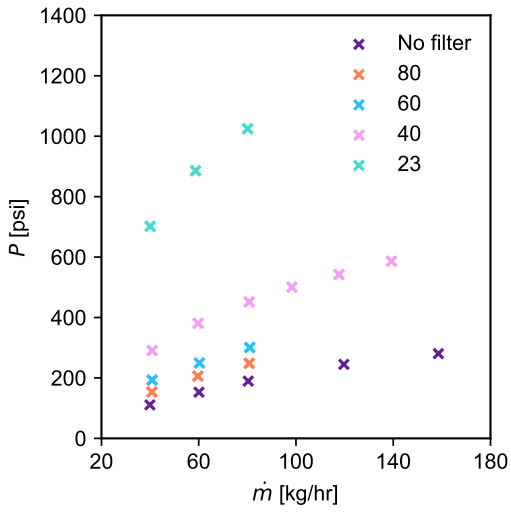

Figure 4.11: Pressure against throughput for each filter.

the model described by the equation (2.9). A 0.58 IV PET melt was used throughout this experiment.

The relationship between mass flow rate and pressure drop across the filter is of interest as this will clarify the physical behaviour of the melt. As the flow in the geometry is in the laminar regime and Re < 1, a Newtonian fluid would follow Darcy's law. Pressure drop across the filter therefore increases linearly with increasing mass flow rate. However, Figure 4.12b shows that viscosity changes significantly over the range of flow rates used in the experiment. If this change in viscosity is not accounted for, the relationship between pressure drop across the filter and mass flow rate could not be established. To account for viscosity varying with temperature, a new variable, the corrected pressure ξ, is defined such that

$$\xi = P/\mu. \tag{4.1}$$

For each throughput in Figure 4.11, an associated temperature was calculated from the line of best fit in Figure 4.12a. This temperature was then used to find the viscosity and calculate ξ using the temperature-viscosity relationship.

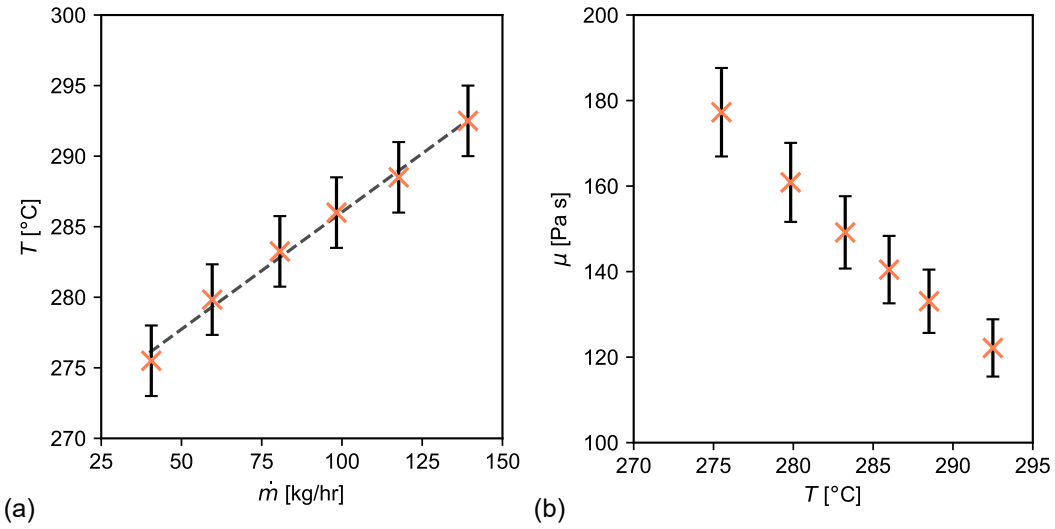

Figure 4.12: (a) The average temperature recorded using the pyrometer at each throughput interval. (b) The relationship between melt viscosity and the temperatures recorded in (a), calculated from (2.9).

Pressure drop across a filter can be determined at a particular throughput by subtracting the pressure reading of the system without a filter from the pressure reading of the system with a filter. Then, to obtain the pressure drop, a line of best fit was created for the no filter case for the pressure-throughput relationship. This gives the predicted pressure output through the system without a filter. This predicted pressure output is then subtracted from the pressure output obtained when the filter is in place to determine the pressure drop across the filter at that specific throughput. Figure 4.13 shows the corrected pressure-throughput relationship at the transducer is linear for the no filter case, showing the pressure-throughput relationship is linear when viscosity is accounted for.

From Darcy's law, dividing by viscosity,

$$\Delta\xi = \Delta P/\mu = (d/kA\rho)\dot{m}, \tag{4.2}$$

where A is the cross-sectional area of the filter, $\dot{m}$ is the throughput and $\Delta\xi$ is the corrected pressure drop across the filter. That is, corrected pressure drop increases linearly with

throughput in Darcy's regime. From Figure 4.14, it appears that corrected pressure drop does indeed increase linearly with throughput. As accounting for temperature in the melt's viscosity recovers Darcy's law, the viscosity varies negligibly with shear rate; its zero shear viscosity limit applies throughout the experiment. Furthermore, as Darcy's law applies, the viscoelastic properties of the polymer melt are demonstrated to have a negligible effect on the flow through a screen filter.

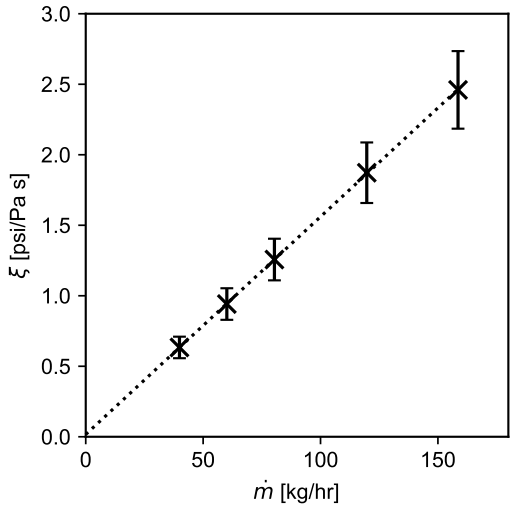

Figure 4.13: Corrected pressure at the transducer against throughput for the no filter case.

From Figure 4.14, the lines of best fit for each filter do not intercept the origin. As the filter grade reduces, thus the permeability of the filter decreases, the intercept increases. The shift may be due to non-linear effects at low throughputs, implying pre-Darcy behavior, where the throughput-pressure drop relationship becomes nonlinear due to factors such as boundary layer effects [125]. Teng et al [126] present a comprehensive review on the literature investigating the pre-Darcy regime.

Temperature variations through the filter may also contribute to the shift. The shift may also be due to complex viscoelastic, non-Newtonian behaviour at low strain rates. As operating throughput decreases, the rate of strain imposed on the melt by the filter decreases. The melt viscosity-rate of strain relationship in porous media shows melt viscosity decreasing with

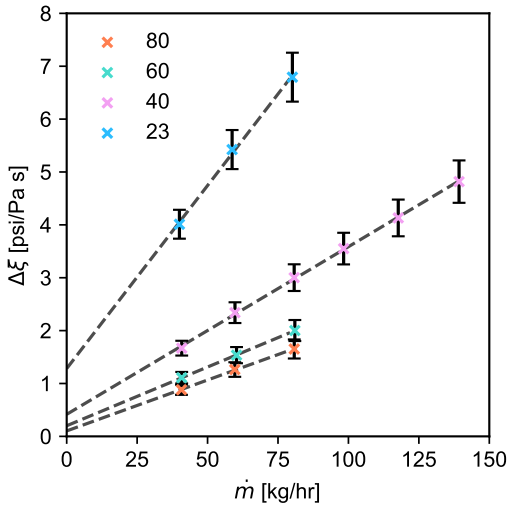

Figure 4.14: Corrected pressure drop across each filter against throughput.

strain rate, with several plateaus [45]. Experimental conditions may impose a range of strain rates on the melt such that the relationship remains in the intermediate plateau. Hence rate of strain would have no influence on melt viscosity throughout experimental conditions. Low operating mass flow rates may then increase melt viscosity due to a decrease in the strain rate imposed by the filter on the melt, resulting in non-linearity for the pressure drop-mass flow rate relationship.

Darcy's law has therefore only been shown to be valid over the range of flow rates shown for the experimental data in Figure 4.14. The exact nature of the pressure drop and mass flow rate relationship as mass flow rates approach zero is beyond the scope of this work since it is outside of the operating regime of any practical applications that I am aware of, nevertheless it may be of scientific interest to investigate more thoroughly in future work.

4.5 Computational results

As Darcy's law (4.2) applies over the range of the experiment, permeability values for each filter grade were calculated by obtaining the gradient from lines of best fit in Figure 4.14.

That is, using

$$k = \frac{d}{A\rho}\frac{1}{m_x}, \tag{4.3}$$

where m_x is the gradient from the line of best fit of an individual filter grade.

Figure 4.10 highlights the screen filter structure, with the thickness of the downstream support mesh, the filter layer and the upstream support mesh prescribed d_D, d_F and d_U respectively. These thicknesses vary between filter grade, and were measured for each filter using a caliper. The total thickness of, for example, the 80 micron filter is therefore given by $d^{80}_{\text{total}} = d^{80}_U + d^{80}_F + d^{80}_D$, where the superscript represents the filter grade. For the 23 micron filter, which is made up of five total layers, d^{23}_D was taken as the sum of the two downstream support meshes and d^{23}_F was taken as the sum of the filter layer and the support mesh between the filter layer and the upstream support mesh. With this structure, three different porous zone configurations were tested to determine the most reliable configuration for predicting pressure drop across a multi-layered woven screen with CFD using the porous media model:

1. The "full length" model. The porous zone, for each filter grade, was prescribed a thickness of $d_{\text{total}} = d_U + d_F + d_D$ and it was placed directly against the filter holder. If this model gives good agreement with the experimental results, then the layers need not be considered, and a single permeability value can be successfully used to predict pressure drop across the multi-layer configuration of a screen filter.

2. The "filter by holder" model. Zero thickness was chosen for d_U and d_D, leaving the porous zone with a thickness d_F and placing it directly against the filter holder. If this model gives good agreement with the experimental results, then only the filter layer need be considered to successfully predict pressure drop across a screen filter.

3. The "filter away from holder" model. The porous zone was enabled only in d_F, placing the porous zone a distance d_D away from the filter holder. If this model gives good agreement with the experimental results, then only the filter layer need be considered when calculating permeability, but the position of the layer must be considered to successfully predict pressure drop across a screen filter.

For each of the porous zone configurations, the permeability of each filter grade was calculated from (4.3). Simulations were then run to match the targeted throughputs in the experiment. For example, for the 80 micron filter using the full length model, a mesh was created with a porous zone of thickness d^{80}_{total}. This was ensured to match the total measured thickness of the actual 80 micron screen filter. A permeability was then calculated from (4.3) using $d = d^{80}_{\text{total}}$, which was then prescribed to the porous zone. Then simulations were run at 40, 60 and 80 kg/hr to match the throughput intervals targeted by the experimental work. Simulations were also run with no porous zone prescribed to the geometry at throughputs in intervals of 20 kg/hr between 40-140 kg/hr. Corrected pressure drop across the filter at each throughput was then calculated by subtracting the corrected pressure output from the no porous zone case away from the corrected pressure with the porous zone enabled. Table 4.7 shows the flow rates and viscosities at which CFD simulations were carried out for each grade of filter. Flow rates were chosen to match with targeted flow rates taken from the experiment. The viscosity input into the CFD was calculated using the model described by equation (2.9).

Table 4.7: Filter grades and viscosities associated with each flow rate inputted into the CFD porous zone model.

$\dot{m}$ [kg/hr]	Filter grades [μm]	μ [Pa s]
40	All	175.01
60	All	162.47
80	All	150.95
100	40	140.38
120	40	130.66
140	40	121.71

4.5.1 Mesh independence study

For each unique geometry, three meshes were generated. All meshes were generated with tetrahedra cell shapes, with curvature capture specified to ensure sufficient mesh resolution in regions of significant changes in curvature. Figure 4.15a shows the pressure drop output for the three meshes generated for the 80 micron filter in the filter away from holder case at a

throughput of 80 kg/hr. There is shown to be less than a 0.025% change between the medium and fine mesh. Results were therefore deemed to be independent of choice of medium or fine mesh.

Figure 4.15b shows a plot of x-velocity along the centreline of the pipe, starting from the inlet. The development length in the CFD model was determined by analysing the x-velocity, pinpointing the point at which its variation along the length of the pipe is 0 m/s to 4 decimal places. It is found to be in good agreement with (3.6), with a percentage error of under 5%. The medium mesh was deemed suitable to proceed with analysis.

Figure 4.15b shows that the flow is fully developed before entering the filter system. This verifies that the inlet pipe was significantly long enough to fully develop the flow before entering the filter system, negating any influence of artificial boundary effects on the flow through the filter system.

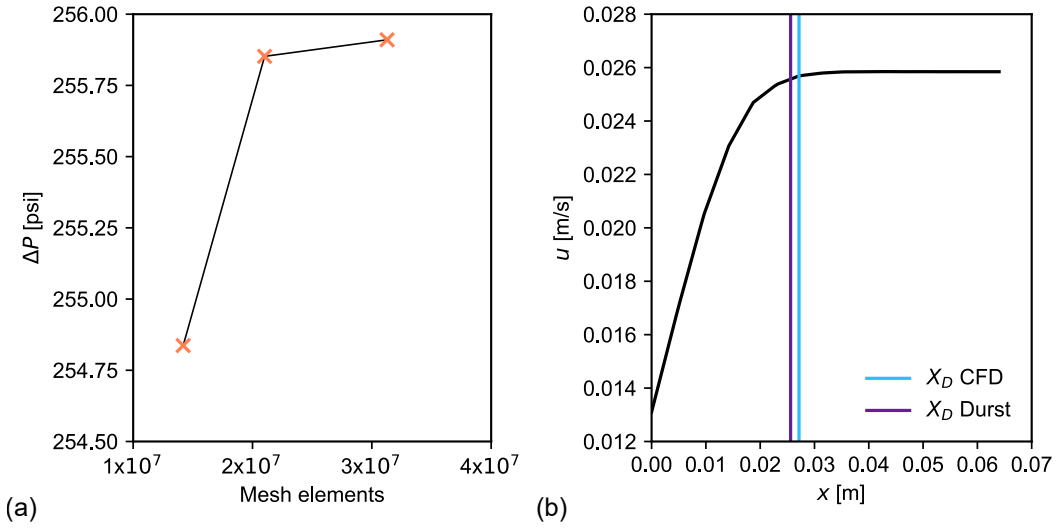

Figure 4.15: (a) Pressure drop against number of mesh elements and (b) x-velocity along the centerline for the 80 micron filter in the filter away from holder medium mesh case at a throughput of 80 kg/hr

4.5.2 Computational validation

The full length model

Figure 4.16 shows the porous zone configuration for the full length model. Table 4.8 gives the thickness and permeability of each porous zone for each filter.

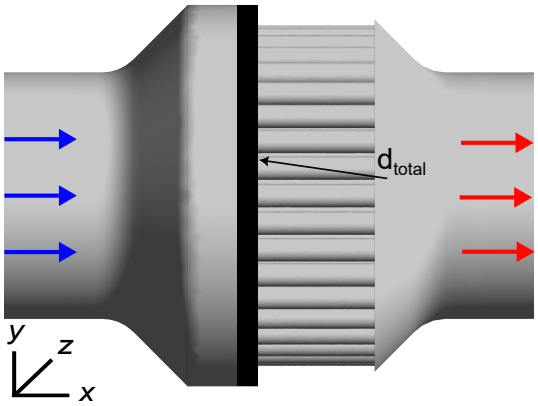

Figure 4.16: Porous zone configuration of the full length model.

Table 4.8: Filter thickness and permeability for each filter for the full length model.

Filter grade [μm]	d_{total} [mm]	k [m^2]
80	0.97	4.99×10^{-10}
60	0.9	4.02×10^{-10}
40	1.15	3.59×10^{-10}
23	1.21	1.73×10^{-10}

Figure 4.17 provides a comparison between the CFD results obtained using the full length model and the corresponding experimental data. The CFD model has been successful in capturing the linear relationship between throughput and pressure drop. However, it is apparent that there is poor agreement between experimental data and the full length model. It is worth noting that the full length model predicts a corrected pressure drop of 0 psi/(Pa s) at a throughput 0 kg/hr, which, as discussed, is not observed in the experimental data. This is a feature of a porous zone, as it is implementing Darcy's law. Thus, to compare the two, it

is essential to focus on the gradients obtained from the CFD model and experimental data. Table 4.9 shows that there is around a 50% discrepancy in results. This poor agreement is because the full length model does not account for the multi-layered structure of the screen filters. Superior agreement is found when the different layers are accounted for.

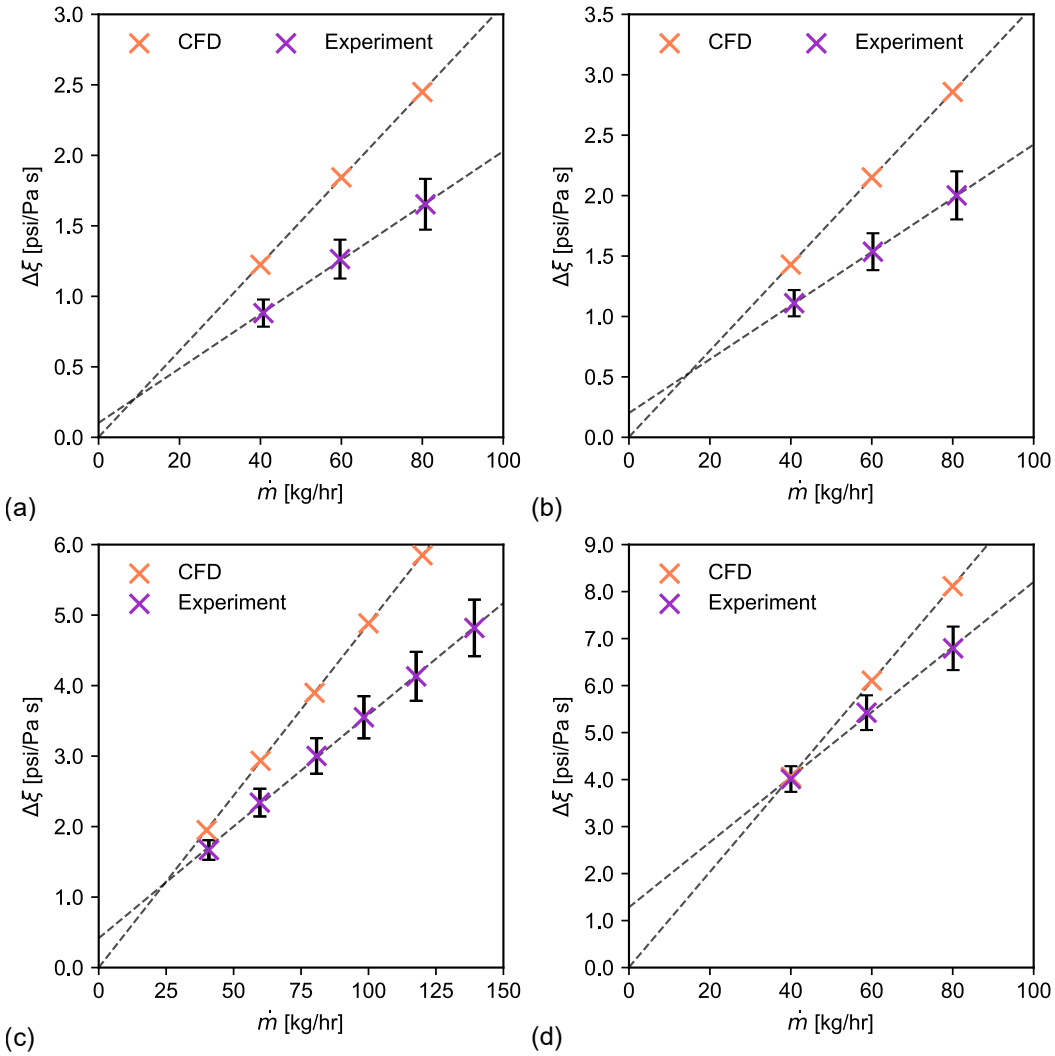

Figure 4.17: Corrected pressure drop through the (a) 80 (b) 60 (c) 40 (d) 23 μm filter against throughput from experimental data and the full length model.

Table 4.9: Comparison between the gradients produced between experimental results and the full length model.

Filter grade [μm]	Experimental gradient	CFD gradient	Gradient error [%]
80	0.0193	0.0306	58.55
60	0.0222	0.0357	60.81
40	0.0317	0.0488	53.94
23	0.0692	0.1014	46.53

The filter by holder model

Figure 4.18 shows the porous zone configuration for the filter by holder model. Table 4.10 gives the thickness and permeability of each porous zone for each filter.

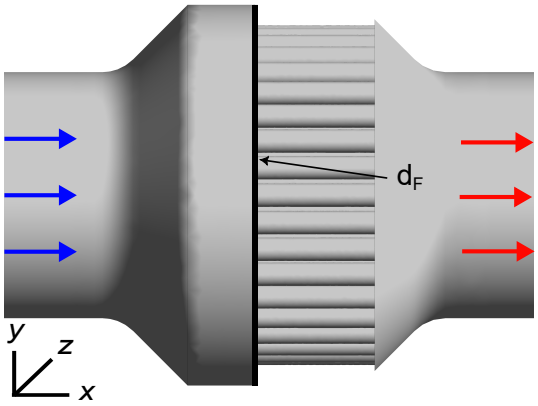

Figure 4.18: Porous zone configuration of the filter by holder model.

Table 4.10: Filter thickness and permeability for each filter grade for the filter by holder model.

Filter grade [μm]	d_F [μm]	k [m^2]
80	170	8.75×10^{-11}
60	120	5.35×10^{-11}
40	350	1.09×10^{-10}
23	240	3.44×10^{-11}

Figure 4.19 provides a comparison between the CFD results obtained using the filter by holder

model and the corresponding experimental data. The filter by holder model has been successful in capturing the linear relationship between throughput and pressure drop. However, it is apparent that there is very poor agreement between experimental data and the CFD model. There is poor agreement between experimental data and CFD model gradients. Table 4.11 shows that CFD predictions are off by around 100%. This suggests that position of the porous zone, relative to the filter holder, must be accounted for.

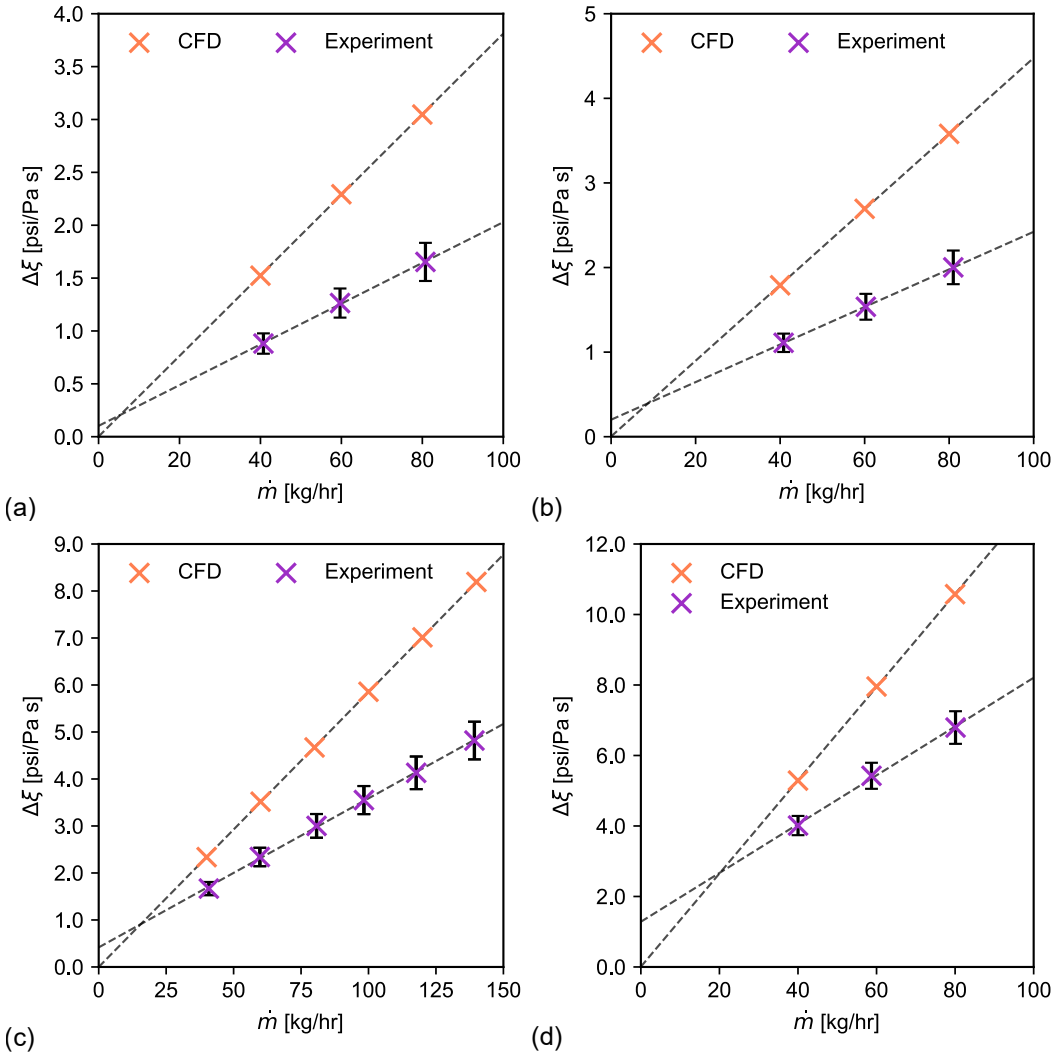

Figure 4.19: Corrected pressure drop through the (a) 80 (b) 60 (c) 40 (d) 23 μm filter against throughput from experimental data and the filter by holder model.

Table 4.11: Comparison between the gradients produced between experimental results and the filter by holder model.

Filter grade [μm]	Experimental gradient	CFD gradient	Gradient error [%]
80	0.0193	0.0381	97.41
60	0.0222	0.0447	101.35
40	0.0317	0.0585	84.54
23	0.0692	0.1322	91.04

The filter away from holder model

Figure 4.20 shows the porous zone configuration for the filter away from holder model. Table 4.12 gives the thickness and permeability of each porous zone for each filter.

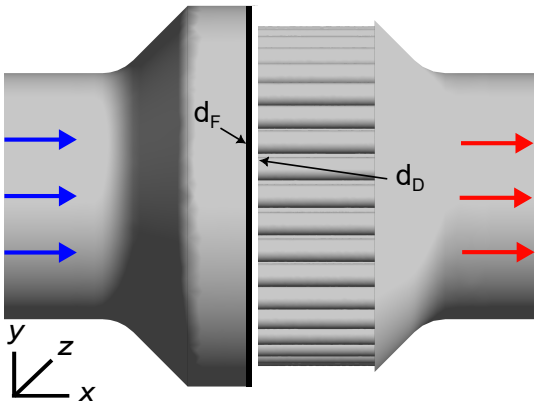

Figure 4.20: Porous zone configuration of the filter away from holder model.

Table 4.12: Filter thickness and the permeability for each filter for the filter away from holder model.

Filter grade [μm]	d_F [μm]	d_D [μm]	k [m^2]
80	170	550	8.75×10^{-11}
60	120	550	5.35×10^{-11}
40	350	550	1.09×10^{-10}
23	240	380	3.44×10^{-11}

In Figure 4.21, a comparison is presented between the filter away from holder results obtained

and the corresponding experimental data. The filter away from holder model has been successful in capturing the linear relationship between throughput and pressure drop. Table 4.13 shows that, in all cases, the gradient error is under 5%, indicating good agreement between the experiment and CFD model. This suggests that only the filter layer needs to be represented by a porous zone, but for good agreement, it should be placed in its correct position relative to the filter holder, hence the thickness of the downstream support mesh is needed.

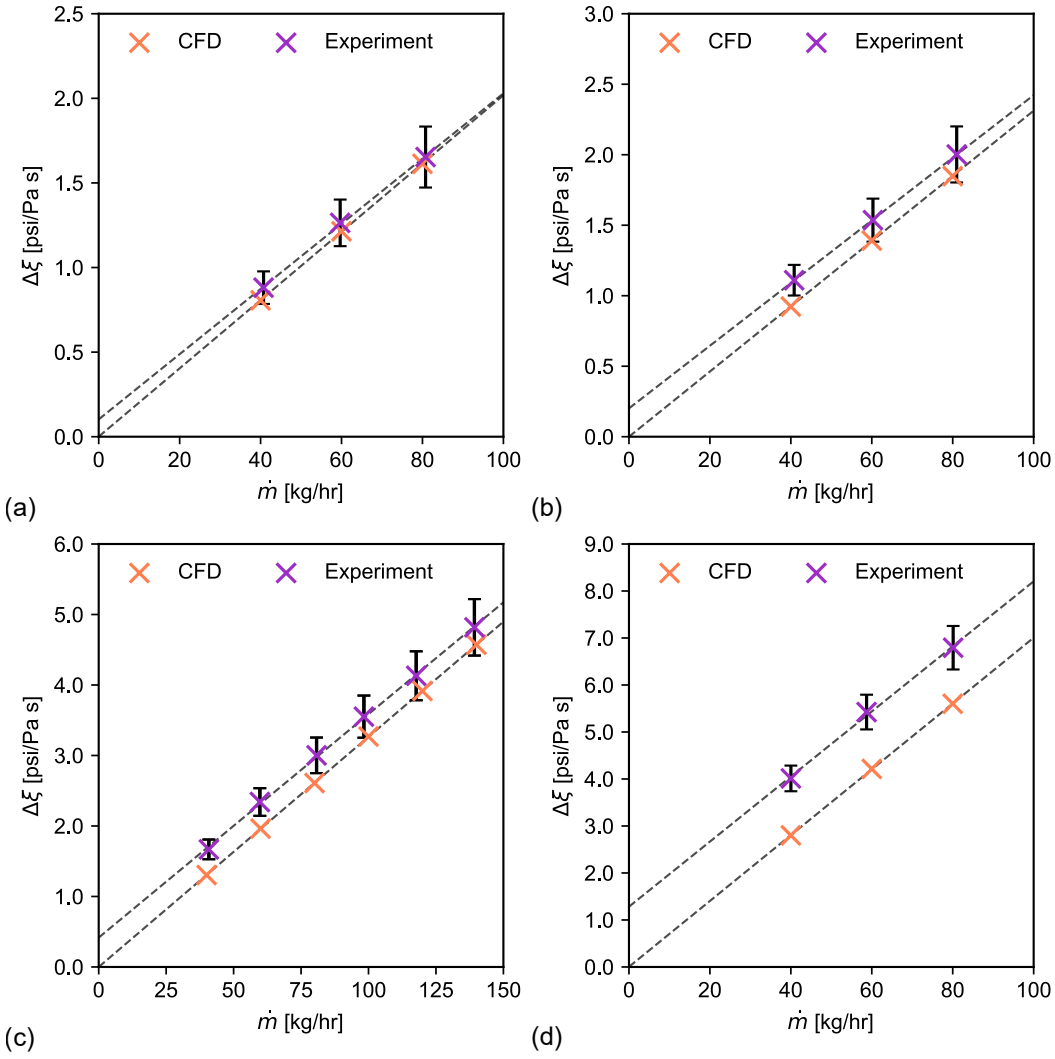

Figure 4.21: Corrected pressure drop through the (a) 80 (b) 60 (c) 40 (d) 23 μm filter against throughput from experimental data and the filter away from holder model.

Table 4.13: Comparison between the gradients produced between experimental results and the filter away from holder model.

Filter grade [μm]	Experimental gradient	CFD gradient	Gradient error [%]
80	0.0193	0.0202	4.66
60	0.0222	0.0231	4.05
40	0.0317	0.0327	3.15
23	0.0692	0.0700	1.16

4.6 Discussion

The away from holder model produces results in best agreement with the experiment because the multi-layered configuration of the filter is accounted for through the thickness of the porous zone and its position relative to the filter holder. The filter medium itself is far less permeable than the support layers, thus the pressure drop caused by flow resistance through the filter layer dominates the pressure drop through the screen filter. However, it is clear that the position of the porous zone relative to the filter holder influences results. By placing the porous medium the distance of the downstream support layer away from the mesh, agreement with the experiment is superior.

Figure 4.22 shows the x-velocity profile upstream of the porous zone for each model. As model accuracy compared to experimental results improves, there is a decrease in fluctuations in x-velocity upstream of the porous zone. This shows that by placing the porous zone a distance away from the holder, the resistance caused by the porous zone has a larger influence on the flow profile. As the porous zone is defined as isotropic and homogeneous, the flow redistributes so that velocity is constant across it. In pipe flow, as flow approaches an isotropic, homogeneous screen, it causes resistance to the flow, flattening the velocity profile [127]. This flattening is most apparent in the filter away from holder model. The flattening is less apparent in the filter by holder and full length models, where the x-velocity profile has a similar shape to the no filter case. As the porous zone is in contact with the holder, the flow distributes to follow the path of least resistance through both the porous zone and the holder.

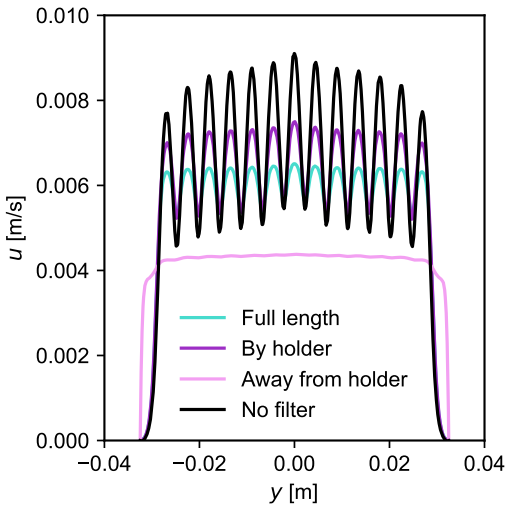

Figure 4.22: Plot of x-velocity along $y = 0$, 1.5 mm upstream of the holder for a no filter case, the full length model ($d_{\text{total}} = 0.9$ mm), the filter by holder model ($d_{\text{F}} = 0.12$ mm) and the filter away from holder model ($d_{\text{F}} = 0.12$ mm, $d_{\text{D}} = 0.55$ mm). All models have a throughput of 60 kg/hr. A 60 micron filter is modelled.

This is further verified by Figure 4.23. In Figure 4.23a, where no filter is inserted, flow is evenly distributed through each channel of the filter holder. In Figure 4.23b , in the filter by holder model, the flow patterns closely resemble those observed in the absence of a filter; the distribution of flow remains well-balanced across each channel. Figure 4.23c shows that, for the filter away from holder model, as the velocity is nearly constant across the porous zone, the majority of the flow must travel through the outer holes, due to the proportion of fluid in their vicinity. Overall, the filter away from model resolves the changes in flow as the melt moves between screen layers and the holder, whereas the other models do not.

The choice of filter grade employed is crucial in optimising the film casting process. A lower grade filter ensures smaller contaminants are captured compared to a higher grade filter. However, Figure 4.14 shows that decreasing filter grade results in a larger pressure drop penalty across the filter. This means that more energy is required for the melt pump to maintain a desired flow rate. It is therefore important to choose a filter grade which will not affect the quality of the final product while minimising pressure drop across the filter to

optimise cost-effectiveness of the process.

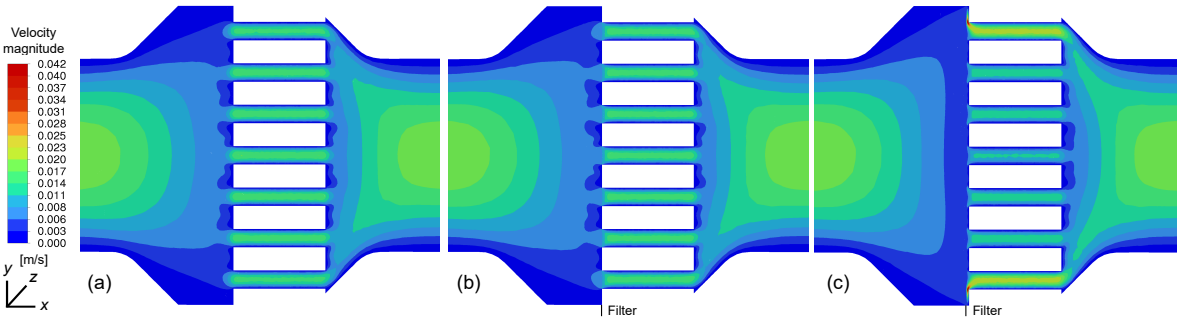

Figure 4.23: Contours of velocity magnitude perpendicular to the holder for (a) a no filter case, (b) the filter by holder model and (c) the filter away from holder model. All models have a throughput of 60 kg/hr; (b) and (c) model a 60 micron filter.

4.7 Conclusion

The structure and thickness of each layer for each screen filter employed by Mylar on the pilot scale line was found. An experimental set-up, designed to investigate how pressure drop changed based on changes to melt throughput and filter permeability, was carried out. A computational model, using a porous zone to represent the screen filter was created to model experimental results. Variations in porous zone length and position, based on the structure of a screen filter, were tested to see what configuration leads to the best agreement with experimental results.

Pressure drop was found to increase with decreasing filter permeability. Furthermore, corrected pressure drop, accounting for temperature variation, was found to increase linearly with increasing throughput for all filter grades at all throughputs investigated. This showed that over the range of the experiment, Darcy's law applied and PET melts act as a Newtonian fluids as they pass through screen filters.

It was found that to computationally model the pressure drop of a flow through a multi-layered woven screen, only the filtration layer needs to be modelled, but the presence of the

downstream support layer needs to be accounted for. Using the sum of the screens as a thickness, or ignoring the support meshes completely, leads to inaccurate modelling. Instead, the filtration layer should be modelled with a porous zone, but placed correctly relative to the filter holder in the actual geometry. This allows for correct capture of changes in flow distribution as the melt moves between screen layers and the holder. The CFD methodology developed is applicable to any CFD model of a filter system which utilizes a multi-layered screen filter, as long as the fluid is Newtonian and obeys Darcy's law across the screen filter.

Chapter 5

Pressure Drop Evolution Across Screen Filters

This chapter extends the work done on the flow of polymer melts through screen filters to include the consideration of filtration. Another experiment with the pilot scale extrusion system, where a polymer chip with agglomerated filler particles was used to block a screen filter over the course of several hours, is detailed and analysed. Filter blocking models are fitted to the pressure drop evolution data, with the most successful model used to find the permeability evolution of the filter as a function of time. Using the permeability evolution model, CFD simulations with the screen filter geometry are undertaken to mimic the pressure drop evolution seen from the experiment. These simulations are used to offer insight into how flow patterns change in the filter system as the screen filter blocks.

5.1 Experimental set-up

The objective of this experiment was to investigate how the pressure drop across a screen filter evolves as the filter blocks with particles. Polymer was extruded and pumped through an 80

micron filter at a targeted constant flow rate of 40 kg/hr and pressure was recorded upstream of the filter. The filter system used was the same as used in Chapter 4, shown in Figure 4.1. Figure 5.1 shows the set-up of the pilot scale extrusion system used for the experiment. A co-extrusion system was used. The primary feeder was fed with a filled polymer; a masterbatch of 0.64 IV PET melt and filler particles at a targeted 26 kg/hr. The secondary feeder was fed with an unfilled polymer; a 0.62 IV PET melt at 14 kg/hr. After extrusion, the melts combined into one pipe upstream of the melt pump. The melt pump aimed to maintain the desired throughput of 40 kg/hr. The masterbatch of PET and filler particles was used as it had been found to increase pressure drop across the system at an accelerated rate compared to other trials on the pilot scale extrusion line. To ensure the filter blocked over a period of hours rather than minutes, the 0.62 IV PET was used to maintain the minimum required flow rate of 40 kg/hr for the pilot scale line while diluting the masterbatch. This is because the pressure tripped in under 30 minutes in a previous run with just the masterbatch at a throughput of 60 kg/hr. Both batches were fed into their respective extruder via a cold feedstock and all pipes were maintained at 275°C by a series of heaters along the extruder. A full vacuum was used on the extruder to remove moisture and minimise trapped air in the melt. The melt then passed through the filter holder and then the die. The melt pump was positioned upstream of filter. The pressure transducer recorded pressure every minute between the melt pump and the filter holder.

Figure 5.2 shows the pressure upstream of the filter and total mass flow rate at the melt pump throughout the experiment. For the first section, (i), no filter was inserted into the pilot scale system. This initially flushed out any debris from previous use and was also used to find the pressure drop across the system excluding a filter. For the second section, (ii), the filter was inserted, and a clear increase in pressure upstream of the filter is observed as time progresses. As with the original screen filter experiment, it took time for the mass flow rate and pressure to stabilise on start up. The final data record shows a pressure output of 0 psi. This is because the previous data record tripped the maximum allowable pressure limit, shutting-down the pilot scale system.

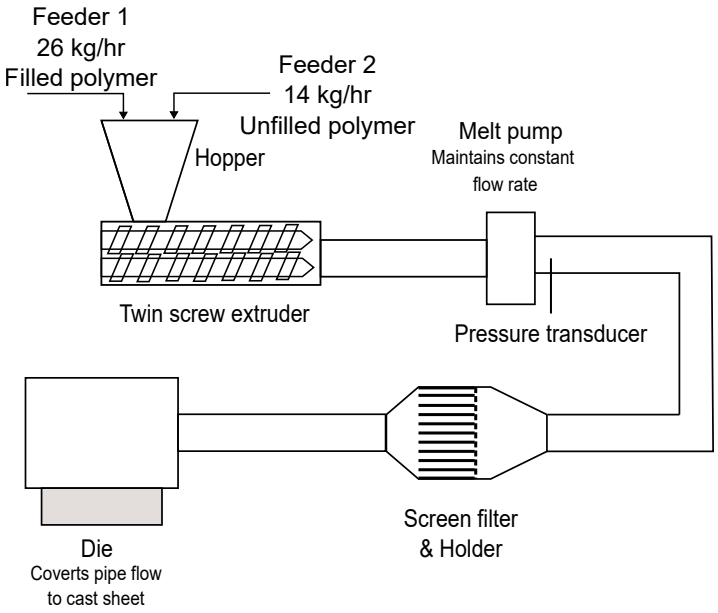

Figure 5.1: Sketch of the pilot scale extrusion system for the filtration experiment.

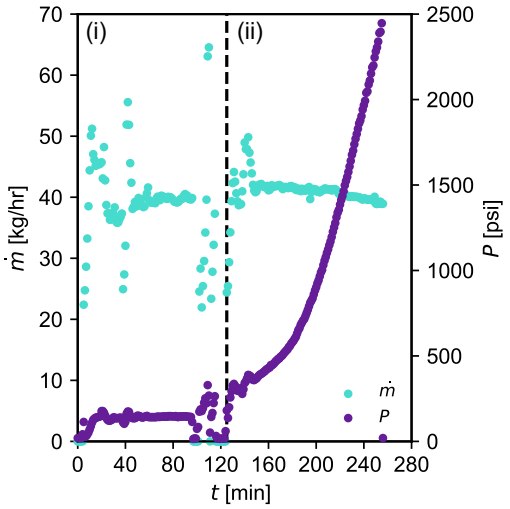

Figure 5.2: Total mass flow rate at the melt pump and pressure upstream of the filter over the course of the filtration experiment. No filter was inserted in (i). An 80 micron filter was inserted in (ii).

Temperature of the melt at the die was recorded with the Minolta/Land Cyclops pyrometer at several times over the course of the experiment. Temperature was recorded at the feed end, blank end and centre of the cast sheet for each time. Figure 5.3a shows temperature against

average pressure at the transducer for each recording. Each measurement was repeated 10 times and averaged to reduce experimental noise. As the temperature was recorded multiple times over the course of a recording, pressure increased throughout. Hence the mean of pressure is plotted in Figure 5.3a. There is no discernible correlation between increasing transducer pressure and melt temperature. Figure 5.2 also shows that the mass flow rate is fairly stable throughout the temperature recordings; it has a range of less than 3.28 kg/hr. Temperature does not appear to vary over the course of the experiment. A temperature of 287.5°C is taken as the temperature of the melt throughout the filtration experiment; this was determined by taking the mean of the averaged centre temperature in Figure 5.3a.

Mylar provided data on the density-temperature relationship for combined melt flow. Figure 5.3b shows the relationship between temperature and density. For the range of temperatures plotted, a linear fit shows exceptional suitability to the density-temperature relationship, with R^2=0.999. From the linear regression line, a melt density of 1331.95 kg/m^3 is calculated from a temperature of 287.5°C. Melt viscosity is calculated from the model described by equation (2.9). At the targeted flow rate ratio between the primary and secondary extruder, the IV of the combined polymers is 0.633. This gives a melt viscosity of 210.53 Pa.s.

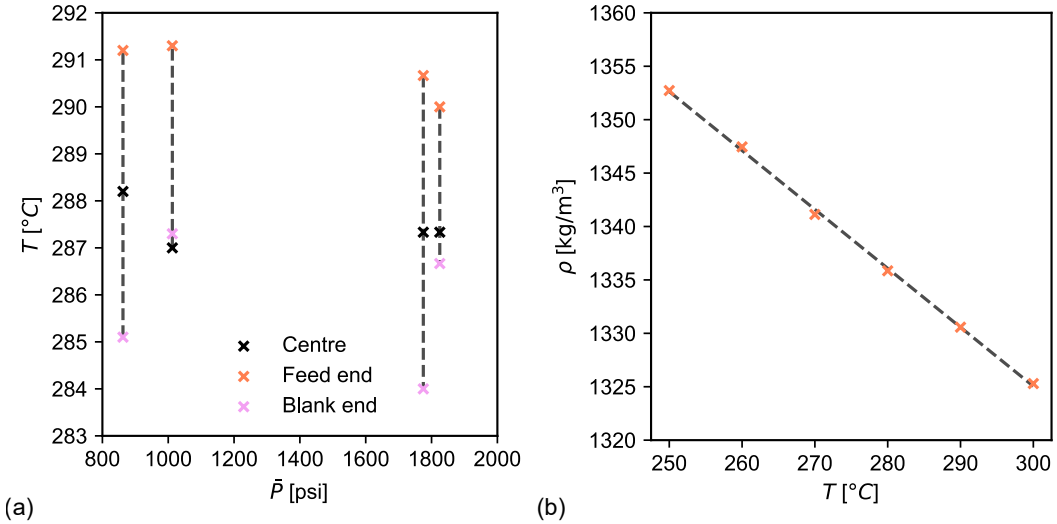

Figure 5.3: (a) Temperature recorded with a pyrometer over a range of transducer pressures. (b) Density against temperature for the combined melt, calculated from an in-house model used by Mylar.

5.2 Experimental results

Figure 5.4a shows pressure upstream of the filter and the mass flow rate at the melt pump for the no filter section of the experiment. The usual noise on start up is apparent. However, mass flow rate remained unstable up until 60 minutes. Figure 5.4b shows the mass flow rate contribution from the primary and secondary feeder for the no filter section. Issues with the secondary feeder caused inconsistent flow rates and the flow rate only began to stabilise towards the target at around 55 minutes. Figure 5.5 shows a linear regression line fitted to the considered no filter mass flow rate and pressure relationship; the trend of increasing pressure with flow rate is apparent. It was also shown in Figure 4.13 in Section 4.4 that over a large range of flow rates, corrected pressure increases linearly with flow rate. As temperature and viscosity remained stable over the course of this experiment, pressure can be directly compared to mass flow rate with the previously established corrected pressure relationships.

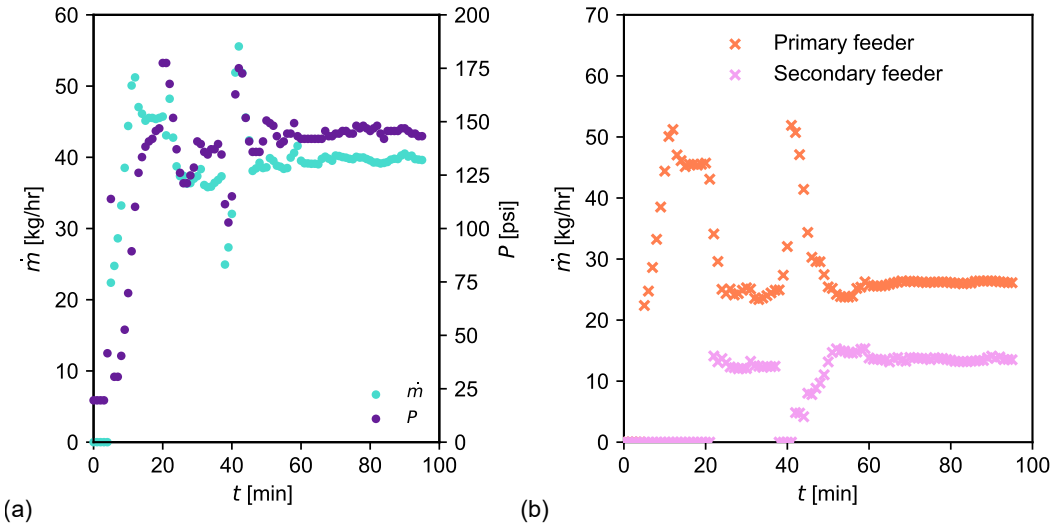

Figure 5.4: (a) Total mass flow rate at the melt pump and pressure upstream of the filter and (b) primary and secondary feeder mass flow rate for the no filter section of the filtration experiment.

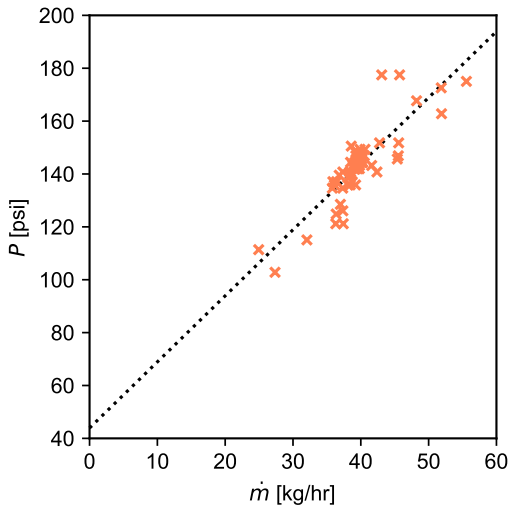

Figure 5.5: Plot of pressure against mass flow rate for the no filter section of the filtration experiment.

Figure 5.6a shows pressure upstream of the filter and total throughput at the melt pump for the filter section of the experiment, with the start of this section set at 0 minutes. The usual noise on start up is apparent. However, the mass flow rate remained unstable up until 20 minutes. Figure 5.6b shows the mass flow rate contribution from the primary and secondary extruder for the filter section. Issues with the secondary extruder again caused inconsistent flow rates and the flow rate only began to stabilise towards the target after around 20 minutes. To account for this instability, only data starting from 25 minutes is considered.

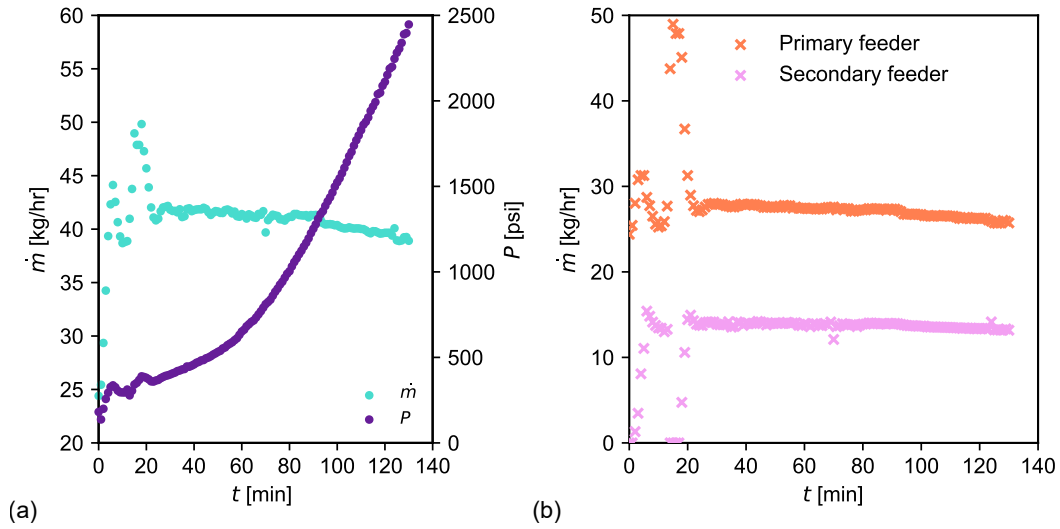

Figure 5.6: (a) Total mass flow rate at the melt pump and pressure upstream of the filter and (b) primary and secondary feeder mass flow rate for the filter section of the filtration experiment.

Figure 5.7a shows evolution of the pressure drop across the filter for the section of the experiment where the filter was in place. Pressure drop across the filter is calculated by taking the pressure recorded at the transducer and subtracting pressure drop contribution from the geometry, calculated from the regression line in Figure 5.5. For example, at time $t = 25$ min in the filtration section, pressure at the transducer was recorded as $P = 368.42$ psi. At the same time, the mass flow rate at the melt pump was recorded as $\dot{m} = 40.98$ kg/hr. From the line of regression in Figure 5.5, the pressure contribution from the geometry at 40.98 kg/hr is 146.4 psi. Then, the pressure drop across the filter at $t = 25$ min is $\Delta P = 222.07$ psi.

Filter permeability can be calculated at a given time from the experimental data by substituting pressure drop data at that time into Darcy's law (2.13) with the thickness and cross-sectional area of an 80 micron screen filter. Such geometrical properties of each screen filter is detailed in Chapter 4. Figure 5.7b shows permeability evolution with time.

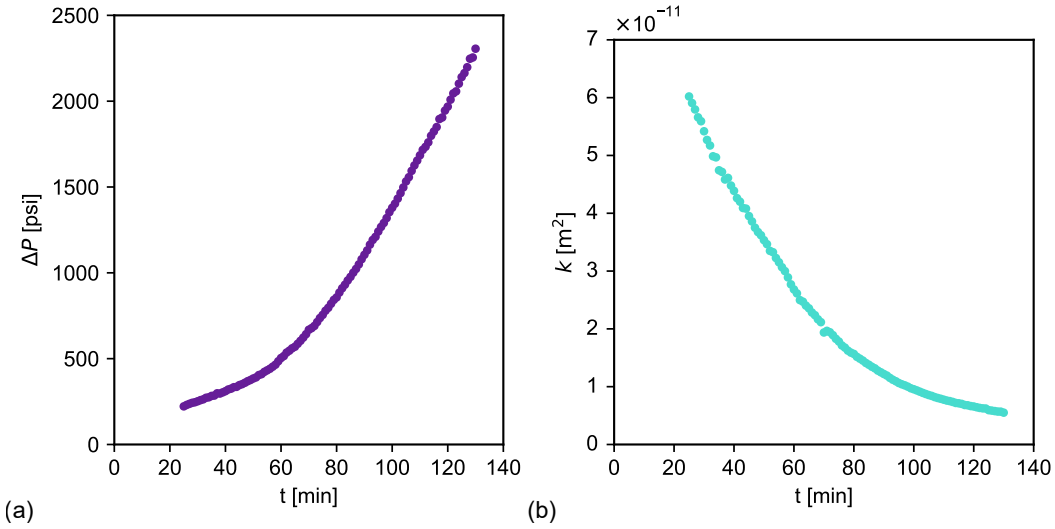

Figure 5.7: (a) Pressure drop across the filter against time and (b) permeability of the filter against time for the filter section of the filtration experiment.

5.3 Screen filter blocking model

As PET melt was shown to obeys Darcy's law across screen filters in Chapter 4, filter blocking models are fitted to the pressure drop evolution curve in Figure 5.7. Filter blocking models were discussed in detail in Section 2.3.1. The four simplest models, complete blocking, standard blocking, intermediate blocking and cake filtration, are fitted. The models require constant rate filtration; Figure 5.6 shows that mass flow rate varied over the course of the experiment from the targeted 40 kg/hr throughput. To account for this, the mean mass flow rate over the filtration experiment (40.87 kg/hr) was used for model fitting. Figure 5.8 shows pressure drop against time, put into a different form for each model, so a linear curve can be fitted to test the suitability of each model. The R^2 value of each fit is also presented in Table 5.1. The intermediate model gives the best fit to the data. The intermediate model mimics the capture of particles on the surface of the filter media, where particles can stack as the filter blocks. Physically, this makes sense as the filter media is composed of a single layer of woven metal wires. Particles could therefore not get caught inside the pores of filter media;

they must be intercepted by the surface of it.

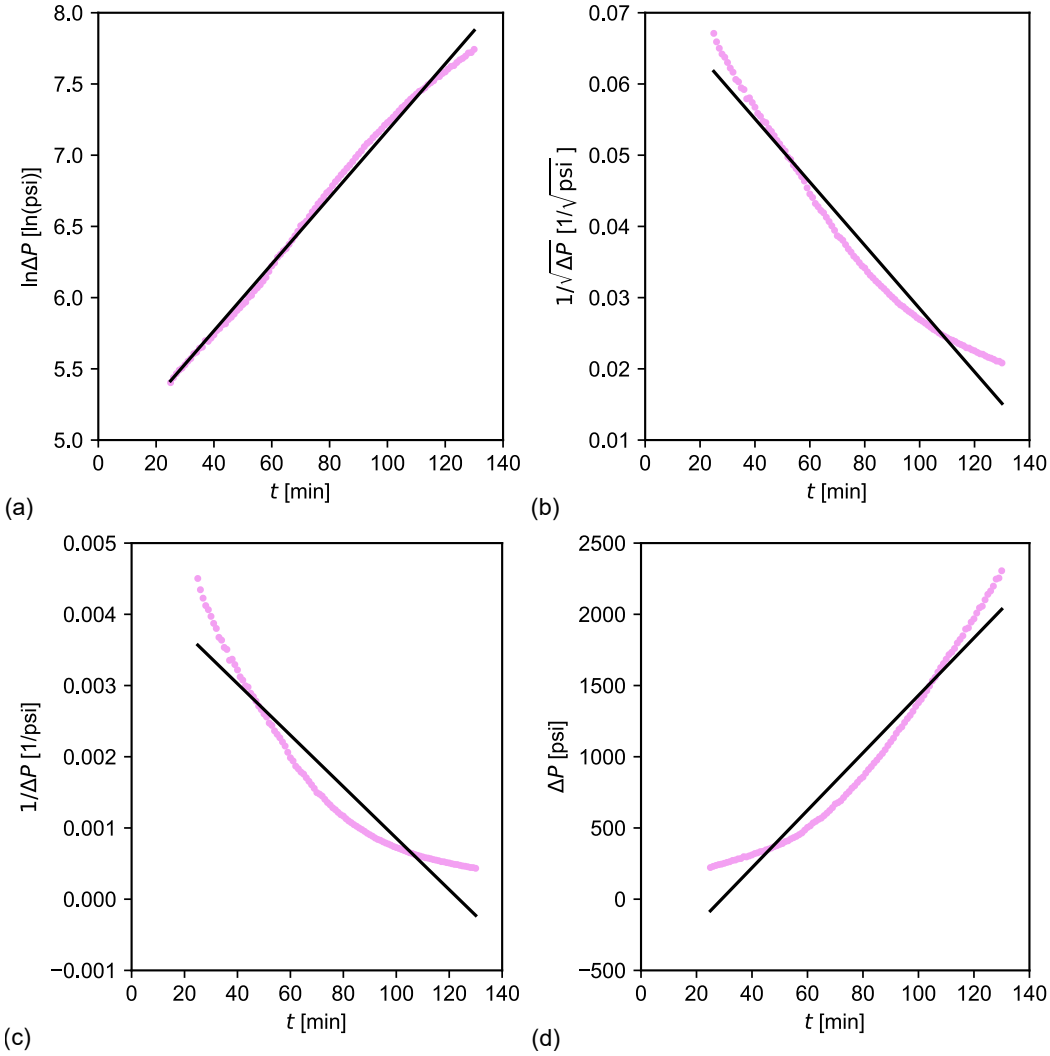

Figure 5.8: Linear curve fitting to the pressure drop evolution across the screen filter from Figure 5.7 for (a) intermediate blocking (b) standard blocking (c) complete blocking and (d) cake filtration.

Table 5.1: R^2 values for the fit of different blocking models to the pressure drop evolution across the screen filter from Figure 5.7.

Blocking model	R^2
Intermediate blocking	0.995
Standard blocking	0.965
Complete blocking	0.904
Cake filtration	0.949

The intermediate blocking model is given by

$$\Delta P = \Delta P_0 \exp(K_i \dot{m} t). \tag{5.1}$$

Figure 5.9 shows a comparison between the intermediate model, with ΔP_0 and K_i chosen from the linear curve fitting, with the pressure drop evolution data. The linear curve fitting gave the fitting parameters as $\Delta P_0 = 125$ psi and $K_i = 2.063$ m^{-1}.

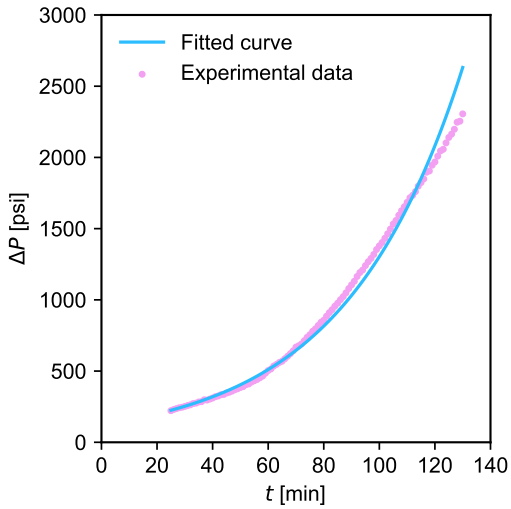

Figure 5.9: Intermediate blocking model fitted to pressure drop across the screen filter against time for the filter section of the filtration experiment.

Substituting Darcy's law into the intermediate model (5.1) and noting that

$$\Delta P_0 = \frac{\dot{m} d \mu}{A \rho k_0}, \tag{5.2}$$

a relationship for permeability evolution with time can be found:

$$k = k_0 \exp(-K_i \dot{m} t). \tag{5.3}$$

Figure 5.10 shows the fit of (5.3) with the same K_i found from fitting the intermediate model to pressure evolution data. This gives $k_0 = 1.10 \times 10^{-10}$ m^2. But an initial permeability for the 80 micron filter was found as $k_0 = 8.75 \times 10^{-11}$ m^2 in Chapter 4. This discrepancy is because the intermediate model was fitted to the filtration data from 25 minutes into the experiment. Due to the sporadic flow rate distribution (which would also result in sporadic melt viscosity and density) in the early part of this experiment, the fitting parameters are only representative of the data to which they were fitted. Therefore ΔP_0, and by extension k_0, are not representative of the actual initial pressure drop across the filter and filter permeability of the experimental set-up.

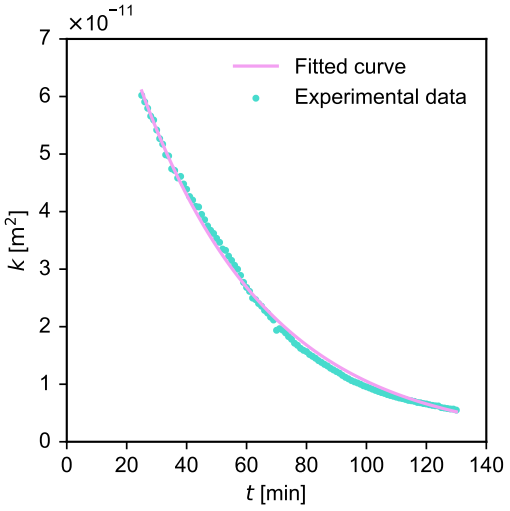

Figure 5.10: Intermediate blocking model fitted to the permeability of the screen filter against time for the filter section of the filtration experiment.

In summary, filter blocking models were fitted to the experimental data for pressure drop evolution through a screen filter from the filtration experiment. After fitting several models, the intermediate model was chosen as it gave the best fit to the data and due to its physical representation of the mechanisms of filtration through a screen filter. This fit is only representative of pressure drop and permeability evolution over the data it was fitted to, due to unstable flow rate distribution in the early stage of the experiment.

5.4 CFD modelling of screen filter blocking evolution

The filter away from holder computational model of the screen filter, shown in Figure 4.12 and detailed in Subsection 4.5.2, can be used to mimic the pressure drop evolution data from the filtration experiment using the intermediate model. Viscous resistance, the inverse of permeability, must be specified for the porous media model:

$$\eta = \eta_0 \exp(K_i \dot{m} t). \tag{5.4}$$

Eleven simulations were undertaken, described in Table 5.2. The first simulation was set to match experimental conditions at $t = 25$ min and simulation time then increased in increments of 10 minutes up until 125 minutes. The viscous resistance at each time was calculated from (5.4).

Five additional simulations were undertaken, with the porous media model disabled. The mass flow rate specified at the inlet was varied between each simulation in order to find a relationship between mass flow rate and pressure drop across the filter system with no screen filter inserted. Figure 5.11 shows the relationship between mass flow rate and pressure drop across the geometry is linear with these CFD simulations.

Table 5.2: The parameters of simulations run with the filter away from holder model to match the filtration experiment.

t [min]	η [m^{-2}]
25	1.640×10^{10}
35	2.073×10^{10}
45	2.620×10^{10}
55	3.312×10^{10}
65	4.186×10^{10}
75	5.291×10^{10}
85	6.687×10^{10}
95	8.453×10^{10}
105	1.068×10^{11}
115	1.350×10^{11}
125	1.707×10^{11}

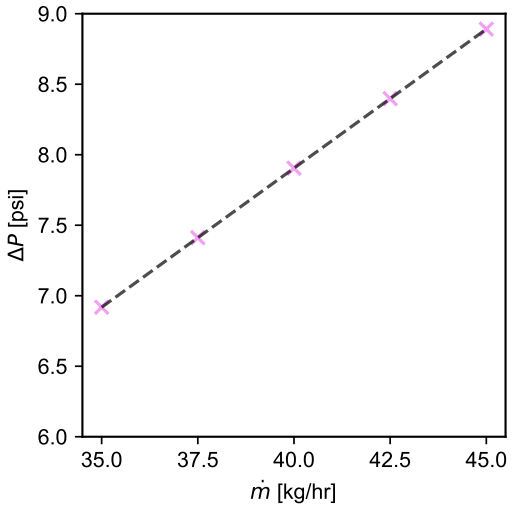

Figure 5.11: Pressure drop across the geometry against mass flow rate for the CFD model of the screen filter system with no porous zone.

Pressure drop across the filter at each time in Table 5.2 can then be calculated by subtracting the pressure across the filter system from the line of regression from the no filter simulations from the pressure drop across the filter system at each time. Figure 5.12 shows a comparison between the calculated CFD pressure drop evolution, the intermediate model fitted in Section 5.3 and experimental data. CFD pressure drop evolution matches the pressure drop profile

calculated from the intermediate model.

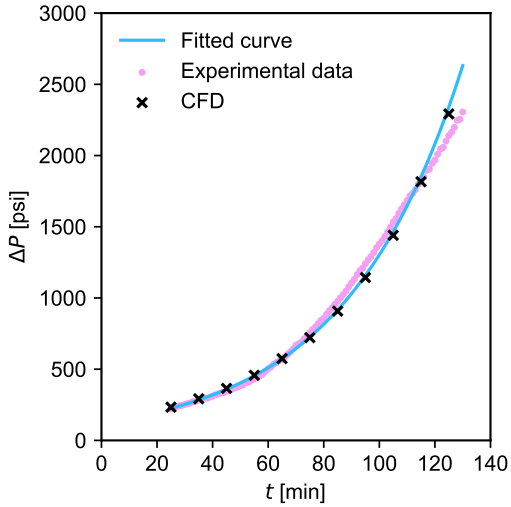

Figure 5.12: CFD pressure drop evolution compared with the intermediate model curve fitted to the experimental data.

Figure 5.13 shows the contours of velocity magnitude perpendicular to the filter holder for the simulations at $t = 25$ min and $t = 125$ min. There is no discernible difference in velocity magnitude contours as the permeability of the porous zone decreases.

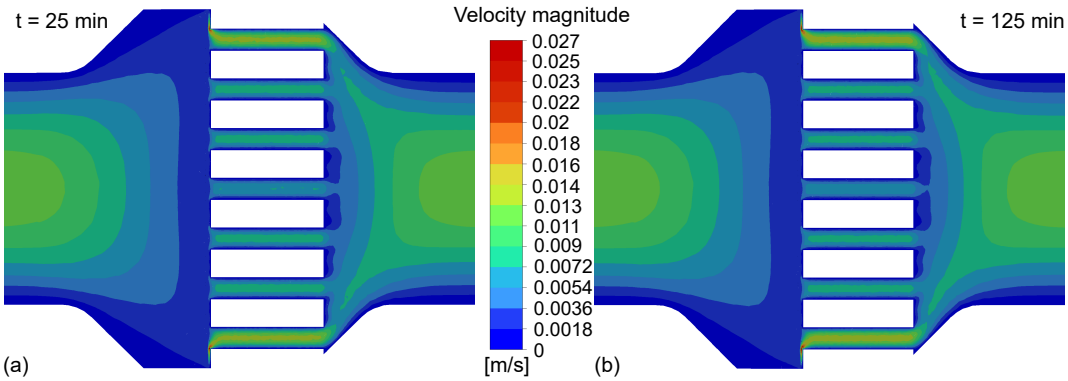

Figure 5.13: Contours of velocity magnitude perpendicular to the holder at (a) $t = 25$ min and (b) $t = 125$ min for the CFD simulations.

Figure 5.14 shows the changes to x-velocity profile upstream of the filter as the permeability of

the porous zone decreases with increasing time. As the permeability decreases, the x-velocity becomes more uniform through the centre of the geometry. Two peaks in x-velocity are seen between the outer holes in the filter holder and the walls of the geometry. A decrease in permeability leads to an increase in resistance imposed on the flow by the filter. Hence, the profile flattens with decreasing permeability. The peaks in x-velocity near the outer holes in the holder are due to the resistance imposed on the fluid by the walls. The resistance imposed on the fluid centrally, away from the influence of the solid walls, results in the fluid spreading out across the filter as fluid flow favours the path of least resistance. Near the walls, the fluid is forced through the filter as it has no other path.

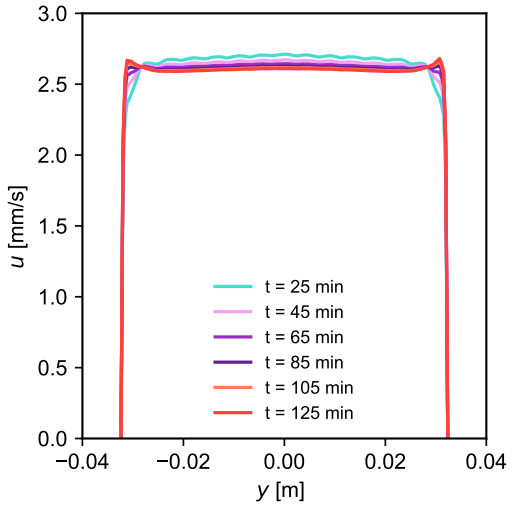

Figure 5.14: Plot of x-velocity along y, 1.5 mm upstream of the holder, for alternate simulations presented in Table 5.2.

5.5 Conclusion

This chapter focused on a second experiment with screen filters on the pilot scale line, where a masterbatch of polymer and filler particles was used to block a screen filter over a short period of time. This experiment was designed to investigate the filtration mechanisms that drive particle deposition across screen filters.

Filter blocking models were fitted to the experimental data and the intermediate model gave the best fit. This suggests that particles in the melt are captured in screen filters by surface filtration. This makes sense physically due to the single layer, woven structure of the filter layer of a screen filter.

In Figure 5.9, the intermediate blocking model fitted to the data decreases in accuracy as time proceeds. This may be due to the formation of a filter cake after the majority of the pores in the filter layer have blocked. The behaviour of the data towards the end of the experiment appears linear; that is the same form as the cake filtration model. Koller et al. [113] were able to recover multi-layered woven screens filled with solid PET particles. Magnified images of the surface of woven screens after blocking show the formation of a filter cake. It therefore seems likely that a cake layer began to form as this experiment proceeded. This would need to be verified experimentally by examining the used filter. If cake formation is confirmed, combined blocking models, such as a complete-cake blocking model, should be fitted and compared to the intermediate fit chosen here.

The filter away from holder CFD model was then used to computationally predict pressure drop using the intermediate model fit. This offered insight into how flow patterns alter around the screen filter as the filter blocks. The pressure drop evolution predicted by the CFD matched the fitted intermediate curve. This shows that correctly configured CFD porous media models give the same output as filter blocking models. This will be crucial when modelling more complicated filters and filter packs in subsequent chapters. Note that the permeability profile of the filter was assumed to increase uniformly over the course of the CFD simulations. In reality, the permeability profile of the filter will vary depending on the position of deposited particles.

Chapter 6

Modelling Polymer Melt Flow Through Candle Filter Packs

This chapter focuses on candle filters. The structure of candle filters is reviewed. Two candle filter packs which are employed by Mylar on industry lines are analysed and computational models of the filter packs are created. Data from past runs on industry production lines, provided by Mylar, which include either single and seven candle filter packs are analysed. CFD models of each pack are analysed, with symmetry exploited to reduce computational cost. The CFD models are calibrated with an appropriate porous zone set-up through results derived from the past run analysis.

This chapter includes analysis of both single and seven candle filter packs as data from runs on film production lines that include seven candle filter packs is crucial to calibrating the porous media model for a porous zone representation of a clean candle filter element. This calibration requires knowledge on the pressure drop across the packs. Single candle production lines implement a co-extrusion system and pressure readings are only possible upstream of the single candle filter pack. For the seven candle filter pack production line, pressure is recorded just upstream and downstream of the filter pack with no interference. Seven candle

filter packs are geometrically more complicated than single candle filter packs. As single candle filter packs are simpler in design, but information from production lines that include seven candle filter packs is required to calibrate the porous zone, the chapter is structured as follows: Initially, single candle filter packs are considered. Data from industrial runs with single candle filter packs is analysed. A computational model of the single candle filter pack is created. These initial simulations verify mesh independence and show how symmetry can be exploited to reduce computational cost. Then, seven candle filter packs are considered. Data from runs is analysed, which is used to assess the initial pressure drop across a seven candle filter pack. A seven candle filter pack CFD model is then created, ensured to be independent of mesh, and symmetry is again exploited to reduce computational cost. The seven candle filter pack CFD model is then used, along with initial pressure drop found from run analysis, to calibrate the permeability of the porous zone for a computational representation of a clean candle filter element. Flow patterns through porous zones representing the candle filters are analysed to understand how candle filters will initially block at the beginning of production. A permeability sensitivity test is undertaken on the single candle pack CFD model to understand how permeability influences flow patterns. The flow distribution between central and outer candles of a seven candle filter pack is explored.

6.1 Structure of a candle filter element

Candle filter elements are long (∼1 m), thin (∼5 cm) cylindrical structures where the filter medium is pleated around a central core. Figure 6.1 shows the structure of a candle filter element. A conical, solid base is attached to a cylindrical central core. The heavy duty central core is a thick metal cylinder with holes throughout its structure which allows melt to pass through and is designed to support the filter layer against high pressure gradients during runs. The filter layer, with a thickness of the order of 1 mm, is pleated around the core and is sandwiched by upstream and downstream support meshes and a Dutch twill layer to add additional protection against high pressure gradients. The filter layer is made of sintered

metal fibre and has a grade of 30 microns. This structure is pleated to maximise filter surface area. Finally, a guard cage surrounds the pleated filter structure which offers further support. Melt must travel through the guard cage, pleated structure and central core into the central cylinder of the candle. The filtered melt may then escape through the pipe at the top of the candle.

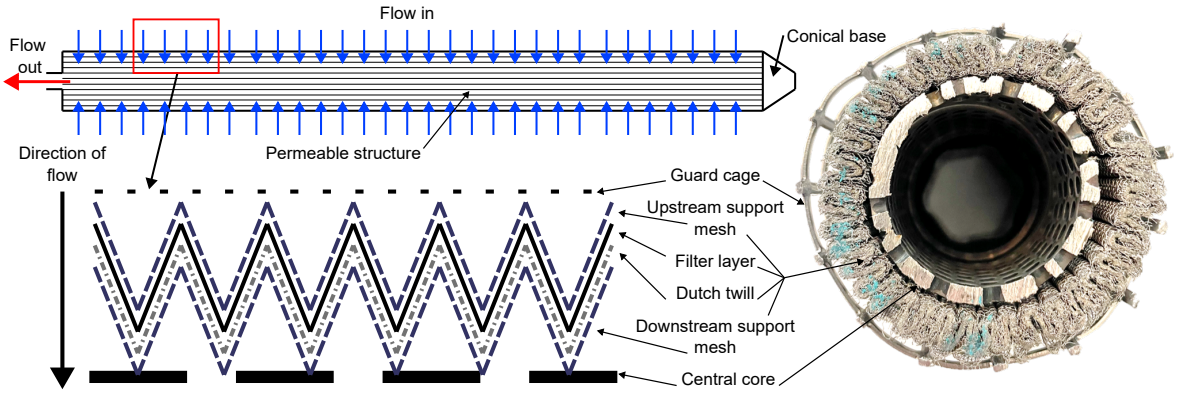

Figure 6.1: Sketch and cross-section of a candle filter element.

6.2 Single candle pack geometry

A filter pack consisting of a single candle filter element is employed by Mylar on a film production line. The design is relatively simple, with cylindrical pipes into and out of the pack. The candle element sits at the centre of a cylindrical pack, forming an annulus between the guard cage and the wall of the pack. The melt must travel from the annulus, through the candle filter to its centre onto the outlet pipe. Figure 6.2 shows a sketch of the geometry and a spider plate. The spider plate sits at the bottom of the candle element, attached onto the bottom of the conical base. This is designed to offer mechanical support to the element.

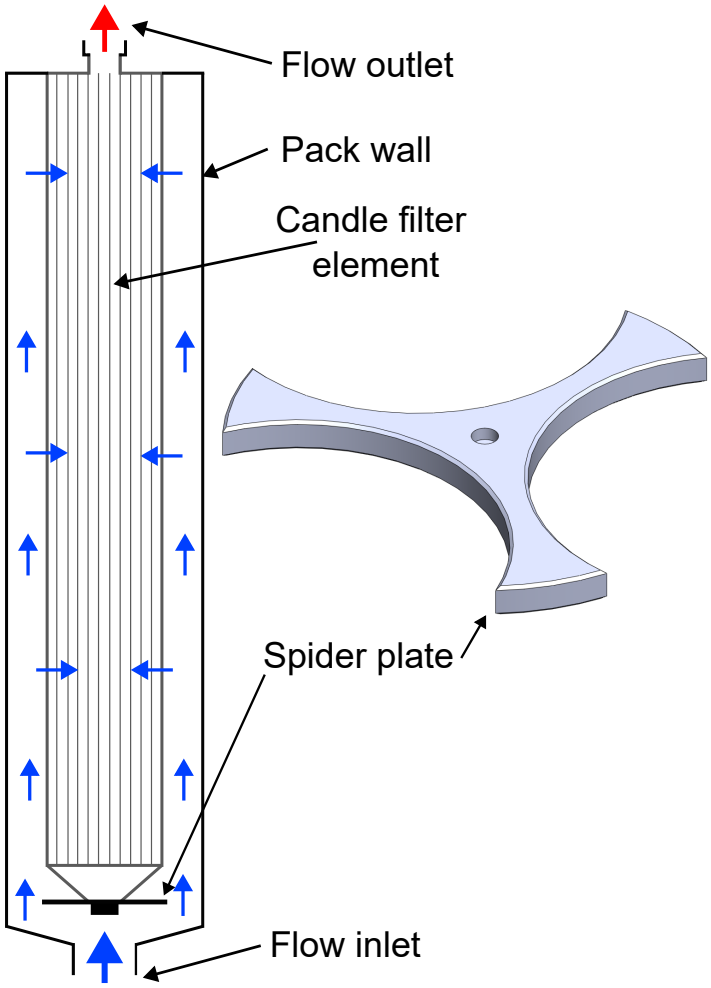

Figure 6.2: Cross-sectional sketch of a single candle filter pack and a 3D model of the spider plate.

6.3 Single candle pack run analysis

Data from fifteen production runs were provided by Mylar from the film production line that includes the single candle filter pack. Figure 6.3 shows the co-extrusion system on the film casting line with the single candle filter pack. The pressure transducer is located between the melt pump and the filter pack. There is no pressure transducer present downstream of the filter pack. Pressure at the transducer is influenced by the primary extruding system, which

branches from the extrusion system with the single candle pack between the filter pack and the die. Therefore, the pressure drop across the filter pack cannot be recovered.

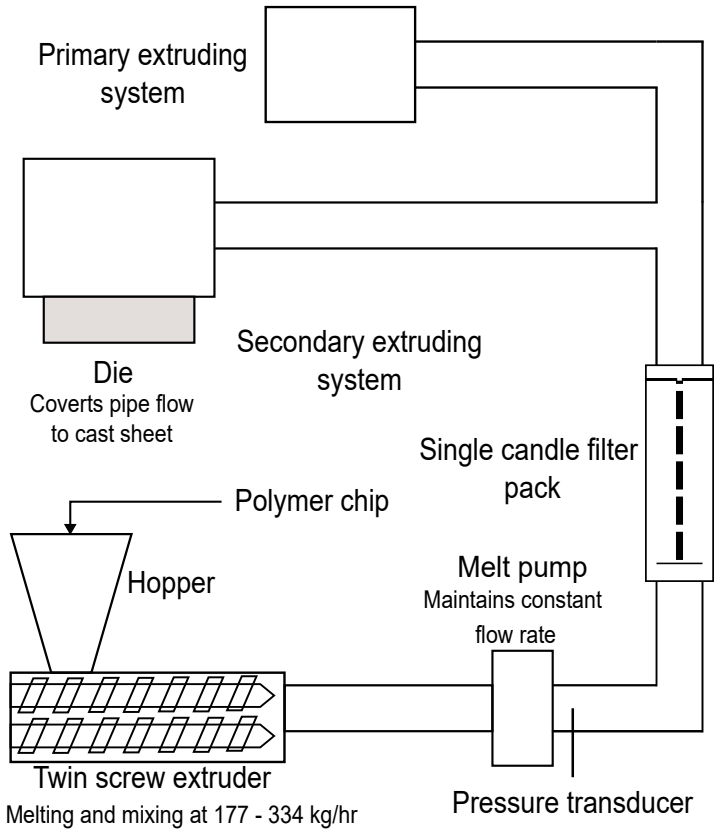

Figure 6.3: Sketch of the co-extrusion system containing the single candle filter pack.

The first task was to consider which of the 15 data sets are suitable for analysis. Figure 6.4a shows the pressure recorded at the pressure transducer and the mass flow rate through the filter pack, recorded every minute, over the course of an example production run. Figure 6.4b shows downtime in production over the course of the run. Many stoppages lead to degradation of the polymer and imply problems with the run. Furthermore, long breaks in a run will allow more degradation of the polymer, affecting fluid properties and artificially increasing the amount of substance that needs to be filtered. Therefore, run shutdowns and the length of each shutdown was considered when deciding suitable data for analysis. Figure 6.4a also shows that it takes time for the pressure to stabilise at the start of each run.

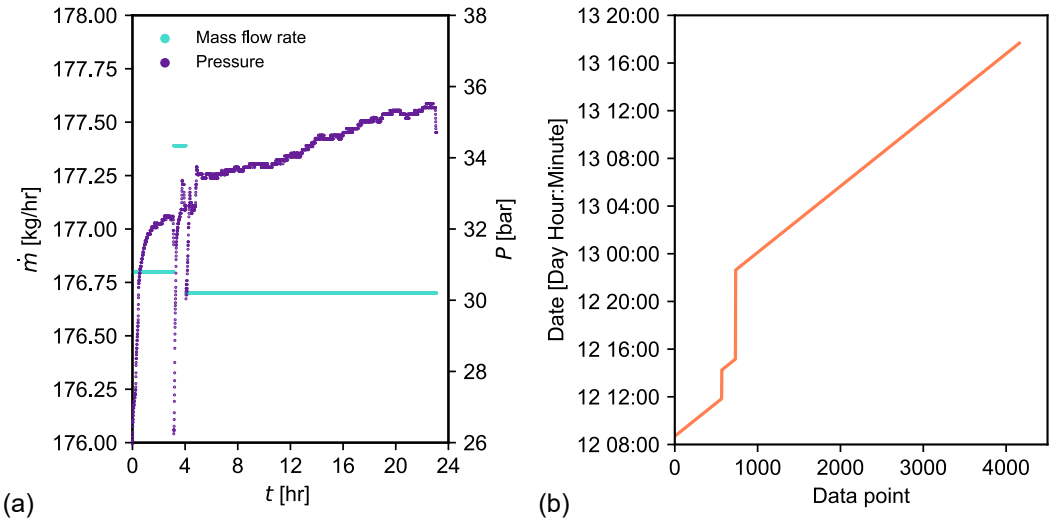

Figure 6.4: (a) Pressure upstream of the single candle pack and mass flow rate at the filter pack over the course of an example production run. (b) Time, to the minute, at which each data point from the example run was recorded. A sudden jump indicates that there was a large gap in time between subsequent recordings, hence the system was shut down.

A set of rules were therefore determined to decide if a run was suitable for analysis:

1. The first four hours of any run will not be considered.
2. There must be a region of no shutdown, or obvious process change, of at least 10 hours for a run to be considered.
3. Runs with three or more shutdowns present before a suitable period are discarded.
4. If there is a single shutdown of more than 8 hours before a suitable period, the run is discarded.
5. If there is a shutdown before a suitable period is found, the following hour will not be counted in the suitable period.
6. The first suitable period of 10 hours is used for analysis, to ensure the initial period of increase in pressure is examined.

A 10 hour length of no shutdown or process change was chosen to ensure that a suitable sample size was analysed to improve accuracy and reliability of analysis. No more than two

shutdowns and no shutdown length of 8 hours or more were chosen to reduce any effects that thermal degradation would have on melt in the system.

The implementation of these rules when analysing each run is summarised in Figure 6.5. In the case of the example shown in Figure 6.4, a ten hour period can be identified after the second shutdown. The longest shutdown is 07:28 hours, therefore the run was included in analysis. Conversely, in the second example shown in Figure 6.6, the run was excluded from analysis as the shutdown is 08:45 hours, and there is no suitable period of 10 hours before the shutdown. In accordance with this exclusion methodology, four of the runs were excluded from analysis. Table 6.1 shows a summary of the runs included in analysis.

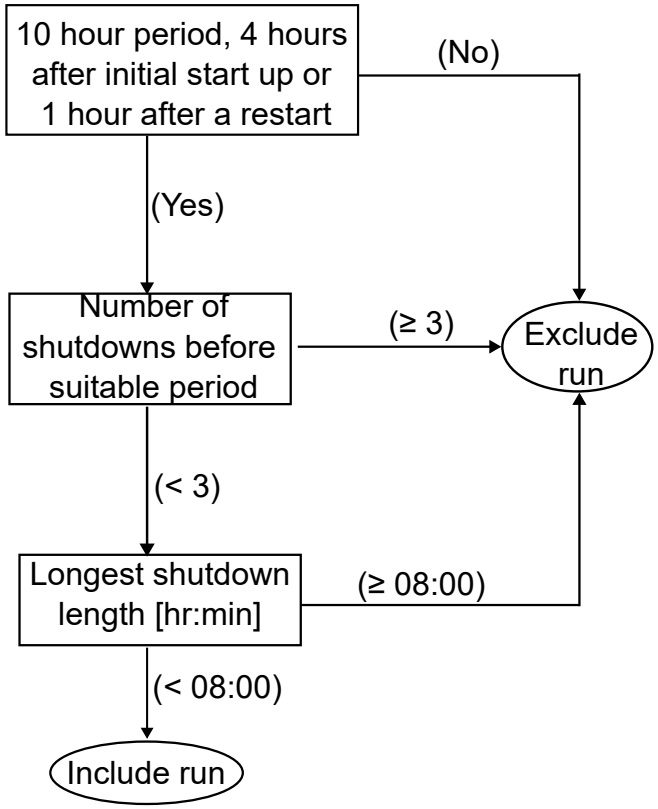

Figure 6.5: Flow chart of the suitability check procedure for a single candle pack production run.

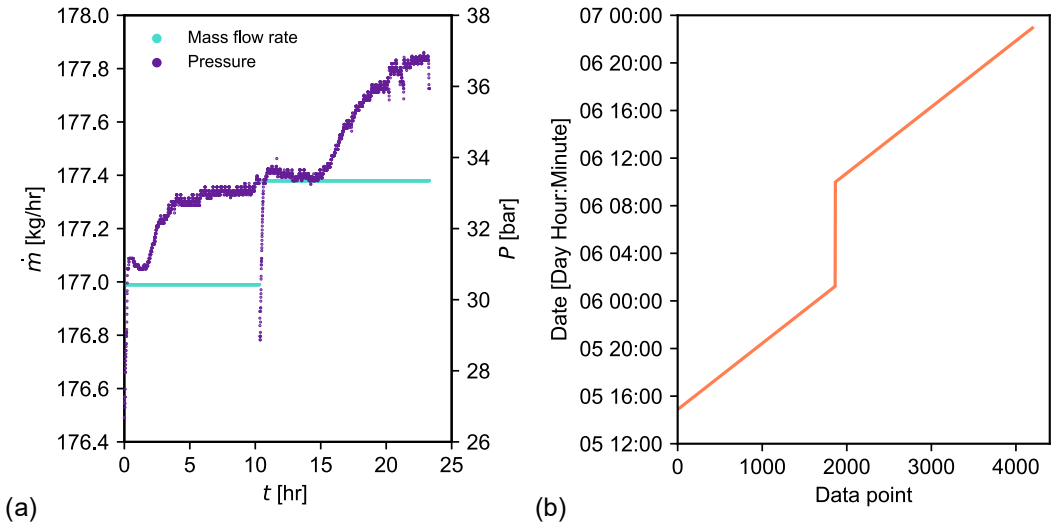

Figure 6.6: (a) Pressure upstream of the filter pack and mass flow rate at the single candle pack over the course of a second example production run. (b) Time, to the minute, at which each data point from the example run was recorded.

Table 6.1: Number of single candle runs included at each flow rate.

$\dot{m}$ [kg/hr]	Number of runs
177	5
212	1
270	3
334	2

All runs in the data-set used the same polymer for production. This means that the fluid properties for each run were determined from a rheological sweep of the same polymer melt, where a melt rheometer was used to measure viscosity for a range of temperatures. Furthermore, temperature of the melt was recorded every minute throughout each run. Figure 6.7 shows the viscosity-temperature relationship determined from a rheological sweep of the polymer melt. For all runs, the temperature was found to sit in a range of 270-285 °C. In this range, the viscosity-temperature relationship is well represented by a fitted linear curve, with an R^2 value of 0.997. The line of best fit was therefore used to determine the viscosity of the polymer melt at each minute for each run.

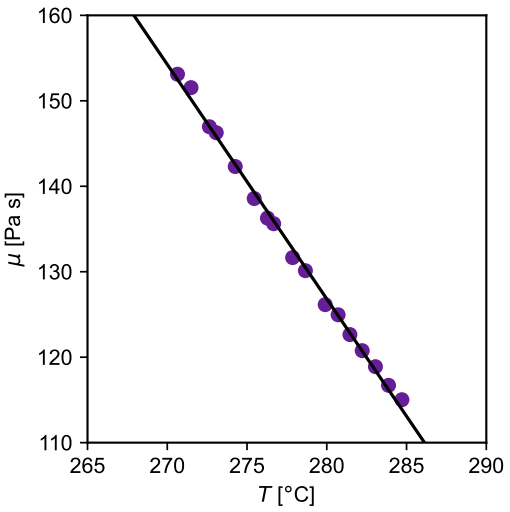

Figure 6.7: Temperature-viscosity relationship for the polymer used in single candle pack runs.

Using the temperature-viscosity relationship, the viscosity of the polymer melt at every minute of each run can be determined. Figure 6.8a shows the viscosity and temperature at every minute of the run for the example run shown in Figure 6.4. Then, the corrected pressure at the transducer may be calculated by dividing pressure at the transducer by viscosity. As in Section 4.4, viscosity is dependent on melt temperature; corrected pressure accounts for this. A linear curve can then be fitted over the suitable period in each run. Due to the position of the pressure transducer and the second extruding system, the interest in this data comes from examining the gradient of the linear part of each run. In the case of the first example, Figure 6.8b shows the highlighted 10 hour period, and the linear curve fitted to it. The gradient of the linear curve can then be recorded for comparisons and analysis.

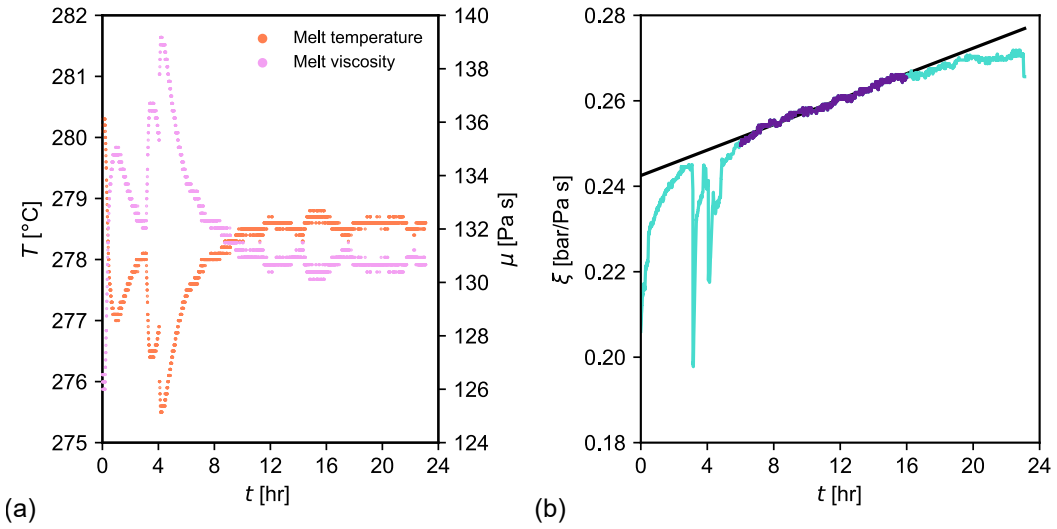

Figure 6.8: (a) Viscosity and temperature of the melt over the course of the first example single candle pack production run. (b) Corrected pressure (pressure/viscosity) over time for the first example production run. The suitable 10 hour run is identified and a linear curve is fitted in this range.

Figure 6.9 shows a comparison of mean gradients of the linear curves fitted to suitable periods in each run. Errors are the maximum and minimum values of each gradient at each flow rate. As the flow rate through a filter pack increases, more mass flows through the filter medium, hence it is expected that the filter medium will see more fouling particles, leading to a faster rate of blocking. It is therefore expected that a larger flow rate will lead to a larger gradient found from the fitted linear curve. This is clearly not the case in Figure 6.9, which shows no correlation between flow rate and average gradient.

This may be due to the state of the candle filter at the beginning of each run. After a run, candle filters are cleaned and then reused in future runs. If the candle filters are damaged from a run or during cleaning, this will influence pressure drop across them, which could explain the lack of correlation between flow rate and average gradient. It is therefore recommended that Mylar perform an experiment designed to evaluate the pressure drop across candle elements in different conditions. For example, the pressure drop across a candle in mint condition could be compared with a candle which has been cleaned and refurbished. Differences in pressure

drop would indicate that candle condition has a significant influence on the initial pressure drop across a pack and pressure drop evolution.

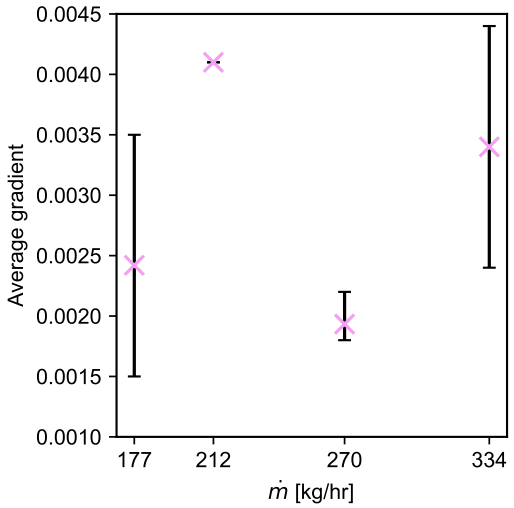

Figure 6.9: Comparison between the average gradient of the linear curves fitted at each flow rate for the single candle pack run data.

6.4 Single candle pack computational model

Figure 6.10 shows the computational geometry of the single candle filter pack that was created in SolidWorks 2019 using CAD drawings of the pack. The origin was placed at the center of the inlet boundary. The filter layer, and each support mesh, are represented by a single porous zone. Furthermore, the guard cage and the central core are represented by the same porous zone. This was done to keep the substantial computational cost of running the simulations down, by not having to resolve mesh in intricate geometry sections. In Chapter 4, it was found that for the screen filter geometry, the thickness of the porous zone, and its position relative to the holder, had to be considered. Here, there is no structure similar to the holder immediately downstream of the screen filter, so the entirety of the porous section of the candle may be represented by one porous zone. The geometry is axisymmetric, except in the inlet section, around the spider plate.

For preliminary analysis, at the inlet, a mass flow rate of 260 kg/hr was specified normal to the boundary and no-slip was specified at the walls. A static pressure outlet was chosen; the inlet and outlet were extended to be sufficiently far away from the core of the pack, as to have no influence on flow development in the pack. An incompressible, Newtonian fluid with $\rho = 1225$ kg/m^3 and a viscosity of 112.86 Pa s was modelled. This viscosity was chosen for preliminary tests as it fits in the range shown in Figure 6.7. This Reynolds number is 0.027, ensuring the laminar regime is maintained throughout. Each porous zone was assigned a permeability of 1×10^{-10} m^2.

Physics and solvers were specified as described in Subsection 3.2.5. Convergence was ensured by following the methodology detailed in Subsection 3.2.7. A steady, pressure-based solver was specified and a viscous, incompressible laminar model was used. As the geometry of single candle filter pack is axisymmetric everywhere other than the spider plate in the xz plane, there exists three planes of symmetry perpendicular to the xz plane through a single candle filter pack. Planes of symmetry are identified in Figure 6.10d. This was exploited by reducing the mesh down to one-sixth, with symmetry boundary conditions used to mimic the full geometry.

6.4.1 Mesh independence study

A mesh of the one-sixth single candle pack was created in ANSYS meshing. Figure 6.11 shows the mesh structure. To ensure sufficient mesh refinement everywhere, the geometry was broken into several sections: the inlet pipe, the geometry around the spider plate and candle base, the outer annulus, the porous zone, the central core and the outlet. Face sizing was specified at the inlet boundary to ensure sufficient mesh resolution in the inlet section. Sweep meshing was utilized in the inlet pipe, porous zone, outer annulus and outlet pipe as the cross section along the direction of the sweep for these sections are topologically constant. This created a structured, hexahedral mesh. In the central core and around the spider plate, mesh was generated with tetrahedra cell shapes, with mesh defeaturing, curvature capture

and capture proximity specified. This ensured that the mesh was refined in regions with complicated topology. A mesh was generated with 1.2 million elements and 0.5 million nodes. Specific meshing details are expanded upon in Appendix A.2.

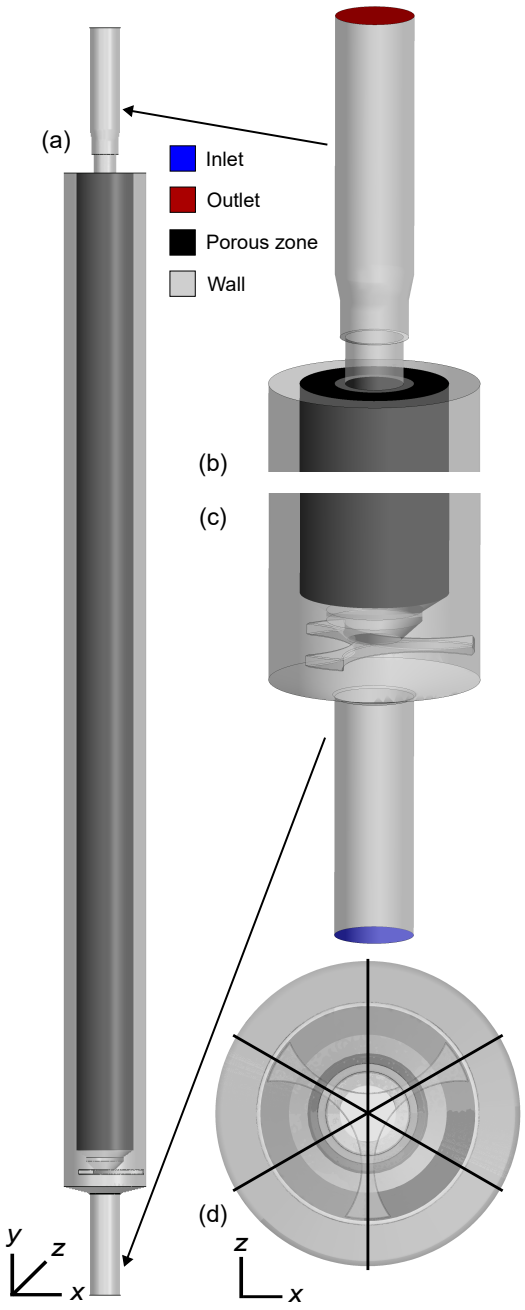

Figure 6.10: (a) The single candle filter pack computational geometry. (b) The outlet section. (c) The inlet section. (d) Birdseye view of the pack, with planes of symmetry identified.

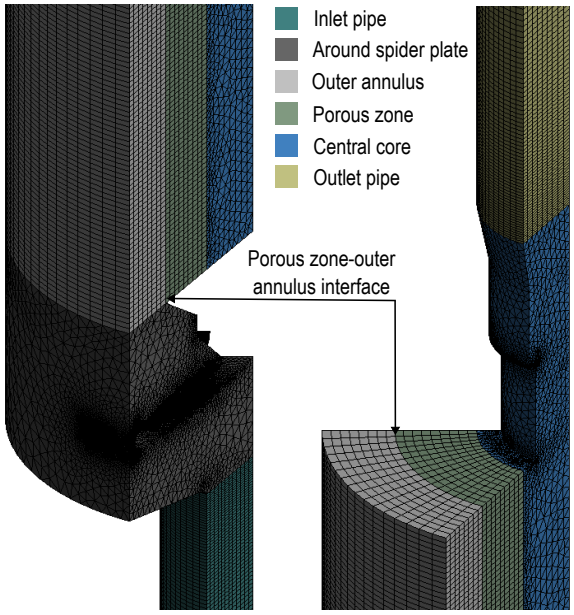

Figure 6.11: One-sixth single candle pack original mesh.

At the interface between the porous zone and the outer annulus, identified in Figure 6.11, an artifact of meshing is observed. At the inlet, for the one-sixth model, a mass flow of 0.0120 kg/s was chosen as the geometry is a sixth of the size of the full geometry. At the outlet, in accordance with convergence criteria, the mass flow was found to be 0.0120 kg/s. However, at the porous zone interface, the mass flow was found to be 0.0135 kg/s. As the flow must obey conservation of mass, and all of the flow must pass through the candle filter element, the mass flow through the interface should be the same as at the inlet and outlet. Due to the nature of CFD simulations, some numerical error is expected, but should not be this significant. This was not found to be resolved with refining the mesh uniformly in sequence, as per a standard mesh independence test.

Figure 6.12 shows the pressure contours across a plane that cuts through the porous zone. This plane only includes the geometry around the inlet. As expected, due to the imposed resistance of the porous zone, there is a large pressure gradient from the region outside the porous zone to the central core of the candle. Mesh adaptation at the porous zone, which refines the mesh in regions of high pressure gradients, was employed.

Mesh adaptation is used for all candle pack models with a porous zone henceforth. This is done to ensure flow around the porous zone is independent of mesh. To ensure independence in such regions, mesh refinement criteria is presented. To allow for numerical error, mass flow at a porous zone interface must be within 1% error of the mass flow rate specified at the inlet, and must not change significantly on further mesh adaptation. Furthermore, on adaptation, pressure drop across the pack must not change by more than 0.5%.

Table 6.2 shows that the mass flow rate at the interface converges towards the mass flow rate specified at the inlet with refinement, with the second and third adaptation mass flow rate through the interface matching that of the inlet. Table 6.2 also shows how the pressure drop across the single candle pack varies with adaptation. Agreement between the second and third adaptation is exceptional, with a 0% difference between pressure drop for each mesh. In accordance with the criteria above, the mesh is deemed to be independent between the second and third adaptation.

Table 6.2: Changes in pressure drop across the one-sixth single candle pack model and the mass flow rate at the porous zone interface as the mesh is refined through adaptation in regions of high pressure gradients.

Mesh	Mesh elements	Pressure drop [bar]	Mass flow at interface [kg/s]
Original	1,200,000	70.26	0.0136
Adapt 1	2,600,000	70.37	0.0124
Adapt 2	5,100,000	70.44	0.0120
Adapt 3	12,000,000	70.44	0.0120

Due to the cylindrical structure of candle filter elements, where flow must travel through the filter medium to enter the central core, cylindrical coordinates, (r,θ,y), are a natural choice for comparison and analysis. Note that r represent the radial coordinate and θ represents the angular coordinate. Radial velocity will show how the flow travels around and through the porous zone. The radial coordinate relative to the origin and the centre of the candle filter is given by

$$r = \sqrt{x^2 + z^2}. \tag{6.1}$$

Radial velocity, $\dot{r}$, and tangential velocity, $\dot{\theta}$, are given by

$$\dot{r} = \frac{xu + zw}{\sqrt{x^2 + z^2}}, \quad \dot{\theta} = \frac{xw - zu}{\sqrt{x^2 + z^2}}. \tag{6.2}$$

Figure 6.13 shows a comparison between the flow through the spider plate for the original and the twice adapted models. The agreement in flow profiles is shown in Figure 6.13c. This shows that the discrepancy in the mass flow rate through the porous zone interface has no influence on the flow around the spider plate.

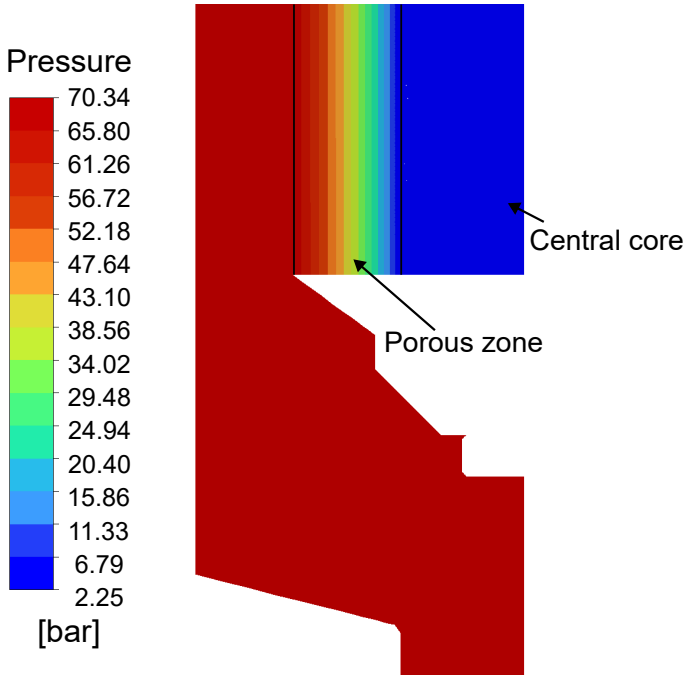

Figure 6.12: Contours of pressure near the inlet on the yz plane for the twice adapted one-sixth single candle filter pack model.

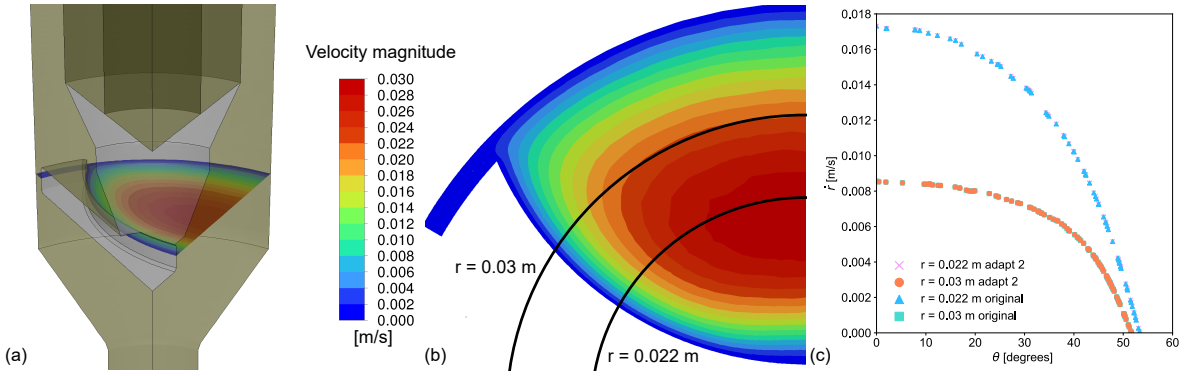

Figure 6.13: (a) Contours of velocity magnitude through a plane that cuts through the spider plate for the twice adapted one-sixth single candle filter pack geometry. The yellow faces identify the symmetry boundary conditions. (b) Perpendicular view of the contour plot. (c) Radial velocity along r =0.022 m and r= 0.03 m, identified in (b), for the original and twice adapted models.

6.4.2 Flow symmetry

Although symmetry boundary conditions were used to reduce the geometry to a one-sixth segment, it has not been verified that flow through the filter pack is symmetrical through the identified lines of symmetry in the geometry. To this end, simulations were run on a full model of the single candle filter pack.

For the one-sixth model, mesh adaptation to resolve the mass flow through the porous zone interface led to a 550% increase in mesh elements. Computational resources available are not able to process simulations at this level of mesh refinement on the full geometry. As Figure 6.13 shows that mesh adaptation at the porous zone has no effect on the flow around the spider plate, so it is reasonable to compare flow patterns around the spider plate between the twice adapted one-sixth model and a full model with no mesh adaptation.

A full model with no mesh adaptation was used. A coarse, medium and fine mesh were created and meshed with same methodology described in Subsection 6.4.1. Pressure drop across the pack for each mesh was compared. The flow redevelopment length for the medium

mesh was also compared with the analytical flow redevelopment length model for creeping flow, discussed in Subsection 3.2.4 and given by (3.6).

The full model can be compared with the twice adapted one-sixth model around the spider plate, where mass flow discrepancy through the porous zone interface was shown in Figure 6.13 to not have an influence on the flow near the spider plate.

Figure 6.14a shows the pressure drop across the full model of the filter pack for each mesh. There is shown to be less than a 0.06% change between the medium and fine mesh. Figure 6.14b shows the y-velocity along the centerline of the inlet pipe, where good agreement is seen for the redevelopment length between the analytical model (3.6) and CFD results. Therefore, the medium mesh is used henceforth for analysis.

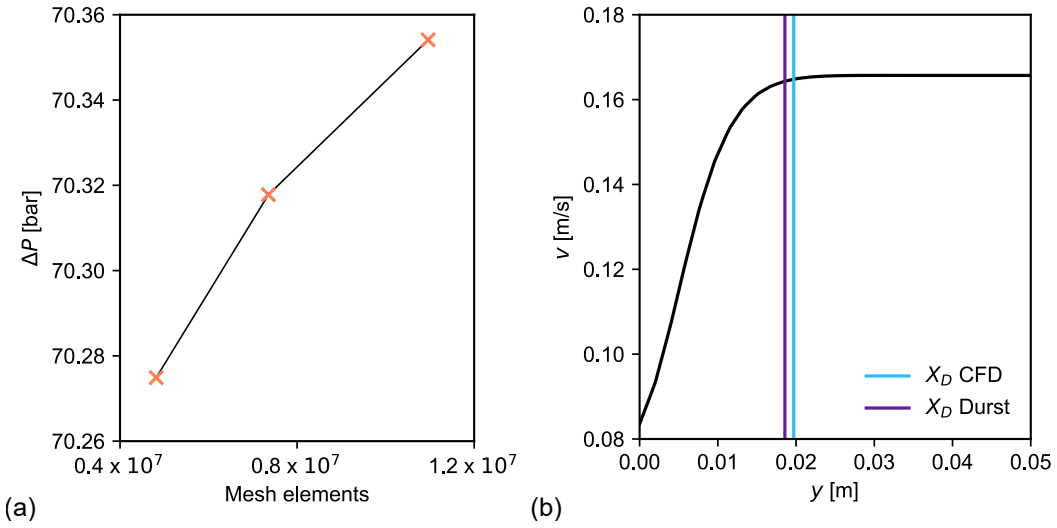

Figure 6.14: (a) Pressure drop across the full single candle filter pack for three meshes. (b) Plot of y-velocity along the centerline of the inlet pipe for the medium mesh, with the CFD redevelopment length and the calculated analytical redevelopment length (3.6) highlighted.

Figure 6.15 shows plots of radial velocity through two lines of constant radius for the full model. The symmetry is clearly apparent from the plots, showing that the flow through the single candle pack follows the same lines of symmetry as the geometry. Table 6.3 shows the average pressure and average velocity magnitude for the full model at the spider plate,

through the full plane and a symmetrically repeatable sixth segment of the full plane, showing exceptional agreement between the two. A single candle filter pack is therefore represented by one-sixth of the geometry.

Table 6.3: Comparison of average pressure and average velocity magnitude through a full plane and a sixth segment of the full single candle pack model at the spider plate.

	Average pressure [bar]	Average velocity magnitude [m/s]
Full plane	70.11	0.0161
Sixth segment	70.11	0.0161

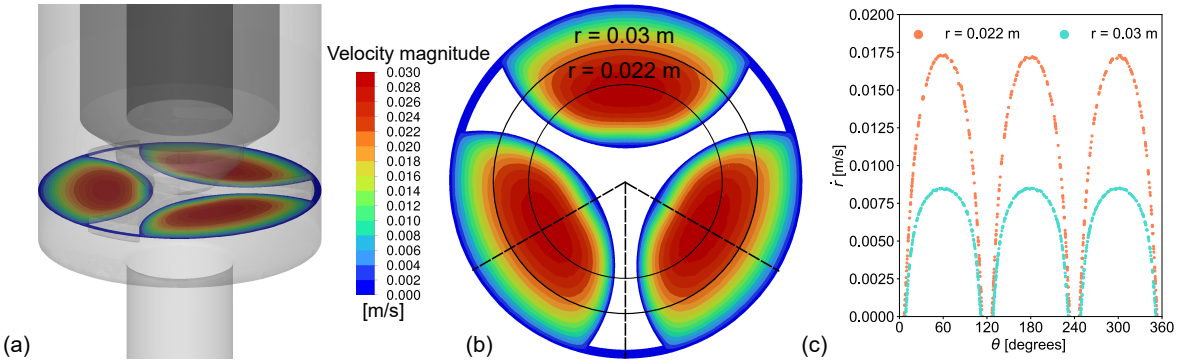

Figure 6.15: (a) Contours of velocity magnitude through a plane that cuts through the spider plate for the full single candle pack model. (b) Perpendicular view of the contour plot. The three lines of symmetry are shown. (c) Radial velocity along r =0.022 m and r= 0.3 m, identified in (b).

Figure 6.16 shows a comparison between the radial velocity, along the same lines of constant radius as in Figure 6.15c, comparing a sixth segment of the full model and the twice adapted one-sixth model. Agreement is again exceptional. It has therefore been verified that the twice adapted one-sixth model sufficiently represents the flow through the whole geometry, while resolving mass flow through the porous zone interface, and is used as the standard single candle filter pack model henceforward.

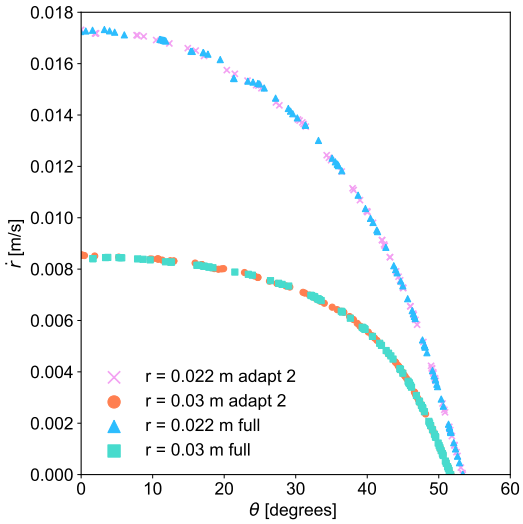

Figure 6.16: Radial velocity along constant radii identified in Figure 6.15 for the full and twice adapted one-sixth single candle pack model.

6.5 Seven candle pack geometry

A filter pack consisting of seven candle filter elements is employed by Mylar on a film production line. Figure 6.17 shows a sketch of the seven candle pack and 3D models of the spider plate and the outlet section. A candle filter sits at the centre of the pack. The other six candle filters surround the central candle, with the centre of their bases positioned at the centre of the outer circular structure of the spider plate. The candle filters and spider plate are kept in place with bolts. The spider plate offers mechanical support and helps to distribute flow between the seven candle filters. Flow travels through the inlet, around the spider plate, and must travel through one of the candle filters to reach the outlet section, onto the next stage of production. At the outlet, the outer six candles have pipes that connect to the central candle outlet.

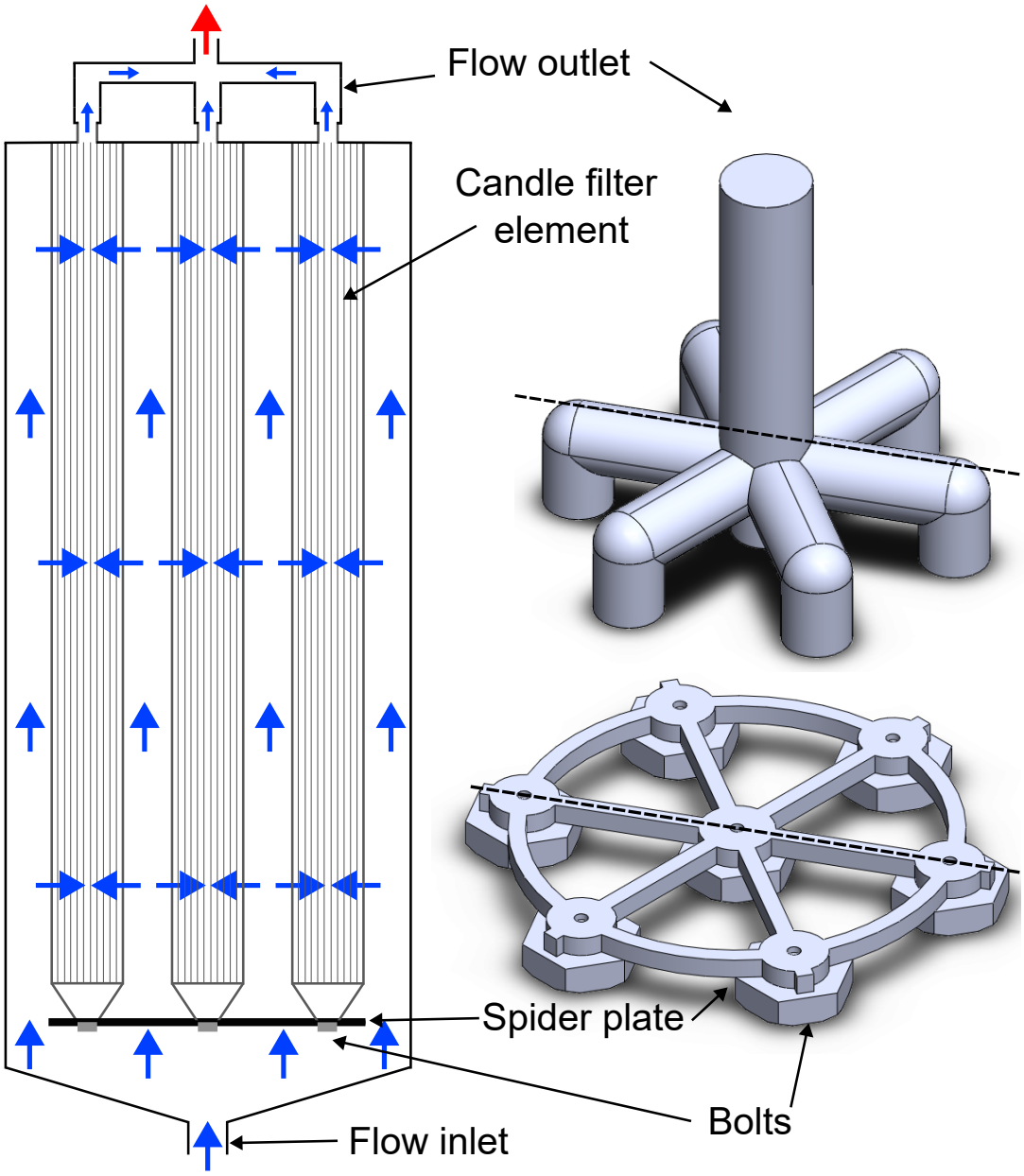

Figure 6.17: Cross-sectional sketch of a seven candle filter pack and a 3D model of the spider plate and outlet section. The dashed line through the 3D models shows the position of the cross-sectional sketch.

6.6 Seven candle pack run analysis

Data from eight production runs was provided by Mylar for the film production line with a seven candle filter pack. Figure 6.18 shows the extruder system on the film casting line with the seven candle filter pack. Two pressure transducers were used to record the pressure and pressure data was recorded every hour. The first pressure transducer is located between the melt pump and the filter pack, 6.38m upstream of the filter pack. The pipe system connecting the pump and filter pack is a straight line pipe, with radius 0.025 m. The second transducer sits directly at the outlet of the filter pack. With data from the two pressure transducers, the pressure drop between them is given by $P_1 - P_2$. All runs provided maintained a constant mass flow rate and the same polymer melt, which are summarised in Table 6.4. Pipe temperature was maintained throughout the extrusion system by a series of heaters and insulation. Polymer IV is intrinsic viscosity of a polymer, and was described in Section 2.1.

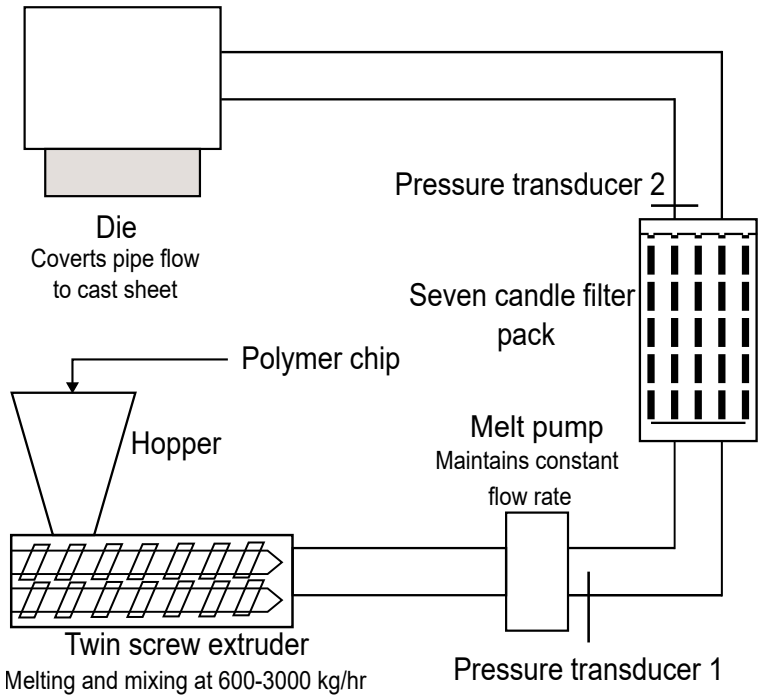

Figure 6.18: Sketch of the extrusion system containing the seven candle filter pack.

Table 6.4: Mass flow rate and fluid properties for the seven candle filter pack production run data.

Mass flow rate [kg/hr]	2700
Melt density [kg/m^3]	1400.1
Pipe temperature [°C]	290
Polymer IV [dL/g]	0.64
Melt viscosity [Pa s]	211

The Hagen-Poiseuille equation may be used to determine the pressure drop in an incompressible, Newtonian fluid in a laminar regime through a cylindrical pipe of constant cross section [128]. It is given by

$$\Delta P = \frac{8\mu L_p Q}{\pi r^4}, \tag{6.3}$$

where L_p is pipe length, r is pipe radius and the volumetric flow rate, Q, is given in m$^3/s$. There is 6.38 m of pipe between pressure transducer 1 and the filter pack inlet pipe. The radius of that pipe is 0.025 m. The volumetric flow rate can be found by converting the mass flow rate to kg/s, then dividing by the density of the melt. Substituting these values into (6.3), the pressure drop contribution from the pipe between the first transducer and the filter pack is 47.01 bar. Hence, pressure drop across the filter pack is given by $\Delta P = P_1 - P_2 - 47.01$.

Figure 6.19a shows pressure drop evolution across the seven candle filter pack for each production run, as well as the average value computed until 4 of 8 runs were terminated. Figure 6.19b shows an error range for the average pressure drop profile, where the error is taken as the standard deviation from the average. The dip around 160 hours is due to the termination of runs 4 and 5, which have a larger pressure drop contribution than other runs and terminate around the same time. As discussed in Section 6.3, the range of initial pressure drop and differences in pressure drop evolution profiles could be influenced by individual candle element conditions. Differences in pressure evolution profiles is also likely influenced by differences in concentration of blocking particles in each melt. Run 4 and run 5 are terminated before other runs due to the pressure drop exceeding the maximal allowable pressure drop which triggered a shutdown. This large rate of increase in pressure drop is likely due to a large concentration

of solid particles.

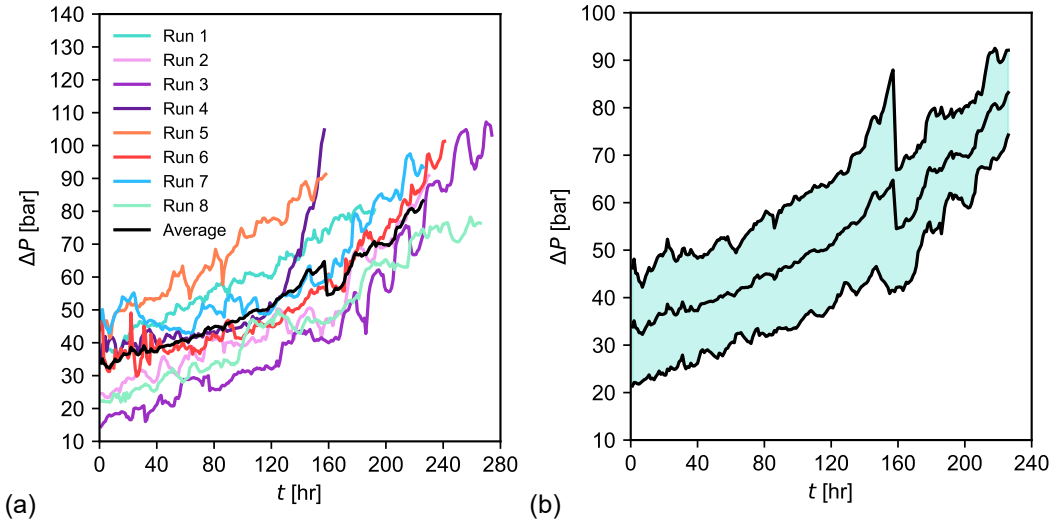

Figure 6.19: (a) Pressure drop evolution across the seven candle filter pack for eight production runs. (b) Average pressure drop, with error calculated from the standard deviation of each run from the average.

6.7 Seven candle pack computational model

Figure 6.20 shows the computational geometry of the seven candle filter pack that was created in SolidWorks 2019 using CAD drawings of the pack. The origin is placed at the center of the inlet boundary. Individual candle filter elements are modelled by individual porous zones. Again, individual candles have their filter medium, support mesh, guard cage and central core modelled by a single porous zone. There are seven porous zones in the model, one for each candle filter. All simulations were implemented in ANSYS Fluent 2022 R1.

For preliminary analysis, at the inlet, a mass flow rate of 2700 kg/hr was specified normal to the boundary and no-slip was specified at the walls. A static pressure outlet was chosen; the inlet and outlet were extended to be sufficiently far away from the core of the pack, as to have no influence on flow development in the pack. An incompressible, Newtonian fluid with $\rho = 1225$ kg/m^3 and a viscosity of 211 Pa s was modelled.

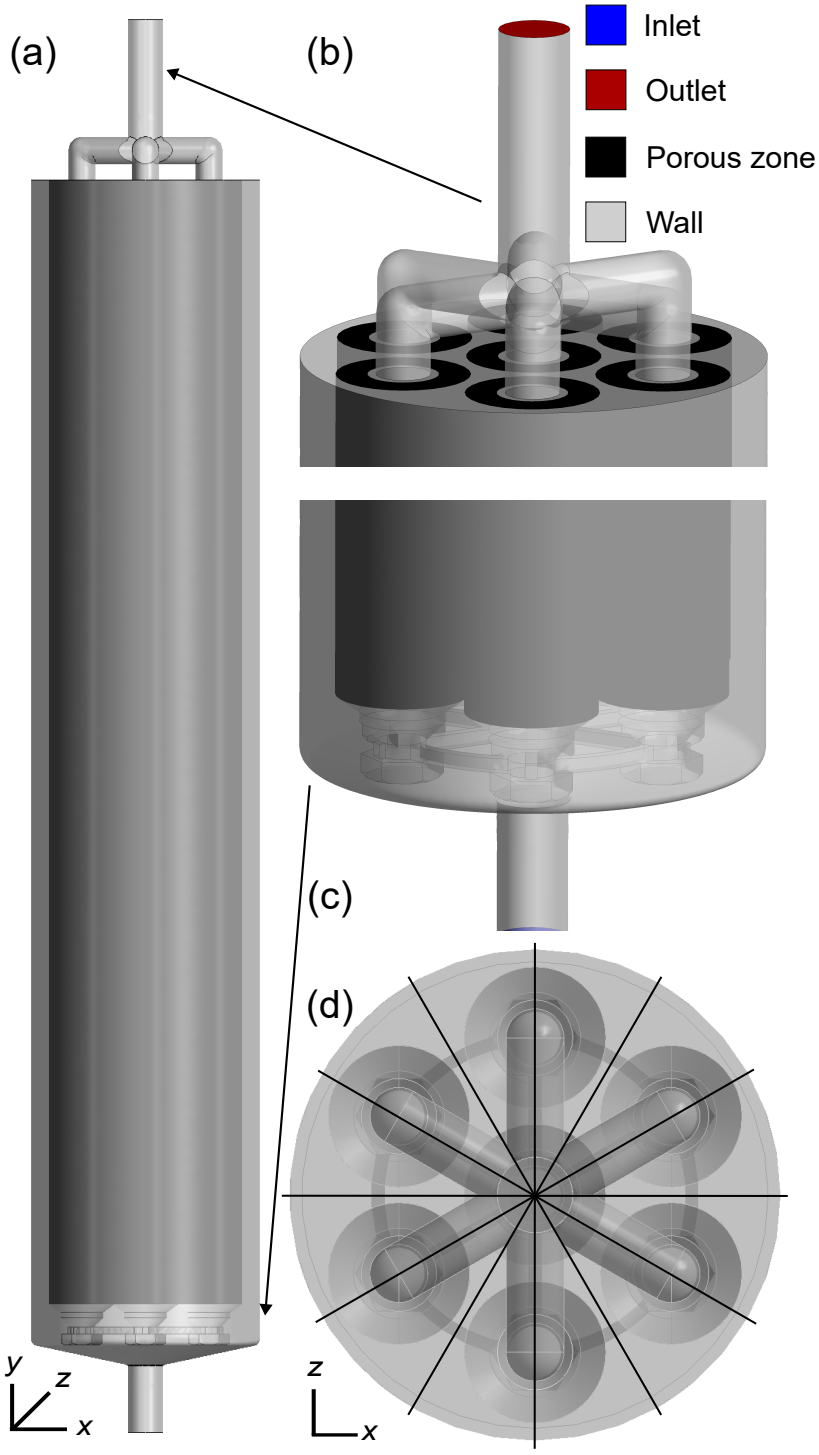

Figure 6.20: (a) The seven candle filter pack CFD model. (b) The outlet section. (c) The inlet section. (d) Birdseye view of the filter pack, with planes of symmetry identified.

The Reynolds number is 0.15, ensuring the laminar regime is maintained throughout. Each porous zone was assigned a permeability of 1×10^{-9} m^2. Physics and solvers were specified as described in Subsection 3.2.5. Convergence was ensured by following Subsection 3.2.7. A steady, pressure-based solver was specified and a viscous, incompressible laminar model was used.

The geometry is symmetrical in six planes, meaning a 30 degree segment of the geometry, with symmetry boundary conditions, can capture the entirety of the flow through the pack if the flow is symmetrical in the same planes as the geometry. This would dramatically reduce computational cost. With the computational power available, it would not be possible to find fully converged solutions without exploiting this symmetry while using mesh adaptation to again resolve mass flow through each candle.

6.7.1 Mesh independence study

A mesh of the one-twelfth seven candle was created in ANSYS meshing. Figure 6.21 shows the mesh structure. To ensure sufficient mesh refinement everywhere, the geometry was broken into several sections: the inlet pipe, the geometry around the spider plate and around the candle filters inside the pack, each porous zone, each central core, the outlet part, which connects the central core to the outlet pipe, and the outlet. Face sizing was specified at the inlet boundary to ensure sufficient mesh resolution in the inlet section. Sweep meshing was utilized in the inlet pipe, porous zone and outlet pipe as the cross section along the direction of the sweep for these sections are topologically constant. This created a structured, hexahedral mesh. In the central core, outlet part and around the spider plate, mesh was generated with tetrahedra cell shapes, with mesh defeaturing, curvature capture and capture proximity specified. This ensured that the mesh was refined in regions with complicated topology. A mesh was generated with 1.7 million elements and 0.5 million nodes. Meshing controls are given in detail in Appendix A.3.

As with the single candle model, the mesh was ensured to be converged with mesh adaptation

by analysing the pressure drop across the pack and the total mass flow through porous zones. At the inlet, for the one-twelfth model, a mass flow rate of 0.0625 kg/s was specified, as this is 2700 kg/hr converted to kg/s for one-twelfth of the geometry. Table 6.5 shows that the mass flow at the interface converges towards the mass flow specified at the inlet with refinement, with the second and third adaptation giving a mass flow through the interface matching that of the inlet.

Table 6.5 also shows how the pressure drop across the seven candle pack varied with adaptation. Agreement between the second and third adaptation is good, with a 0.15% difference between pressure drop for each mesh. In accordance with the criteria specified in Subsection 6.4.1, the mesh is deemed to be independent between the second and third adaptation.

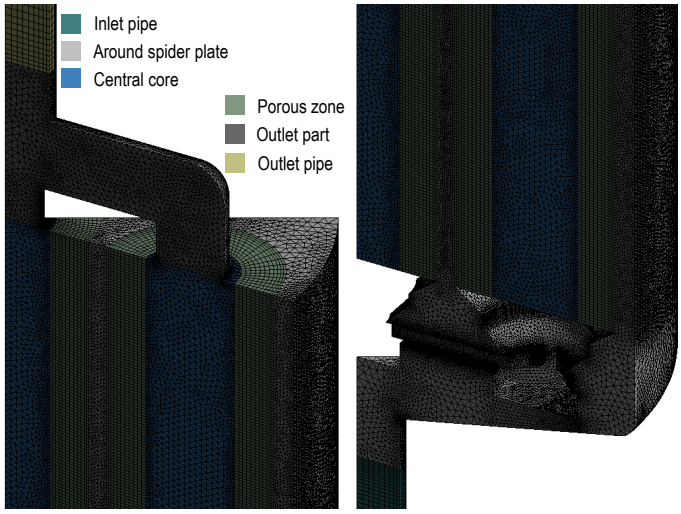

Figure 6.21: One-twelfth seven candle filter pack original mesh.

Table 6.5: Changes in pressure drop across the one-twelfth seven candle pack model and the total mass flow through the sum of each porous zone interface as the mesh is refined through adaptation in regions of high pressure gradients.

Mesh	Mesh elements	Pressure drop [bar]	Total mass flow at interfaces [kg/s]
Original	1,800,000	33.05	0.0567
Adapt 1	3,900,000	33.47	0.0612
Adapt 2	13,400,000	33.75	0.0624
Adapt 3	17,500,000	33.80	0.0624

6.7.2 Flow symmetry

Due to the number of elements needed to generate a mesh for the entire geometry of the seven candle filter pack, only the inlet section of the full pack was modelled to check symmetry around the spider plate. Due to the position of the seven candle filters in the pack, and the structure of the outlet, the geometry inside the pack is not axisymmetric downstream of the spider plate, which was the case for the single candle filter pack. However, the same six lines of symmetry exist throughout the geometry, identified in Figure 6.20. As the structure of the geometry is most complicated around the spider plate, it is enough to show that if the flow is symmetrical around it, it will remain symmetrical downstream. The seven candle inlet geometry modelled is shown in Figure 6.22. The candle filters were removed and replaced with walls. The geometry extends up to ensure that the outlet position did not affect the flow upstream.

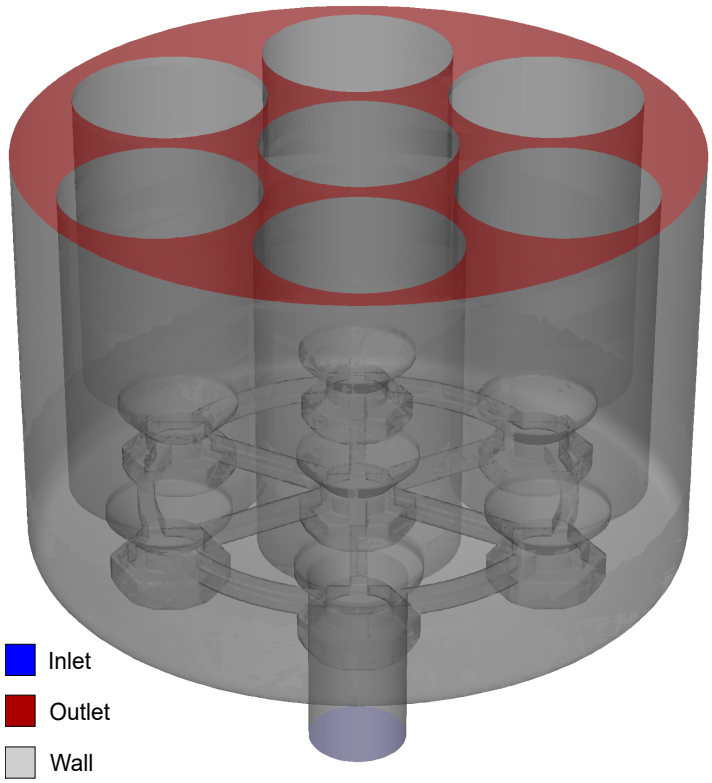

Figure 6.22: Seven candle pack inlet model geometry.

Mesh independence for the seven candle filter pack inlet model was checked by generating a coarse, medium and fine mesh, which were meshed with same methodology described in Subsection 6.4.1. Meshing controls are given in detail in Appendix A.3. Figure 6.23a shows the pressure drop across the inlet model for each mesh. There is shown to be less than a 0.5% change between the medium and fine mesh. The flow redevelopment length for the medium mesh was also compared with the analytical flow redevelopment length model for creeping flow, discussed in Subsection 3.2.4 and given by (3.6). Good agreement is seen between the analytical model and CFD medium mesh results. The medium mesh is therefore used for analysis of the inlet geometry.

Figure 6.24a-b shows contour plots of velocity magnitude through a plane across the spider plate. The lines of symmetry are clearly apparent from the plots. Furthermore, Figure 6.24c shows the plots of radial velocity through two lines of constant radius for the full model, again highlighting the symmetry of the flow. Table 6.6 shows the average pressure and average velocity magnitude through the full plane, and a twelfth segment of the plane, showing an exceptional match. The flow through a seven candle filter pack is symmetrical along the lines of symmetry identified through its geometry.

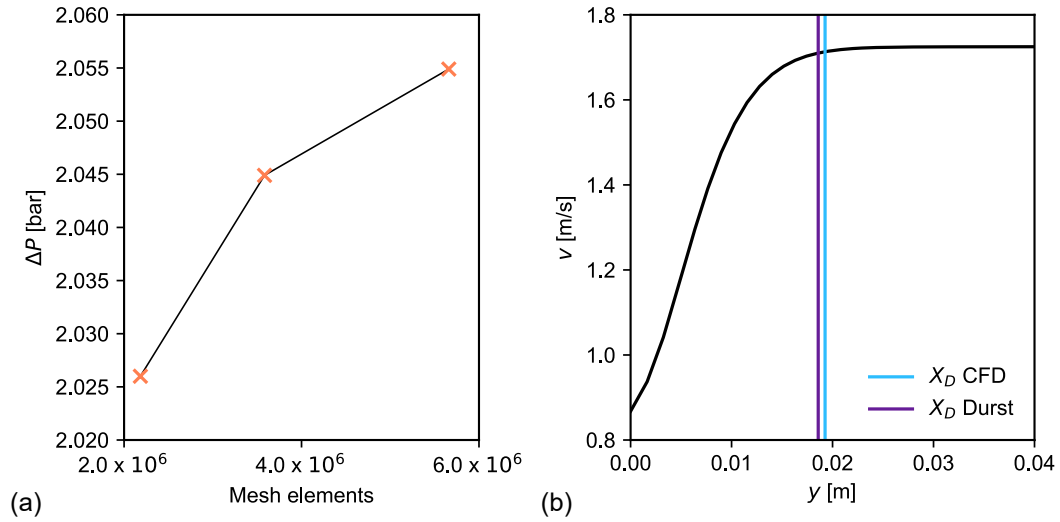

Figure 6.23: (a) Pressure drop across the seven candle pack inlet model for three meshes. (b) Plot of y-velocity along the centerline of the inlet pipe, with the medium mesh CFD and the calculated analytical redevelopment length (3.6) highlighted.

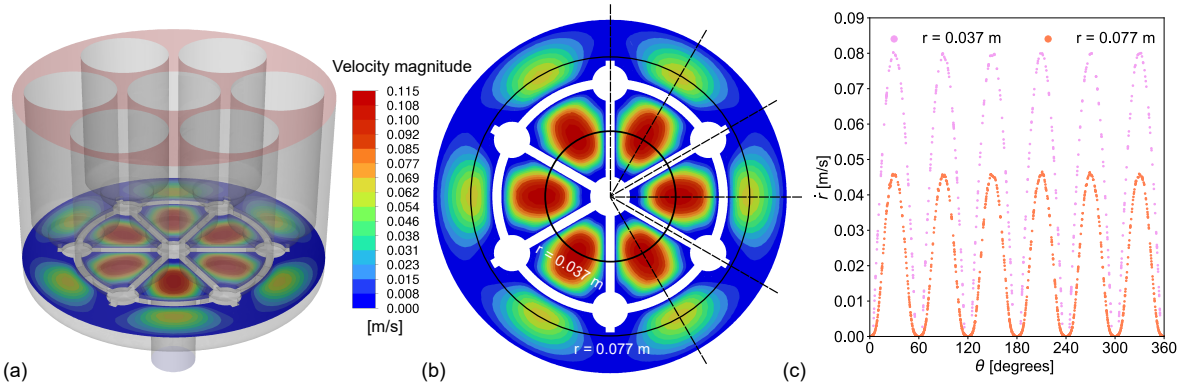

Figure 6.24: (a) The seven candle pack inlet model, with contours of velocity magnitude through a plane which cuts through the spider plate. (b) Perpendicular view of the contour plot, with lines of symmetry identified. (c) Radial velocity along $r = 0.037$ m and $r = 0.077$ m, identified in (b).

Table 6.6: Comparison of average pressure and average velocity magnitude through a full plane and a twelfth segment of the seven candle pack inlet model at the spider plate.

	Average pressure [bar]	Average velocity magnitude [m/s]
Full plane	4.71	0.0330
Twelfth segment	4.71	0.0330

Figure 6.25 shows a comparison between the radial velocity, along the same lines of constant radius as in Figure 6.24c, comparing the twice adapted one-twelfth and inlet models. Agreement is very good between the two models, and the one-twelfth model certainly captures the radial velocity profile of the inlet model along the two lines. It has therefore been verified that the twice adapted one-twelfth model sufficiently represents the flow through the whole geometry, while resolving mass flow through the porous zone interface, and is used as the standard seven candle filter pack model henceforward.

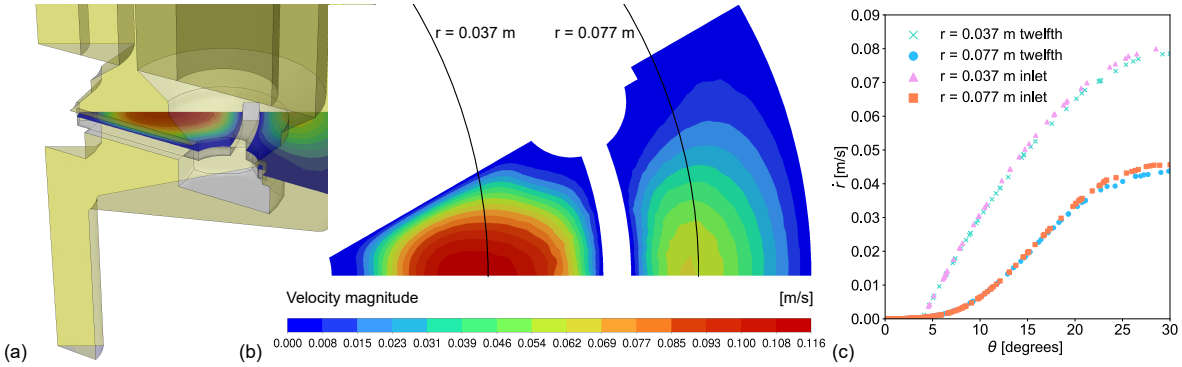

Figure 6.25: (a) The one-twelfth seven candle pack model, with contours of velocity magnitude on a plane which cuts through the spider plate. Yellow faces identify symmetry boundary conditions. (b) Perpendicular view of the contour plot. (c) Comparison of radial velocity between the inlet and one-twelfth model along $r = 0.037$ m and $r = 0.077$ m, identified in (b).

6.8 Permeability calibration

Throughout the computational work, it is assumed that the candle filters are new. This means that every candle filter in the seven and single candle filter pack models will initially have a porous zone with the same permeability. This permeability value must be found through calibrating the seven candle filter pack model, matching its pressure drop output to run data from Section 6.6. Here, the mass flow rate at the inlet, melt density and melt viscosity of the seven candle pack model were therefore set to match Table 6.4.

Figure 6.26 shows how changing the viscous resistance of the porous zone changes the pressure drop output for the seven candle pack model, where viscous resistance is inputted into the porous media model and is the reciprocal of permeability. In accordance with Darcy's law, the relationship between the reciprocal of permeability and pressure drop is linear. Hence, the calibrated permeability can be found from the linear curve fit. Table 6.7 shows the viscous resistance found from the line of best fit in Figure 6.26 needed to give a pressure drop that matches the initial average pressure drop in Figure 6.19b. It also shows the pressure drop found from inputting that viscous resistance into the seven candle CFD model. As the

agreement between the observed run pressure drop and the seven candle CFD model pressure drop is good, the permeability input for the porous zone of a candle filter element for the CFD models is chosen as 8×10^{-10} m^2.

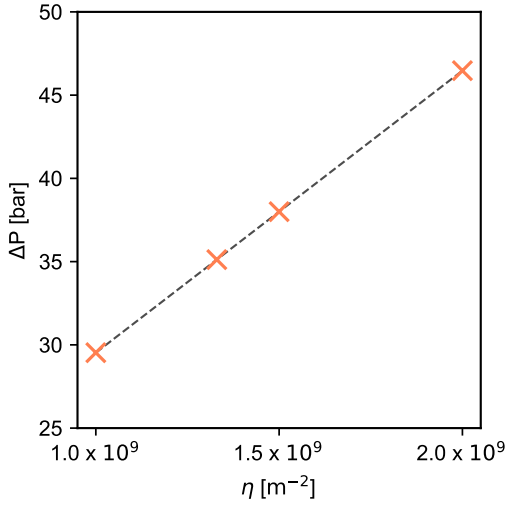

Figure 6.26: Pressure drop against viscous resistance, found by running the seven candle pack model with four different viscous resistance inputs.

Table 6.7: Comparison between the initial pressure drop found from the seven candle run data, discussed in Section 6.6, and the calibrated seven candle pack model.

η [m^{-2}]	ΔP [bar]	Average run pressure drop [bar]
1.25×10^9	33.81	33.83

6.9 Single candle pack model results

This section analyses the flow through the single candle filter pack model where the porous zone has been calibrated with the viscous resistance for a clean candle filter element found in Section 6.8. The flow distribution in the pack is analysed and a permeability sensitivity analysis is performed to see how flow through the porous zone changes with viscous resistance magnitude. It was found in Section 6.4 that the twice adapted one-sixth model sufficiently

represents flow through the whole geometry, while resolving mass flow through the porous zone interface. This mesh will henceforth be used in all analyses. Table 6.8 shows the pressure drop across the filter pack with this model with the calibrated viscous resistance. It also shows that the mass flow through the porous zone interface remains resolved.

Table 6.8: Pressure drop across the pack and the mass flow rate at the porous interface for the single candle pack model.

Mesh elements	Pressure drop [bar]	Mass flow at interface [kg/s]
5,100,000	11.36	0.0120

6.9.1 Flow distribution through the candle

Figure 6.27 shows contours of the tangential and radial component of velocity at equidistant distances along the porous zone representing the candle filter. Radial velocity appears to only depend on radial coordinate as tangential velocity is found to be two orders of magnitude less than radial velocity. This suggests flow is sufficiently represented by an axisymmetric configuration in the porous zone. As particles follow streamlines, this means that the filter medium will block independently of azimuthal position. This is further verified in Figure 6.28, which shows the radial and tangential velocity along constant r identified in Figure 6.27d. Although there is some noticeable variation in radial velocity around $r = 0.028$, near the porous zone interface, it is oscillating and does not change by more than 1.5 % from minimum to maximum. This oscillation in radial velocity is damped as r is taken further away from the interface. The tangential velocity is also found to be at least two orders of magnitude lower than the radial velocity. The single candle results show that the flow through the porous zone may be considered axisymmetric.

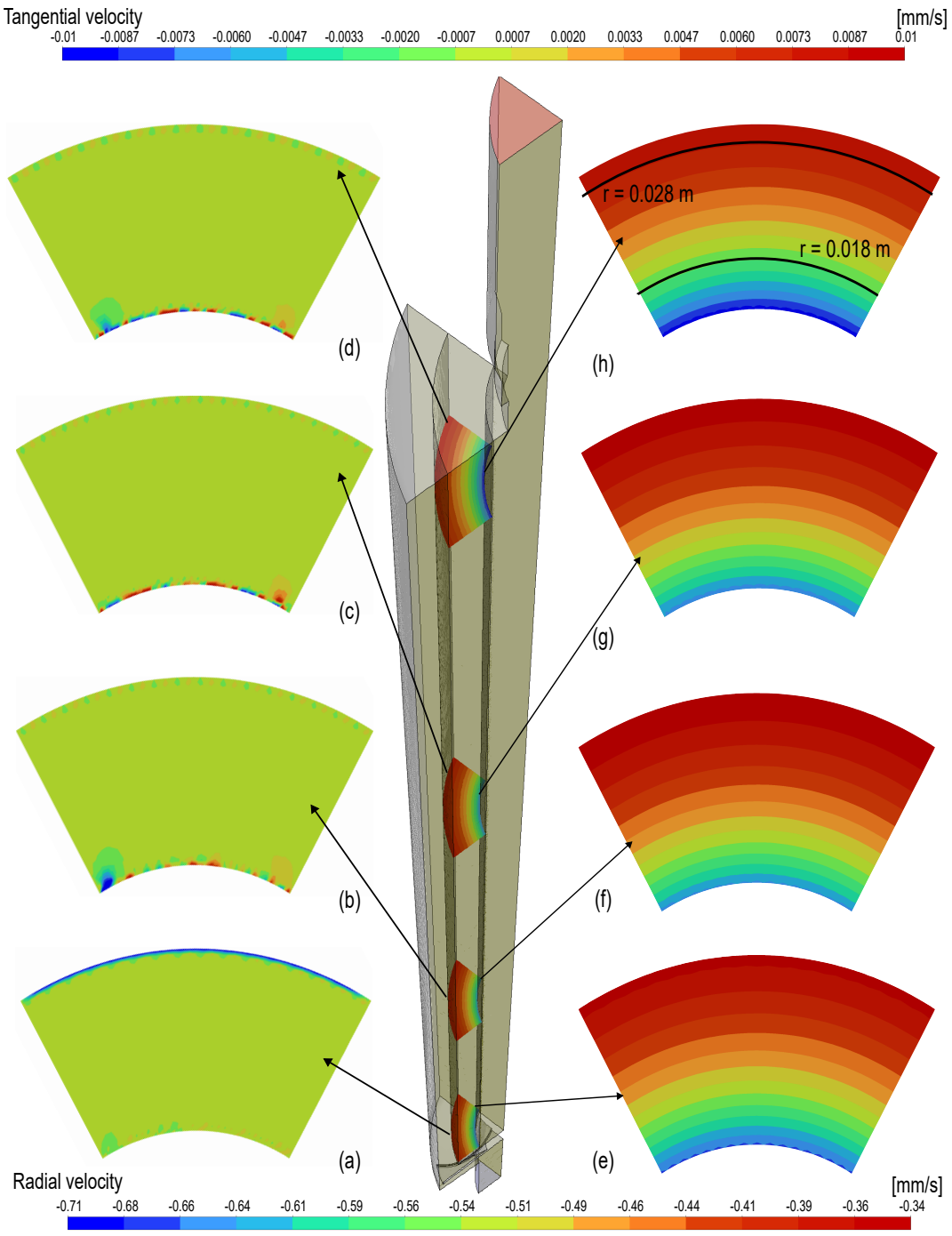

Figure 6.27: Tangential velocity contours in the porous zone of the single candle pack model on the plane (a) $y = 0.15$, (b) $y = 0.45$ m, (c) $y = 0.75$ m and (d) $y = 1.05$ m. Radial velocity contours in the porous zone of the single candle pack model on the plane (e) $y = 0.15$ m, (f) $y = 0.45$ m, (g) $y = 0.75$ m and (h) $y = 1.05$ m.

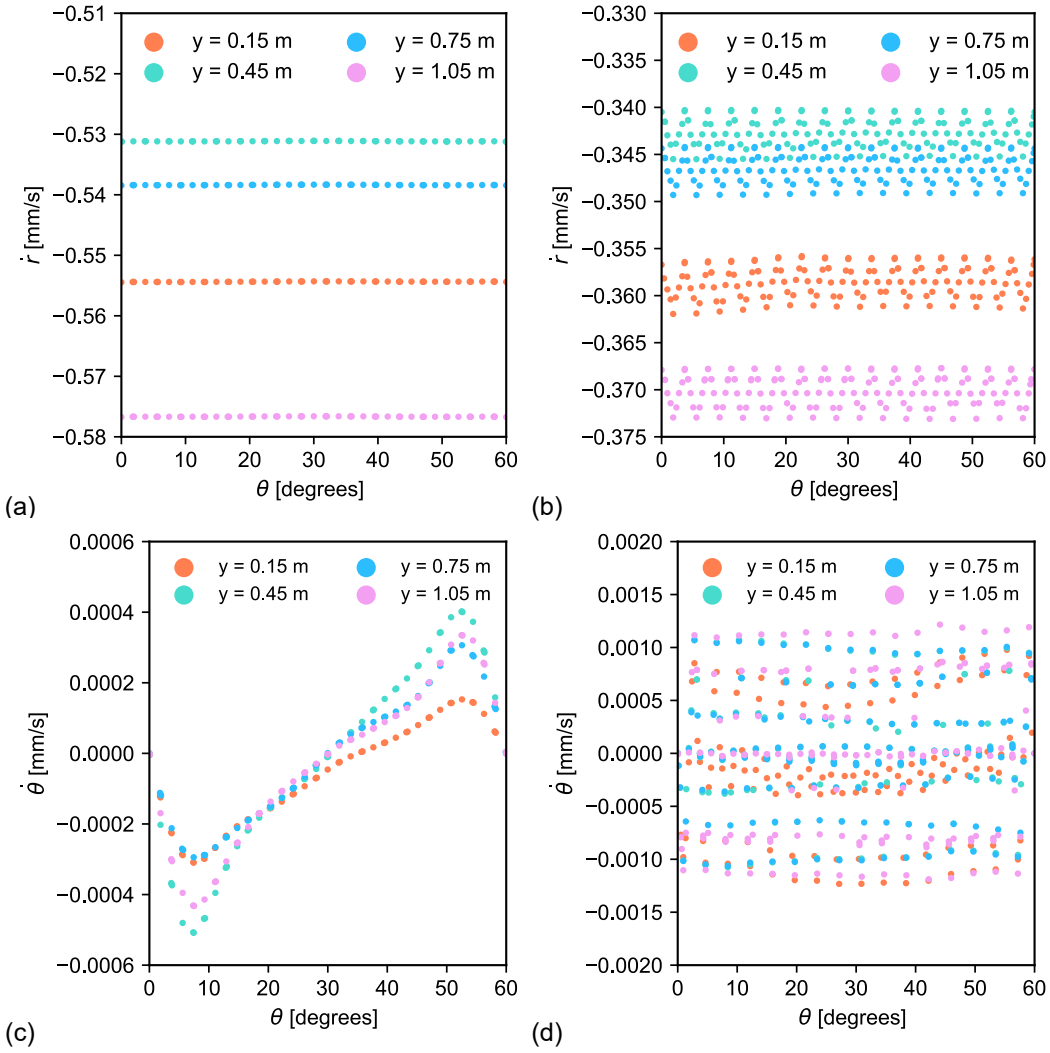

Figure 6.28: Radial velocity along (a) $r = 0.018$ m and (b) $r = 0.028$ m and tangential velocity along (c) $r = 0.018$ m and (d) $r = 0.028$ m for y indicated in Figure 6.27.

Figure 6.29 shows the radial velocity along y at $r = 0.028$ m and $r = 0.018$ m. There is significant variation in radial velocity along y, suggesting that the filter medium will block at different rates, at least initially, along the y-axis. Mass flow through a cylinder of constant radius can be calculated from the surface integral

$$\dot{m} = \int \int_A \rho \boldsymbol{u}.\hat{\boldsymbol{n}} dA. \tag{6.4}$$

The surface element on a surface of constant radius is $dA = rd\theta dy$ and the unit normal to a cylinder is $(r, \theta, y) = (1, 0, 0)$. Hence, the integral over a cylinder of constant r in the porous zone is given by

$$\dot{m} = \int_{y_1}^{y_2} \int_{0}^{2\pi} r\rho\dot{r} d\theta dy. \tag{6.5}$$

If the flow is axisymmetric, then $\dot{r}$ is independent of θ and

$$\dot{m} = \int_{y_1}^{y_2} 2\pi r\rho\dot{r}(y) dy \tag{6.6}$$

is equal to the mass flow rate at the inlet, where y_1 and y_2 is y at the bottom and the top of the candle filter medium respectively. Table 6.9 shows the mass flow rate through the porous zone, calculated at a single point along the chosen r using (6.6), showing that the mass flow calculated is in agreement with the inlet mass flow rate (0.072 kg/s) for both radii. This further verifies the axisymmetry of the flow in the porous zone.

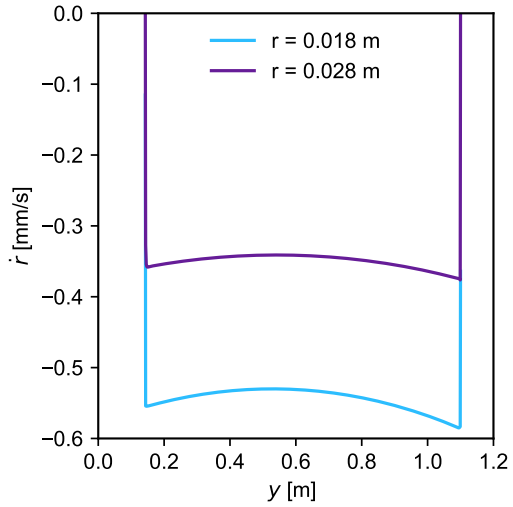

Figure 6.29: Variation in radial velocity along y from the bottom to the top of the candle inside the porous zone for the single candle pack model.

Table 6.9: Mass flow rate through cylinders of constant r in the porous zone, calculated from (6.6) for the single candle pack model.

Radius [m]	Mass flow rate through cylinder [kg/s]
0.028	0.072
0.018	0.072

As the porous zone may be considered axisymmetric, flow patterns will not alter around the candle filter as the filter medium blocks. There is variation in radial velocity along the length of the candle filter. This suggests that flow patterns alter along the candle filter as it blocks.

6.9.2 Permeability sensitivity analysis

The influence of porous zone permeability is examined here. Table 6.10 shows a summary of six simulations with the single candle pack model, where the permeability of the porous zone was changed, including a simulation with no porous zone. Fluid properties, boundary conditions and the mesh were not varied between simulations. There is little resistance imposed upon the flow up to and including $k = 1 \times 10^{-6}$ m^2. From $k = 1 \times 10^{-8}$ m^2, pressure drop across the candle filter increases by an order of magnitude as the permeability decreases by an order of magnitude. Figure 6.30a shows how the radial velocity along the candle at $r = 0.028$ m changes with decreasing permeability. With no porous zone, due to the structure of the geometry, the vast majority of the fluid passes through the cylinder $r = 0.028$ m at the bottom and the top of the candle. As the permeability of the porous zone decreases, the profile of the radial velocity converges towards a uniform 'box' profile, with little variation in r along y, which can be seen more clearly in Figure 6.30b. As the permeability of the porous zone decreases, the resistance imposed on the flow by it increases, increasing its influence on the flow. This results in the uniform profile at low enough permeability values, as the isotropic, homogeneous porous zone imposes such a large resistance on the flow that its influence dominates the flow behaviour in its vicinity.

Table 6.10: Single candle pack model simulations run with different values of permeability, the mass flow rate through $r = 0.028$ m, and pressure drop across the candle filter.

k [m^2]	$\dot{m}$ at $r = 0.028$ m [kg/s]	ΔP across candle filter [Pa]
No porous zone	0.073	6
1x 10^{-4}	0.073	12
1x 10^{-6}	0.072	696
1x 10^{-8}	0.072	68470
1x 10^{-9}	0.072	665800
1x 10^{-10}	0.072	6847000

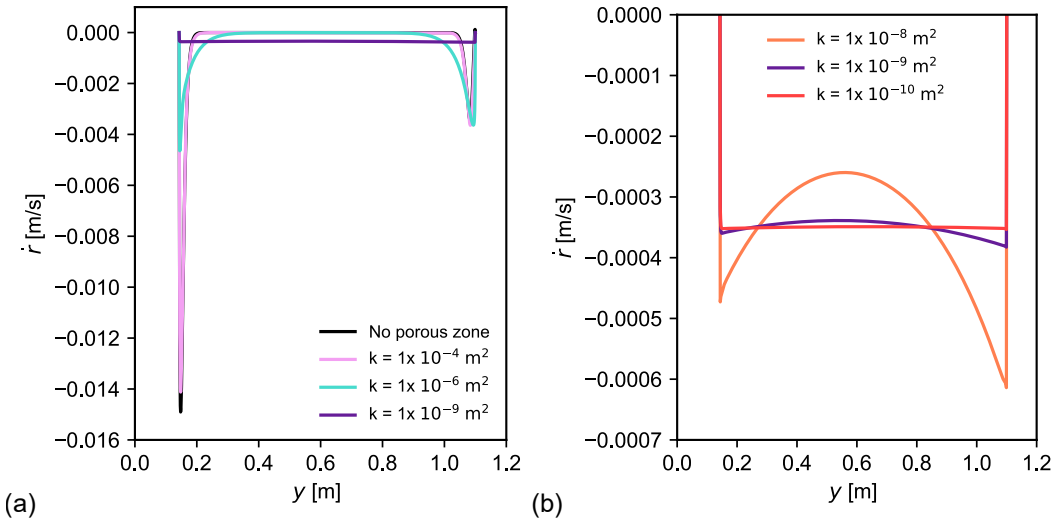

Figure 6.30: Variation in radial velocity at $r = 0.018$ m along y from the bottom to the top of the candle inside the porous zone for different magnitudes of permeability for the single candle pack model.(a) No porous zone enabled to $k = 1\text{x}10^{-9}$ m^2. (b) $k = 1\text{x}10^{-8}$ m^2 to $k = 1\text{x}10^{-10}$ m^2.

6.10 Seven candle pack model results

This section analyses the flow through the seven candle filter pack model where the porous zone has been calibrated with the viscous resistance for a clean candle filter element found in Section 6.8. The flow distribution in the pack is analysed and a model with multiple outlets is created to determine how pressure influences flow distribution between the candles. It was

found in Section 6.7 that the twice adapted one-twelfth model sufficiently represents the flow through the whole geometry, while resolving mass flow through the porous zone interface. This mesh will henceforth be used in all analyses.

6.10.1 Flow distribution through central and outer candles

The flow distribution through the pack, including the porous zone of the central candle and outer candle is examined. Again, radial coordinates are employed to examine flow through the central candle, with central radial position denoted as r_c and central radial velocity denoted $\dot{r}_c$. Through the outer candle, radial coordinates are transformed for analysis so that the y-axis is positioned through the centre of the outer candle. The outer radial coordinate is therefore given by

$$r_o = \sqrt{(x - x_o)^2 + (z - z_o)^2}, \tag{6.7}$$

where (x_o, z_o) is the position of the centre of the outer candle. Therefore, outer radial velocity is found from

$$\dot{r}_o = \frac{(x - x_o)u + (z - z_o)w}{\sqrt{(x - x_o)^2 + (z - z_o)^2}}. \tag{6.8}$$

Figure 6.31 shows velocity magnitude contours at equidistant distances through the pack. Figure 6.31a shows contours near the bottom of the candles. Most of the fluid has not transferred through the candles, as fluid moves faster in regions upstream of porous zones. As the fluid rises, more passes through each porous zone, until the majority of the fluid has transferred into the core of each candle, which can be seen in Figure 6.31d. Figure 6.32 shows radial velocity plotted along $r_c = 0.018$ and 0.028 m for the central candle and outer radial velocity along $r_o = 0.018$ and 0.028 m for the outer candle. There is little variation along θ_c for the chosen radii in the central candle, suggesting flow is independent of θ_c. Through the outer candle, there is significant variation in outer radial velocity for the chosen radii, indicating that the flow is dependent on θ_o.

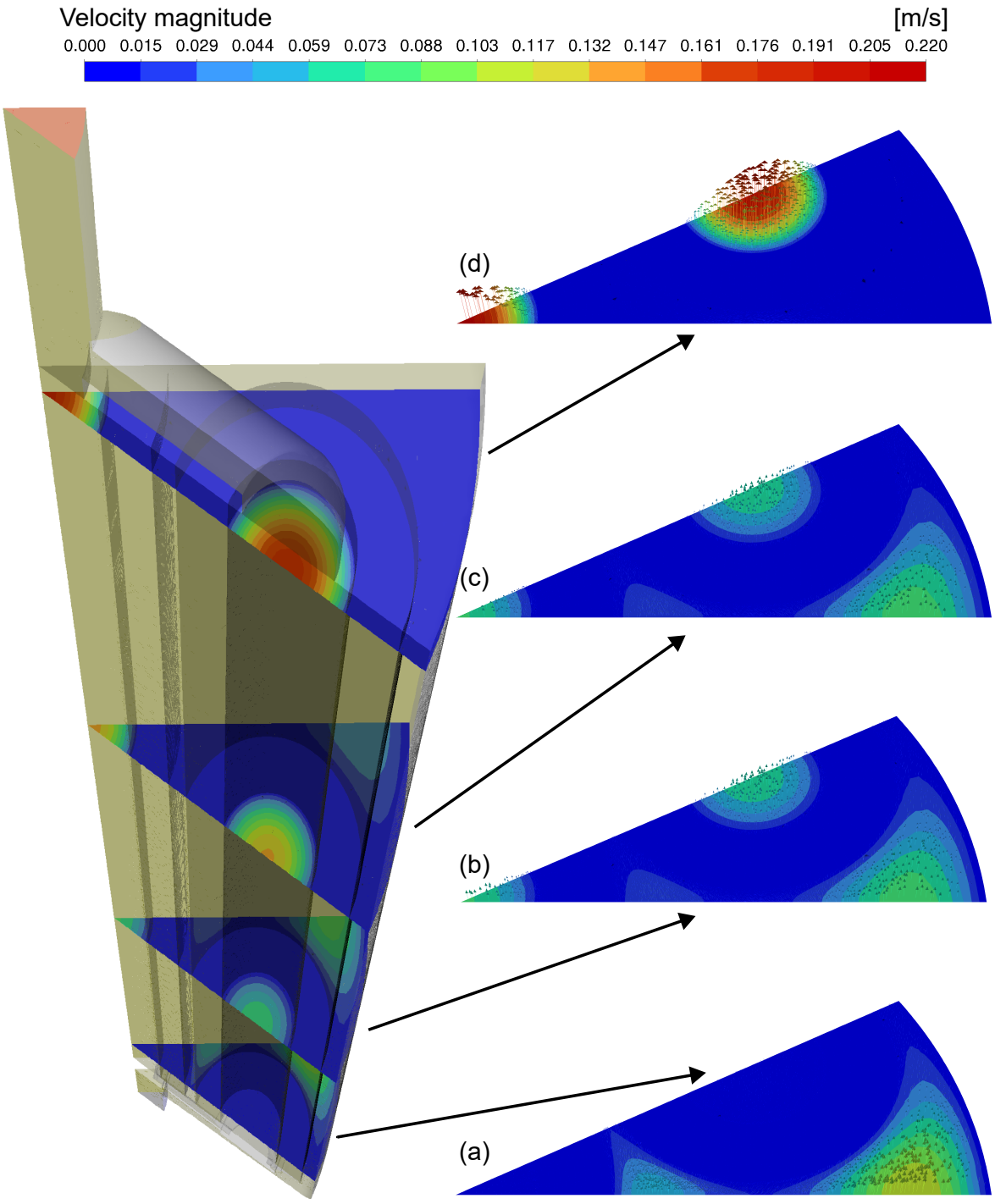

Figure 6.31: Velocity magnitude contours with velocity vectors on the plane (a) $y = 0.15$ m, (b) $y = 0.45$ m, (c) $y = 0.75$ m and (d) $y = 1.05$ m for the seven candle pack model.

As the fluid moves up the pack, there is clearly variation in central radial velocity and outer radial velocity. Figure 6.33 illustrates this, with significant variation in both central and outer radial velocity along the central and outer candle respectively. Central radial velocity is greater in magnitude along the candle as the central candle sees a greater proportion of the inlet throughput.

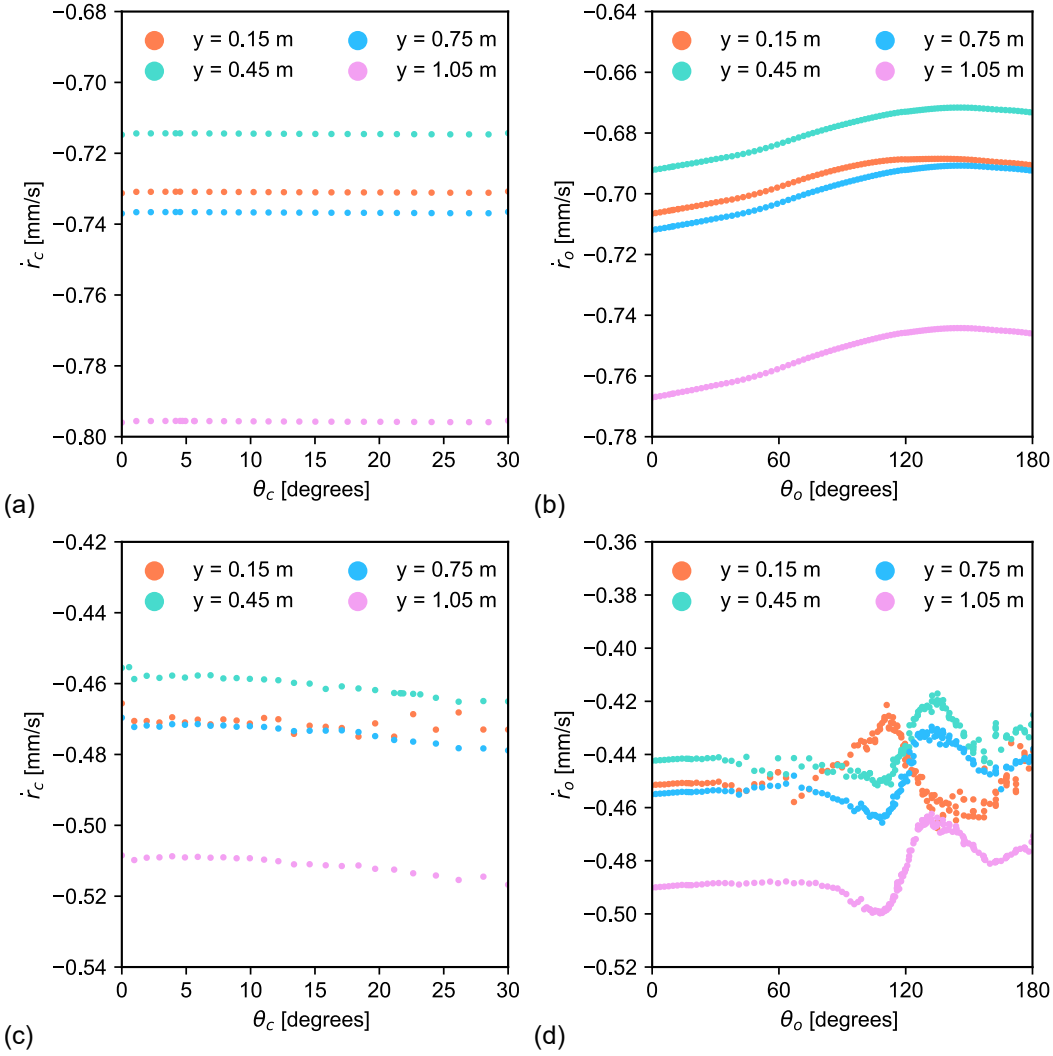

Figure 6.32: Central radial velocity around (a) $r_c = 0.018$ m and (b) $r_c = 0.028$ m for the central candle and outer radial velocity around (c) $r_o = 0.018$ m and (d) $r_o = 0.028$ m for the outer candle for the seven candle filter pack model.

By summing the total mass flow rate through the whole central candle and a whole outer candle, the percentage split of this through both candles can be calculated and the distribution of melt flow between candles in the pack can be assessed. Due to the symmetry of the pack, an even split of 50% of this total indicates that the melt is evenly distributed between all candles in the pack. The central candle sees 51.26% of the total flow through the whole central candle and a whole outer candle.

Flow varies between, along and around candle filters in the seven candle filter pack. This suggests that flow patterns will alter around, along and between candle filters as runs advance and each candle filter blocks.

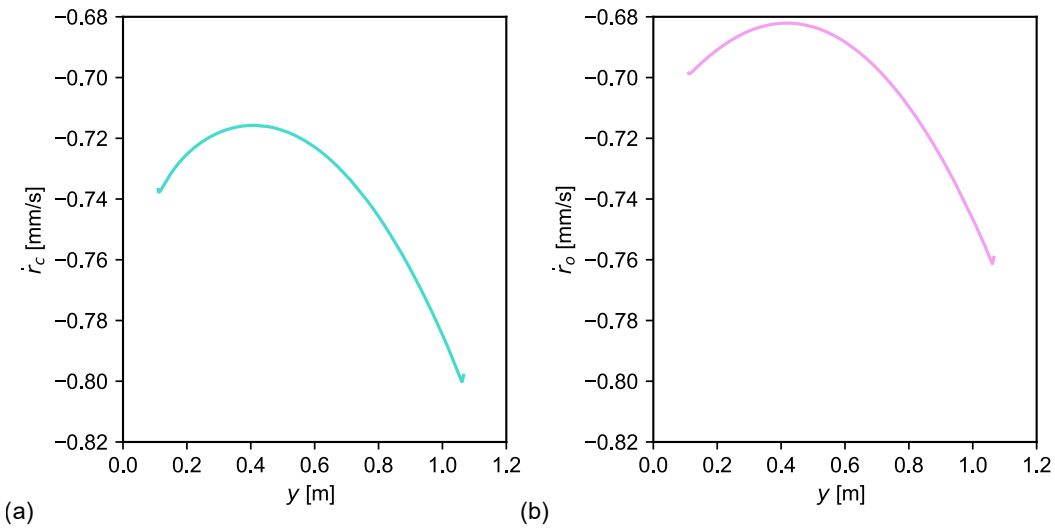

Figure 6.33: (a) Central radial velocity and (b) outer radial velocity along the central and outer candle at a point on $r_c = 0.018$ m and $r_o = 0.018$ m respectively for the seven candle pack model.

6.10.2 Pressure distribution between central and outer candles

A new model was created to examine the influence of the outlet geometry on the flow distribution in the pack. Figure 6.34 shows the outlet region of this new multiple outlet geometry, where the connecting outlet, shown in Figure 6.20, was replaced by individual straight pipe

outlets at the end of the candles.

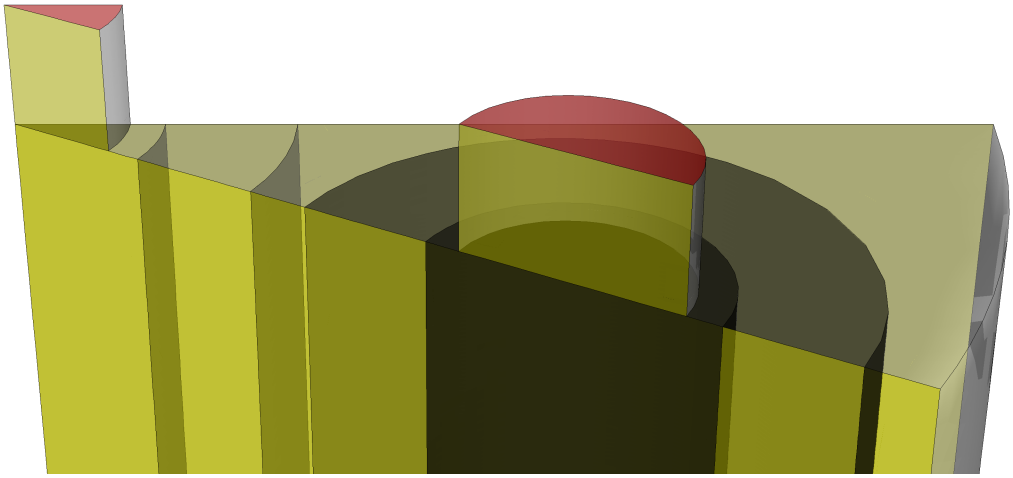

Figure 6.34: The outlet section of the seven candle pack multiple outlet model.

The mesh was ensured to be converged with mesh adaptation, analysing the pressure drop across the pack and the total mass flow through porous zones. At the inlet, a mass flow rate of 0.0625 kg/s was specified. The mesh controls for the original mesh are specified in Appendix A.3. Table 6.11 shows that the mass flow rate at the interface converges towards the mass flow rate specified at the inlet with refinement, with the second and third adaptation giving a mass flow rate through the interface matching that of the inlet. Table 6.11 also shows how the pressure drop across the seven candle pack varies with adaptation. Agreement between the second and third adaptation is exceptional, with a 0.030% difference between pressure drop for each mesh. In accordance with the criteria specified in Subsection 6.4.1, the mesh is deemed to be independent between the second and third adaptation.

Table 6.11: Changes in pressure drop across the one-twelfth multiple outlet seven candle pack model and the total mass flow through the sum of each porous zone interface as the mesh is refined through adaptation in regions of high pressure gradients.

Mesh	Mesh elements	Pressure drop [bar]	Total mass flow at interfaces [kg/s]
Original	1.700,000	25.92	0.0561
Adapt 1	3,900,000	26.37	0.0611
Adapt 2	13,000,000	26.49	0.0626
Adapt 3	17,000,000	26.50	0.0626

Figure 6.33 shows that the radial velocity through the central candle is of larger magnitude compared to the outer radial velocity through the outer candle for the original seven candle pack model. It was shown that the central candle sees a greater proportion of the inlet throughput compared to the outer candles. Table 6.12 shows the percentage split of the total mass flow rate between the whole central candle and a whole outer candle for the original and multiple outlet model. For the original model, more of the fluid passes through the central candle. For the multiple outlet case, the distribution of flow through each candle is identical to two decimal places. This is because the extended outlet sections for the outer candles result in a larger resistance to flow, hence more of the fluid initially travels through the central candle. Figure 6.35a shows the pressure contours through the plane parallel to the y-axis which cuts through the centre of both candles for the seven candle model. The pressure gradient is steeper through the outer candle due to the increased resistance imposed by the extended outlet. Figure 6.35b confirms this, showing that pressure is evenly distributed between the central and outer candle outlets for the multiple outlet model, as there is no additional contribution to resistance from the design of the outer candle outlet section. This results in an even distribution of the flow between the central and outer candles.

Candles are cleaned and reused after the termination of a run. If the flow is not homogenised, some candles in the pack would block at a faster rate compared to others, increasing pressure drop across the candles which see more throughput. This makes it more likely that the structure of those candles is damaged during production. This could spoil the candle, leading to expensive replacements rather than cleaning and reuse. If structural damage is not picked up on, then over several runs, the likelihood of significant damage to candles during runs increases, which would result in costly early termination of the runs and filter replacement. Hence, an even distribution of flow between candles is desirable.

Table 6.12: Mass flow rate through $r_c, r_o = 0.018$ m between the outer and central candles for the original and multiple outlet seven candle pack model.

Model	Central flow distribution [%]	Outer flow distribution [%]
Original	51.26	48.74
Multiple outlets	50.00	50.00

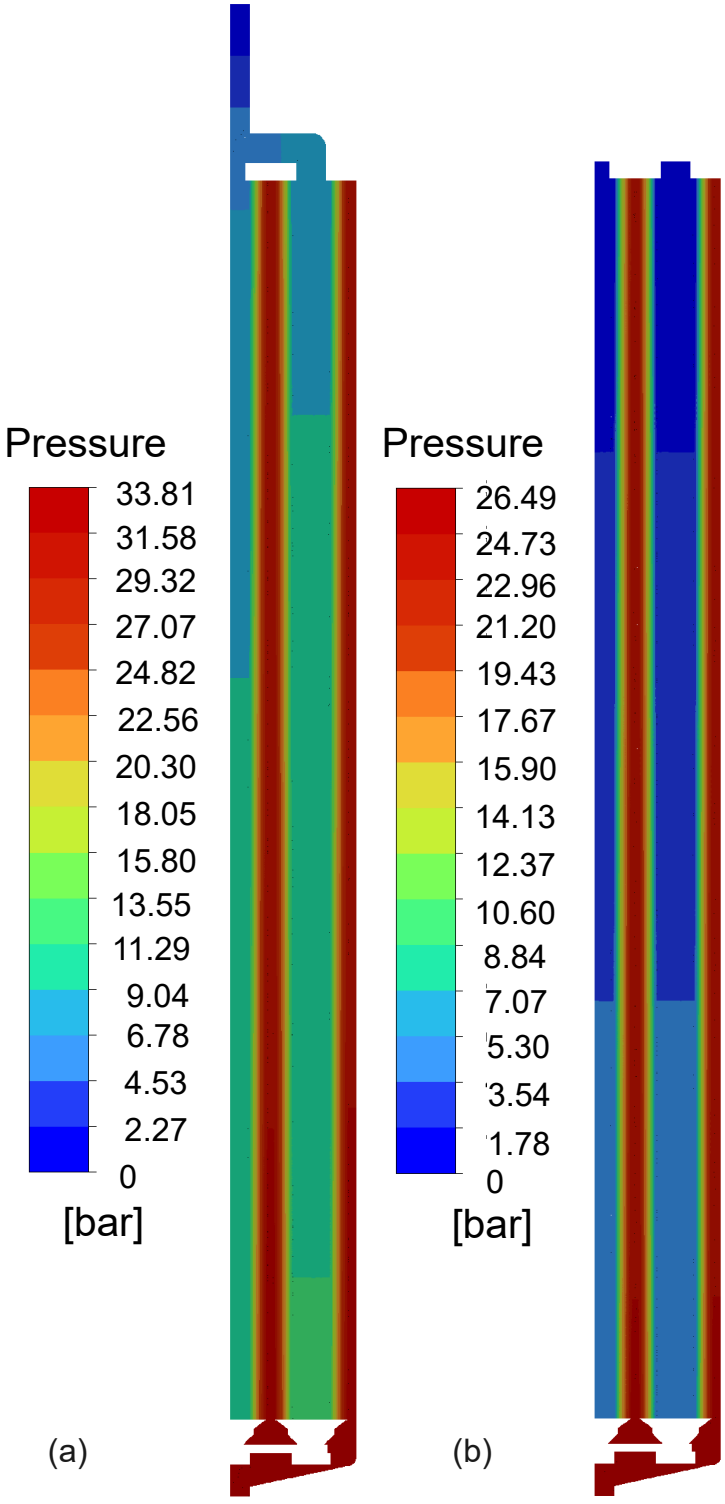

Figure 6.35: Contours of pressure on the plane parallel to the y-axis which cuts through the centre of the central and outer candle for (a) the seven candle pack model and (b) the multiple outlet model.

6.11 Conclusion

This chapter focused on the preliminary analysis of candle filter packs. Candle filter elements were described. Two of the filter packs used on film production lines were detailed: single and seven candle filter packs. Data from past runs which included a single candle filter pack was analysed and, surprisingly, it was found that there was no increase in pressure gradient over time as run flow rate increased. It is suggested that an experiment should be performed to determine the influence of candle element condition on the pressure drop across it.

A single candle filter pack computational model was created, and preliminary simulations were run to test if the symmetry of the geometry led to flow symmetry. The flow was found to be symmetrical in the same three planes as the geometry. Hence, the model could be reduced to a sixth of the original, exploiting symmetry boundary conditions. This saved significant computational cost.

Data from several runs from a film manufacturing line with a seven candle filter pack was analysed. As pressure was recorded at transducers upstream and downstream of the filter pack, it was possible to find information on the initial pressure drop across the pack. A seven candle filter pack computational model was created, and preliminary results verified and exploited flow symmetry to reduce the geometry down to a twelfth of its original size, saving significant computational cost on a sizeable geometry. Analysis from run data was then used to calibrate the permeability input for a porous zone representation of a candle filter.

Finally, results for the CFD models were analysed to understand how melt initially flows through each filter pack, before particle fouling influences flow patterns. Axisymmetry was verified in the porous zone of a single candle filter pack. The radial velocity was found to vary from the bottom to the top of the candle filter. This ensures that as the filter medium blocks over time, the permeability of the filter medium will change depending on only position along it. A permeability sensitivity analysis study was was undertaken, showing that as the permeability of the porous zone decreases, it exerts a greater resistance to flow, decreasing

the influence of the geometry on flow patterns as the radial velocity along the candle filter converges towards a uniform 'box' profile.

For the seven candle filter pack, it was found that the flow is not axisymmetric throughout each porous zone, and the flow is not evenly distributed between the central and outer candles. This means that the permeability of the central candle will vary at a different rate compared to the outer candles as the respective filter medium blocks. Furthermore, as the flow is not axisymmetric throughout the outer porous zone, the permeability will vary along and around each candle element as filter media blocks. The outlet part was shown to be the reason why the central and outer filters do not block evenly. This is due to the increased resistance caused by the bend in the pipe in the outlet part that connects to the outer candle.

In Chapter 7, the computational models discussed in this chapter are coupled with filter blocking models to examine how flow patterns alter as runs advance and candle filters block. As particles follow streamlines, analysis from this chapter suggests that candle filters will not block evenly. For the single candle filter pack, this chapter suggests that candle elements will not block uniformly along the filter. Flow patterns through the seven candle filter pack are more interesting; it appears that filter media will not block uniformly around, along and between candle elements.

Chapter 7

Pressure Drop and Flow Evolution in Candle Filter Packs

This chapter continues the computational work on single and seven candle filter packs. So far, only the initial flow through each pack has been modelled, before any blocking takes place. As filter packs block over the course of an industrial film production run, candle filter permeability decreases and resistance imposed on the flow by the filter medium increases. This leads to an increase in pressure drop across both the filter medium and the filter pack. In Chapter 6, it was shown that the radial velocity varies along the candle in the single candle filter pack and that the radial velocity varies along, across and between candles in the seven candle filter pack. The Stokes number for melts in filter media was calculated in Subsection 3.1.3. This confirms that particles in melts follow streamlines. Therefore, particle deposition is directly related to flow velocity. More particles will deposit in regions of higher velocity through the filter medium. This will lead to a greater increase in flow resistance in regions of higher velocity, which in turn will alter flow patterns across the filter pack, as the melt will adjust to travel through regions of lower resistance.

This chapter focuses on the development of a novel filtration model and its implementation

into the single and seven candle CFD filter pack models. The model is implemented through user-defined functions (UDFs) which allow customisation in Fluent. The methodology uses established mechanistic filter blocking models to couple the permeability of a filter medium to local fluid velocity. This allows CFD to be used to analyse complex industrial standard filter systems, with a focus on pressure drop evolution and flow pattern evolution as filter media blocks without directly modelling particle transport and deposition, which is computationally intractable. Through modification and implementation of the filtration model into a CFD model of the filter system, it is possible to capture the profiles of pressure drop evolution data from actual runs, gain insight into flow pattern evolution through the system and understand how filter elements in the system block over time.

The filter blocking model, which depends on radial velocity through the porous zone of a candle filter, is defined. The methodology for implementation and execution of this model is outlined. An axisymmetric version of the single candle filter pack is defined, which simplifies the geometry and saves computational expense. The axisymmetric model is used for initial implementation and validation of the filter blocking model. The model is then implemented into the 3D single candle filter pack CFD model. It is then implemented into the seven candle filter pack CFD model. A parameter study is undertaken to understand melt behaviour inside a seven candle filter pack through the range of melt properties and operational conditions utilized in actual production runs. Finally, design suggestions are given to improve flow distribution through the seven candle filter pack.

7.1 Candle filter blocking model

As with the screen filter work in Chapter 5, a filter blocking model may be prescribed to this average seven candle filter pack run data presented in Figure 6.19 in Section 6.6. The four simplest models: complete blocking, standard blocking, intermediate blocking and cake filtration, are again fitted. As filter blocking models only model pressure drop across a filter medium, and there is no data available for pressure drop across filters inside the seven candle

filter pack, the calibrated seven candle filter pack CFD model, detailed in Section 6.7 and calibrated in Section 6.8, was used to find an estimate for pressure drop across the filters inside the seven candle filter pack. As there are seven candle filters inside a pack in parallel, the averaged run data was modified to give the mean pressure drop across an averaged filter inside the geometry.

From the CFD model, pressure drop across the outer candle filter, ΔP_o, is calculated by subtracting the averaged pressure across the interface between the outer porous zone and the central core from the averaged pressure across the interface between the outer porous zone and the geometry upstream of the filter. Similarly, the pressure drop across the central candle filter, ΔP_c, is calculated in the same way with the central porous zone. Taking the mean of these values gives the average pressure drop across a filter in the seven candle filter pack, ΔP_{filter}. Then, the pressure drop contribution from the geometry, $\Delta P_{\text{geometry}}$, is calculated from

$$\Delta P_{\text{geometry}} = \Delta P_{\text{pack}} - \Delta P_{\text{filter}}.$$

Table 7.1 shows the pressure drop contributions throughout the seven candle filter pack CFD model. The average pressure drop across a filter inside the seven candle filter pack from the averaged run data, ΔP_{fd}, can then be calculated from

$$\Delta P_{\text{fd}} = \Delta P_{\text{data}} - \Delta P_{\text{geometry}},$$

where ΔP_{data} is the averaged pressure drop across the pack from the seven candle run analysis from Section 6.6.

Table 7.1: Pressure drop across different sections of the seven candle filter pack CFD model.

ΔP_c [bar]	ΔP_o [bar]	ΔP_{filter} [bar]	ΔP_{pack} [bar]	$\Delta P_{\text{geometry}}$ [bar]
21.48	20.50	20.99	33.81	12.82

Figure 7.1 shows the pressure drop across a filter in the seven candle filter pack calculated from averaged run data, put into a different form for each model, so a linear curve can be fitted to test the suitability of each model. The R^2 value of each fit is also presented in Table 7.2. There is little difference in R^2 values between the standard and intermediate fits. This is different to the screen filter, where the intermediate blocking model clearly gave the best fit.

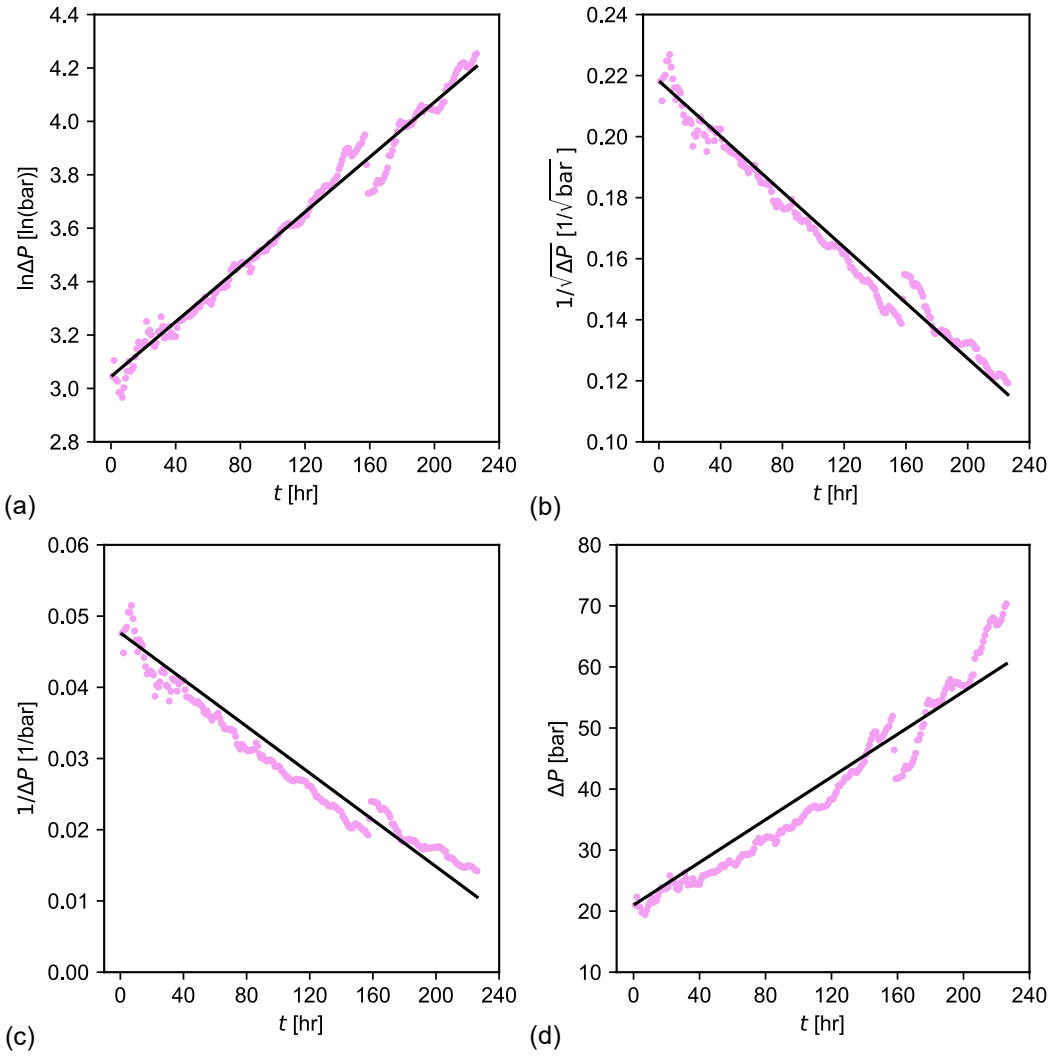

Figure 7.1: Linear curve fitting to the average pressure drop evolution across a candle element in the seven candle pack for (a) intermediate blocking, (b) standard blocking, (c) complete blocking and (d) cake filtration.

Table 7.2: R^2 values for the fit of different blocking models to average run pressure drop evolution across a candle element in the seven candle pack presented in Figure 7.1.

Blocking model	R^2
Intermediate blocking	0.982
Standard blocking	0.973
Complete blocking	0.937
Cake filtration	0.927

A key difference between candle filters and screen filters is the material. Where a screen filter layer comprises of a single, woven filter layer, a candle filter layer comprises of a thick, sintered fibre structure, where particles are likely to get captured inside the pores. The manufacturer of candle filters also confirmed that the sintered fibre structure is a depth filtration medium [119]. The standard model mimics the capture of small particles inside pores. Even though the intermediate model gives a slightly superior fit, the standard model is chosen as the fit is good and it is a better physical representation of the filtration mechanism driving particle capture in a sintered fibre material.

Figure 7.2 shows the standard model fit to the run average pressure drop across a filter in the seven candle filter pack. The fit clearly gives a good representation of the averaged pressure drop across a filter inside the seven candle filter pack.

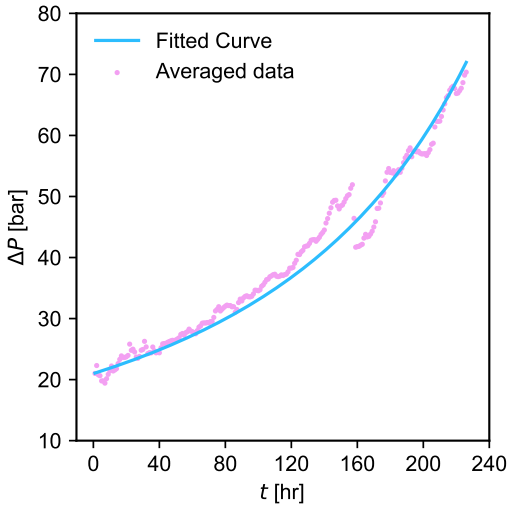

Figure 7.2: Standard blocking model fit to the average run pressure drop evolution across a candle element in the seven candle pack.

In summary, the averaged pressure drop evolution data through the seven candle filter pack, which was calculated in Section 6.6, has been used to investigate which filter blocking mechanism best represents filtration in the seven candle filter pack. The seven candle CFD model was used in conjunction with the data to find a mean pressure drop across a filter in the pack. After fitting several models, the standard model was chosen due to its good fit to the data and its physical representation of the mechanisms of filtration through a candle filter.

7.2 Permeability evolution model

The standard blocking model is given by

$$\Delta P = \frac{\Delta P_0}{\left(1 - \frac{K_s \dot{m} t}{2}\right)^2}, \tag{7.1}$$

where ΔP is the pressure drop across a candle filter, ΔP_0 is the initial pressure drop across the filter, $\dot{m}$ is the mass flow rate, t is time and K_s is a fitting parameter. From Darcy's law

(2.13),

$$\dot{m} = \frac{\Delta P A \rho k}{d\mu}, \tag{7.2}$$

where A is the cross-sectional area of the filter, ρ is the fluid density, k is the permeability, μ is the fluid viscosity and d is the thickness of the filter. Initially, pressure drop across a filter is given by

$$\Delta P_0 = \frac{\dot{m} d \mu}{A \rho k_0}, \tag{7.3}$$

where k_0 is the initial, clean permeability of the candle filter before any blocking has taken place. Substituting (7.1) into (7.2) gives

$$k = \frac{d\mu\dot{m}}{A\rho\Delta P_0}\left(1 - \frac{K_s \dot{m} t}{2}\right)^2. \tag{7.4}$$

Then, substituting (7.3) into (7.4) gives an expression for the permeability evolution using the standard model:

$$k = k_0\left(1 - \frac{K_s \dot{m} t}{2}\right)^2. \tag{7.5}$$

As radial velocity has been shown to vary along and around candle filters in Sections 6.9 and 6.10, and particles follow streamlines, the filter medium will not block evenly. The permeability evolution model is modified to allow the permeability of candle filters to vary based on radial velocity:

$$k(r,\theta,z) = k_0\left(1 - \frac{K_s 2\pi r h \rho \dot{r}(r,\theta,z) t}{2}\right)^2, \tag{7.6}$$

where h is the length of a candle filter and r and $\dot{r}$ are radial coordinate and radial velocity relative to the centre of the candle filter. Consider a cylinder of constant radius in the porous zone for the single candle filter pack. By conservation of mass, the mass flow rate through this cylinder must equal that of the mass flow rate specified at the inlet of the filter pack. Taking the mean of (7.6) at constant r gives

$$\bar{k} = k_0\left(1 - \frac{K_s 2\pi r_d h \rho \bar{\dot{r}} t}{2}\right)^2,$$

where r_d is some constant radius inside the porous zone. But $\bar{\dot{r}} = \frac{\dot{m}}{2\pi r_d h \rho}$ by conservation of mass. Hence, (7.6) allows the permeability of the candle filter to vary, while recovering (7.5) on averaging.

Fluent does not use permeability as an input in porous zones. Instead, the viscous resistance must be used. Viscous resistance is simply the reciprocal of permeability. Hence, on implementation in Fluent, (7.6) is transformed into

$$\eta = \eta_0 \left(1 - \frac{K_s 2\pi r h \rho \dot{r} t}{2}\right)^{-2}, \tag{7.7}$$

where η is the viscous resistance of the porous zone and $\eta_0 = 1/k_0$. Before the implementation of (7.7) into CFD models of the filter packs, simpler models are tested and analysed. Initially, (7.4) is chosen. This model has no velocity dependence, and will ensure the viscous resistance increases but remains uniform throughout the porous zone over time. This gives a viscous resistance formulation of

$$\eta = \eta_0 \left(1 - \frac{K_s \dot{m} t}{2}\right)^{-2}. \tag{7.8}$$

Then, a model with linear dependence on radial velocity is defined, given by

$$\eta = \eta_0 (1 + K_s \pi \rho h r \dot{r} t). \tag{7.9}$$

A model with quadratic dependence on radial velocity is also tested, given by

$$\eta = \eta_0 \left(1 + (K_s \pi r h \rho \dot{r} t)^2\right). \tag{7.10}$$

The models build up in complexity. The constant model will ensure that the standard model, with no velocity dependence, integrates into CFD simulations. The linear model then tests the integration of a simple permeability-radial velocity relationship. The quadratic model then tests that a more complicated relationship, before moving onto the standard model (7.7).

7.3 Methodology and implementation

Blocking models detailed in Section 7.2 were implemented into the CFD as a series of quasi steady-state simulations. Filter packs block over a period of tens of hours, and productions runs last days. Small changes to the flow therefore happen gradually, over several hours. The blocking model couples porous zone viscous resistance and radial velocity. As particles follow streamlines, the local viscous resistance of a filter medium inside the pack depends on the local radial velocity. The velocity must then adapt to changes in the viscous resistance profile, and so on.

7.3.1 User-defined functions

The blocking models were implemented into Fluent with user-defined functions. A user-defined function (UDF) is a C function that can be loaded in to Fluent to enhance standard features [129]. UDFs are defined using `DEFINE` macros, source files which contain the UDFs can be interpreted directly into Fluent via its GUI.

Two `DEFINE` macros were used for the implementation of the blocking models. Once interpreted, `DEFINE_ON_DEMAND` is a macro that is manually executable at any time by the user. This macro was used to save the radial velocity cell centroid values in user-defined memory (UDM). A UDM acts as any other variable in FLUENT; it can be used in other UDF macros, and can be used for analysis in post-processing.

The macro `DEFINE_PROFILE` was also used. This macro creates a custom profile which can be implemented in specific cell zones. It was used to create the chosen viscous resistance evolution profile. This UDF loops over every cell in the domain, calculating, for example, (7.7) at every cell centroid. It saves calculated values in a profile, which can be enabled on the porous zone. It also saves the calculated values at every cell centroid as a second UDM. This allows analysis of the viscous resistance profile inside the porous zone. The UDF also

accesses the UDM saved by the `DEFINE_ON_DEMAND` macro, which was defined as the radial velocity. The radial velocity is accessed from the UDM using `DEFINE_ON_DEMAND` rather than a direct variable access as if radial velocity was directly used, the viscous resistance profile would update at every iteration, rather than at the end of a quasi-steady time step. This would update the viscous resistance profile with a not yet converged radial velocity profile, invalidating results. Example source files are presented in Appendix B.

7.3.2 Simulation workflow

The workflow for completion of a successful simulation using UDFs is:

1. Complete an initial CFD simulation of flow through a filter pack with the constant clean viscous resistance of a candle filter element, η_0.
2. Interpret the C file which contains the `DEFINE_ON_DEMAND` and `DEFINE_PROFILE` UDFs.
3. Save the case and data files.
4. Execute the `DEFINE_ON_DEMAND` UDF, saving the current radial velocity field to a UDM variable.
5. Hook the `DEFINE_PROFILE` UDF to the porous zone viscous resistance with the `time` variable chosen as the first time step.
6. Solve the updated simulation until convergence criteria met. Save the case and data files.
7. Execute the `DEFINE_ON_DEMAND` UDF again, saving the updated radial velocity field.
8. Hook the `DEFINE_PROFILE` UDF to the porous zone viscous resistance with the `time` variable chosen as the next time step.
9. Solve the updated simulation until convergence criteria met. Save the case and data files.

10. Repeat 7-9 until a predetermined maximum time is met.

This process was fully automated for execution on high performance computing facilities. The implementation of this workflow is summarised in Figure 7.3.

7.4 Axisymmetric single candle pack model

An axisymmetric model of the single candle filter pack was used for initial tests of the permeability evolution model. In Subsection 6.9.1, flow in the porous zone of a single candle filter pack was found to be axisymmetric. However, the geometry and flow around the spider plate is not axisymmetric. Here, the geometry was simplified to exploit this region of axisymmetry for the purpose of blocking model testing. Figure 7.4 shows the simplified axisymmetric single candle filter pack geometry. The spider plate has been removed, and the bottom of the base of the candle is in line with the top of the inlet pipe. The green line shows the axis of revolution. Fluent requires that the x-axis is parallel with the axis of revolution for axisymmetric modelling.

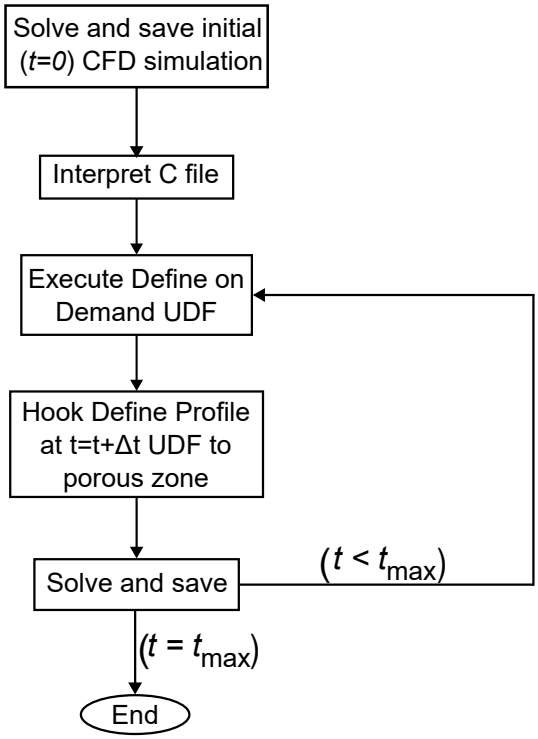

Figure 7.3: Flow chart of the workflow for execution of a filter blocking simulation.

For preliminary analysis, at the inlet, a mass flow rate of 260 kg/hr was specified normal to the boundary and no-slip was specified at the walls. A static pressure outlet was chosen; the inlet and outlet were extended to be sufficiently far away from the core of the pack, as to have no influence on flow development in the pack. An incompressible, Newtonian fluid with $\rho = 1225$ kg/m^3 and a viscosity of 112.86 Pa s was modelled. These values were chosen to match properties specified for the single candle filter pack CFD model.

This set-up gives a Reynolds number of 0.027, ensuring the laminar regime is maintained throughout. Each porous zone was assigned the clean candle viscous resistance value found in Section 6.8: 1.25×10^9 m^{-2}. Physics and solvers were specified as described in Subsection 3.2.5. Convergence was ensured by following Subsection 3.2.7. A steady, pressure-based solver is specified and a viscous, incompressible laminar model is used.

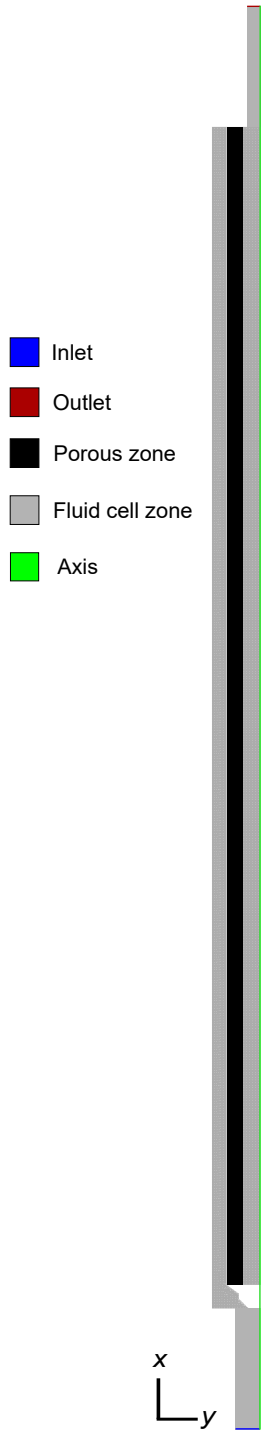

Figure 7.4: Axisymmetric single candle pack geometry.

7.4.1 Mesh independence

A mesh of the axisymmetric model was created in ANSYS meshing. Figure 7.5 shows the mesh structure. To ensure sufficient mesh refinement everywhere, the geometry was broken into three sections: the porous zone and the fluid cell zones upstream and downstream of the porous zone. As the axisymmetric model is a two-dimensional geometry, significant computational cost was saved. The mesh was generated with structured, quadrilateral mesh, with mesh defeaturing, curvature capture and capture proximity specified. This ensured that the mesh was refined in regions with complicated topology. Mesh details are expanded upon in Appendix A.2.

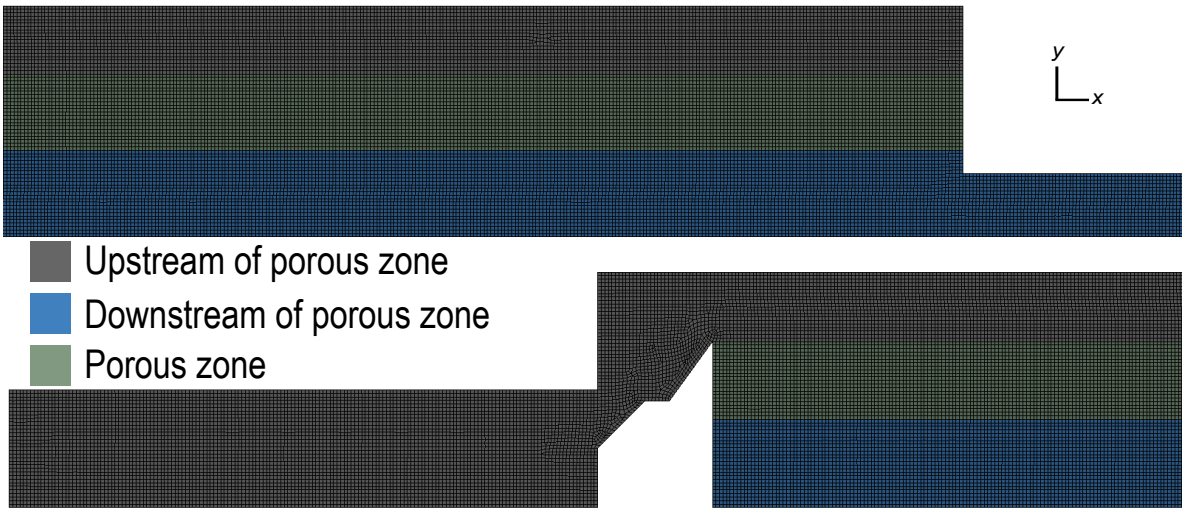

Figure 7.5: Axisymmetric single candle filter pack mesh. The bottom image shows the inlet section of the geometry. The top image shows the outlet section.

A coarse, medium and fine mesh were created. Table 7.3 gives the number of elements for each mesh. Pressure drop across each pack was compared and the flow redevelopment length for the medium mesh was compared to the analytical flow redevelopment length model for creeping flow, discussed in Subsection 3.2.4 and given by (3.6). This was done with no porous zone enabled, to ensure mesh independence away from the filter medium. Figure 7.6a shows pressure drop across the pack for each mesh and agreement between models is good, with a

0.1% difference between pressure drop outputs for the medium and fine mesh. Figure 7.6b also shows the medium mesh gives a good prediction for the flow redevelopment length. The simulation is therefore deemed to be independent of mesh resolution and the medium mesh is used for porous zone mesh adaptation.

Table 7.3: Number of elements for the coarse, medium and fine mesh generated for the axisymmetric single candle CFD model.

Mesh	Mesh elements
Coarse	177,000
Medium	247,000
Fine	359,000

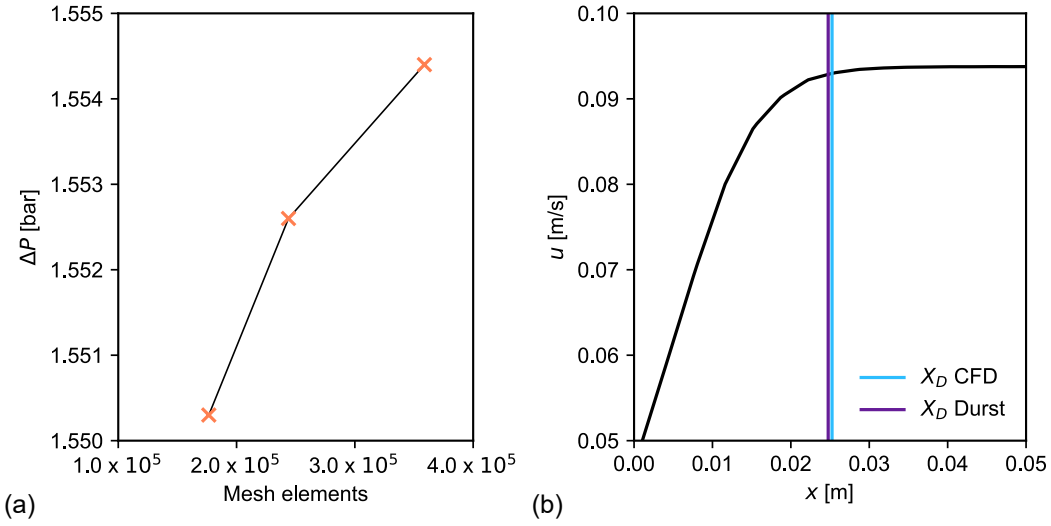

Figure 7.6: (a) Pressure drop across the axisymmetric single candle pack for three meshes. (b) Plot of x-velocity along the centreline of the inlet pipe, with medium mesh CFD and the calculated analytical redevelopment length (3.6) highlighted.

As with the single candle model, with the porous zone enabled, the mesh was ensured to be converged through the filter medium with mesh adaptation by analysing the pressure drop across the pack and the total mass flow rate through porous zone. At the inlet a mass flow rate of 0.0722 kg/s was specified. Table 7.4 shows that the mass flow rate at the interface converges towards the mass flow rate specified at the inlet with refinement, with the second

and third adaptation giving a mass flow rate matching that of the inlet.

Table 7.4 also shows how the pressure drop across the axisymmetric model varies with adaptation. Agreement between the second and third adaptation is exceptional, with a 0% difference between pressure drop for each mesh. In accordance with the criteria specified in Subsection 6.4.1, the solution is deemed to be mesh independent between the second and third adaptation.

Table 7.4: Changes in pressure drop across the axisymmetric single candle pack model and the total mass flow through the porous zone interface as the mesh is refined through adaptation in regions of high pressure gradients.

Mesh	Mesh elements	Pressure drop [bar]	Total mass flow at interface [kg/s]
Original	250,000	11.85	0.0742
Adapt 1	480,000	11.92	0.0725
Adapt 2	660,000	11.92	0.0723

The solution was shown to be independent of mesh away from the porous zone and adapting the medium mesh showed the twice adapted medium mesh also produced results independent of the mesh around the porous zone. The solution is therefore deemed to be mesh independent throughout the geometry and is used for analysis.

7.4.2 Comparison of 2D axisymmetric and 3D single candle pack model

The axisymmetric model matches the fluid properties, porous zone viscous resistance and mass flow rate prescribed to the one-sixth single candle filter pack CFD model from Section 6.9. It was found in Section 6.9 that flow around and through the porous zone of the single candle filter pack was axisymmetric and unaffected by the spider plate. Flow through the porous zone of the axisymmetric model should therefore match that of the one-sixth single candle filter pack model. Figure 7.7 shows radial velocity along y at $r = 0.028$ m and $r = 0.018$ m for both models. It is clear that flow through the axisymmetric porous zone matches that of the 3D model. The number of mesh elements is an order of magnitude less for the axisymmetric model. This, coupled with the reduced complexity of variables and discretised

equations for a 2D simulation, dramatically reduces computational costs. A quasi-steady state simulation with the one-sixth single candle model takes an order of hours, compared to an order of minutes for a quasi-steady state simulation with the axisymmetric model. The axisymmetric model is the ideal model for initial implementation of the blocking model, due to its significantly reduced computational cost and similarity in flow patterns in the porous zone, where the blocking model is implemented.

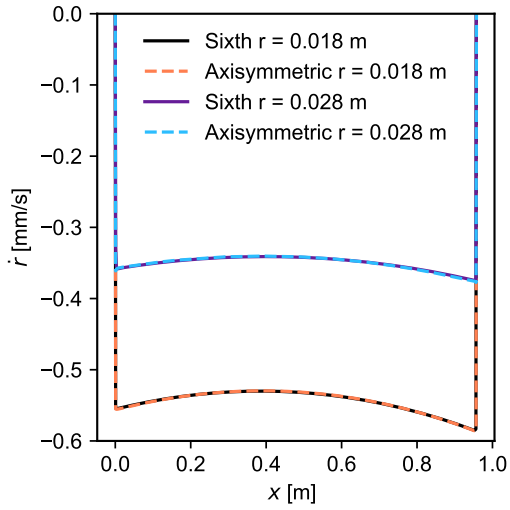

Figure 7.7: Variation in radial velocity along the filter medium for the axisymmetric model and the single candle pack model. Position along the geometry is shifted in this plot for both cases so that the bottom of the candle is positioned at $x = 0$ m.

7.5 Axisymmetric single candle pack blocking evolution

In this section, the blocking models (7.7)-(7.10) are tested with the axisymmetric CFD model. As the CFD model is already axisymmetric, radial coordinates and radial velocity are already built-in to the configuration and can be saved to a UDM at each time step directly. For each blocking model, the fitting parameter was assigned as $K_s = 0.0358$. The initial viscous resistance, η_0, was chosen as the viscous resistance of a clean candle filter determined in Section 6.8.

The quasi-steady state simulations must be independent of time step size. To show this, three time step sizes were chosen: 5, 10 and 15 hours. A maximum time of 500 hours was chosen. Figure 7.8 shows the pressure drop across the pack from $t = 0$ hr to $t = 500$ hr for simulations using the blocking models (7.7)-(7.10) for the three different time step sizes. The different time steps show matching agreement for pressure drop evolution throughout the pack up to 500 hours for the constant, linear and quadratic models, and up to 450 hours for the standard model. For each blocking model, the 10 hour time-stepping results are used for analysis henceforth.

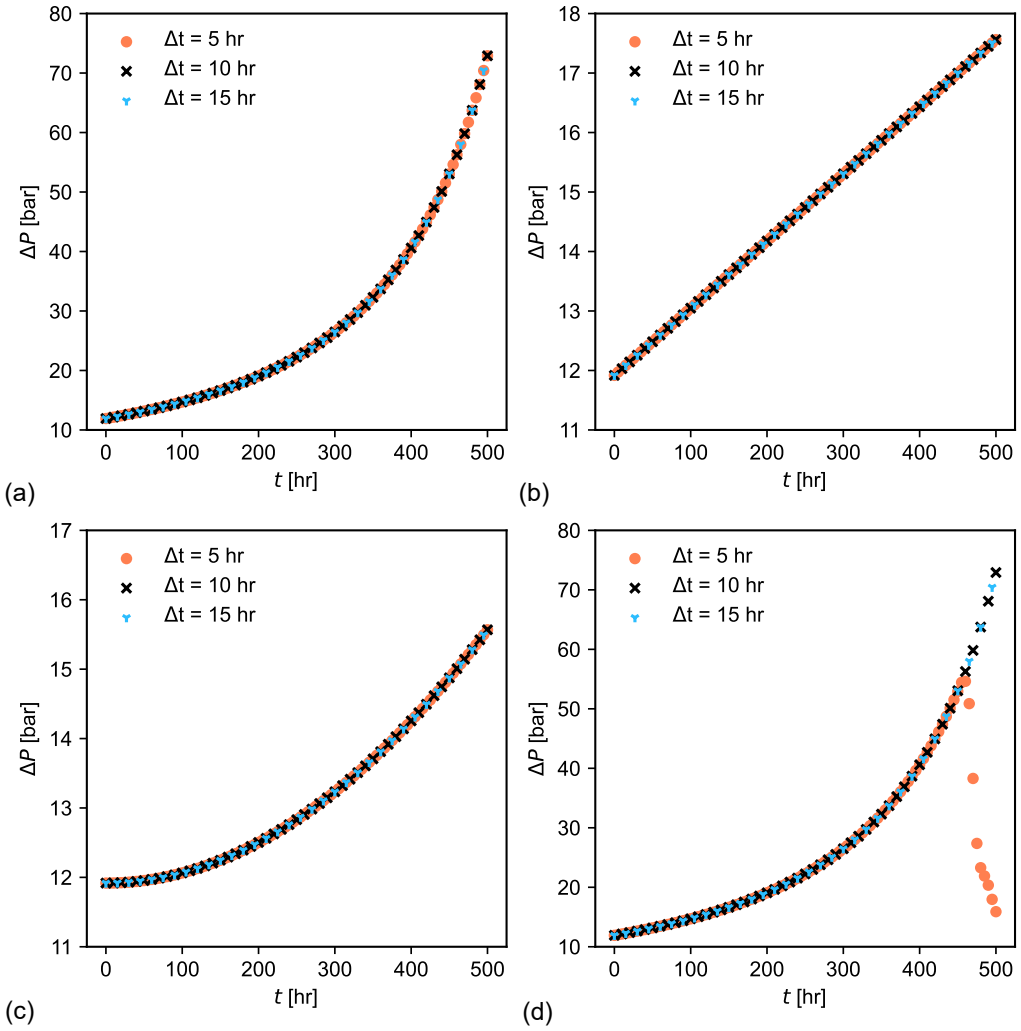

Figure 7.8: Pressure drop evolution across the pack for the axisymmetric (a) constant (b) linear (c) quadratic (d) standard blocking model with time steps of 5, 10 and 15 hours.

7.5.1 Constant blocking model

The constant model (7.8) was implemented into the axisymmetric CFD model through the workflow described in Subsection 7.3.2. This means that the viscous resistance of the porous zone does not depend on radial velocity. Viscous resistance of the porous zone depends only on time; the viscous resistance profile is uniform throughout the porous zone for all times at this stage. To match conditions of the axisymmetric CFD model, $\dot{m}$ was chosen to match the inlet mass flow rate.

Figure 7.9 shows the linear relationship between pressure drop across the pack and viscous resistance of the filter medium. The linear regression fit to the data is exceptional, with an R^2 value of 1. This is expected as pressure is directly proportional to resistance through a filter medium from Darcy's law. However, the fitted line does not cross through the origin; the intercept, P_I, is calculated as $P_I = 3.19$ bar. This is because there is a contribution to the pressure drop across the pack from both the filter medium and the geometry of the pack. The intercept is an approximation for pressure contribution from the geometry.

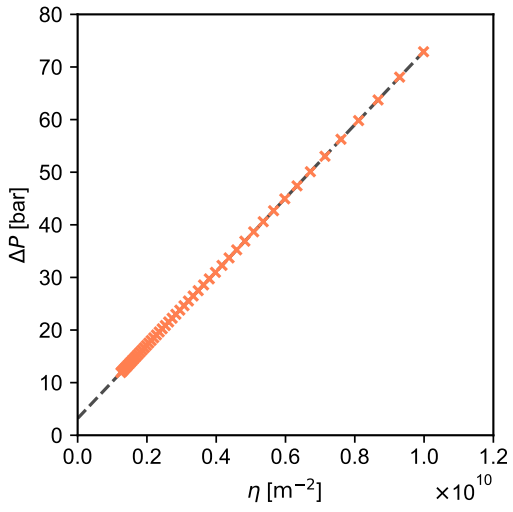

Figure 7.9: Pressure drop across the pack against viscous resistance for the axisymmetric constant blocking model.

Figure 7.10a shows pressure drop across the filter medium, calculated by taking the average pressure at the interface of the porous zone and the central core from the average pressure at the interface of the porous zone and outer annulus of the pack. Figure 7.10b shows the pressure drop across the filter medium against filter viscous resistance. Here, linear regression again gives an R^2 value of 1 and now passes through the origin, following Darcy's law.

Pressure drop across the filter medium can be calculated directly from the standard model, given by

$$\Delta P = \Delta P_0 \left(1 - \frac{K_s \dot{m} t}{2}\right)^{-2}, \tag{7.11}$$

by substituting ΔP_0 from CFD results.

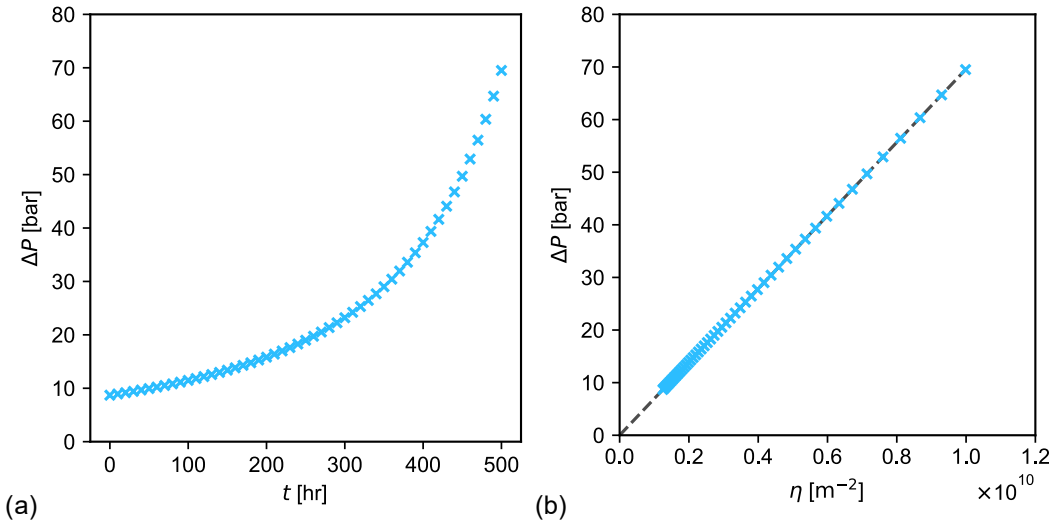

Figure 7.10: (a) Pressure drop evolution across the filter medium and (b) pressure drop across the filter medium against viscous resistance for the axisymmetric constant blocking model.

Figure 7.11a shows an exceptional match between the CFD model and a direct calculation based upon (7.11) for pressure drop across the filter medium. Figure 7.11b again compares a direct calculation and the CFD pressure outputs, but for pressure drop across the pack. The direct calculation fails to agree with the CFD model as the standard blocking model can only be used to predict pressure drop across a porous medium.

Figure 7.12a shows how the radial velocity profile changes over time for the constant blocking model. The radial velocity appears to converge towards a uniform 'box' profile, where flow is evenly distributed throughout the filter medium. Figure 7.12b shows how the viscous resistance profile changes over time. Due to the form of (7.8), the rate of increase of the viscous resistance grows on each time step. It was shown in Subsection 6.9.2 that as the viscous resistance of the filter medium in the single candle CFD model increased, the radial velocity converged towards a uniform distribution along the filter medium. Hence, as the viscous resistance increases over time, the radial velocity converges towards a uniform distribution.

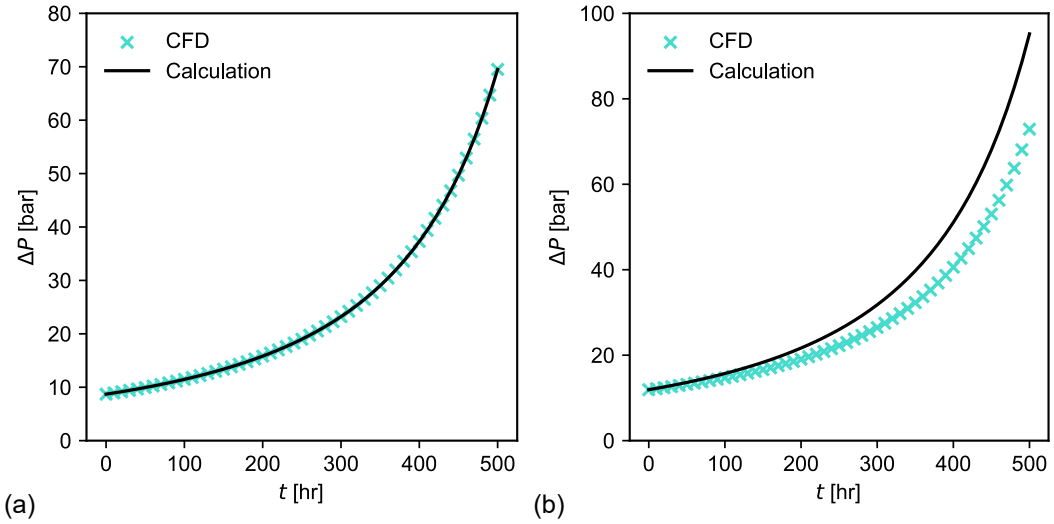

Figure 7.11: Comparison of the pressure drop evolution (a) across the filter medium and (b) across the pack between the CFD results and direct calculation from (7.11) for the axisymmetric constant blocking model.

So far, it has been shown that implementing the constant blocking model (7.8) into the CFD simulations through UDFs using the workflow described in Subsection 7.3.2 successfully replicates a direct calculation with the standard blocking model.

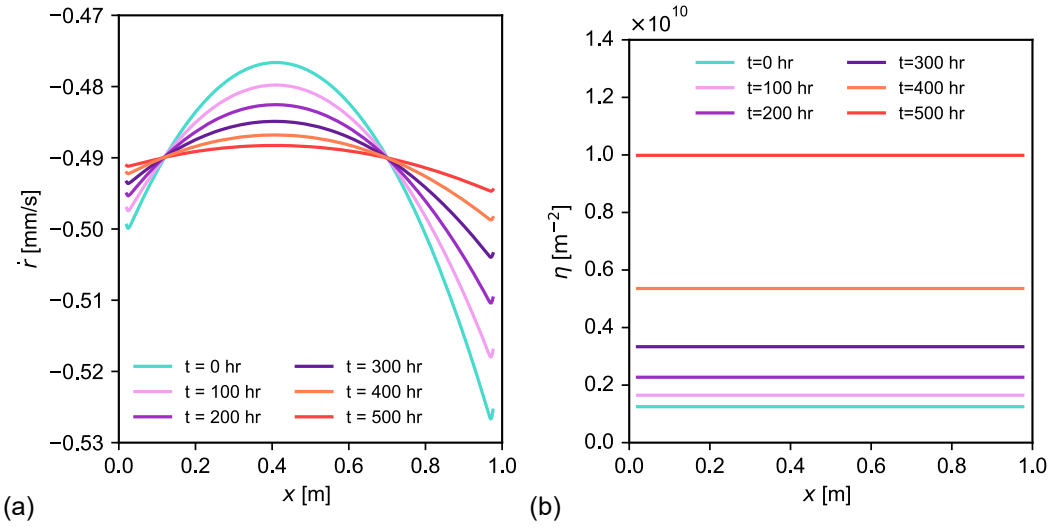

Figure 7.12: (a) Radial velocity and (b) viscous resistance evolution along the candle at $r = 0.02$ m for the axisymmetric constant blocking model.

7.5.2 Linear blocking model

The linear model (7.9) was implemented into the axisymmetric CFD model through the workflow described in Subsection 7.3.2 to test a simple implementation of the relationship between radial velocity and permeability. Here, the viscous resistance profile of the porous zone was not uniform due to its dependence on radial velocity.

Pressure drop across the filter medium can be calculated directly from the linear blocking model, given by

$$\Delta P = \Delta P_0 \left(1 + \frac{K_s \dot{m} t}{2}\right), \tag{7.12}$$

through substituting ΔP_0 from the CFD simulation and taking $\dot{m}$ as the throughput through the pack. Even though the CFD model does not directly include $\dot{m}$ and changes viscous resistance based on radial velocity, conservation of mass dictates that the throughput through the filter medium must always equal that of the throughput through the pack. Hence, as

shown in Section 7.2, the average viscous resistance in the porous zone should recover

$$\bar{\eta} = \eta_0 \left(1 + \frac{K_s \dot{m} t}{2}\right). \tag{7.13}$$

From Darcy's law, the pressure drop across the filter medium is then described by (7.12). Hence, if the model was implemented successfully, pressure drop evolution across the filter medium should match a direct calculation from (7.12). Figure 7.13 shows an exceptional match between the CFD model and a direct calculation for pressure drop across the filter medium. The linear model, with a coupling between radial velocity and porous zone viscous resistance, was implemented into the axisymmetric CFD model successfully.

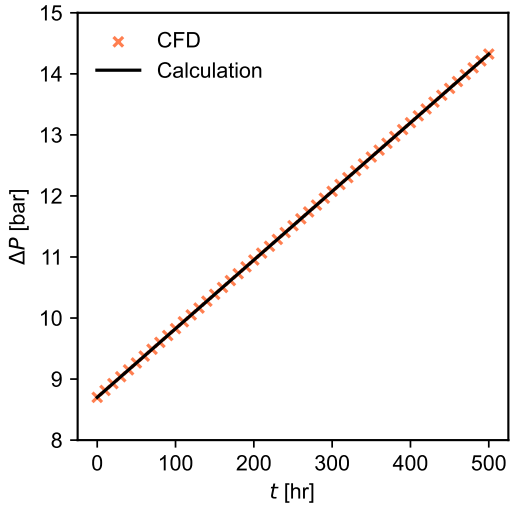

Figure 7.13: Comparison of the pressure drop evolution across the filter medium between the CFD results and direct calculation from (7.12) for the axisymmetric linear blocking model.

As the profile of the viscous resistance of the porous zone changes over time, the flow distribution through the porous zone will change to compensate. Figure 7.14a shows how the radial velocity profile changes over time for the linear blocking model. Again, the radial velocity appears to converge towards a uniform 'box' profile, where flow is evenly distributed along the length of the filter medium. Figure 7.14b shows how the viscous resistance profile changes over time. After a quasi-steady time step, local resistance through the candle is larger in

regions of higher radial velocity. On the next time step, this leads to a reduction in radial velocity in regions of higher viscous resistance. This process repeats on further time stepping such that the radial velocity converges towards a uniform profile along the filter medium. The viscous resistance profile becomes less uniform over time. Figure 7.15b highlights the profile of the viscous resistance after one quasi-steady time step. The model calculates this profile using (7.9) with the radial velocity along the same profile from the initial simulation, shown in Figure 7.15a. The viscous resistance is greater in regions corresponding to a greater magnitude of radial velocity. This is because the filter medium has seen more flow in these regions, meaning a higher concentration of particles have been captured by the filter medium in regions of higher radial velocity. Figure 7.14a shows that the magnitude of radial velocity remains larger near the top and bottom of the filter medium as time progresses. This means that more flow continues to pass through these regions relative to the centre of the filter medium which causes the viscous resistance profile to become less uniform on every time step.

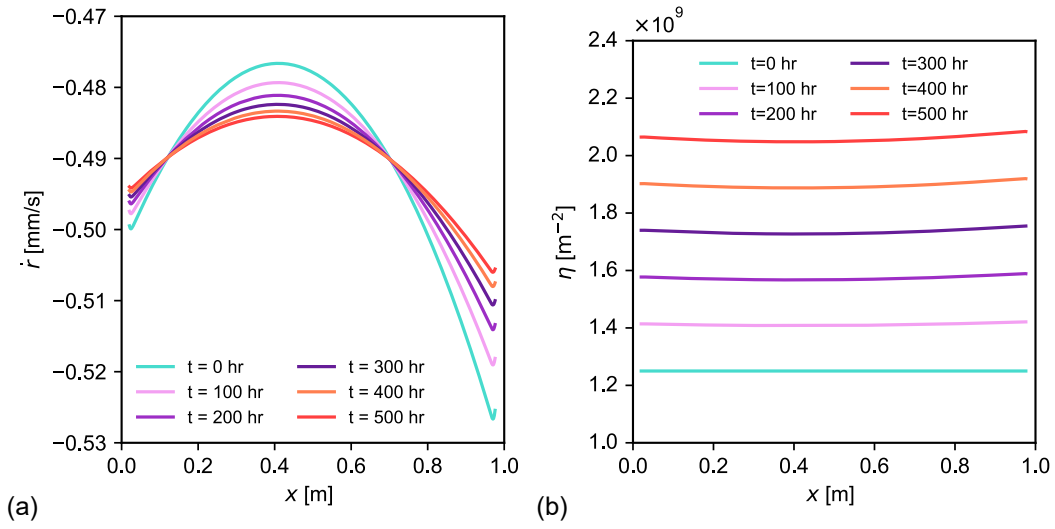

Figure 7.14: (a) Radial velocity and (b) viscous resistance evolution along the candle at $r = 0.02$ m for the axisymmetric linear blocking model.

Physically, this makes sense as particles follow streamlines. Hence, particle deposition through the filter medium is proportional to radial velocity. Regions with larger radial velocity see

a higher rate of blocking, which leads to a greater resistance to the flow. The flow then redistributes to account for this non-uniform resistance, increasing flow distribution through regions which have seen less flow and decreasing distribution through regions which have seen more flow. Over time, this leads to a more even distribution of flow throughout the filter medium.

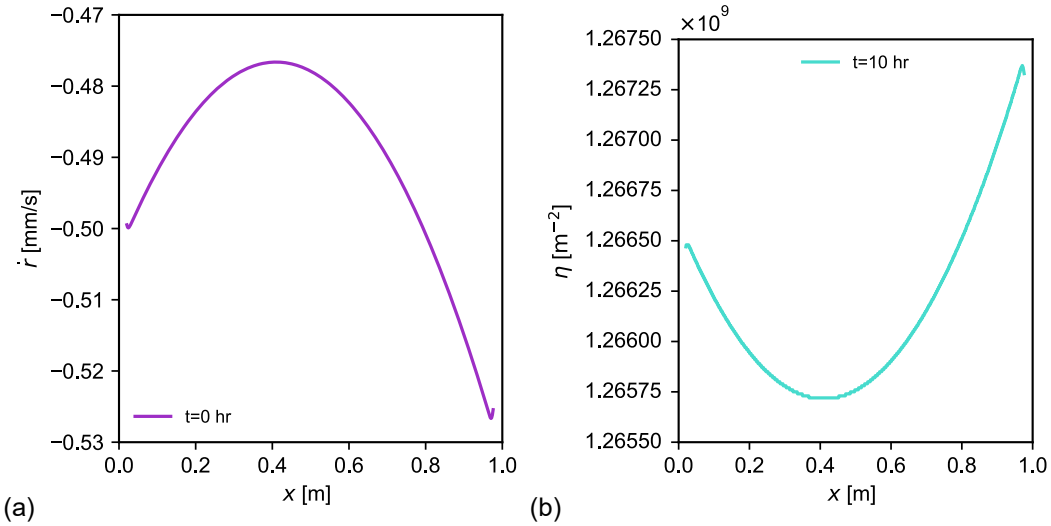

Figure 7.15: (a) Radial velocity at $t = 0$ hr and (b) viscous resistance at $t = 10$ hr along the candle at $r = 0.02$ m for the axisymmetric linear blocking model.

7.5.3 Quadratic blocking model

The quadratic model (7.10) was implemented into the axisymmetric CFD model through the workflow described in Subsection 7.3.2. Here, the viscous resistance profile of the porous zone is still dependent on radial velocity and the relationship between viscous resistance and radial velocity is quadratic. This means that small changes in local radial velocity in the porous zone should result in a more significant change to the local viscous resistance, compared to the linear model.

Pressure drop across the filter medium can be calculated directly from the quadratic blocking

model, given by

$$\Delta P = \Delta P_0 \left(1 + \left(\frac{K_s \dot{m} t}{2}\right)^2\right), \tag{7.14}$$

with ΔP_0 taken from the initial CFD simulation and $\dot{m}$ as the throughput through the pack. Again, if this model has worked successfully, pressure drop evolution across the filter medium should match a direct calculation from (7.14). Figure 7.16 shows an exceptional match between the CFD model and a direct calculation for pressure drop evolution across the filter medium. The quadratic model, with a coupling between radial velocity and porous zone viscous resistance, has been implemented into the axisymmetric CFD model successfully.

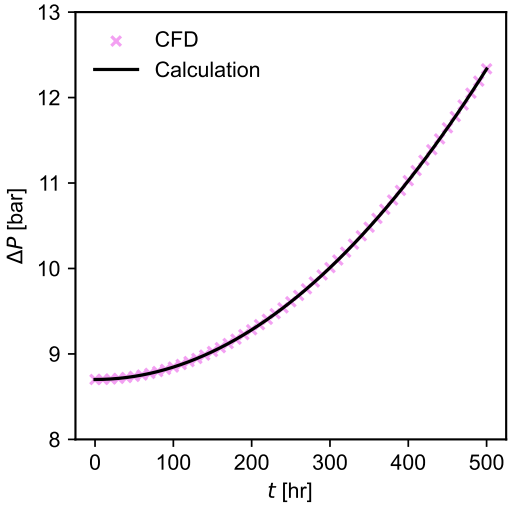

Figure 7.16: Comparison of pressure drop evolution across the filter medium between the CFD results and a direct calculation from (7.14) for the axisymmetric quadratic blocking model.

Figure 7.17a shows how the radial velocity profile along the filter medium changes over time for the quadratic blocking model. The radial velocity again appears to converge towards a uniform profile, where flow is evenly distributed along the filter medium. Figure 7.17b shows how the viscous resistance profile changes over time. After a quasi-steady time step, resistance through the candle is larger in regions of higher radial velocity. On the next time step, this leads to a reduction in radial velocity in regions of higher viscous resistance. This process repeats on further time stepping such that the radial velocity converges towards a

uniform profile throughout the filter medium and the viscous resistance profile becomes more pronounced in regions of greater radial velocity magnitude along the filter medium.

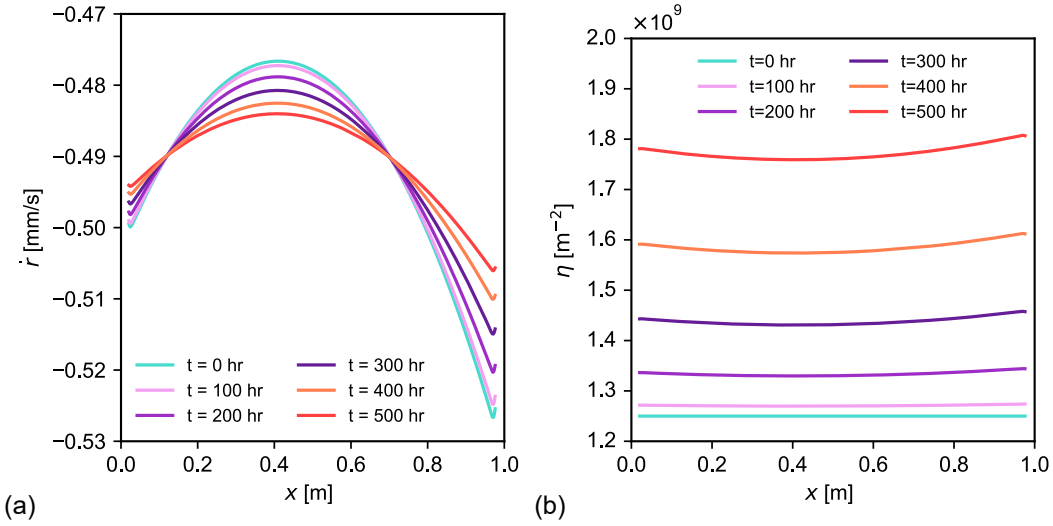

Figure 7.17: (a) Radial velocity and (b) viscous resistance evolution along the candle at $r = 0.02$ m for the axisymmetric quadratic blocking model.

7.5.4 Standard blocking model

The standard model (7.7) was implemented into the axisymmetric CFD model through the workflow described in Subsection 7.3.2. Here, the viscous resistance profile of the porous zone is dependent on radial velocity and the relationship between viscous resistance and radial velocity now follows the form of the standard filter blocking model.

Figure 7.8d shows that the different time steps show matching agreement for pressure drop evolution throughout the pack up to 450 hours. After this, the 5 hour time step model begins to decrease in pressure drop. The model has failed at this point. The reason for this is investigated and discussed in Section 7.8. The 10 hour time stepping model is used for analysis for the rest of this section, with velocity profiles checked to ensure stability up to 500 hours.

Pressure drop across the filter medium can be calculated directly from the standard model, given in (7.11), by substituting ΔP_0 from the initial CFD simulation and $\dot{m}$ as the throughput through the pack. Figure 7.18a shows that pressure drop across the filter medium from direct calculation matches the CFD output. The pressure drop across the pack should also match the output from the constant model as the average viscous resistance calculated from (7.7) at each time step should match the viscous resistance calculated from (7.8). Figure 7.18b shows that this is the case. The standard model has successfully been implemented with a 10 hour time step up to a maximum time of 500 hours.

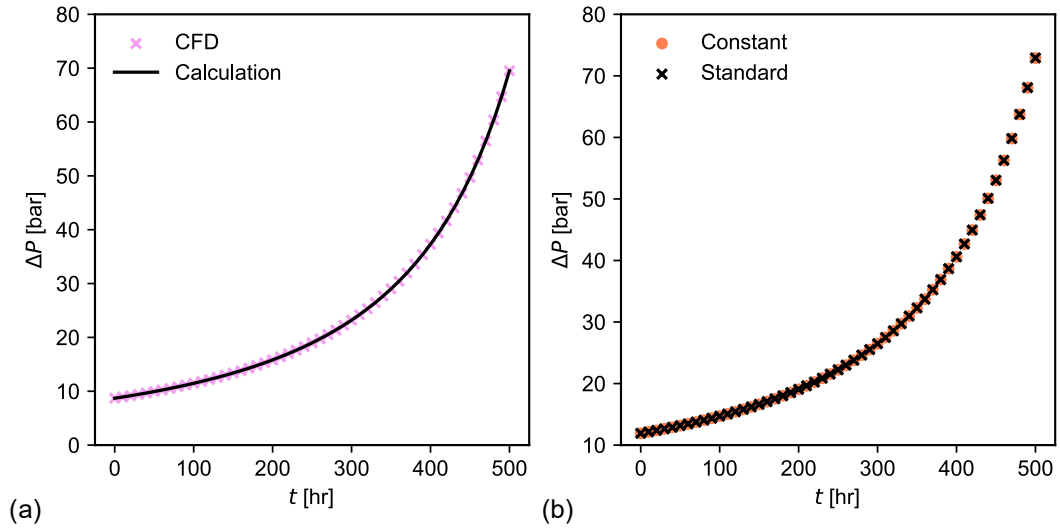

Figure 7.18: (a) Pressure drop across the filter medium against time between the CFD results and a direct calculation from (7.7) for the axisymmetric standard blocking model. (b) Comparison of pressure drop evolution across the pack between the axisymmetric constant and standard blocking models.

Figure 7.19a shows how the radial velocity profile changes over time for the standard blocking model. Again, radial velocity appears to converge towards a uniform 'box' profile, where flow is evenly distributed throughout the filter medium. Figure 7.19b shows how the viscous resistance profile changes over time. Similar trends are clear between the constant model and all the models with dependence on radial velocity, where the flow converges towards a uniform, even distribution through the filter medium. Note that there are pronounced perturbations

forming along the viscous resistance and radial velocity profiles at $t = 500$ hr, which are particularly pronounced at the top and bottom of the candle. Similar to the 5 hr time step, even though the pressure drop across the filter pack is still reasonable, the model has failed at this point. Again, this is discussed in detail in Section 7.8.

Figure 7.20a shows a radial velocity comparison at two quasi-steady time steps between the constant and standard blocking models. Figure 7.20b shows the difference in viscous resistance profiles at $t = 100$ hr. By including radial velocity dependence, it is clear that the process of redistributing flow along the filter medium is accelerated as the local viscous resistance through the filter medium is dependent on radial velocity. Radial velocity dependence accelerates the homogenisation of flow along the filter medium.

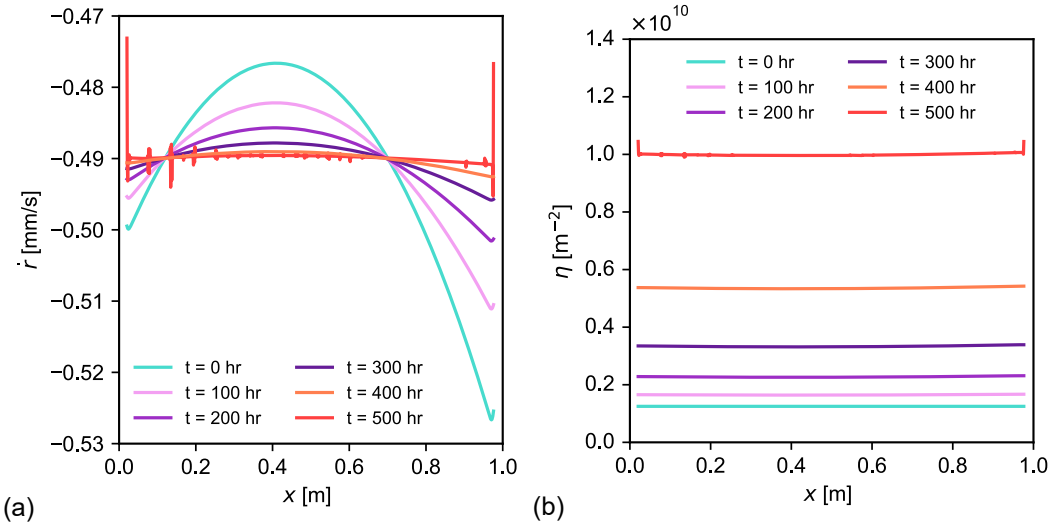

Figure 7.19: (a) Radial velocity and (b) viscous resistance evolution along the candle at $r = 0.02$ m for the axisymmetric standard blocking model.

In summary, all models discussed were implemented successfully and work as expected for the axisymmetric geometry. However, when including viscous resistance dependence on radial velocity, the models appear to break down after a substantial amount of quasi-steady state time steps. This is analysed in detail in Section 7.8.

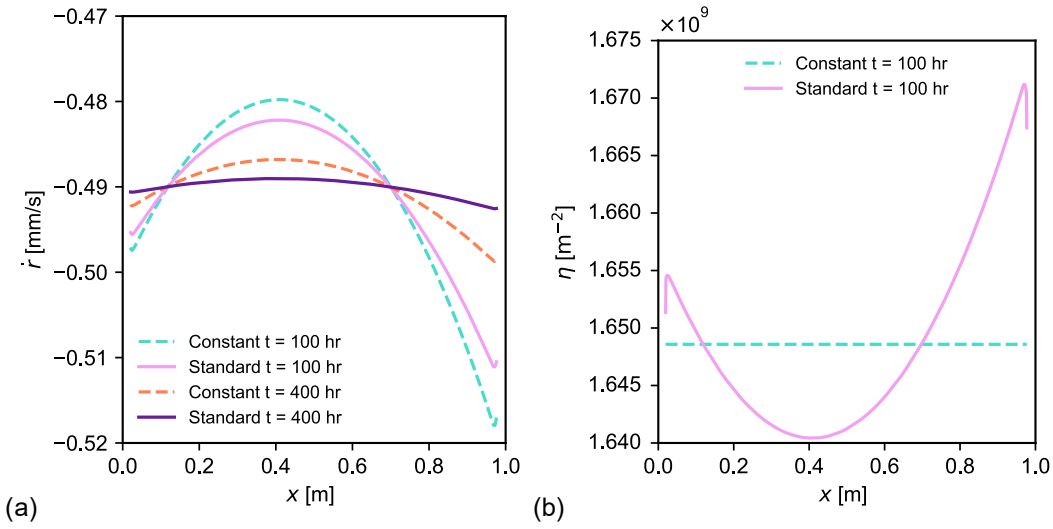

Figure 7.20: (a) Radial velocity at two time steps and (b) viscous resistance at $t = 100$ hr along the candle at $r = 0.02$ m for the axisymmetric standard and constant blocking models.

7.6 Single candle pack blocking evolution

In this section, the blocking models (7.7)-(7.10) are tested with the one-sixth single candle CFD model, described in Section 6.4 and shown in Figure 6.21, to verify that the blocking methodology translates to three dimensions. As the CFD geometry is not axisymmetric in this case, the UDFs must calculate radial coordinates and radial velocity based on Cartesian coordinates. Hence UDFs calculate the radial coordinate from (6.1) and radial velocity from (6.2). For each blocking model, the fitting parameter was assigned as $K_s = 0.0358$. The initial viscous resistance, η_0, was chosen as the viscous resistance of a clean candle filter determined in Section 6.8.

7.6.1 Constant blocking model

The constant model, given by (7.8) was implemented into the single candle CFD model through the workflow described in Subsection 7.3.2. The viscous resistance of the porous zone

does not depend on radial velocity. To match conditions of the single candle CFD model, $\dot{m}$ was chosen to match the inlet mass flow rate.

Figure 7.21a shows the pressure drop across the pack from $t = 0$ hr to $t = 500$ hr for simulations using (7.8) for three different time step sizes. The different time steps show matching agreement for pressure drop evolution throughout the pack. The 10 hour time stepping model is used henceforth. Figure 7.21b shows that pressure drop across the filter medium from direct calculation matches the CFD output. The match is good so the constant blocking model was successfully implemented into the single candle CFD model.

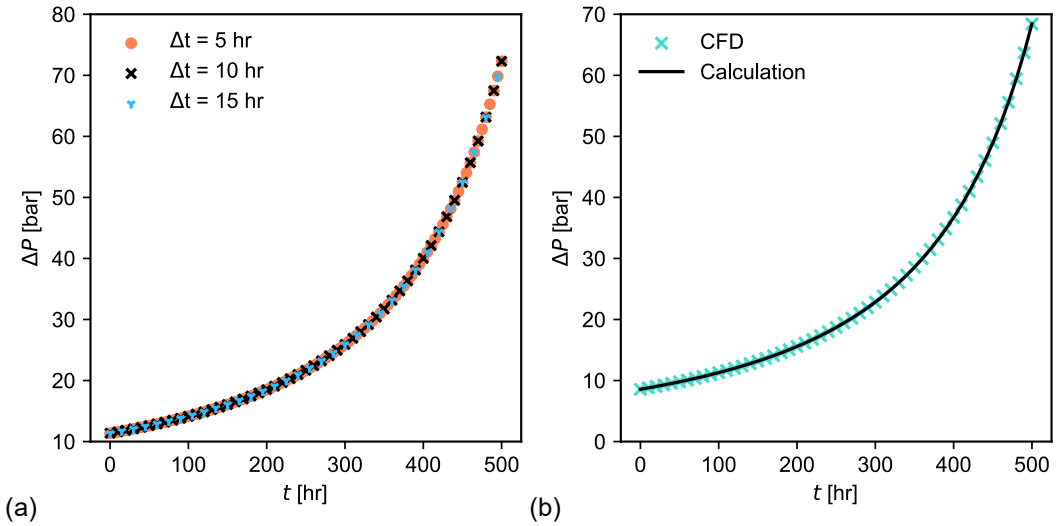

Figure 7.21: (a) Pressure drop evolution across the pack for the single constant blocking model with time steps of 5, 10 and 15 hours. (b) Pressure drop across the filter medium against time between the CFD results and a direct calculation from (7.11) for the single constant blocking model.

Figure 7.22a shows how the radial velocity profile changes over time for the constant blocking model. The radial velocity again appears to converge towards a uniform 'box' profile, where flow is evenly distributed throughout the filter medium. Figure 7.22b shows how the viscous resistance profile changes over time. Due to the form of (7.8), the rate of increase of the viscous resistance grows on each time step.

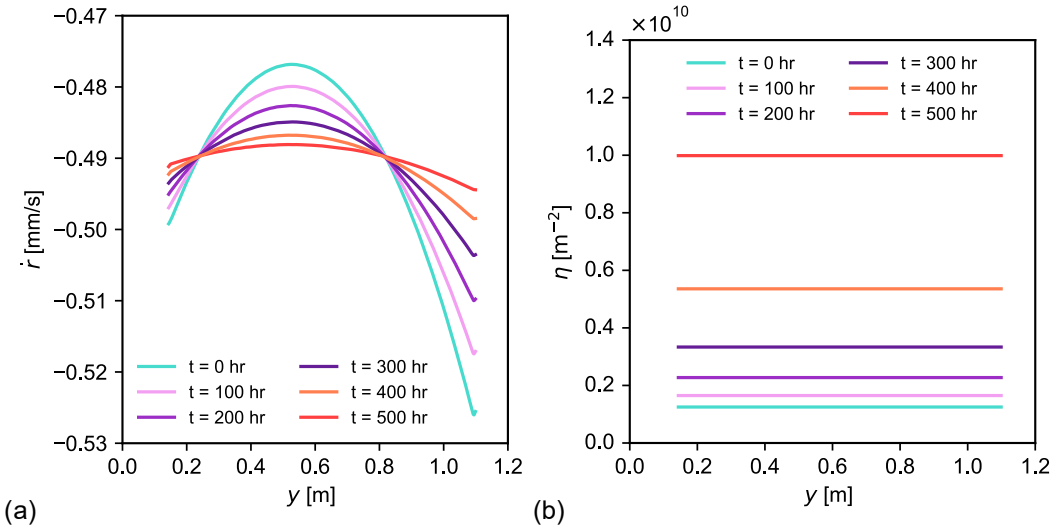

Figure 7.22: (a) Radial velocity and (b) viscous resistance evolution along the candle at $r = 0.02$ m for the single constant blocking model.

7.6.2 Linear blocking model

The linear blocking model, given by (7.9), was implemented into the single candle CFD model through the workflow described in Subsection 7.3.2. The viscous resistance profile of the porous zone is not uniform due to its dependence on radial velocity.

Figure 7.23a shows the pressure drop across the pack from $t = 0$ hr to $t = 500$ hr for simulations using (7.9) for the three different time step sizes. The different time steps show matching agreement for pressure drop evolution across the pack. The 10 hour time stepping model is used henceforth. Figure 7.23b shows an exceptional match between the CFD model and a direct calculation for pressure drop evolution across the filter medium. The linear model, with a coupling between radial velocity and porous zone viscous resistance, has been implemented into the single candle CFD model successfully.

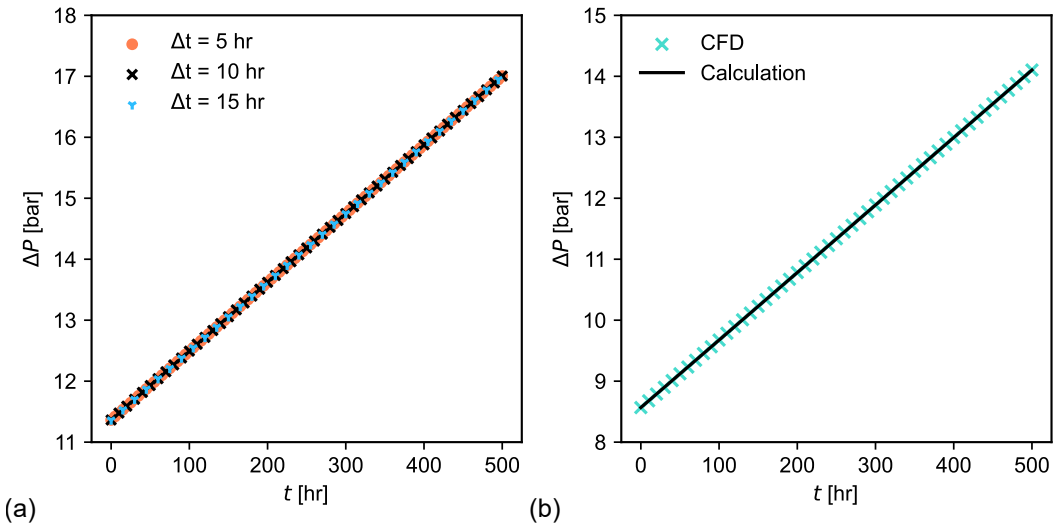

Figure 7.23: (a) Pressure drop evolution across the pack for the single candle linear blocking model with time steps of 5, 10 and 15 hours. (b) Comparison of pressure drop evolution across the filter medium between the CFD results and a direct calculation from (7.12) for the single linear blocking model.

Figure 7.24 shows how the radial velocity and viscous resistance profiles change over time for the linear blocking model. Again, the radial velocity appears to converge towards a uniform 'box' profile, where flow is evenly distributed throughout the filter medium. The viscous resistance increases over time, with increases more pronounced in regions of larger radial velocity magnitude.

The linear blocking model can be compared to the axisymmetric single candle linear blocking model results. Due to the exclusion of the geometry around the spider plate for the axisymmetric model, pressure drop across the pack is larger for the 3D model. Non-dimensionalised pressure drop across the filter medium for each model is compared to eliminate any influence caused by this difference in pressure drop, given by

$$\Delta P^* = \frac{\Delta P}{\Delta P_0}.$$

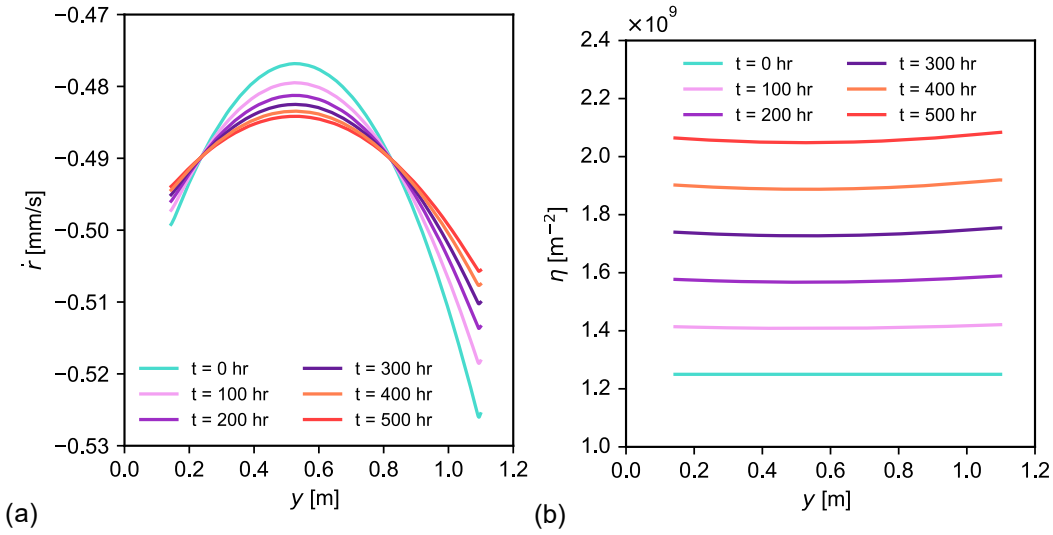

Figure 7.24: (a) Radial velocity and (b) viscous resistance evolution along the candle at $r = 0.02$ m for the single linear blocking model.

Figure 7.25 shows non-dimensionalised pressure drop across the filter medium for each model matches. There has been no change in model functionality when translating the model from a 2D axisymmetric geometry to a 3D geometry.

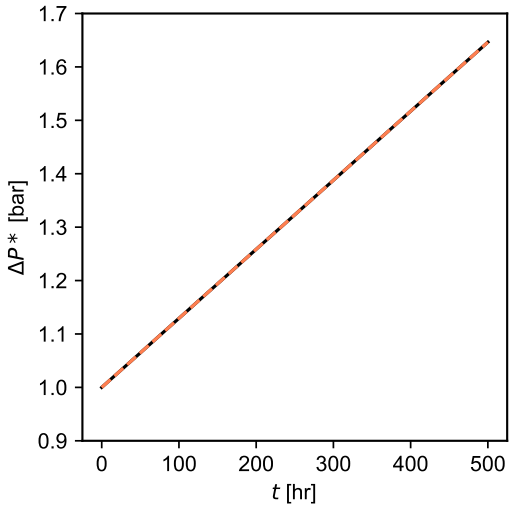

Figure 7.25: Non-dimensional pressure drop evolution across the pack for the single candle and axisymmetric single candle linear blocking model.

7.6.3 Quadratic blocking model

The quadratic model, given by (7.10), was implemented into the single candle CFD model through the workflow described in Subsection 7.3.2. The viscous resistance profile of the porous zone is dependent on radial velocity and the relationship between viscous resistance and radial velocity is now quadratic.

Figure 7.26a shows the pressure drop across the geometry from $t = 0$ hr to $t = 500$ hr for simulations using (7.10) for the three different time step sizes. The different time steps show matching agreement. The 10 hour time stepping model is used for the rest of this section. Figure 7.26b shows an exceptional match between the CFD model and a direct calculation for pressure drop evolution across the filter medium. The quadratic model, with a coupling between radial velocity and porous zone viscous resistance, has been implemented into the single candle CFD model successfully.

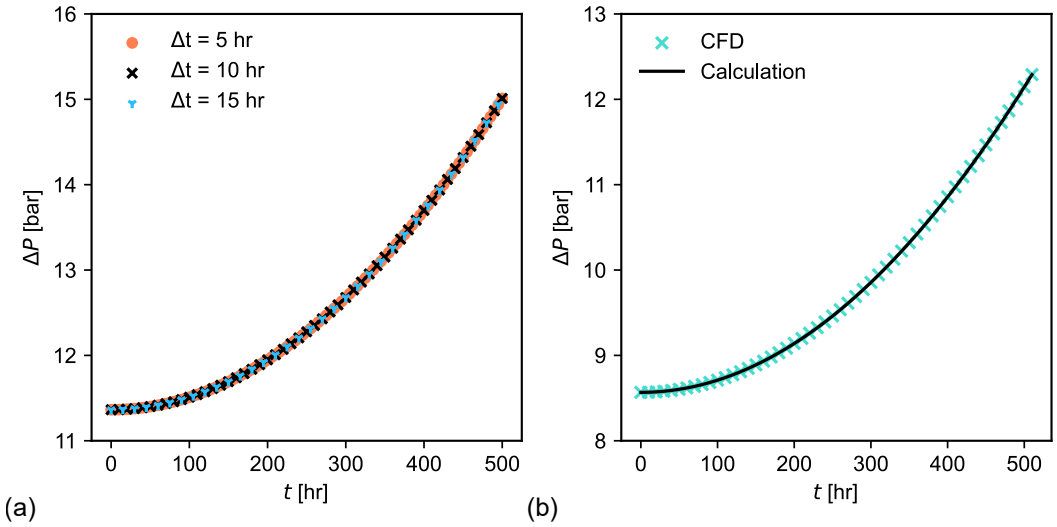

Figure 7.26: (a) Pressure drop evolution across the pack for the single candle quadratic blocking model with time steps of 5, 10 and 15 hours. (b) Comparison of pressure drop evolution across the filter medium between the CFD results and a direct calculation from (7.14) for the single quadratic blocking model.

Figure 7.17a shows how the radial velocity profile along the filter medium changes over time

for the quadratic blocking model. The radial velocity again converges towards a uniform profile, where flow is evenly distributed along the filter medium. Figure 7.17b shows how the viscous resistance profile changes over time.

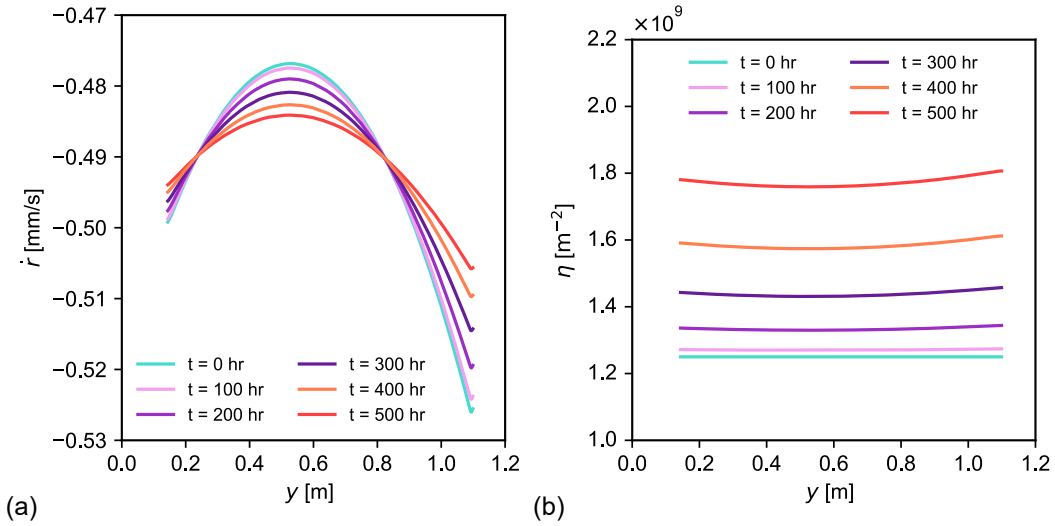

Figure 7.27: (a) Radial velocity and (b) viscous resistance evolution along the candle at $r = 0.02$ m for the single quadratic blocking model.

7.6.4 Standard blocking model

The standard model, given by (7.7), was implemented into the single candle CFD model through the workflow described in Section 7.3.2. The relationship between viscous resistance and radial velocity follows the form of the standard filter blocking model.

Figure 7.28 shows the pressure drop across the geometry from $t = 0$ hr to $t = 500$ hr for simulations using (7.7) for the three different time step sizes. The different time steps show matching agreement for pressure drop evolution throughout the pack up to 440 hours. After this, the 5 hour time step model begins to decrease in pressure drop. Similarly to the axisymmetric standard model, the model has failed at this point. The 10 hour time step also fails before the 500 hour mark. The reason for this is investigated, discussed and compared with the axisymmetric model in Section 7.8. The 10 hour time stepping model is used for the rest

of this section. Figure 7.28b shows that pressure drop across the filter medium from direct calculation matches the CFD output. The standard model has successfully been implemented with a 10 hour time step up to a maximum time of 450 hours, where pressure output for the 10 hour time step is stable.

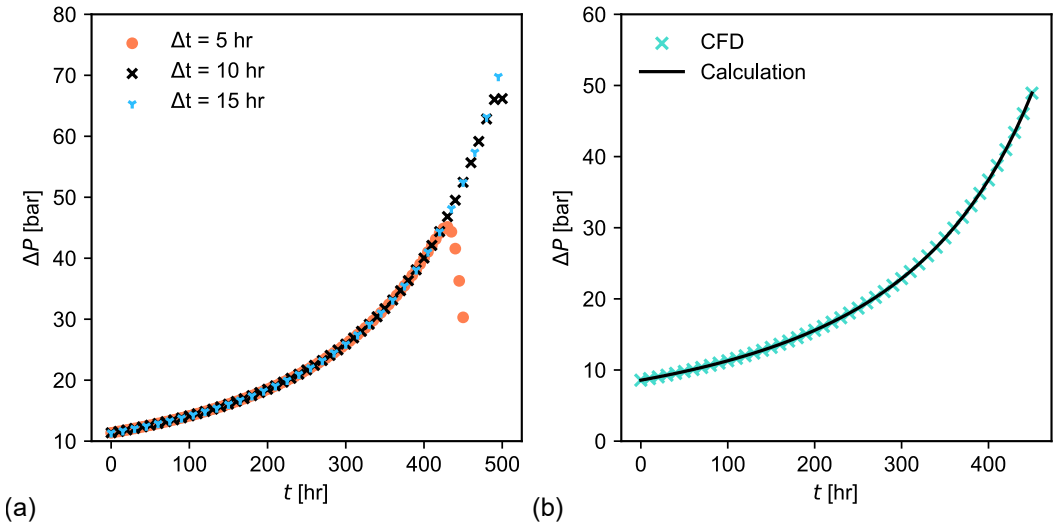

Figure 7.28: (a) Pressure drop evolution across the pack for the single candle standard blocking model with time steps of 5, 10 and 15 hours. (b) Comparison of pressure drop evolution across the filter medium between the CFD results and a direct calculation from (7.11) for the single standard blocking model.

Figure 7.29a shows how the radial velocity profile along the filter medium changes over time for the standard blocking model. The radial velocity again converges towards a uniform profile, where flow is evenly distributed along the filter medium. Figure 7.29b shows how the viscous resistance profile changes over time. The model is on the precipice of breaking at 450 hours, which is seen in the local variations along the radial velocity profile at this time.

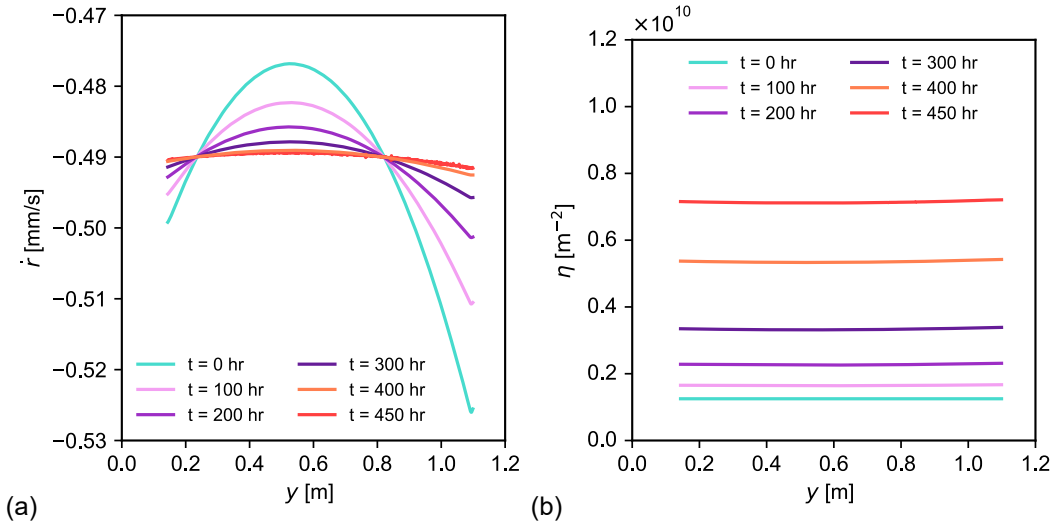

Figure 7.29: (a) Radial velocity and (a) viscous resistance evolution along the candle at $r = 0.02$ m for the single standard blocking model.

Figure 7.30 shows contours of velocity magnitude through the spider plate at 0 and 400 hours. Qualitatively, there is negligible difference between the flow. Figure 7.31 shows the radial velocity at 0 and 400 hours along two lines of constant r highlighted in Figure 7.30. There is no discernible difference in the radial velocity along the lines; filter blocking has negligible influence on the flow around and upstream of the spider plate.

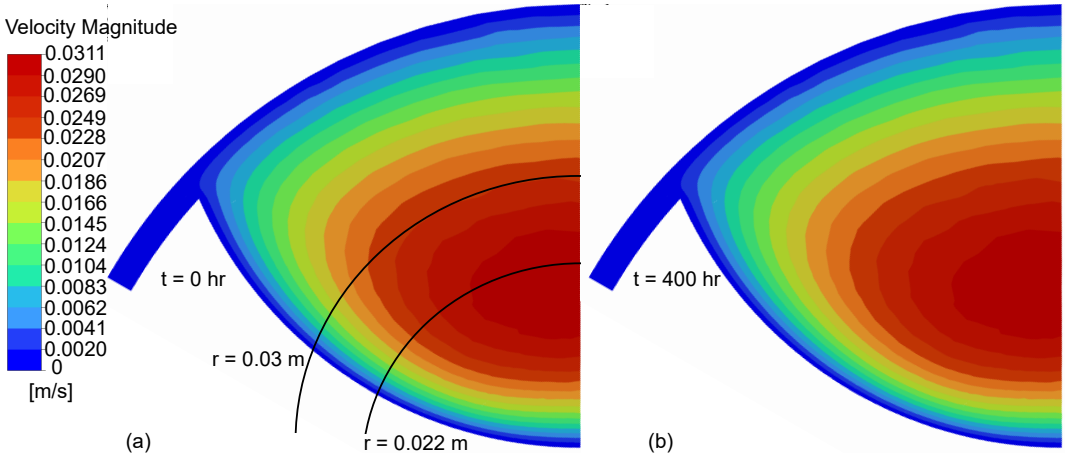

Figure 7.30: Contours of velocity magnitude on a plane that cuts through the spider plate for the single candle standard blocking model at (a) 0 hours and (b) 400 hours.

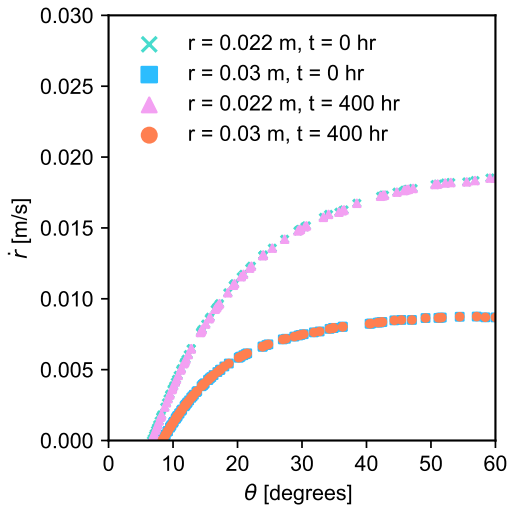

Figure 7.31: Radial velocity along the lines $r = 0.022$ m and $r = 0.03$ m at $t = 0$ and $t = 400$ hours on a plane that cuts through the spider plate for the single candle standard blocking model.

Figure 7.32 shows contours of velocity magnitude through a plane that cuts through the middle section of the candle filter at 0 and 400 hours. Flow patterns are structurally identical at each time. However, velocity magnitude is larger through the plane at 400 hours. From Figure 7.29, this is expected as the radial velocity through the middle of the candle filter has increased as the viscous resistance is lower compared to the bottom and top of the candle. Flow patterns do not change structurally as the flow is axisymmetric around the filter medium.

In summary, over time, flow through the candle filter in the single candle filter pack converges towards a uniform distribution. Hence, after enough time has passed, flow is evenly distributed along and around the candle filter in the pack. Due to the axisymmetric nature of the flow through and around the filter medium, no significant changes in flow patterns are seen over the course of a run. The filter medium regions near the top and bottom of the candle will see more fouling over the course of a run due to the proportion of throughput that these regions see. Filter blocking has no discernible influence on flow patterns around and upstream of the spider plate and has negligible influence on flow patterns downstream of the central core.

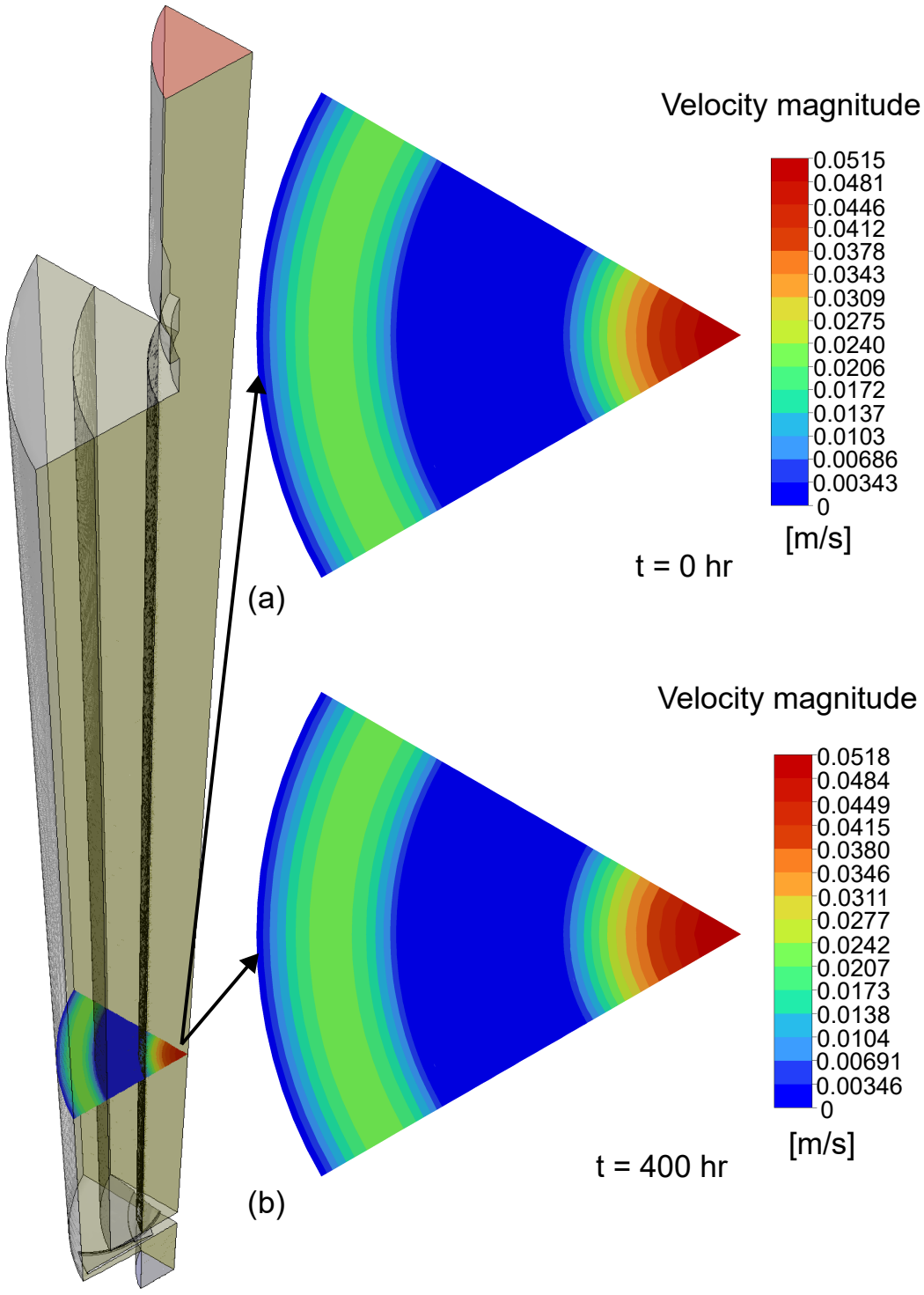

Figure 7.32: Contours of velocity magnitude for the single candle standard blocking model at $y = 0.45$ m for (a) 0 hours and (b) 400 hours.

7.7 Seven candle pack blocking evolution

For the seven candle filter pack, only the standard blocking model is considered. This is because work in Sections 7.5 and 7.6 showed that the standard model has been successfully implemented into the CFD models regardless of dimensions up to the stability issue. Results are then compared to the standard model fitted to the data given in Section 7.1. To this end, fluid properties, flow rate and the fitting parameter are chosen to match seven candle pack runs.

The one-twelfth seven candle filter pack CFD model, detailed in Section 6.7 and shown in Figure 6.21, was used. The inlet mass flow rate and fluid properties were chosen to match the runs that are given in Table 6.4. The fitting parameter was assigned as $K_s = 0.038$, matching the fitting parameter found for the standard model fitted to the run data. The initial viscous resistance, η_0, was again chosen as the viscous resistance of a clean candle filter determined in Section 6.8.

In the one-twelfth geometry, there are two candles, one-twelfth of the central candle and half of an outer candle. Therefore, there are two porous zones, and the standard model must be specified for each candle filter. For the central candle, the standard model is given by

$$\eta_c = \eta_0 \left(1 - K_s \pi r_c h \rho \dot{r}_c t\right)^{-2}, \tag{7.15}$$

where η_c is the viscous resistance through the central candle, r_c is the radial position relative to the origin and $\dot{r}_c$ is the radial velocity relative to the origin. For the outer candle, the standard model assigned is given by

$$\eta_o = \eta_0 \left(1 - K_s \pi r_o h \rho \dot{r}_o t\right)^{-2}, \tag{7.16}$$

where η_o is the viscous resistance through the outer candle, r_o is the radial position relative to the centre of the outer candle and $\dot{r}_o$ is the radial velocity relative to the centre of the outer candle.

The quasi-steady state simulations must be independent of time step size. To show this, three time step sizes were chosen: 5, 10 and 15 hours. A maximum time of 250 hours was chosen, which exceeds the maximum time of the averaged run data. Figure 7.33 shows the pressure drop across the pack from t = 0 hr to t = 250 hr for simulations using (7.15)-(7.16) for the three different time step sizes. The different time steps show matching agreement for pressure drop evolution across the pack. The 10 hour time stepping model is used henceforth.

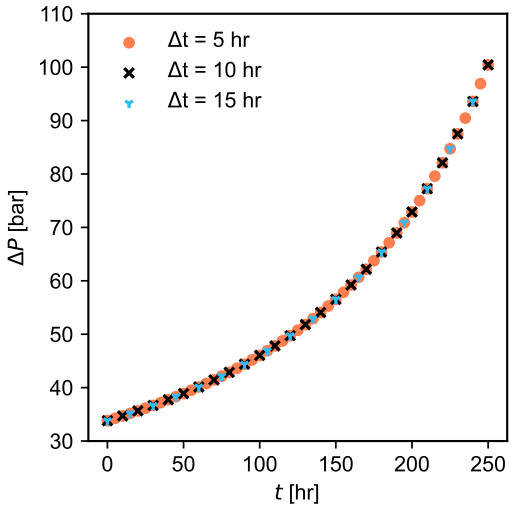

Figure 7.33: Pressure drop evolution across the pack for the seven candle standard blocking model with time steps of 5, 10 and 15 hours.

Figure 7.34 shows a comparison between the CFD average pressure drop across the filter medium, calculated by averaging the pressure drop across the central and outer filter medium, and the standard model fit to run data given in Figure 7.2. The match is exceptional suggesting that the standard blocking model has successfully been implemented into the seven candle filter pack CFD model. The blocking model is used to offer insight into flow behaviour inside the seven candle filter pack over time.

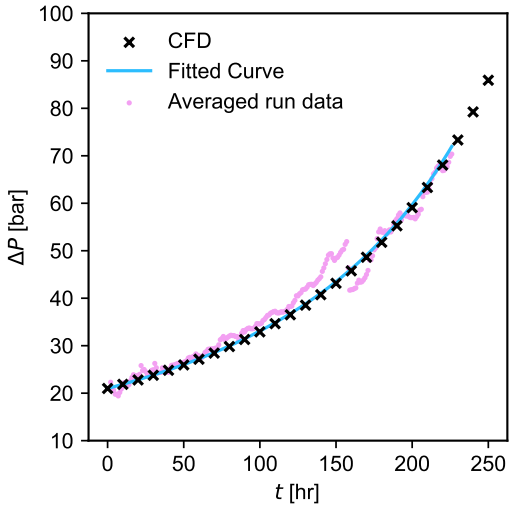

Figure 7.34: Averaged pressure drop evolution across a filter medium inside the seven candle standard blocking model compared to the standard model curve fitted to the run data in Section 7.1.

By summing the total mass flow rate through the whole central candle and the whole outer candle, the percentage split of this through both candles can be calculated and the distribution of melt flow between candles in the pack can be assessed at a given time. Due to the symmetry of the pack, an even split of 50% of this total indicates that the melt is evenly distributed between all candles in the pack. Initially, the percentage split of the total mass flow rate for the central candle is 51.26%. At 250 hours, the percentage split for the central candle is 50.12%. Figure 7.35 shows the mass flow rate through the central and outer candles over time. As discussed in Section 6.10, initially, the central candle sees a larger proportion of pack throughput due to the resistance imposed on the flow through the outer candle by the outlet section. Over time, mass flow rate through the central candle decreases and mass flow rate through the outer candle increases. Both appear to be converging towards an even proportion of flow through each candle. As the central candle sees more flow, the average viscous resistance through it will increase at a faster rate compared to the outer candle. The flow will redistribute in response to this.

Table 7.5 estimates the total throughput that the central candle and an outer candle have seen

after 250 hours. This is calculated by multiplying the mass flow rate at each point in Figure 7.35 by ten (due to the 10 hour time step size) and summing. There is a 2.17% difference in cumulative throughput between each candle filter after 250 hours.

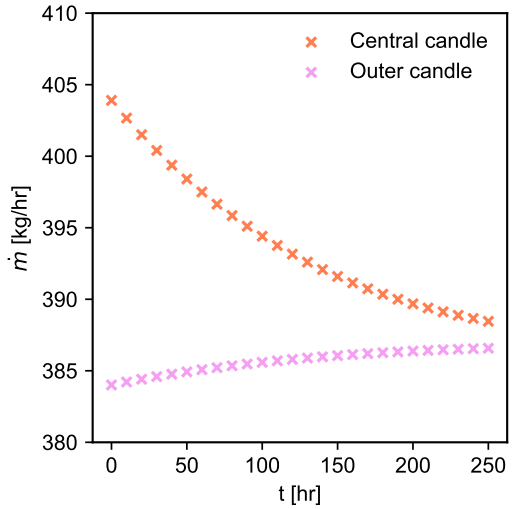

Figure 7.35: Mass flow rate through the central and outer candles over time for the seven candle standard blocking model.

Table 7.5: Cumulative melt throughput for each candle after 250 hours for the seven candle standard blocking model.

	Total throughput [kg]
Central candle	102450
Outer candle	100270

Figure 7.36 shows the central and outer radial velocity through a line along the central and outer candle respectively. As with the single and axisymmetric models, the flow appears to be converging towards a uniform 'box' profile along the candle filters. Furthermore, the central radial velocity is decreasing in magnitude. Table 7.6 shows the mean central and outer radial velocity initially and at 250 hours for the central and outer candles respectively. The mean central radial velocity has decreased significantly compared to a slight increase in mean outer radial velocity. As the distribution of melt flow between candle filters homogenises, the mass

flow rate through the central candle redistributes through the six outer candles, significantly reducing the central radial velocity along the central candle, while slightly increasing outer radial velocity along each outer candle.

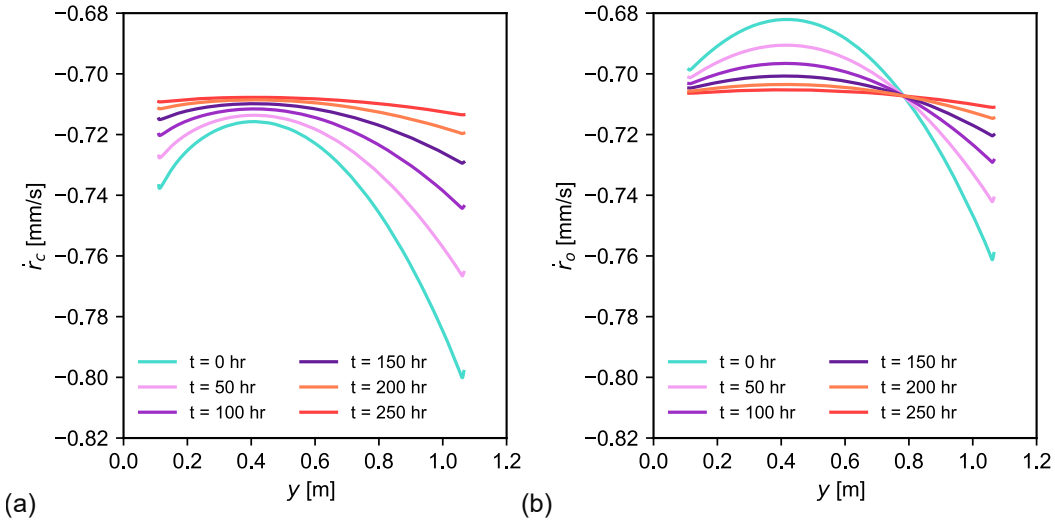

Figure 7.36: (a) Central radial velocity and (b) outer radial velocity evolution for the seven candle standard blocking model along the central and outer candle at a point along $r_c = 0.018$ m and $r_o = 0.018$ m respectively.

Table 7.6: Mean central and outer radial velocity for the profiles in Figure 7.36 initially and after 250 hours.

Time [hr]	$\bar{\dot{r}}_c$ [mm/s]	$\bar{\dot{r}}_o$ [mm/s]
0	-0.737	-0.702
250	-0.709	-0.707

Figure 7.37 shows the central and outer viscous resistance profiles along the same line along each candle filter. The mean viscous resistance through the central candle is 0.89% larger than through the outer candle after 250 hours. This is because the central candle has seen a greater throughput, leading to more blocking, resulting in a larger resistance to the flow.

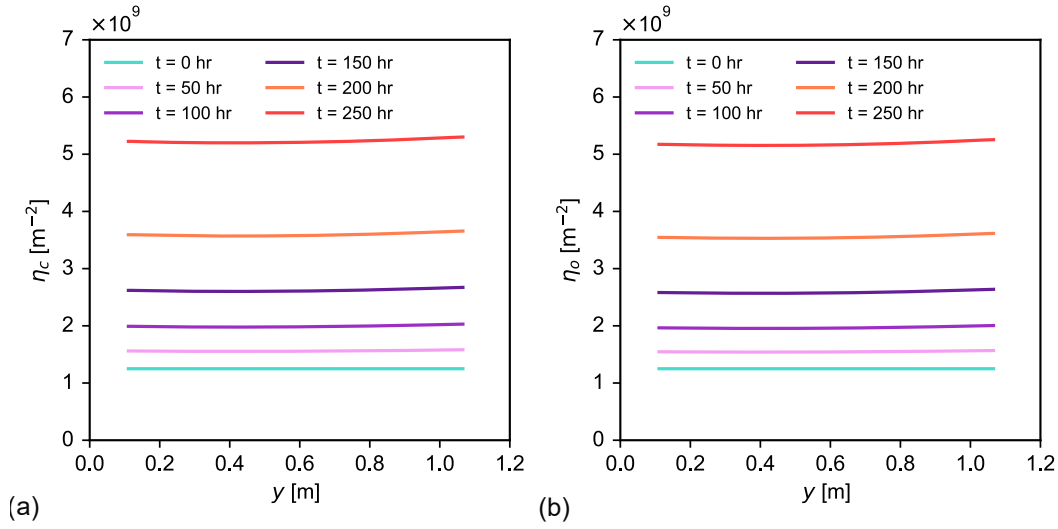

Figure 7.37: (a) Central viscous resistance and (b) outer viscous resistance evolution for the seven candle standard blocking model along the central and outer candle at a point along $r_c = 0.018$ m and $r_o = 0.018$ m respectively.

As shown in Figure 6.32 in Section 6.10, flow is not considered locally axisymmetric around the outer candle. Figure 7.38 shows the radial central evolution and outer velocity evolution around constant r_c and r_o respectively on the plane $y = 0.45$ m. The magnitude of central radial velocity has decreased around the central filter and the magnitude of the outer radial velocity has increased around the outer filter. Table 7.7 shows the range of central and outer radial velocity for the plots in Figure 7.38 for the 0 hour and 250 hour time step. There is little change in radial velocity profiles around the candle filters on this plane. It does not appear that the blocking model is homogenising flow around the outer filter.

Table 7.7: Range of $\dot{r}_c$ and $\dot{r}_o$ at $t = 0$ hr and $t = 250$ hr around $r_c = 0.018$ m and $r_o = 0.018$ m on the plane $y = 0.45$ m for the seven candle standard blocking model.

	Time [hr]	Range [m/s]
$\dot{r}_c$	0	2.32×10^{-7}
	250	1.07×10^{-7}
$\dot{r}_o$	0	2.07×10^{-5}
	250	2.00×10^{-5}

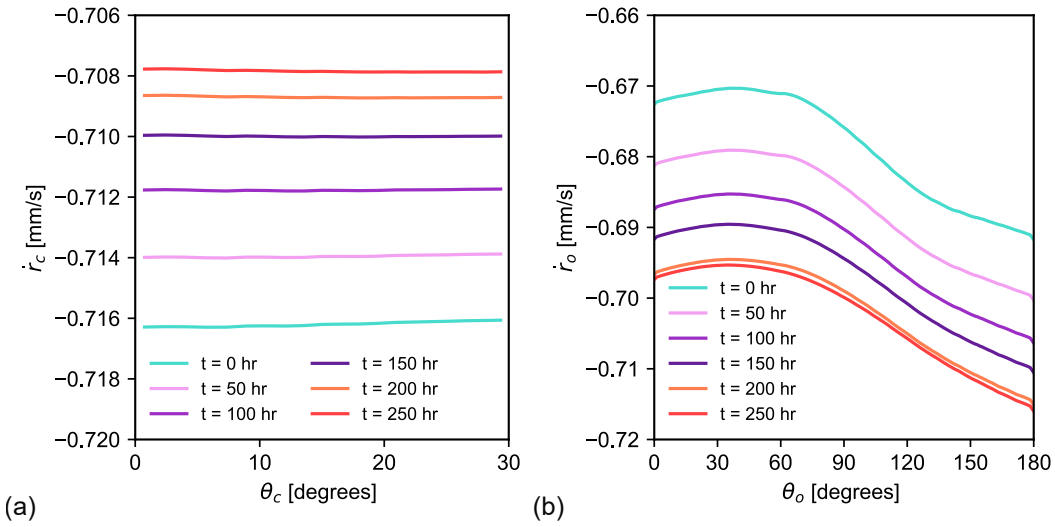

Figure 7.38: (a) Central radial velocity and (b) outer radial velocity evolution for the seven candle standard blocking model around the central and outer candle on the plane $y = 0.45$ m at $r_c = 0.018$ m and $r_o = 0.018$ m respectively.

As time advances and the candle filters block, flow between and along candle filters in the seven candle filter pack homogenize. Figure 7.39 shows contours of velocity magnitude through the spider plate at 0 and 250 hours. There is no qualitative difference in the two contours plots at the spider plate over the course of blocking model simulations. Figure 7.40 show radial velocity profiles along lines of constant r highlighted in Figure 7.39a. There is no discernible difference in radial velocity along the lines; filter blocking has negligible influence on the flow around and upstream of the spider plate.

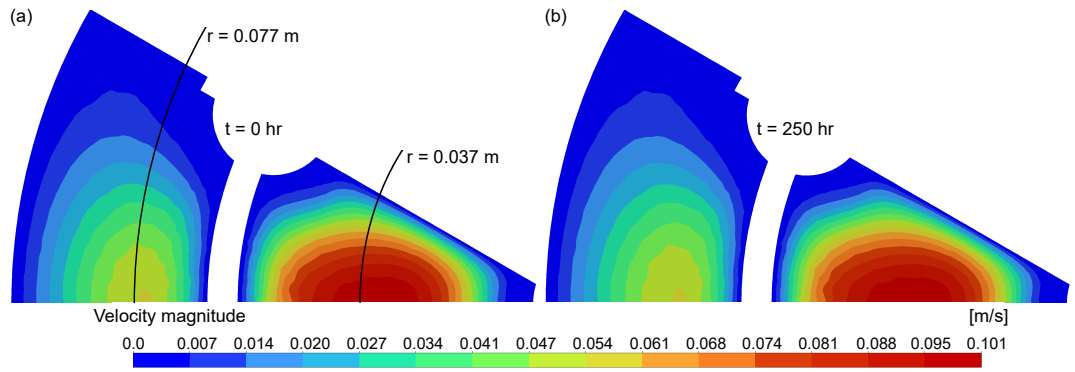

Figure 7.39: Contours of velocity magnitude on a plane that cuts through the spider plate for the seven candle standard blocking model at (a) 0 hours and (b) 250 hours.

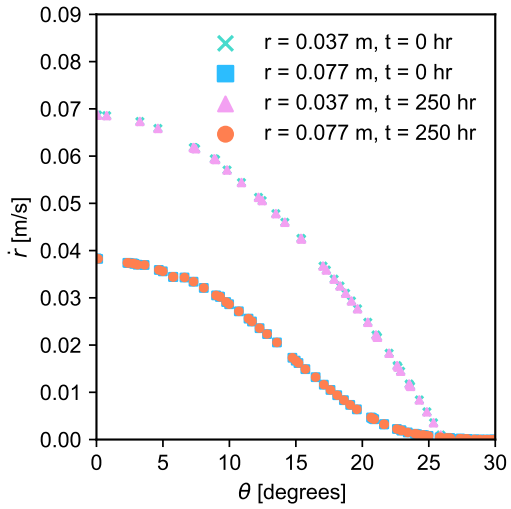

Figure 7.40: Radial velocity along the lines $r = 0.037$ m and $r = 0.077$ m, highlighted in Figure 7.39, at $t = 0$ and $t = 250$ hours.

Figure 7.41 shows contours and vectors of velocity magnitude through a plane that cuts through the middle section of the seven candle filter pack at 0 and 250 hours. Flow patterns are structurally similar at each time. However, velocity magnitude is smaller through the core of the central candle at 250 hours. From Figure 7.36, this is expected as the central radial velocity through the core of the central candle filter has decreased as the flow between candles has homogenised. Flow patterns do not change significantly as there was little change

to radial velocity profiles around each candle filter.

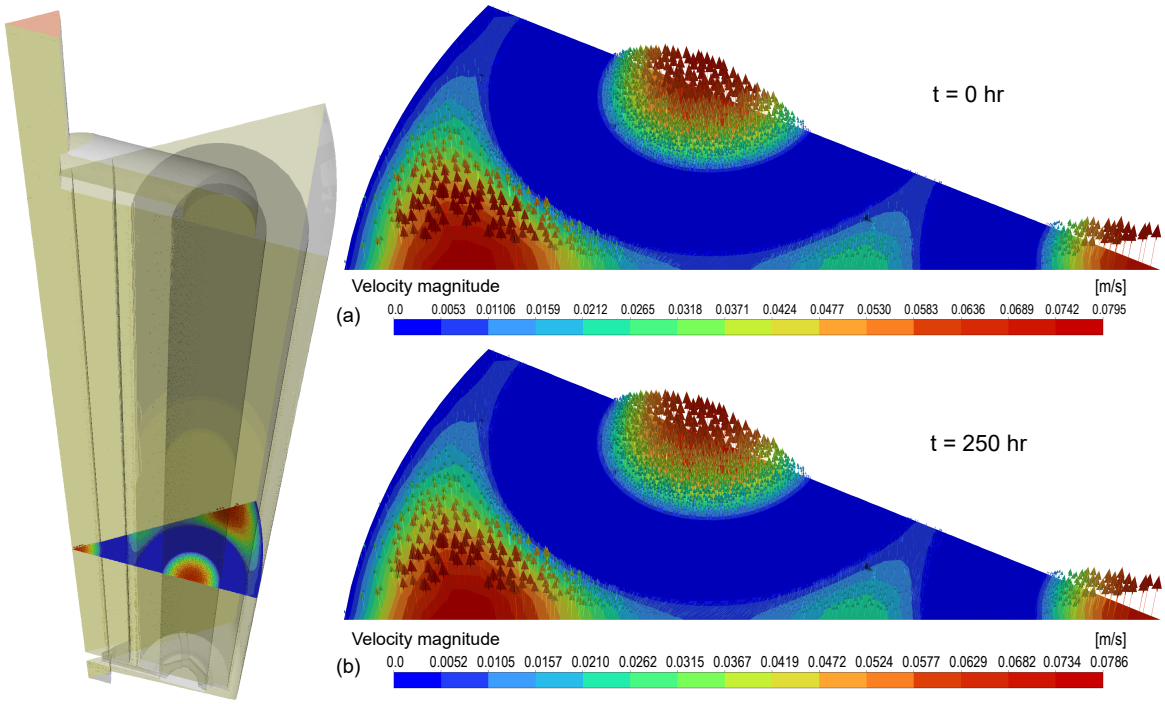

Figure 7.41: Contours and vectors of velocity magnitude for the seven candle standard blocking model at $y = 0.45$ m at (a) 0 hours and (b) 250 hours.

In summary, the standard blocking model has been successfully implemented into the seven candle filter pack CFD model, with results remaining stable beyond the maximum time of the averaged run data. As time advances, flow between and along candle filters in the pack homogenise. Flow around the outer candle filter does not appear to homogenise as time advances.

7.8 Blocking evolution model limitations

Figure **??** shows that the pressure drop across the pack decreases for the 5 hour time step axisymmetric standard blocking model after around 450 hours. The pressure should not decrease, and this deviates from the pressure drop across the pack for the 10 and 15 hour time

step. Furthermore, Figure 7.19 shows unusual behaviour for the viscous resistance and radial velocity profiles along the candle with a 10 hour time step at 500 hours. The pressure drop output is still reasonable at this time. Figure 7.42 shows the pressure evolution continued up to a maximum time of 600 hours for the 10 hour axisymmetric standard and constant blocking model simulations. The standard pressure drop begins to deviate from the constant pressure drop and decreases shortly beyond 500 hours; the standard model has failed. The constant model remains stable. This is because the viscous resistance profile does not depend on radial velocity.

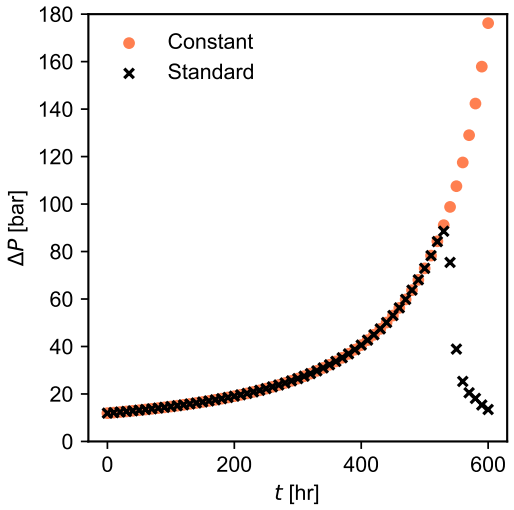

Figure 7.42: Pressure drop evolution across the pack for the axisymmetric standard and constant blocking models with a time step size of 10 hours and a maximum time of 600 hours.

Figure 7.43 shows radial velocity profiles at $r = 0.02$ m along the candle between 430-480 hours for the standard model. The radial velocity profile is smooth and reasonable up to 440 hours. At 450 hours, the profile has changed at the bottom and the top of the filter medium; the radial velocity appears to suddenly increase in magnitude next to the walls of the pack. Slight local variations in radial velocity also begin to emerge over the length of the candle. At 460 hours, variations in local velocity appear to get slightly larger. Beyond this point, perturbations emerge and grow, particularly at the top and bottom of the filter medium. Figure 7.44 shows viscous resistance along the same line at the same time steps. It follows

similar profile changes compared to the radial velocity but remains stable at 450 hours. The profile changes at 460 hours. This delay is because the viscous resistance profile calculated at 460 hours is calculated using the radial velocity profile at 450 hours.

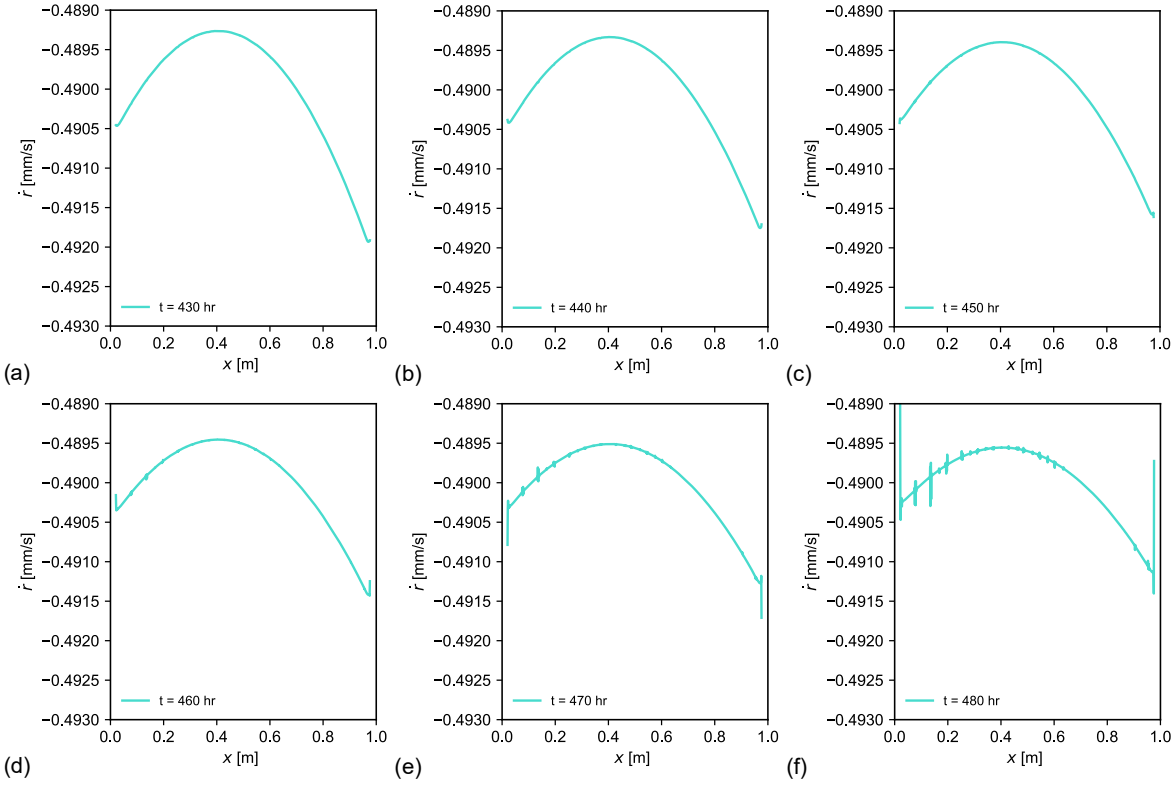

Figure 7.43: Radial velocity between 430 and 480 hours along the candle at $r = 0.02$ m for the axisymmetric standard blocking model.

Perturbations along the candle in viscous resistance and radial velocity have emerged around 450 hours into the simulations and increase on each time step. Perturbations are particularly large near the top and the bottom of the candle. Once perturbations emerge, the model will break. Perturbations also emerge at a later time compared to the 5 hour model, hence why the pressure drop across the pack deviates from the constant model at a later time.

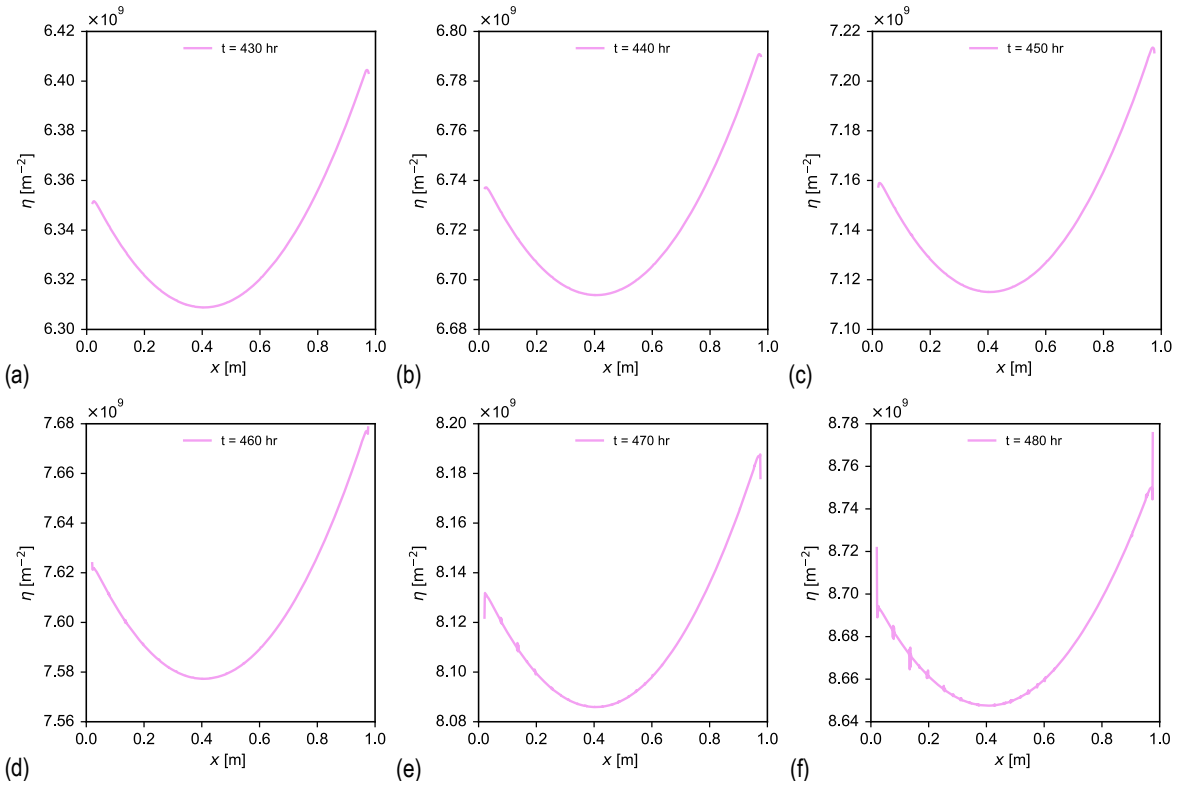

Figure 7.44: Viscous resistance between 430 and 480 hours along the candle at $r = 0.02$ m for the axisymmetric standard blocking model.

There are two factors which cause these blocking models to break. The first factor comes from the standard model behaviour at large times. The viscous resistance in the filter medium is updated on each quasi-steady state time step according to

$$\eta = \eta_0 \left(1 - K_s \pi r h \rho \dot{r} t\right)^{-2} . \tag{7.17}$$

A singularity is present in the standard model as $K_s \pi r h \rho \dot{r} t \to 1$. For the constant model, given in (7.8), as $0.5 K_s \dot{m} t \to 1$, $\eta \to \infty$. For the values specified in the axisymmetric constant model, the singularity occurs as $t \to 774$ hr. Figure 7.45 shows pressure drop across the filter medium calculated from (7.11). Beyond the singularity, pressure drop across the filter medium is reflected across the line $t = t_s$, where $t_s = 774$ hr is the time where the singularity occurs.

This is obviously an unphysical representation of filter blocking and the standard model should only be used to predict pressure drop up to a time $t_{\max}$ such that $t_{\max} \ll t_s$.

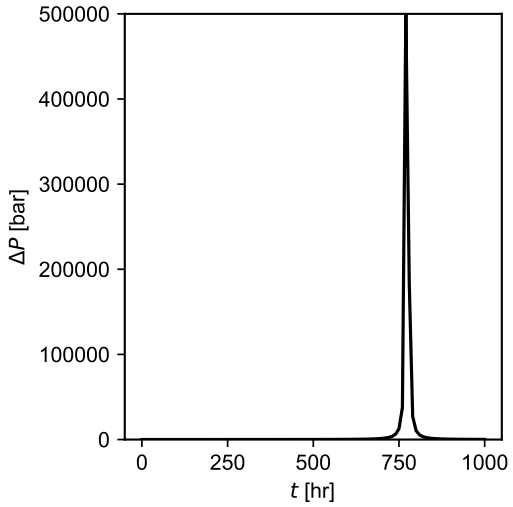

Figure 7.45: Pressure drop evolution across a filter medium from a direct calculation of the constant model using (7.11).

For the standard model, where the local viscous resistance depends on local radial velocity as well as time, as $K_s \pi r h \rho \dot{r} t \to 1$, $\eta \to \infty$. Hence, a significant spike in local radial velocity could result in the model breaking due to a local η approaching the singularity before t_s. However, the model breaks after around 450 hours, significantly before t_s. Figure 7.43c shows that there is little difference in radial velocity along the filter at this time. Although radial velocity along the filter medium is only plotted for a single radius, due to conservation of mass, as r decreases, the mass flow through r in the porous zone must remain constant. Hence the mean of $r\dot{r}$ remains constant. For the maximum radial velocity along the filter medium, $K_s \pi r h \rho \dot{r} t = 0.58$.

As t increases, the average value of the difference in viscous resistance at each time step increases. After enough time has passed, there are significantly larger changes to the viscous resistance upon each time step. Locally, between two successive nodes in the mesh, this means that small differences in radial velocity lead to more significant variations in viscous resistance

at later times. Once a local variation in radial velocity is established, at the next time step, the viscous resistance profile is recalculated, accentuating the local variation in its profile. This process continues, as local variations in the radial velocity profile accentuate local variations in the viscous resistance profile, which, in turn, further accentuate local variations in the radial velocity, all while the difference in local viscous resistance is further accentuated by increasing time. This continues as local perturbations in viscous resistance and radial velocity continue to grow until the model breaks.

This instability at large times is also present in the quadratic model, given by (7.10), with a larger K_s choice than in Subsection 7.5.3. Figure 7.46 shows pressure drop evolution for the quadratic model with $K_s = 0.2$ and a 10 hour time step. The model has become unstable around 550 hours and failed. This is reflected in Figure 7.47, where again perturbations have formed and caused the model to fail. This suggests that instability is not caused by the singularity in the standard model.

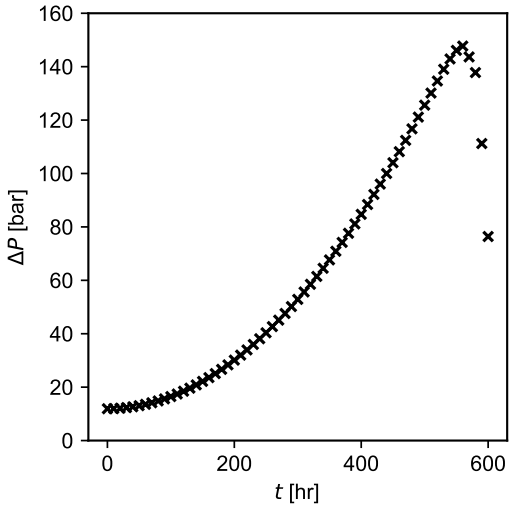

Figure 7.46: Pressure drop evolution across the axisymmetric quadratic blocking model with $K_s = 0.2$.

Perturbations are particularly pronounced at the ends of the filter medium. This is because of the walls at the top and the bottom of the porous zone. Local extrema are present in

both radial velocity and viscous resistance profiles near the walls. The magnitude of radial velocity must then decrease to a value of zero at the walls due to no-slip. Such a large gradient in profiles near the walls then results in large differences between local radial velocity along successive nodes in this region, resulting in the pronounced perturbations on each time step at large times.

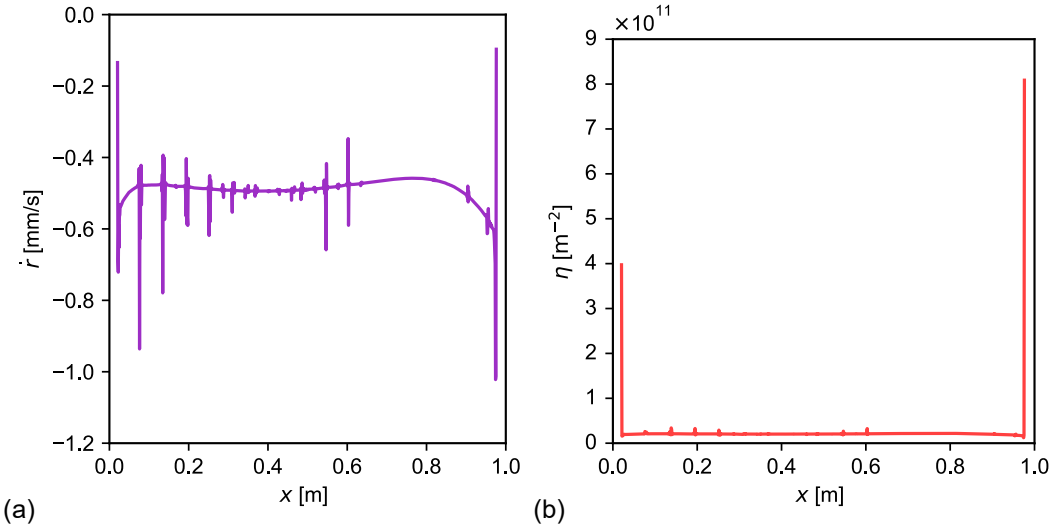

Figure 7.47: (a) Radial velocity and (b) viscous resistance at 550 hours along the candle at $r = 0.02$ m for the axisymmetric quadratic blocking model with $K_s = 0.2$.

The second factor is the time step size. Figure 7.48 shows that the perturbations begin at an earlier time, around 400 hours compared to 450 hours, for the 5 hour time step case compared to the 10 hour time step. An unphysical decrease in pressure can also be seen to happen at lower times with decreasing time step size in Figure 7.49a. A smaller time step size means more quasi-steady state simulations compared to a larger time step size up to the same maximum time. This means that the viscous resistance and radial velocity profiles are recalculated more often compared to a larger time step size. For two successive nodes in the mesh, small variations are updated at a more frequent rate, further accentuating the growth of perturbations in the viscous resistance and radial velocity profiles, breaking the model at an earlier time. Figure 7.49b shows the relationship between time step size and the point in time which the pressure drop across the pack begins to decrease. This shows that the point

at which the model begins to break continues to decrease as time step size decreases.

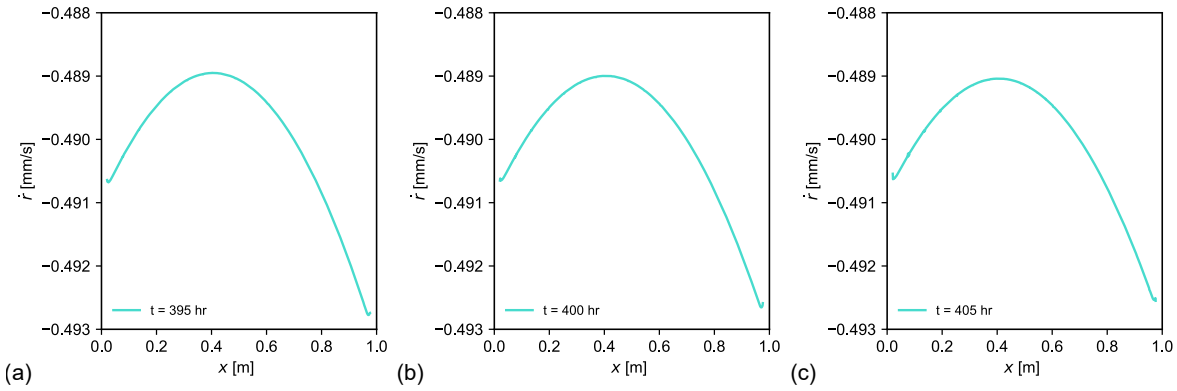

Figure 7.48: Radial velocity between 395 and 410 hours along the candle at $r = 0.02$ m for the axisymmetric standard blocking model with a time step size of 5 hours.

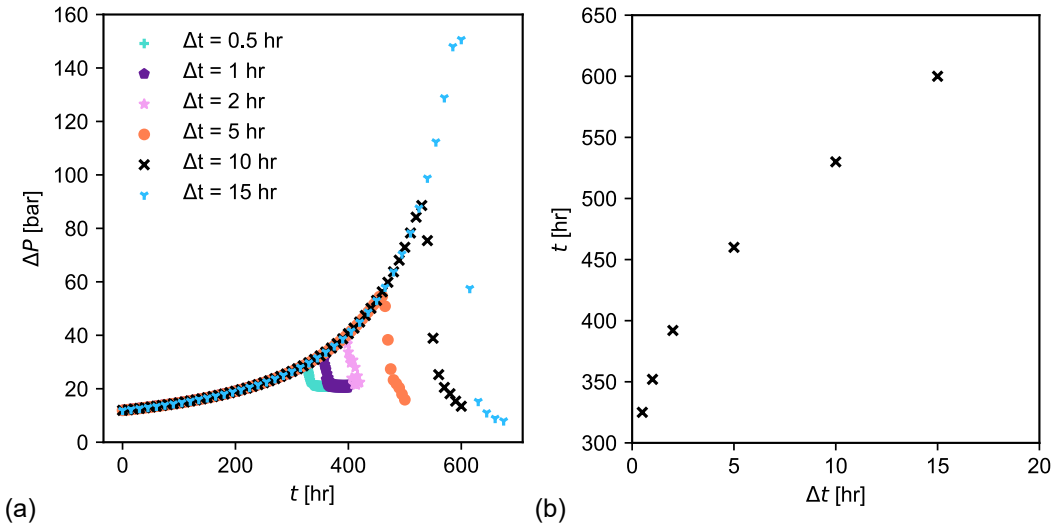

Figure 7.49: (a) Pressure drop evolution for the axisymmetric standard model for several time steps. (b) The point at which the pressure drop across the pack begins to decrease for each time step size.

For the single candle blocking models, similar behaviour is observed. Figure 7.50 shows radial velocity on a line inside the filter along the candle for the standard blocking model with a 10 hour time step. Local perturbations become noticeable at 430 hours, only one time step before they emerge in the axisymmetric standard model. The local perturbations are more common

and pronounced compared to the axisymmetric model at the same time, which results in the radial velocity profile becoming more erratic over less time. Figure 7.51 shows a similar trend with the viscous resistance. This results in pressure drop across the pack breaking earlier than the axisymmetric case, before 500 hours, as seen in Figure 7.28. This is because of the mesh. As the 3D mesh is less dense and structured than the axisymmetric model due to computational expense, node position is less consistent and local variations in radial velocity in the filter medium are more common.

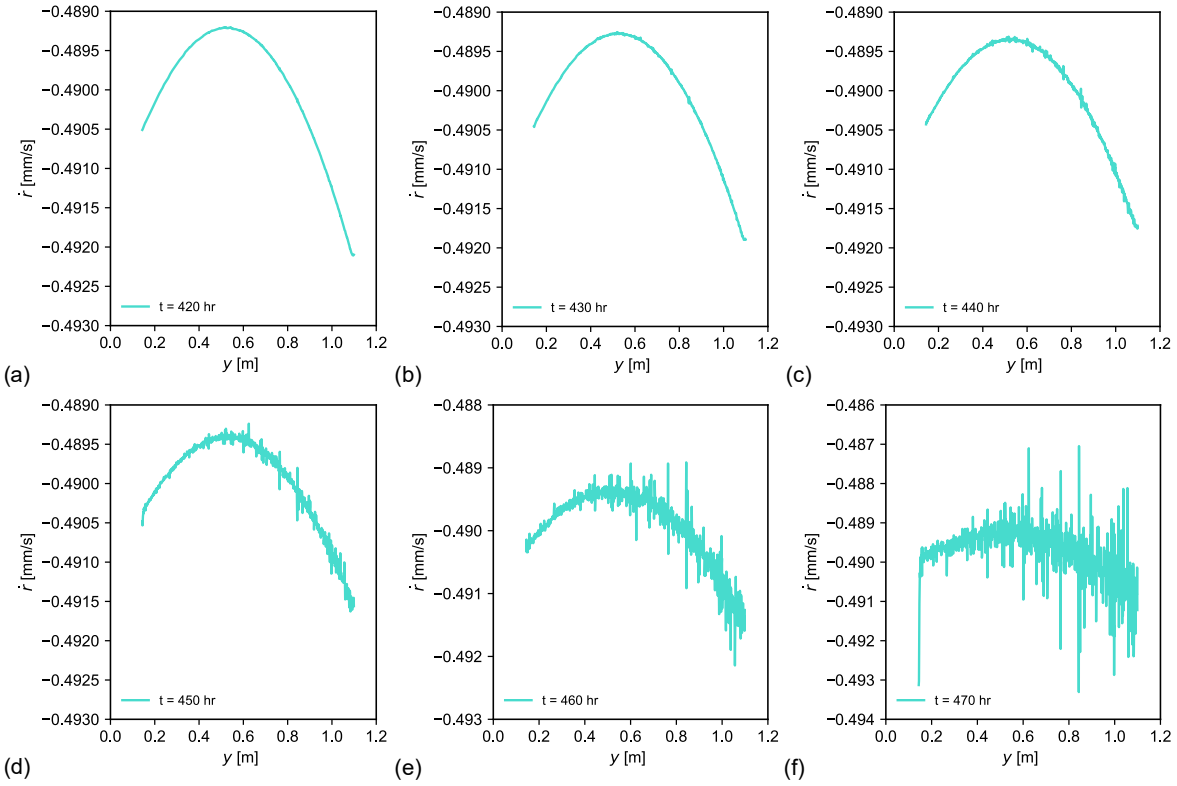

Figure 7.50: Radial velocity between 420 and 470 hours along the candle at $r = 0.02$ m for the single standard blocking model.

In summary, instability arises in blocking models with viscous resistance dependence on radial velocity due to the increasing rate of increase of viscous resistance as time advances and the frequency of quasi-steady state simulations. To increase model stability, filtering algorithms could be used to smooth the radial velocity profile at each time step before calculating the

viscous resistance. Smoothing the radial velocity profile would reduce local variations in radial velocity between successive nodes, eliminating local perturbations in both the radial velocity and the viscous resistance inside the filter medium.

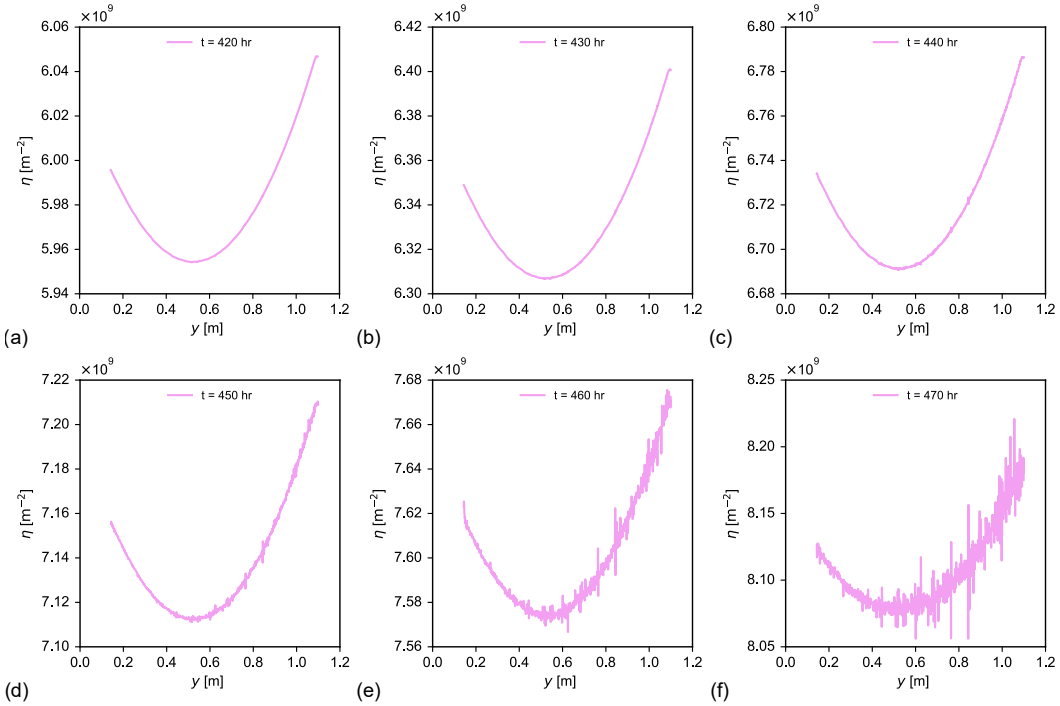

Figure 7.51: Viscous resistance between 420 and 470 hours along the candle at $r = 0.02$ m for the single standard blocking model.

Note however that this is not necessary for the scope of this work. Figure 7.52 shows that individual production runs with the seven candle filter pack do not exceed a maximum time of 280 hours. Figure 7.52 shows that the pressure drop across the pack for the standard seven candle filter blocking model remains stable beyond this maximum time. Furthermore, Run 4 was terminated as pressure drop across the pack exceeded a maximum allowable pressure drop. Figure 7.52 shows that the pressure drop across the pack for the standard seven candle filter blocking model remains stable beyond this maximum allowable pressure drop. Therefore, the blocking model remains stable within permissible time and pressure drop constraints for seven candle filter pack run conditions.

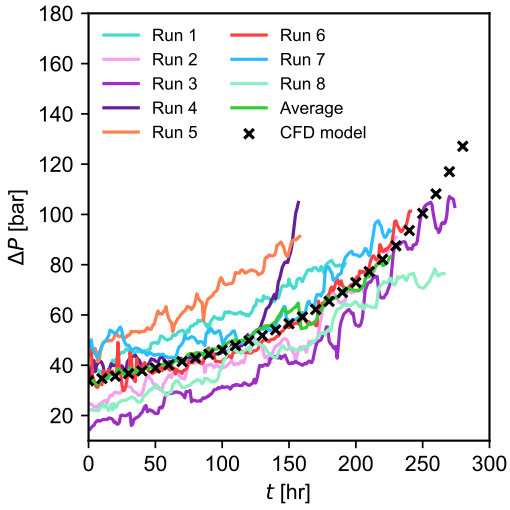

Figure 7.52: Pressure drop evolution across the pack for each production run and pressure drop evolution across the pack for the standard seven candle filter blocking model.

7.9 Seven candle pack parameter study

The production line with the seven candle filter pack operates over a large range of throughputs and temperatures. This section uses the seven standard blocking model to explore the influence of melt viscosity and throughput on pressure drop and flow pattern evolution.

Operating throughput for a seven candle filter pack can vary between 250-3000 kg/hr. The viscosity of PET is highly dependent on temperature. Between 285°C and 295°C, which are typical temperatures specified through the extrusion system, PET melt viscosity varies from 120-400 Pa.s. The Reynolds number at the inlet can be calculated from

$$\mathrm{Re} = \frac{4\dot{m}}{\pi D \mu}, \tag{7.18}$$

where D is the diameter of the inlet pipe and $\dot{m}$ is specified in kg/s. A maximum Re for PET through the seven candle filter pack can be calculated by taking $\dot{m} = 3000$ kg/hr and $\mu = 120$ Pa.s. A minimum Re can be calculated by taking $\dot{m} = 250$ kg/hr and $\mu = 400$

Pa.s. Tests 1-5 in Table 7.8 were calculated from an arithmetic sequence of five throughputs and viscosities across the ranges provided. Throughputs and viscosities were then used for individual simulations of the seven standard blocking model and compared.

Two further tests were undertaken. Table 7.8 shows tests 6 and 7, which were chosen as they represent configurations which produce a maximum and minimum pressure drop across the pack; pressure drop is proportional to mass flow rate and viscosity. Actual runs would not operate at the operating throughput and melt viscosity of test 7 due to the large pressure drop penalty. It was nevertheless included in this parameter study to give an upper bound on pressure drop evolution.

For this parameter study it was assumed that all melts contain the same proportion of blocking material per kg. Hence, the standard fitting parameter K_s was identical throughout all the tests and was chosen to match the fitting parameter in Section 7.7.

Table 7.8: Values of viscosity, mass flow rate and Reynolds number for seven different tests with the seven candle pack.

Test number	$\dot{m}$ [kg/hr]	μ [Pa.s]	Re
1	250	400	0.0074
2	937.5	330	0.0335
3	1625	260	0.0737
4	2312.5	190	0.1435
5	3000	120	0.2947
6	250	120	0.0245
7	3000	400	0.0884

Figure 7.53a shows pressure drop evolution across the pack for each test. As expected, tests 6 and 7 provide lower and upper bounds on the pressure drop across the pack for the entire duration of run time. Figure 7.53b shows pressure evolution across the pack for test 6. The increase appears linear at this stage. This is because of the operating throughput for this test, which was set at the minimum operating throughput. After 250 hours, the pack has seen a cumulative throughput of 62,500 kg, an order of magnitude less than the 675,000 kg than the configuration presented in Section 7.7 after the same time. The same apparent linear increase

can be seen for the pressure evolution for test 1, where again the minimum throughput was chosen.

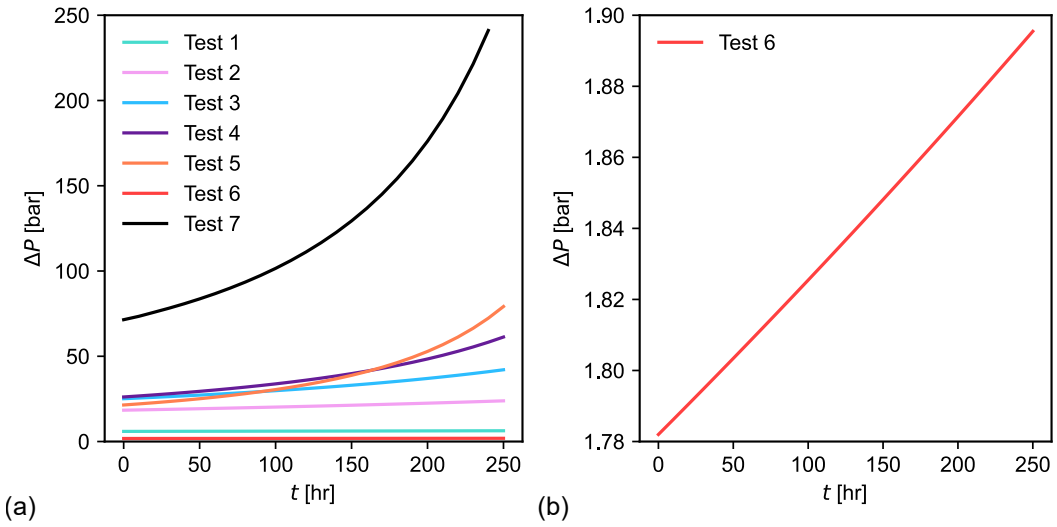

Figure 7.53: (a) Pressure drop evolution across the filter pack for the seven tests described in Table 7.8. (b) A closer look at pressure drop evolution for test 6.

Figure 7.54 shows a comparison of non-dimensionalised pressure drop evolution between each test. For tests with matching flow rates, such as tests 5 and 7, non-dimensional pressure drop evolution matches. It is clear from Figure 7.53a that the rate of increase of pressure evolution is larger for test 7 compared to test 5. Hence, initial pressure drop across the pack and rate of pressure drop evolution scale with viscosity. Figure 7.54 also shows that the rate of pressure drop evolution scales with flow rate. Furthermore, from tests 1 and 6 in Figure 7.53a, which have the same viscosity, initial pressure drop differs. Hence initial pressure drop scales with throughput, which is consistent with Darcy's law.

This scaling is apparent from the standard model where pressure drop across a candle filter is given by

$$\Delta P = \Delta P_0 \left(1 - \frac{K_s \dot{m} t}{2}\right)^{-2}.$$

Clearly, increasing throughput increases the pressure drop across a candle filter outputted by the standard model. Increasing operating throughput increases the cumulative melt through-

put through the filters over the course of a run, increasing the rate of filter fouling. None of the variables within the brackets are influenced by viscosity. However, from Darcy's law, ΔP_0 does depend on viscosity. Increasing ΔP_0 will increase the value of ΔP at all times. Hence, the rate of pressure drop evolution scales with viscosity. In summary, the initial pressure drop across the pack and rate of increase of pressure drop evolution scales with operating throughput and melt viscosity; increasing either of these parameters will increase the initial pressure drop across the pack and the rate of increase of pressure drop evolution.

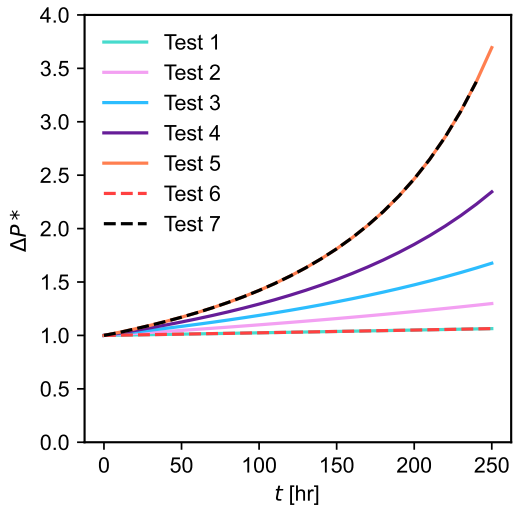

Figure 7.54: Non-dimensionalised pressure drop evolution across the seven candle pack for each test.

Table 7.9 shows the initial percentage split of total mass flow rate between the whole central and an outer candle for each test. Melt viscosity and throughput have no influence on the distribution of flow between each candle initially. This is because these parameters do not contribute to the initial resistance on the flow imposed by the candle filters. Furthermore, the Reynolds number for all tests remains in the creeping flow regime. This suggests that flow through the pack may initially be dynamically similar over the range of operating throughputs and melt viscosities.

Table 7.9: Initial distribution of flow between the central and outer candle for each test.

Test number	Central flow distribution [%]	Outer flow distribution [%]
1	51.26	48.74
2	51.26	48.74
3	51.26	48.74
4	51.26	48.74
5	51.26	48.74
6	51.26	48.74
7	51.26	48.74

Initial dynamic similarity over the range of operating conditions can be tested by comparing velocity and flow profiles between the most extreme Reynolds number cases: test 1 and test 5. To show dynamic similarity, velocity can be non-dimensionalised by dividing radial velocity and velocity magnitude by the averaged inlet velocity, U_I, such that

$$\dot{r}^* = \frac{\dot{r}}{U_I}, \quad |u|^* = \frac{|u|}{U_I},$$

where $|u|$ is velocity magnitude and $\dot{r}^*$ and $|u|^*$ are the non-dimensionalised radial velocity and velocity magnitude respectively. The averaged inlet velocity can be calculated from

$$U_I = \frac{\dot{m}}{\rho A},$$

where A is the cross-sectional area of the inlet pipe and $\dot{m}$ is converted into kg/s. Figure 7.55 shows that flow patterns are dynamically similar through the spider plate; flow patterns remain the same through the spider plate over the range of operating conditions and melt viscosities.

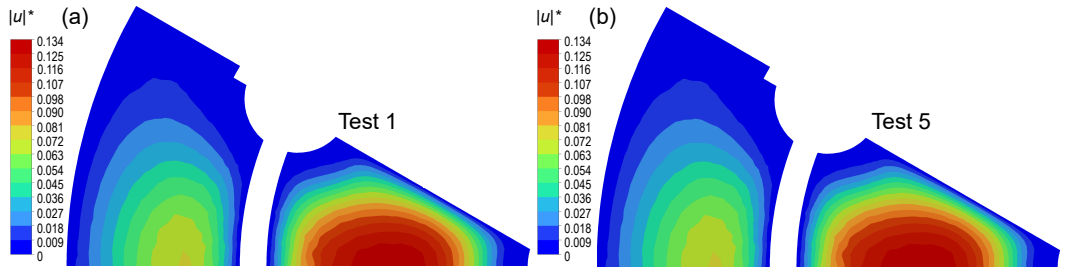

Figure 7.55: Initial contours of non-dimensionalised velocity magnitude on a plane that cuts through the spider plate for the seven candle pack for (a) test 1 and (b) test 5.

Figure 7.56 compares the non-dimensionalised central and outer radial velocity profiles on lines along each candle filter for tests 1 and 5; the profiles match. Figure 7.57 shows contours of non-dimensionalised velocity magnitude through a plane that cuts through the middle section of the seven candle filter pack between test 1 and test 5. Flow patterns are identical through the plane. Table 7.9 also shows that the distribution of flow between the candles is identical for each test. This means that flow patterns initially remain the same around, between and along candle filters in the pack. Therefore, the flow is initially dynamically similar throughout the seven candle filter pack over the chosen ranges of operating throughputs and melt viscosities.

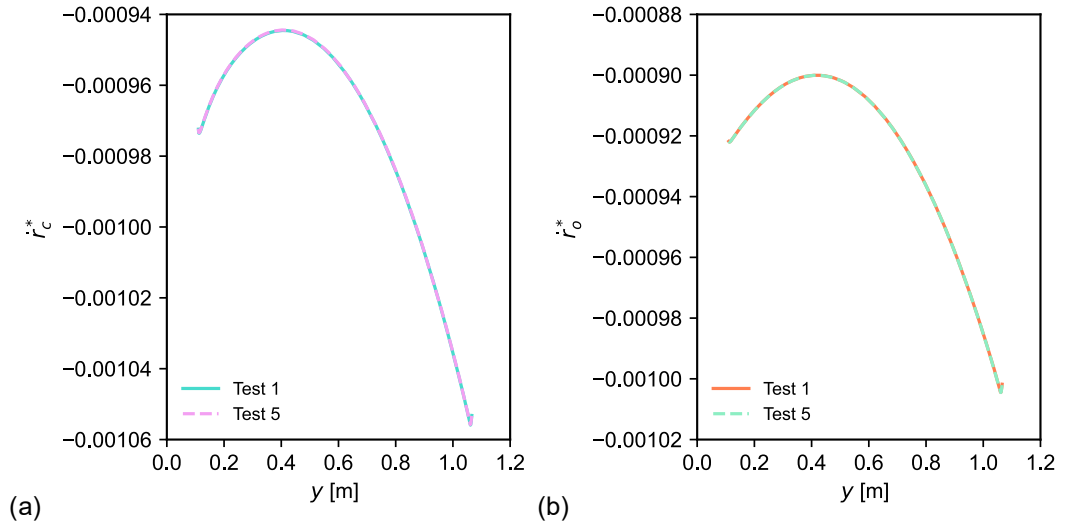

Figure 7.56: Non-dimensionalised (a) central radial velocity and (b) outer radial velocity for the seven candle filter pack for test 1 and test 5 at a point along $r_c = 0.018$ m and $r_o = 0.018$ m respectively.

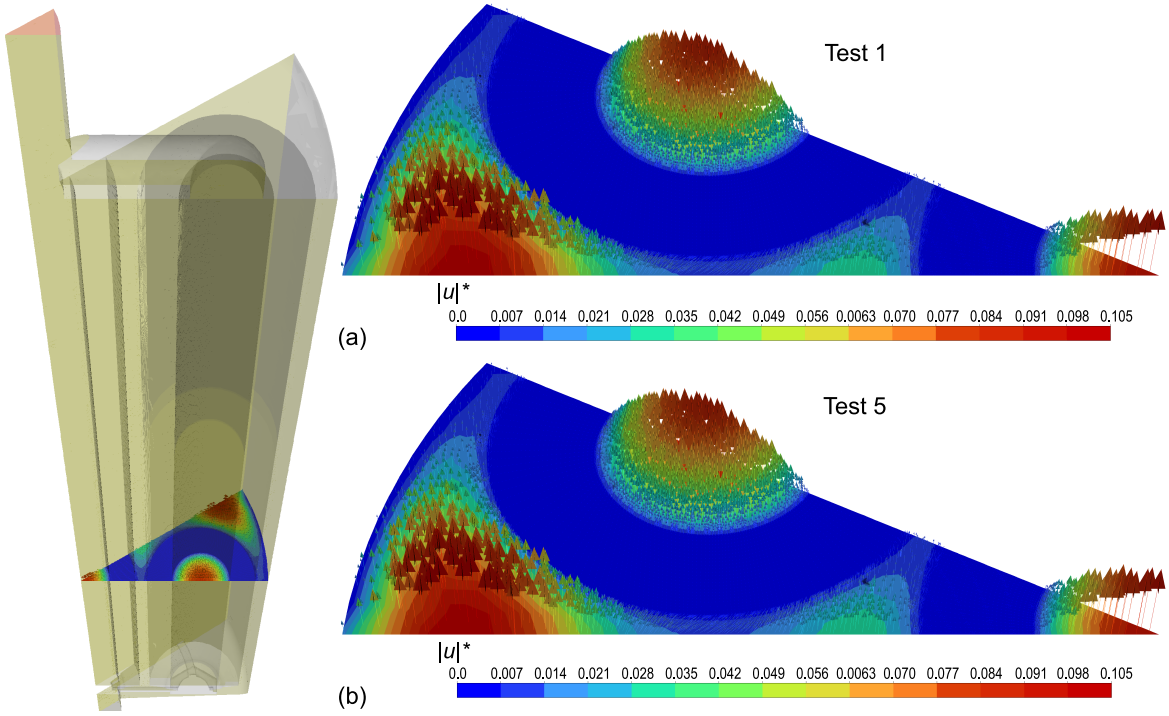

Figure 7.57: Initial contours and vectors of non-dimensionalised velocity magnitude for the seven candle filter pack for (a) test 1 and (b) test 5 at the plane $y = 0.45$ m.

Table 7.10 shows the percentage split of mass flow between the central and outer candles for each test after 200 hours. The distribution through all tests has changed and is converging towards an even split between central and outer candles. The tests with a larger operating throughput see a more even distribution between each candle after 200 hours. The larger the operating throughput, the more cumulative throughput of melt through each candle filter, the faster the distribution converges towards an even split. Tests 1 and 6 have the same distribution between candle filters after 200 hours. These tests have the same operating throughput, but different melt viscosities. The same is true for tests 5 and 7. This suggests that viscosity has little influence on flow distribution evolution.

Table 7.10: Distribution of flow between the central and outer candle for each parameter test after 200 hours.

Test number	Central flow distribution [%]	Outer flow distribution [%]
1	51.11	48.89
2	50.75	49.25
3	50.48	49.52
4	50.29	49.71
5	50.17	49.83
6	51.11	48.89
7	50.17	49.83

To test if flow distribution depends only on operating throughput, tests 5 and 7 can be compared as they operate at the maximum flow rate but differ in melt viscosity. Figure 7.58 shows the central and outer radial velocity on lines along each candle filter at 200 hours. Table 7.10 shows the distribution of flow between the candles matches and Figure 7.58 shows the velocity profiles along each candle filter match between the tests. This means that viscosity does not influence flow pattern evolution.

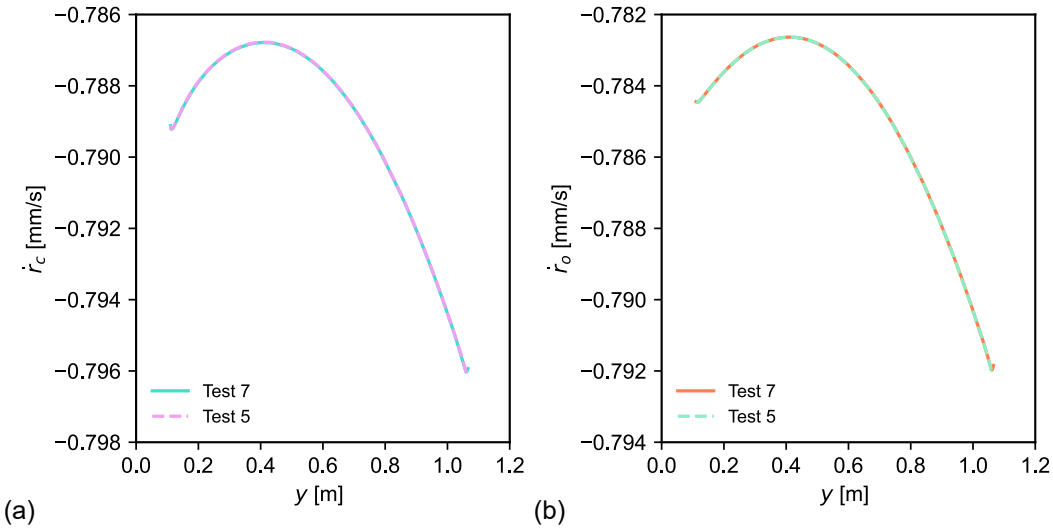

Figure 7.58: (a) Central radial velocity and (b) outer radial velocity for the seven candle pack for test 5 and test 7 at 200 hours at a point along $r_c = 0.018$ m and $r_o = 0.018$ m respectively.

In summary, the initial pressure drop across the pack and the rate of pressure drop evolution

are dependent on both melt viscosity and operating throughput. Viscosity has no influence on flow patterns through the pack. Flow patterns are initially dynamically similar over the range of operating throughputs through the seven candle filter pack; operating throughput dictates the magnitude of velocity of the flow and viscosity has no influence. The choice of melt viscosity will only change the work needed from the pump to maintain a desired operating throughput.

As with the original seven candle filter pack blocking model, all tests converge towards a uniform distribution along and between candle filters. As runs proceed and filter media blocks, flow pattern evolution is strongly influenced by operating throughput; a larger operating throughput means that more cumulative mass has travelled through each candle filter at a given time, resulting in more blocking in each candle filter.

Ideally, the distribution between candles would be homogenised. Candles are cleaned and reused after the termination of a run. If the flow is not homogenised, some candles in the pack would block at a faster rate compared to others, increasing pressure drop across the candles which see more throughput. This makes it more likely that the structure of those candles is damaged during production. If each candle sees a more even distribution of flow over several runs, the lifetime of each candle will also be homogenised. If structural damage is not noticed in the cleaning process, then over several runs, the likelihood of significant damage to individual candles which have seen a greater total throughput during runs increases, which would result in costly early termination of the runs and candle replacement.

Lifetime of candles is better homogenised in a seven candle filter pack when a film casting run is operated at high throughputs. This ensures a more homogenised distribution along and between candle filters at run termination. A larger throughput also has the additional benefit of reducing pack residence time. The greater the residence time, the more likely the occurrence of melt thermal degradation. A high operating throughput has drawbacks, as the work required by the pump to maintain a constant throughput increases due to the increased pressure drop across the pack. The pressure drop across the pack could be minimised by

operating at a high temperature, reducing melt viscosity. However, when considering the film casting process as a whole, it may be best to minimise melt temperature to reduce thermal degradation. Although candle lifetime is homogenised, larger throughputs result in larger pressure gradients across candle filters. This could warp or damage the filter medium, reducing its effectiveness. Instead, the pack could be modified to better homogenise distribution.

7.10 Design suggestions for improved seven candle pack performance

As shown in Table 7.5, the central candle sees a higher mass flow rate compared to an outer candle over the course of a run. Although the difference is low, ideally, the flow would be evenly distributed between each candle. Homogenised flow between candles would ensure each candle blocks at the same rate, reducing the likelihood of structure damage to an individual candle which could lead to early run termination and candle replacement. In Subsection 6.10.2, it was shown that by creating a multiple outlet geometry, which removed the bend in the outer outlet pipe, the resulting decrease in resistance through the outer candle resulted in an even distribution of flow between the central and outer candles. The multiple outlet geometry is not a practical design, as flow through the central and outlet pipes must recombine and exit through a single pipe onto the next stage of production.

This section investigates how a practical change to the geometry which artificially increases resistance through the central outlet pipe can homogenise flow between candles. Figure 7.59 shows the new outlet geometry. The diameter of the outlet pipe from the central candle was reduced, increasing resistance through the central candle. The radius of the central core, upstream of the outlet pipe, was unchanged. Fluid properties and the flow rate were chosen to match the run and original blocking model conditions, specified in Section 7.1. The new central outlet radius was reduced so that the new diameter is 72% the length of the original diameter.

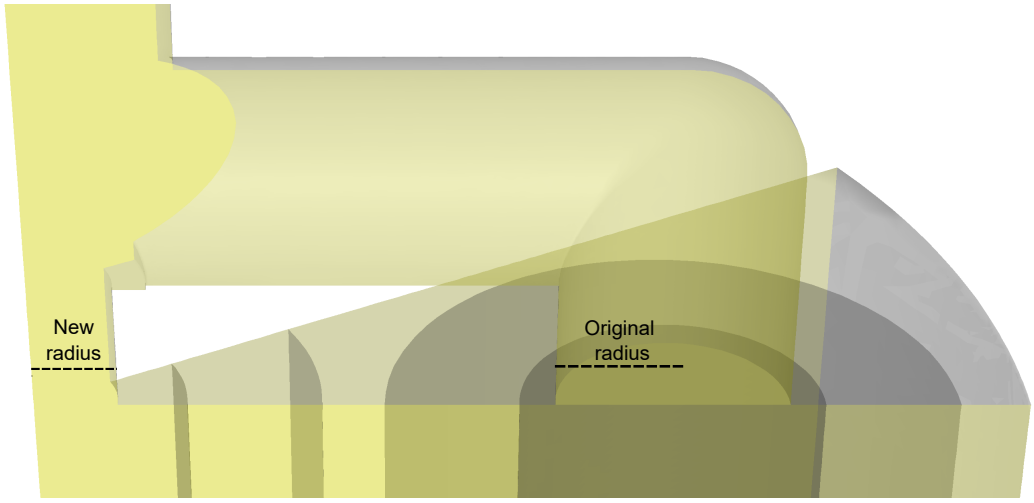

Figure 7.59: The modified outlet proposed for the seven candle filter pack. The diameter of the outlet pipe from the central candle is shortened.

Table 7.11 shows the initial percentage split of mass flow rate between the central and an outer candle and the pressure drop across the pack for the original and modified geometry. Reducing the radius of the central candle outlet has increased the resistance through the pack which has lead to an increase in pressure drop across it. The percentage split of mass flow rate between the central and an outer candle is much closer for the modified geometry due to this additional resistance. Homogenising the distribution further would require increased precision to the central outlet pipe radius which is an unrealistic specification for industrial equipment.

Table 7.11: Flow rate distribution and pressure drop across the pack for the original and modified seven candle filter pack geometries.

Geometry	Central flow distribution [%]	Outer flow distribution [%]	ΔP [bar]
Original	51.26	48.74	33.81
Modified	49.85	50.15	33.99

Figure 7.60 shows the pressure distribution for the original and the modified geometry. Pressure is more evenly distributed through the modified geometry. Table 7.12 shows the pressure drop from the central core of each candle to the pack outlet for the original and modified

geometries. Pressure between the candles is very similar for the modified geometry, showcasing that the resistance imposed on the flow between each candle's respective outlet pipes is significantly more even for the modified geometry.

Table 7.12: Pressure drop from the central core of each candle to the pack outlet for the original and modified seven candle pack.

Geometry	Central ΔP [bar]	Outer ΔP [bar]
Original	10.66	9.69
Modified	10.74	10.75

Figure 7.61 shows the outer and central radial velocity for a line along the outer and central candle for the original and modified geometry. As the flow is more evenly distributed between the candles, by conservation of mass, the radial velocity has decreased in magnitude along the central candle and the outer radial velocity has increased in magnitude along the outer candle. Interestingly, the shape of the profiles has altered. Table 7.13 shows this, where the range of outer and central radial velocity has decreased with the modified geometry. This means that altering the central outlet pipe has marginally improved homogeneity along the candle filters; the range of radial velocity along the central and outer candle has decreased by more than 7% and 2% of its original value respectively.

Table 7.13: The range of $\dot{r}_c$ and $\dot{r}_o$ for the modified and original geometry for the plots given in Figure 7.60.

	Geometry	Range [mm/s]
$\dot{r}_c$	Original	0.0844
	Modified	0.0780
$\dot{r}_o$	Original	0.0791
	Modified	0.0768

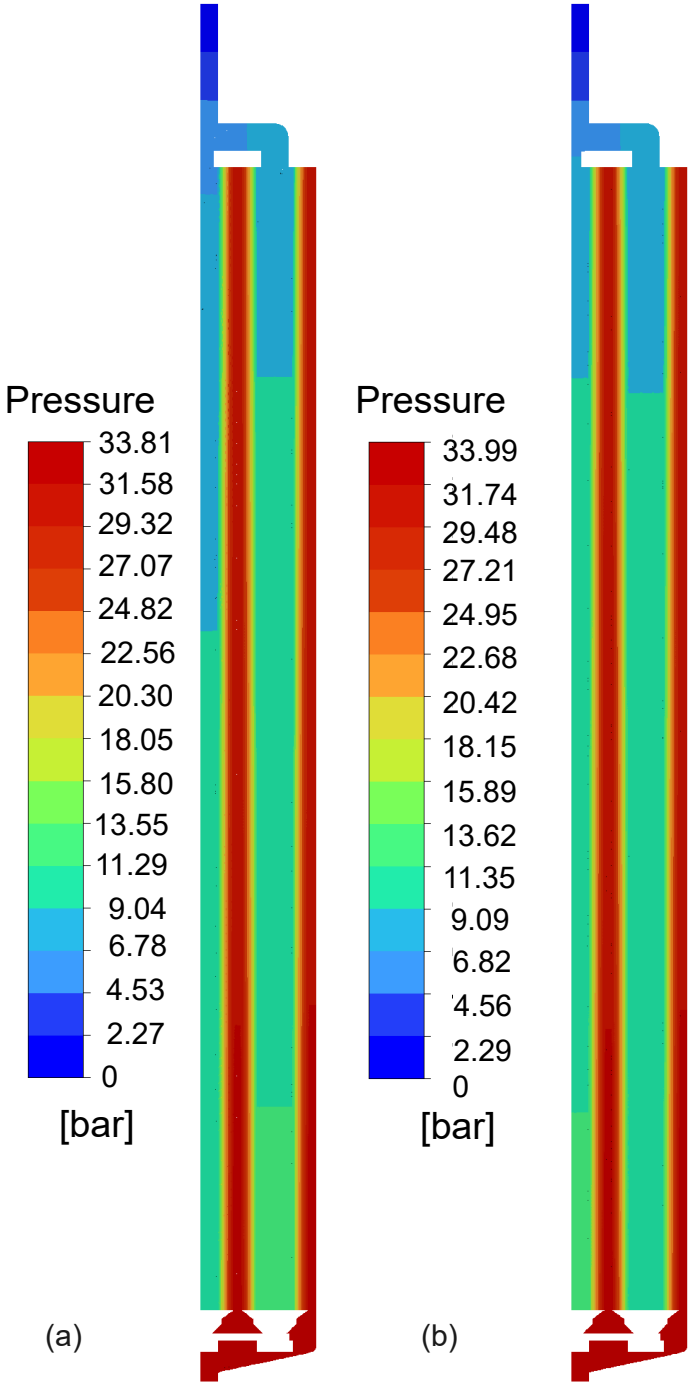

Figure 7.60: Pressure contours on the plane parallel to the y-axis which cuts through the centre of the central and outer candle for (a) the seven candle model and (b) the modified model.

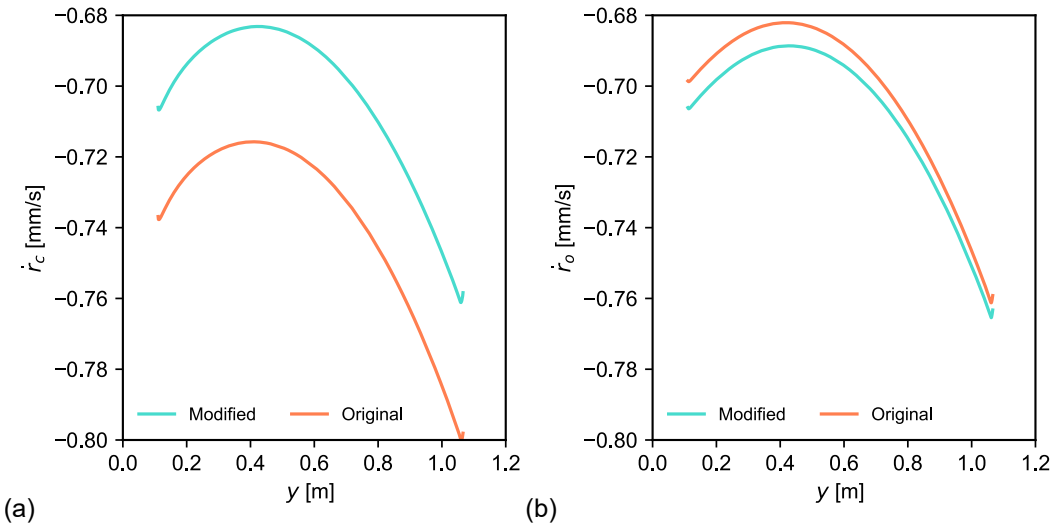

Figure 7.61: Initial (a) central radial velocity and (b) outer radial velocity for the modified and original geometry of the seven candle filter pack at a point along $r_c = 0.018$ m and $r_o = 0.018$ m respectively.

Figure 7.62 compares contours of velocity magnitude and vectors of velocity through the plane $y = 0.45$ m for the two geometries. There is little difference in the structure of flow patterns between the two. Velocity magnitude appears larger in the core of the pack closer to the outer candle for the modified geometry. This is a result of the redistribution of flow between the candles. As more flow travels through the outer candle, velocity is greater in regions of the core of the pack where flow is likely to travel through the outer candle. Figure 7.63 shows the central and outer radial velocities as functions of respective azimuthal position along $r_c = 0.018$ m and $r_o = 0.018$ m respectively at equidistant distances along the candle filters. There is little difference in shapes of radial velocity profiles around candle filters. The magnitude of outer and central radial velocity has increased around the outer candle and decreased around the central candle respectively. This is expected as the outer candle sees a greater proportion of flow due to the modified outlet. Modifying the outlet has had insignificant influence on flow patterns around each candle filter. In summary, initially, decreasing the diameter of the central outlet pipe has increased resistance through the central candle. With the modified geometry, flow is evenly distributed between central and outer candles. Homogeneity has also

marginally improved along candles. There is no discernible difference to flow patterns around the candle filter.

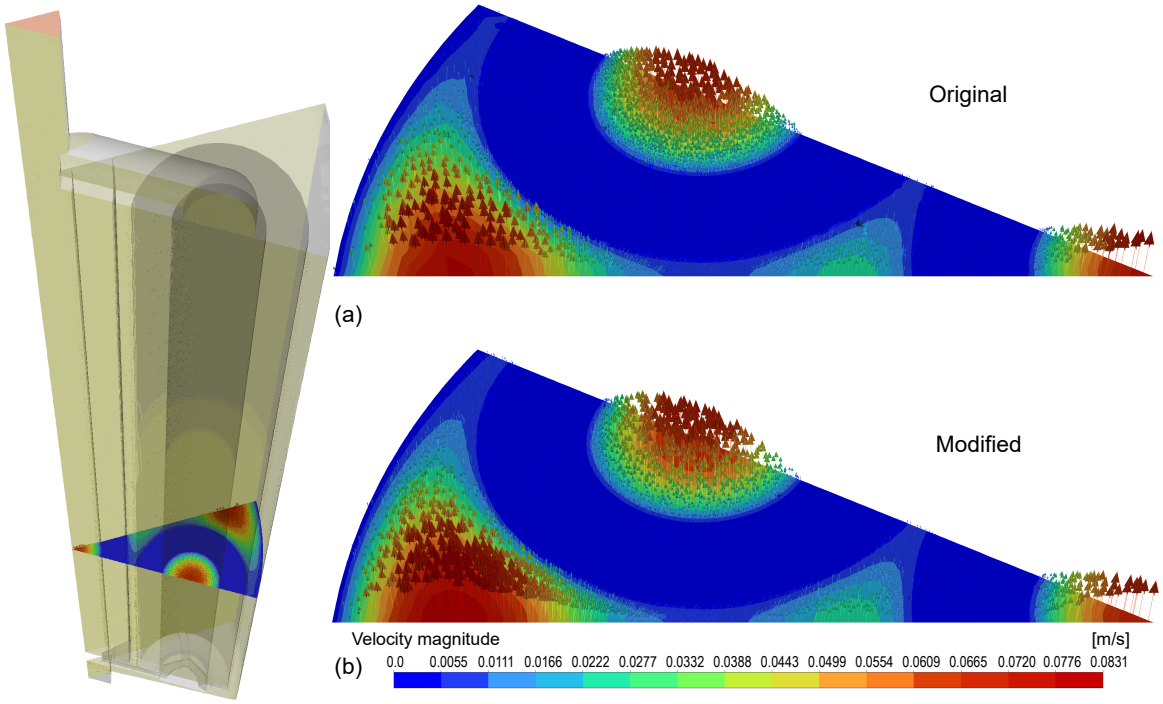

Figure 7.62: Initial contours and vectors of velocity at $y = 0.45$ m for (a) the original and (b) the modified geometry of the seven candle pack.

The standard blocking model was applied to the modified geometry with $K_s = 0.038$; the same K_s used for the original geometry in Section 7.7. Figure 7.64 shows pressure drop evolution across the pack for the modified and the original geometry. Pressure drop evolution across the pack is very similar between the two models, with the modified pressure drop slightly greater across the pack. As the fitting parameter, viscosity and throughput are identical, this is expected, with the only additional pressure contribution coming from the resistance imposed on the flow by the modified central outlet pipe.

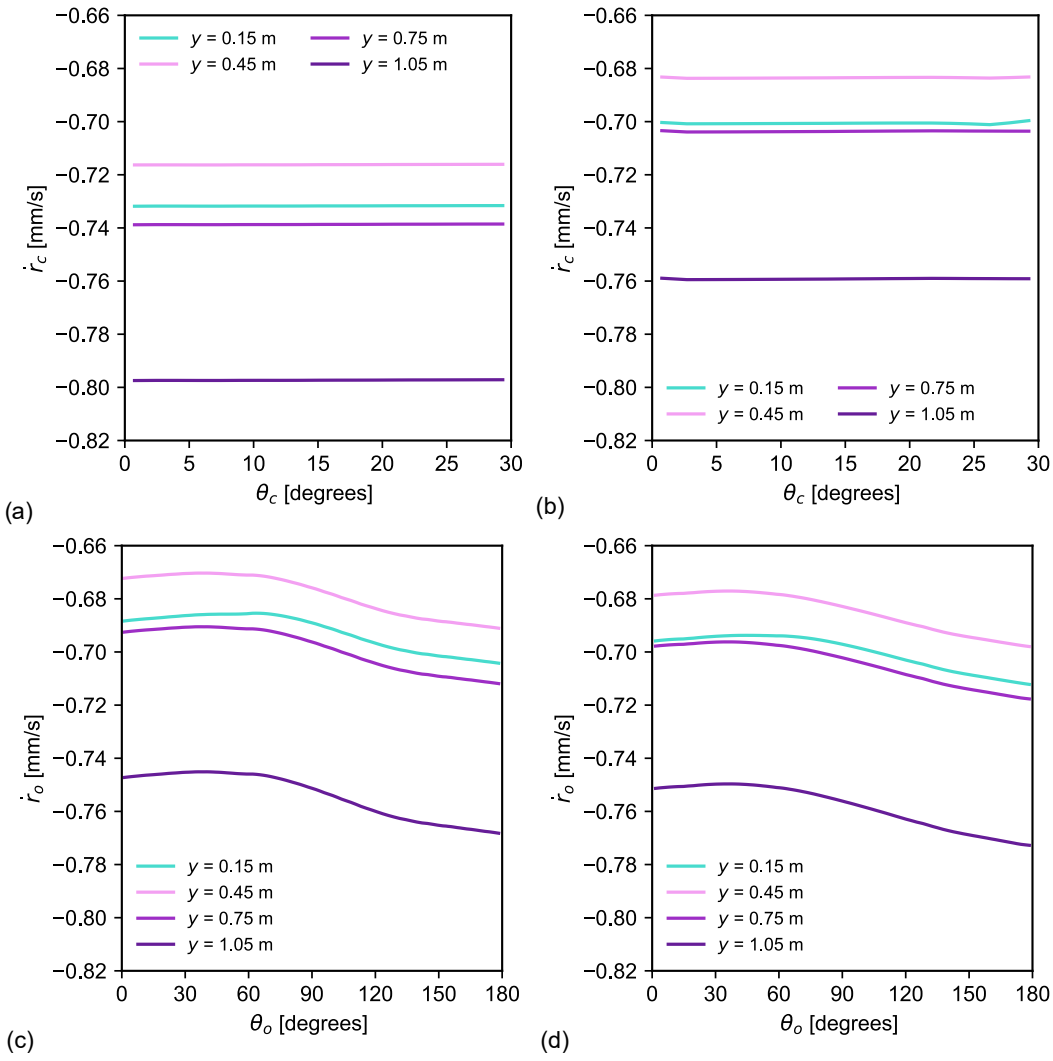

Figure 7.63: Initial central radial velocity around the central candle at $r_c = 0.018$ m for (a) the original geometry and (b) the modified geometry and initial outer radial velocity around the outer candle at $r_o = 0.018$ m for (c) the original geometry and (d) the modified geometry at four equidistant planes through the seven candle pack.

Figure 7.65 shows the mass flow rate through the whole central and a whole outer candle over time. Even with the relatively even percentage split of mass flow rate between the central and an outer candle, flow between candles appears to be converging towards an even proportion of flow between each candle. Table 7.14 estimates the total throughput that the central candle and an outer candle have seen for both the original and modified geometries after 250 hours.

The modified geometry has reduced a 2.17% percentage difference in cumulative throughput between each candle filter to 0.27%. This shows that modifying the geometry has improved distribution through the pack over the course of a run.

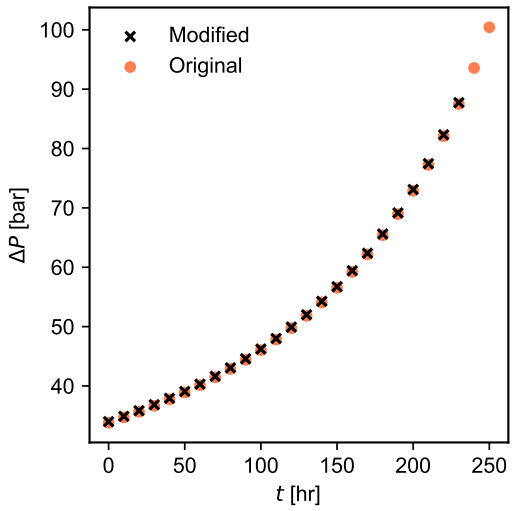

Figure 7.64: Pressure drop evolution across the pack for the original and modified geometries of the seven candle pack with the standard model.

Table 7.14: Estimated cumulative melt throughput for each candle after 250 hours for the modified geometry with the standard blocking model.

	Total throughput [kg]
Central candle	100239
Outer candle	100510

Figure 7.66 shows the central and outer radial velocity through a line along the central and outer candle respectively. Flow is again homogenising along each candle filter. Figure 7.67 shows central and outer viscous resistance profiles along the same line as the respective radial velocity profiles in Figure 7.66. Table 7.15 shows the mean viscous resistance of each candle for the original and modified geometry after 250 hours. As both candles have seen a more even distribution for flow throughout the run, mean viscous resistance difference between each candle has reduced from 0.89% to 0.15% after 250 hours.

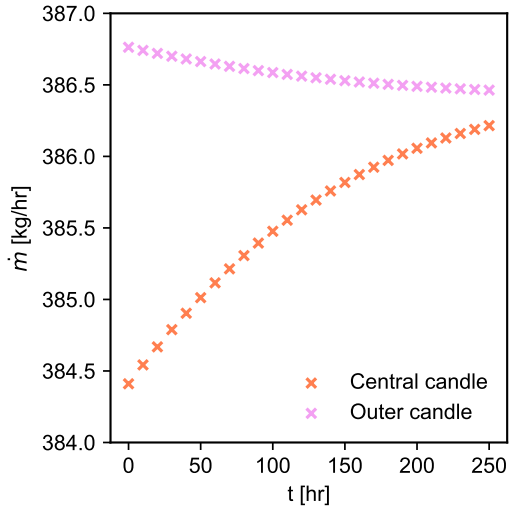

Figure 7.65: Mass flow rate through the central and outer candles over time for the modified geometry with the standard blocking model.

Table 7.15: Mean viscous resistance of the central and outer candle for the original and modified geometry with the standard blocking model after 250 hours.

Geometry	$\bar{\eta_c}$ [m^{-2}]	$\bar{\eta_o}$ [m^{-2}]
Original	5.225×10^{9}	5.179×10^{9}
Modified	5.180×10^{9}	5.188×10^{9}

Figure 7.68 shows the central radial velocity evolution and outer radial velocity evolution around constant r_c and r_o respectively on the plane $y = 0.45$ m for the modified geometry. The magnitude of central radial velocity has increased as the filters block around the central filter and the magnitude of the outer radial velocity has increased around the outer filter. As the distribution between candles is well homogenised, respective radial velocity increases to reflect the homogenisation along each candle filter over time. Table 7.16 shows the range of central and outer radial velocity for the plots in Figure 7.68 for the 0 hour and 200 hour time step. There is little change in radial velocity profiles around the candle filters on this plane. It does not appear that the blocking model is homogenising flow around either candle filter.

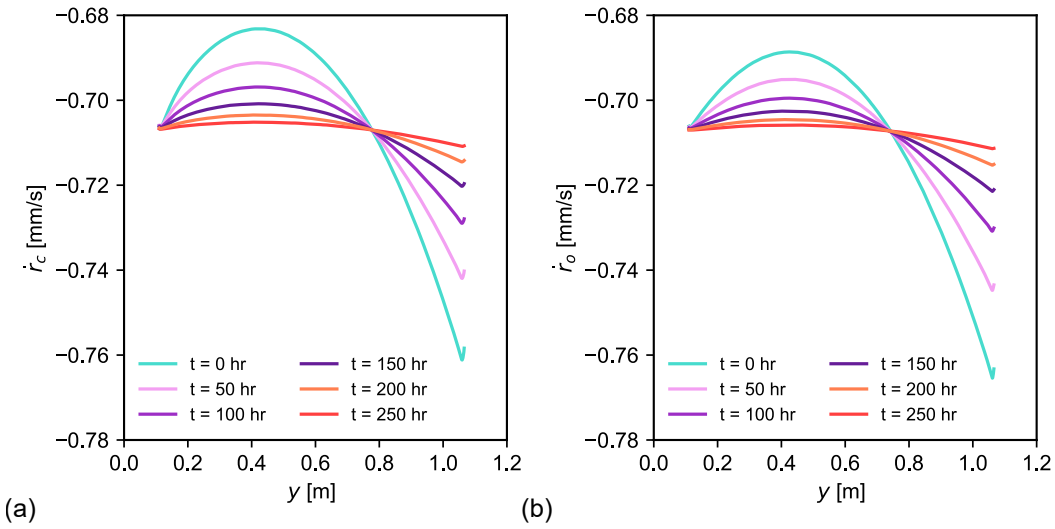

Figure 7.66: (a) Central radial velocity evolution and (b) outer radial velocity evolution for the modified geometry of the seven candle pack with the standard blocking model at a point along $r_c = 0.018$ m and $r_o = 0.018$ m respectively.

It is recommended that the central outlet pipe diameter is reduced to 72% the length of the original diameter as this will improve distribution along and between filters in the seven candle filter pack throughout production runs. Reducing the radius of the central outlet pipe imposes a greater resistance on flow through the central filter, countering the increased resistance imposed on flow through the outer candle caused by the extension and turn in the outer outlet pipe. Homogenised resistance between candles homogenises the flow between candles, as there is no path of lower resistance for the flow to favour. An added benefit is this geometry results in an initially more homogenised flow along candles. This improved homogenisation between and along candles will reduce the likelihood of the central candle failing due to a disproportionate amount of cumulative mass flow through it. It is a marginal gain, but this may improve candle filter lifetime and pack performance over several runs.

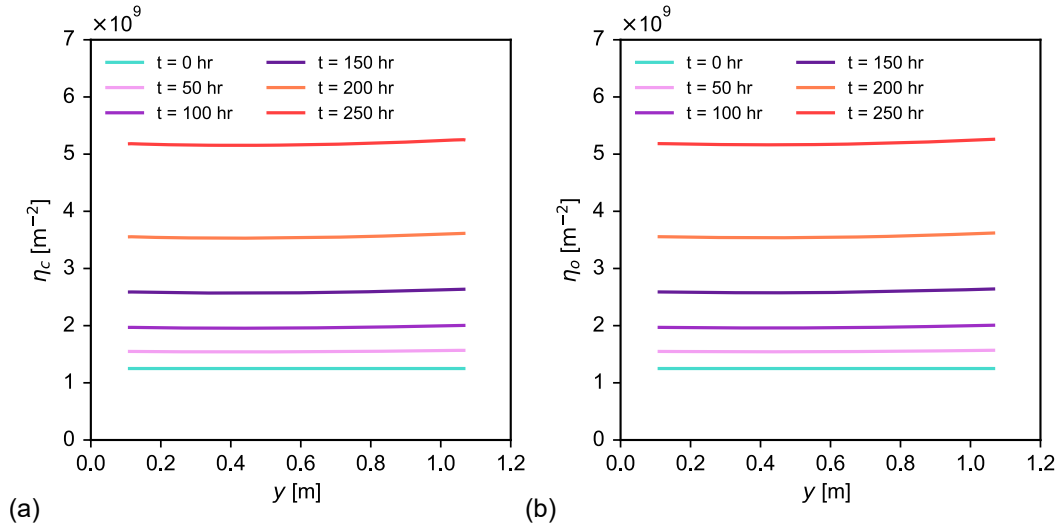

Figure 7.67: (a) Central viscous resistance evolution and (b) outer viscous resistance evolution for the modified geometry of the seven candle pack with the standard blocking model at a point along $r_c = 0.018$ m and $r_o = 0.018$ m respectively.

Table 7.16: The range of $\dot{r}_c$ and $\dot{r}_o$ at $t = 0$ hr and $t = 250$ hr around $r_c = 0.018$ m and $r_o = 0.018$ m on the plane $y = 0.45$ m for the modified geometry with the standard blocking model.

	Time [hr]	Range [m/s]
$\dot{r}_c$	0	4.99×10^{-7}
	250	4.96×10^{-7}
$\dot{r}_o$	0	2.09×10^{-5}
	250	2.02×10^{-5}

Section 7.9 showed that flow homogenised between candle filters over less time as operating throughput increased. The work in this section showed that modifying the geometry homogenised the flow between candles before any blocking takes place. Mylar have a higher minimum operating throughput for candle filter packs compared to disc filter packs. This disadvantage of candle packs is because pressure drop across the pack remains low over the course of a run at low operating throughputs. Therefore, the distribution between candles remains uneven throughout. The modified geometry overcomes this disadvantage as the distribution between candles is homogenised. This geometry change does result in a pressure

drop penalty. However, the pressure drop penalty imposed on the flow by the change in central outlet pipe diameter is small over the course of a run.

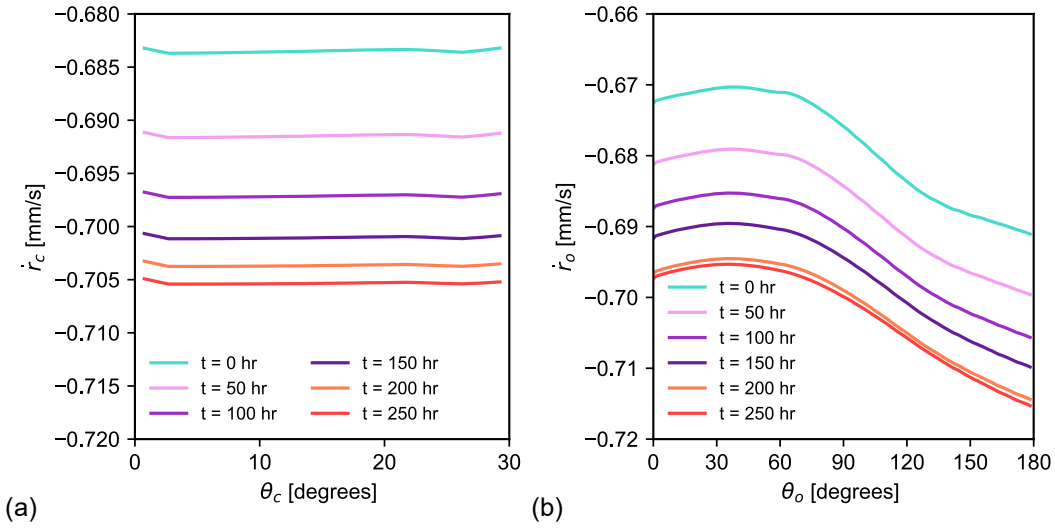

Figure 7.68: (a) Central radial velocity evolution and (b) outer radial velocity evolution for the modified seven candle pack standard blocking model around the central and outer candle on the plane $y = 0.45$ m at $r_c = 0.018$ m and $r_o = 0.018$ m respectively.

7.11 Conclusion

This chapter detailed the creation of a novel filter blocking model, which modified a common filter blocking model to include dependence on local radial velocity, and its implementation into the single and seven candle filter pack CFD models established in Chapter 6. Through modification and implementation of the novel filtration model into filter pack CFD work, it was possible to capture the profiles of averaged pressure evolution data from actual runs, gain insight into flow pattern evolution inside complex industrial filter packs and understand how candle filters block in such packs over time.

The novel coupling between modified filter blocking models and CFD models to predict pressure drop evolution, filter blocking evolution and flow pattern evolution across geometrically complex filtration packs on a macroscopic scale has been shown to work for axisymmetric 2D

models, as well as 3D models of varying complexity. The framework detailed in this chapter is applicable to a range of actual filter systems in industry. This novel coupling does have certain physical requirements. The fluid must act as a Newtonian fluid throughout the pack. Furthermore, Darcy's law must apply to the fluid as it flows through the filter medium. Particles should be ensured to follow streamlines in the flow as the model is physically based on this assumption. If particles do not follow streamlines, permeability will not decrease proportionally to local velocity in the filter medium. The appropriate filter blocking model should also be chosen; in the case of candle filter packs, the standard blocking model was chosen as it gave a good fit to average run data and it was defined based on the same particle deposition mechanism that drives particle deposition in candle filter media.

Parameter tests, where operating throughput and melt viscosity were varied, showed that homogenisation along and between candle filters over the course of a run in the seven candle filter pack was superior when operating at the maximum flow rate. A modification to the central outlet pipe is recommended; reducing the diameter of the pipe homogenises the distribution along and between candles throughout the course of a run, regardless of operating conditions.

Chapter 8

Summary

8.1 Conclusions

The purpose of this research was to use CFD to better understand how the blocking of filter packs over time affects performance for polymer melt filtration. This work has successfully created a methodology capable of computationally modelling the degradation of filter elements in geometrically complex filter packs. This has allowed analysis of flow pattern evolution in packs and has been used to offer recommendations on operating conditions and improvements to filter pack design. Alongside this, the research has highlighted the general lack of theoretical understanding surrounding polymer melt filtration, and has made inroads into better understanding the physical mechanisms driving it. The main outcomes of this research, detailed in Chapters 4-7, are summarised below.

8.1.1 Chapter 4: Modelling Polymer Melt Flow Through Screen Filters

- PET melt behaviour through a screen filter over a range of operating throughputs was shown to obey Darcy's law, when viscosity change due to temperature was accounted

for. This was achieved through executing an experimental methodology on the pilot scale line developed by Mylar.

- A computational geometry of the screen filter system was created and the porous media model was shown to be a suitable tool for modelling the flow of polymer melts across filters.

- A computational methodology was developed for modelling the flow of any fluid, so long as it is Newtonian and obeys Darcy's law, across a multi-layered woven screen using the porous media model.

- The filter layer of the screen filter should be modelled with a porous zone, but placed correctly relative to the filter holder in the actual geometry. Any other porous zone configuration leads to inaccurate modelling.

8.1.2 Chapter 5: Pressure Drop Evolution Across Screen Filters

- An experiment was undertaken to artificially speed up the blocking of a screen filter on the pilot scale lane. A pressure drop evolution curve was obtained from this experiment.

- The common filter blocking models, discussed in Subsection 2.3.1, were fitted to the experimental data and the intermediate model was shown to give the best fit. This makes sense physically due to the structure of the screen filter.

- The CFD model developed in Chapter 4 for the screen filter system was used in conjunction with the intermediate blocking model to predict the pressure drop evolution across a screen filter. This showed that filter blocking models may be used in conjunction with CFD models to macroscopically mimic filtration processes.

8.1.3 Chapter 6: Modelling Polymer Melt Flow Through Candle Filter Packs

- Computational models were generated for the single and seven candle filter packs. Flow symmetry was analysed and exploited to reduce the single candle pack model to one-sixth of the original geometry and the seven candle pack model to one-twelfth of the original geometry. This saved substantial computational cost.
- Data from runs with seven candle filter packs were analysed and an average initial pressure drop across the seven candle pack was found. This information was used to find an appropriate permeability value for use in the porous media model.
- Results from the CFD models visualized and described initial flow patterns through single and seven candle filter packs. The single candle pack model showed that the flow could be considered axisymmetric around the candle filter element. Radial velocity was found to vary from the top to the bottom of the candle filter element. A permeability sensitivity study showed that decreasing permeability imposed a greater resistance on the flow. This showed that the radial velocity along the filter element converged towards a uniform 'box' profile with decreasing permeability along the candle filter.
- The seven candle pack model showed that the flow varied between, around and along candles in the pack. The central candle saw a greater proportion of the total throughput. This was found to be due to the increased resistance imposed on the fluid due to the outer candle outlet pipe. Modifying the outlet pipes so that the outlet section from each candle was identical resulted in a uniform distribution of throughput between candles.

8.1.4 Chapter 7: Pressure Drop and Flow Evolution in Candle Filter Packs

- Common filter blocking models were fitted to the pressure evolution data from runs with the seven candle filter pack model. The standard model gave a very good fit, and was chosen due to it representing depth filtration, the filtration mechanism that drives filtration in candle filter media.

- A novel computational filter blocking model was developed, based on modifications to a common filter blocking model, and was coupled to the candle filter pack CFD models. This model coupled porous media model permeability and local radial velocity. The novel blocking model was successful in matching predicted pressure drop across both modified axisymmetric and 3D single candle filter pack simulations with a direct calculation. The model successfully captured the profiles of averaged pressure drop evolution data from actual runs with the seven candle filter pack. The model was used to inform on flow pattern evolution inside the complex candle filter packs.

- Parameter tests, where operating throughput and melt viscosity were varied, showed that homogenisation along and between filters over the course of a run in the seven candle filter pack was superior when operating at the maximum flow rate. A modification to the central outlet pipe was created, which increased resistance through the central candle. This homogenised throughput between all candle filters in the pack at the cost of an marginal increase to pressure drop across the whole pack at a throughput of 2700 kg/hr. This modified geometry has proven to overcome a disadvantage of candle packs; it will perform better with a more even flow distribution between the candles at lower throughputs and pressure drops across the pack.

8.2 Implications and further work

Understanding and categorising the physical mechanisms driving the transport and deposition of contaminants in polymer melt filtration requires further work and should be confirmed experimentally. It was possible to make informed assumptions on particle transport, deposition and filtration mechanisms based on a combination of dimensionless numbers, experimental work, common models from the literature and knowledge from manufacturers. However, such mechanisms should be confirmed conclusively through dedicated experimental rigs and methodology, as was confirmed for the mechanisms driving the flow of a PET melt through screen filters. Experimentally exploring such mechanisms is no easy feat and would require

substantial technical resources and planning. A recommended starting point is the classification of the nature of transport in polymer melt flow with particles representative of typical solid contaminants.

The experimental methodology developed in Chapter 4 could be used to verify the melt rheology of a variety of polymers in porous media. Furthermore, it was observed that the corrected pressure drop and mass flow rate relationship did not intercept with the origin. It was also seen that the intercept deviated further from the origin with decreasing screen filter grade. This could be explained by non-linear effects at low flow rates. Although industrial processes are unlikely to operate flow rates approaching 0 kg/hr, it would certainly be an interesting academic exercise to understand the mechanisms that may drive this divergence from linearity. It is unfeasible to operate the pilot scale line at such low flow rates, so to experimentally investigate this divergence, a custom experimental rig would have to be developed.

There were several assumptions made to simplify CFD modelling of melt flow through filter packs in this project. Further model development could incorporate particle transport, particle deposition and fluid structure interaction. If a representative particle distribution for contaminants in melt was found, a Langevin equation with the appropriate forces could be used to incorporate particle transport into the model. This could then be linked to the filter blocking model, updating porous zone permeability based on the position of particles upon entering a porous zone. Pore scale simulations of particle transport and deposition could be undertaken. This would offer an insight into flow patterns inside, for example, the sintered fibre structure of a candle filter medium. Particle transport at the pore scale could offer insight into particle deposition. Furthermore, the pore scale model could be linked to the macroscale filter pack model, creating a state of the art multiscale filtration model for complex filter packs in polymer melt filtration.

Pressures imposed on the filter medium in polymer melt filtration is substantial, as evidenced by the use of support mesh and the rigid structure of candle filter elements. Fluid-structure

interaction could be considered if there is interest in modelling filter deformation evolution. Modelling thermal degradation of polymer melts was not considered in this project. Thermal degradation leads to the formation of gels in the melt, which may be captured by the filter medium. Shearing imposed on the melt by the filter may also lead to the deformation of the gels. A mixture of experimental work and computational modelling could be undertaken to better understand how such gels interact with various filtration media.

This project only analysed some of the filter packs utilized by Mylar around the world. Different types of candle filter packs are also used for filtration on different production lines. A CFD model could feasibly be created for these other packs and the filter blocking model developed here could be applied and used to suggest design improvements. Disc filter packs are also utilized by Mylar. Again, the same methodology could be applied to study flow pattern evolution and propose design improvements. The novel filter blocking model developed here is not only applicable to filter systems utilized by Mylar or the film casting industry. For a filter system where the fluid acts as a Newtonian fluid, particles follow streamlines and Darcy's law is observed, with appropriate choice of filter blocking model (based on fit to experimental data and physical similarity), the methodology presented in this thesis may be used to inform on flow pattern evolution and used to suggest filter pack design improvements.

Analysis on single candle run data highlighted that the influence of candle element condition on filter system performance may be significant. Through analysis, it was observed that there was no correlation between pressure evolution gradient and mass flow rate. As candles are cleaned and refurbished, it is possible that the expected increase in pressure gradient with flow rate was not observed due to varying initial candle condition. An experiment designed to evaluate the pressure drop across candle elements of different conditions was proposed. This experiment was postulated as a hydraulic pressure drop test, where a candle sample would be attached to a hydraulic pressure drop test experimental rig. Several candle samples of varying condition would be tested. If there is found to be a discrepancy in pressure drop across samples, the filter blocking model could be used to inform on differences in pressure drop and flow pattern evolution depending on initial candle condition.

Bibliography

[1] M. M. Denn, Polymer melt processing: foundations in fluid mechanics and heat transfer, Cambridge University Press, 2008.

[2] D. Stratiychuk-Dear, Enhancing product differentiation through direct extrusion addition, Ph.D. thesis, University of Birmingham, Birmingham (12 2018).

[3] W. A. MacDonald, Polyester Films, in: Encyclopedia of Polymer Science and Technology, John Wiley and Sons, Inc., 2002.

[4] J. Markarian, Choosing a melt filtration system, Plastics, Additives and Compounding 10 (3) (2008).

[5] S. Pachner, M. Aigner, J. Miethlinger, Modeling and optimization of melt filtration systems in polymer recycling, in: AIP Conference Proceedings, Vol. 1914, American Institute of Physics Inc., 2017, pp. 1–5. doi:10.1063/1.5016744.

[6] S. Pachner, M. Aigner, J. Miethlinger, A heuristic method for modeling the initial pressure drop in melt filtration using woven screens in polymer recycling, Polymer Engineering and Science 59 (6) (2019) 1105–1113. doi:10.1002/pen.25088.

[7] P&S Intelligence, Polymer Market Share Analysis by Type (Thermoplastics, Thermosets, Elastomers), Base Material (Polyethylene, Polypropylene, Polyvinyl Chloride, Polyethylene Terephthalate, Polystyrene, Polyurethane), Application (Packaging, Construction, Automotive, Agriculture, Electrical & Electronics, Textile) - Global Industry

Trends and Growth Forecast to 2030 (2024).
URL https://www.psmarketresearch.com/

[8] Statista, Demand for polyethylene terephthalate worldwide from 2010 to 2020, with a forecast for 2021 to 2030 (2024).
URL https://www.statista.com/

[9] Omnexus, What are the main applications of PET? (2024).
URL https://omnexus.specialchem.com/

[10] O. Iliev, R. Kirsch, Z. Lakdawala, S. Rief, K. Steiner, Modeling and simulation of filtration processes, in: Currents in Industrial Mathematics: From Concepts to Research to Education, Springer Berlin Heidelberg, 2015, pp. 163–228.

[11] Porvair, Polymer Melt Filtration Handbook, [Leaflet]. United Kingdom: Porvair Plc, 2005.

[12] Pall, Polymer Segment Filters For The Manufacture of High Performance Fibres, Films, and Resins, [Leaflet]. Pall Corporation, 2006.

[13] Gneuss, Filtration Technology, [Leaflet]. Bad Oeynhausen: Gneuss Kunststofftechnik GmbH, 2024.

[14] ANSYS Inc., ANSYS FLUENT 12.0/12.1 Documentation, ANSYS, Inc., Canonsburg, Pennsylvania, United States, 2012.

[15] M. Rubinstein, R. H. Colby, Polymer physics, Vol. 23, Oxford university press New York, 2003.

[16] J. Vlachopoulos, N. Polychronopoulos, Basic Concepts In Polymer Melt Rheology and Their Importance In Processing, in: Applied Polymer Rheology: Polymeric Fluids with Industrial Applications, John Wiley & Sons, Inc., 2011, Ch. 1, pp. 2–26.

[17] F. Cogswell, Future Developments in Polymer Rheology, Polymer Melt Rheology (2003) 133–134doi:10.1533/9780857092984.133.

[18] J. Champion, Use of Computational Fluid Dynamics to improve the layer thickness control of polyester based multilayered films, Ph.D. thesis, University of Birmingham, Birmingham (6 2015).

[19] J. Vlachopoulos, D. Strutt, The Role of Rheology in Polymer Extrusion, Tech. rep., Polydynamics, Inc. (2003).

[20] M. Wozniak, A. Rylski, M. Lason-Rydel, M. Orczykowska, A. Obraniak, K. Siczek, Some rheological properties of plastic greases by Carreau-Yasuda model, Tribology International 183 (2023) 108372. doi:10.1016/J.TRIBOINT.2023.108372.

[21] D. Sybilski, Non-newtonian viscosity of polymer-modified bitumens, Materials and Structures 26 (1) (1993) 15–23.

[22] C. A. Hieber, H. H. Chiang, Shear-rate-dependence modeling of polymer melt viscosity, Polymer Engineering & Science 32 (14) (1992) 931–938. doi:10.1002/pen.760321404.

[23] J. Vlachopoulos, D. Strutt, The Role of Rheology in Polymer Extrusion, Tech. rep., polydynamics (2012).

[24] M. Ikeda, M. Aniya, Understanding the Vogel-Fulcher-Tammann law in terms of the bond strength-coordination number fluctuation model, Journal of Non-Crystalline Solids 371-372 (2013) 53–57. doi:10.1016/j.jnoncrysol.2013.04.034.

[25] J.-s. S. Wang Roger Porter, J. Wang, R. S. Porter, On the viscosity.temperature behavior of polymer melts, Rheologica Acta 34 (1995) 496–503.

[26] Tangram, Thermal degradation of plastics (2024).
URL http://www.tangram.co.uk

[27] C. David, Degradation of Polymers, in: Comprehensive Chemical Kinematics, Elsevier Scientific Publishing Company, 1975.

[28] ExxonMobil, Gels in polyethylene films, [Leaflet]. Irving, Texas, United States: Exxon Mobil Corporation, 2018.

[29] A. D. Bordoloi, D. Scheidweiler, M. Dentz, M. Bouabdellaoui, M. Abbarchi, P. de Anna, Structure induced laminar vortices control anomalous dispersion in porous media, Nature Communications 13 (1) (12 2022). doi:10.1038/s41467-022-31552-5.

[30] P. Cheremisinoff, Nicholas, Liquid Filtration, 2nd Edition, Butterworth-Heinemann, 1998.

[31] S. Ripperger, W. Gösele, C. Alt, Filtration, 1. Fundamentals, in: Ullmann's Encyclopedia of Industrial Chemistry, Wiley-VCH Verlag GmbH & Co. KGaA, 2009, pp. 678–708.

[32] P. Bacchin, Q. Derekx, D. Veyret, K. Glucina, P. Moulin, Clogging of microporous channels networks: Role of connectivity and tortuosity, Microfluidics and Nanofluidics 17 (1) (2014) 85–96. doi:10.1007/s10404-013-1288-4.

[33] S. Aramideh, P. P. Vlachos, A. M. Ardekani, Pore-scale statistics of flow and transport through porous media, Physical Review E 98 (1) (7 2018). doi:10.1103/PhysRevE.98.013104.

[34] A. Xu, B.-R. Xu, H.-D. Xi, Pore-scale statistics of temperature and thermal energy dissipation rate in turbulent porous convection, Phys. Rev. Fluids 8 (6 2023).

[35] S. Berg, J. van Wunnik, Shear Rate Determination from Pore-Scale Flow Fields, Transport in Porous Media 117 (2) (2017) 229–246. doi:10.1007/s11242-017-0830-3.

[36] J. Fu, H. R. Thomas, C. Li, Tortuosity of porous media: Image analysis and physical simulation, Earth-Science Reviews 212 (2021) 103439. doi:10.1016/J.EARSCIREV.2020.103439.

[37] M. A. Kendouci, B. Kharroubi, R. Khelfaoui, A. Bendida, B. Dennai, A. Maazouzi, Simulation of water filtration in porous zone based on Darcy's law, in: Energy Procedia, Vol. 36, Elsevier Ltd, 2013, pp. 163–168. doi:10.1016/j.egypro.2013.07.019.

[38] M. Hafiz Hamdan, Numerical simulation of flow through porous media, Ph.D. thesis, University of Windsor (1989).

[39] N. Rott, NOTE ON THE HISTORY OF THE REYNOLDS NUMBER, Annu. Rev. Fluid Mech 990 (1990).

[40] W. F. Brace, J. B. Walsh, W. T. Frangos, Permeability of granite under high pressure, Journal of Geophysical Research 73 (6) (1968) 2225–2236. doi:10.1029/JB073I006P02225.

[41] Y. Wang, G. Yang, Y. Huang, Y. Huang, R. Zhuan, J. Wu, Analytical model of flow-through-screen pressure drop for metal wire screens considering the effects of pore structures, Chemical Engineering Science 229 (1 2021). doi:10.1016/j.ces.2020.116037.

[42] A. Erić, D. Dakić, S. Nemoda, M. Komatina, B. Repić, Experimental method for determining Forchheimer equation coefficients related to flow of air through the bales of soy straw, International Journal of Heat and Mass Transfer 54 (19-20) (2011) 4300–4306. doi:10.1016/j.ijheatmasstransfer.2011.05.015.

[43] C. A. Bowers, C. T. Miller, Non-Newtonian fluid flow in porous media, Tech. rep., University of North Carolina (11 2019).
URL https://arxiv.org/abs/1911.10570v1

[44] S. De, J. A. Kuipers, E. A. Peters, J. T. Padding, Viscoelastic flow simulations in random porous media, Journal of Non-Newtonian Fluid Mechanics 248 (2017) 50–61. doi:10.1016/J.JNNFM.2017.08.010.

[45] T. Sochi, Non-Newtonian flow in porous media, Polymer 51 (22) (2010) 5007–5023. doi:10.1016/j.polymer.2010.07.047.

[46] U. Eberhard, H. J. Seybold, M. Floriancic, P. Bertsch, J. Jiménez-Martínez, J. S. Andrade, M. Holzner, Determination of the effective viscosity of non-Newtonian fluids flowing through porous media, Frontiers in Physics 7 (MAY) (2019). doi:10.3389/fphy.2019.00071.

[47] D. Purchas, K. Sutherland, Handbook of filter media, Elsevier, 2002.

[48] Pall Corporation, Pall Porous Inorganic Media Guide, [Leaflet]. New York: Pall Corporation, 2007.

[49] C. Tien, Principles of filtration, Elsevier, 2012.

[50] T. Sparks, Filters and filtration handbook, 6th Edition, Elsevier, Oxford, England: Butterworth-Heinemann, 2016.

[51] L. Svarovsky, Solid-liquid separation, 4th Edition, Butterworth-Heinemann, Oxford, 2000.

[52] O. Iliev, R. Kirsch, S. Osterroth, Combined Depth and Cake Filtration Model Coupled with Flow Simulation for Flat and Pleated Filters, Chemical Engineering and Technology 41 (1) (2018) 70–78. doi:10.1002/ceat.201700115.

[53] C. Tien, Introduction to Cake Filtration: Analyses, Experiments and Applications, Elsevier, 2006.

[54] C. Tien, Granular filtration of aerosols and hydrosols: Butterworths series in chemical engineering, Butterworth-Heinemann, 2013.

[55] F. M. Mahdi, R. G. Holdich, Laboratory cake filtration testing using constant rate, Chemical Engineering Research and Design 91 (6) (2013) 1145–1154. doi:10.1016/J.CHERD.2012.11.012.

[56] R. Singh, Introduction to membrane technology, Hybrid Membrane Systems for Water Purification (2005) 1–56doi:10.1016/B978-185617442-8/50002-6.

[57] V. Calabrò, A. Basile, Fundamental membrane processes, science and engineering, Advanced Membrane Science and Technology for Sustainable Energy and Environmental Applications (2011) 3–21doi:10.1533/9780857093790.1.3.

[58] D. R. Chen, D. Y. Pui, B. Y. Liu, Optimization of pleated filter designs using a finite-element numerical model, Aerosol Science and Technology 23 (4) (1995) 579–590. doi:10.1080/02786829508965339.

[59] E. Iritani, A Review on Modeling of Pore-Blocking Behaviors of Membranes During Pressurized Membrane Filtration (1 2013). doi:10.1080/07373937.2012.683123.

[60] G. Bolton, D. LaCasse, R. Kuriyel, Combined models of membrane fouling: Development and application to microfiltration and ultrafiltration of biological fluids, Journal of Membrane Science 277 (2006) 75–84.

[61] M. Hlavacek, F. Bouchet, Constant flowrate blocking laws and an example of their application to dead-end microfiltration of protein solutions, Journal of Membrane Science 82 (1993) 285–295.

[62] T. ITO, X. Liao, S. Lee, T. Hanada, Implementation of filtration models for filter performance prediction in bioprocess dead-end membrane filtration, Biochemical Engineering Journal 208 (2024) 109358. doi:10.1016/J.BEJ.2024.109358.

[63] W. R. Bowen, Q. Gan, Properties of microfiltration membranes: flux loss during constant pressure permeation of bovine serum albumin, Biotechnology and bioengineering 38 (7) (1991) 688–696. doi:10.1002/BIT.260380703.

[64] E. M. Tracey, R. H. Davis, Protein Fouling of Track-Etched Polycarbonate Microfiltration Membranes, Journal of Colloid and Interface Science 167 (1) (1994) 104–116. doi:10.1006/JCIS.1994.1338.

[65] M. Taghavijeloudar, J. Park, M. Han, A. Taghavi, A new approach for modeling flux variation in membrane filtration and experimental verification, Water Research 166 (2019) 115027. doi:10.1016/J.WATRES.2019.115027.

[66] A. Y. Kirschner, Y. H. Cheng, D. R. Paul, R. W. Field, B. D. Freeman, Fouling mechanisms in constant flux crossflow ultrafiltration, Journal of Membrane Science 574 (2019) 65–75. doi:10.1016/J.MEMSCI.2018.12.001.

[67] Y. L. Cheng, D. J. Lee, J. Y. Lai, Filtration blocking laws: Revisited, Journal of the Taiwan Institute of Chemical Engineers 42 (3) (2011) 506–508. doi:10.1016/J.JTICE.2010.09.004.

[68] E. Iritani, H. Sumi, T. Murase, Analysis of Filtration Rate in Clarification Filtration of Power-Law Non-Newtonian Fluids–Solids Mixtures under Constant Pressure by Stochastic Model, JOURNAL OF CHEMICAL ENGINEERING OF JAPAN 24 (5) (1991) 581–586. doi:10.1252/JCEJ.24.581.

[69] L. Chen, A. He, J. Zhao, Q. Kang, Z. Y. Li, J. Carmeliet, N. Shikazono, W. Q. Tao, Pore-scale modeling of complex transport phenomena in porous media, Progress in Energy and Combustion Science 88 (2022) 100968. doi:10.1016/J.PECS.2021.100968.

[70] I. Battiato, P. T. Ferrero V, D. O' Malley, C. T. Miller, P. S. Takhar, F. J. Valdés-Parada, B. D. Wood, Theory and Applications of Macroscale Models in Porous Media, Transport in Porous Media 130 (1) (2019) 5–76. doi:10.1007/s11242-019-01282-2.

[71] S. Abishek, A. J. King, R. Mead-Hunter, V. Golkarfard, W. Heikamp, B. J. Mullins, Generation and validation of virtual nonwoven, foam and knitted filter (separator/coalescer) geometries for CFD simulations, Separation and Purification Technology 188 (2017) 493–507. doi:10.1016/j.seppur.2017.07.052.

[72] W. Sambaer, M. Zatloukal, D. Kimmer, 3D modeling of filtration process via polyurethane nanofiber based nonwoven filters prepared by electrospinning process, Chemical Engineering Science 66 (4) (2011) 613–623. doi:10.1016/j.ces.2010.10.035.

[73] P. J. Withers, C. Bouman, S. Carmignato, V. Cnudde, D. Grimaldi, C. K. Hagen, E. Maire, M. Manley, A. Du Plessis, S. R. Stock, X-ray computed tomography (12 2021). doi:10.1038/s43586-021-00015-4.

[74] A. Georgiadis, S. Berg, A. Makurat, G. Maitland, H. Ott, Pore-scale micro-computed-tomography imaging: Nonwetting-phase cluster-size distribution during drainage and imbibition, Physical Review E - Statistical, Nonlinear, and Soft Matter Physics 88 (3) (9 2013). doi:10.1103/PhysRevE.88.033002.

[75] S. Jung, M. Sabharwal, A. Jarauta, F. Wei, M. Gingras, J. Gostick, M. Secanell, Estimation of Relative Transport Properties in Porous Transport Layers Using Pore-Scale

and Pore-Network Simulations, Journal of The Electrochemical Society 168 (6) (2021) 064501. doi:10.1149/1945-7111/ac03f2.

[76] S. Song, Q. Liu, X. Cao, T. Zhang, Q. Tu, Construction of pore structure geometry model from digital images of porous media and its application in pore-scale flow simulation, Geoenergy Science and Engineering 229 (2023) 212079. doi:10.1016/J.GEOEN.2023.212079.

[77] M. Aminpour, S. A. Galindo-Torres, A. Scheuermann, L. Li, Pore-Scale Behavior of Darcy Flow in Static and Dynamic Porous Media, Physical Review Applied 9 (6) (2018) 064025.

[78] G. Yang, R. Xu, Y. Wang, Y. Zhu, F. Ren, C. Li, J. Wu, Pore-scale numerical simulations of flow and convective heat transfer in a porous woven metal mesh, Chemical Engineering Science 256 (2022) 117696. doi:10.1016/J.CES.2022.117696.

[79] S. Osterroth, Mathematical models for the simulation of combined depth and cake filtration processes, Ph.D. thesis, Fraunhofer ITWM (2017).

[80] A. Zamani, B. Maini, Flow of dispersed particles through porous media - Deep bed filtration, Journal of Petroleum Science and Engineering 69 (1-2) (2009) 71–88. doi:10.1016/j.petrol.2009.06.016.

[81] D. Pashchenko, I. Karpilov, R. Mustafin, Numerical calculation with experimental validation of pressure drop in a fixed-bed reactor filled with the porous elements, AIChE Journal 66 (5) (5 2020). doi:10.1002/aic.16937.

[82] I. Cornejo, P. Nikrityuk, R. E. Hayes, Pressure correction for automotive catalytic converters: A multi-zone permeability approach, Chemical Engineering Research and Design 147 (2019) 232–243. doi:10.1016/j.cherd.2019.05.017.

[83] M. Teitel, Using computational fluid dynamics simulations to determine pressure drops on woven screens, Biosystems Engineering 105 (2) (2010) 172–179. doi:10.1016/j.biosystemseng.2009.10.005.

[84] M. Teitel, On the applicability of the Forchheimer equation in simulating flow through woven screens, Biosystems Engineering 109 (2) (2011) 130–139. doi:10.1016/j.biosystemseng.2011.02.009.

[85] S. K. Garg, B. Premachandran, M. Singh, Numerical study of the regenerator for a miniature Stirling cryocooler using the local thermal equilibrium (LTE) and the local thermal nonequilibrium (LTNE) models, Thermal Science and Engineering Progress 11 (2019) 150–161. doi:10.1016/j.tsep.2019.03.005.

[86] G. Trilok, K. E. S. Srinivas, D. Harikrishnan, N. Gnanasekaran, M. Mobedi, Correlations and Numerical Modeling of Stacked Woven Wire-Mesh Porous Media for Heat Exchange Applications, Energies 15 (7) (4 2022). doi:10.3390/en15072371.

[87] S. C. Hauswirth, C. A. Bowers, C. P. Fowler, P. B. Schultz, A. D. Hauswirth, T. Weigand, C. T. Miller, Modeling cross model non-Newtonian fluid flow in porous media, Journal of Contaminant Hydrology 235 (2020) 103708. doi:10.1016/J.JCONHYD.2020.103708.

[88] S. Rath, A. Terzis, Pore-scale hydrodynamics of non-Newtonian power-law fluids across a partially blocked porous medium in a confined channel, Journal of Non-Newtonian Fluid Mechanics 322 (2023) 105150. doi:10.1016/J.JNNFM.2023.105150.

[89] T. Tosco, D. L. Marchisio, F. Lince, R. Sethi, Extension of the Darcy-Forchheimer Law for Shear-Thinning Fluids and Validation via Pore-Scale Flow Simulations, Transport in Porous Media 96 (1) (2013) 1–20.

[90] C. L. Perrin, P. M. Tardy, K. S. Sorbie, J. C. Crawshaw, Experimental and modeling study of Newtonian and non-Newtonian fluid flow in pore network micromodels, Journal of Colloid and Interface Science 295 (2) (2006) 542–550. doi:10.1016/J.JCIS.2005.09.012.

[91] M. Zhang, M. Prodanović, M. Mirabolghasemi, J. Zhao, 3D Microscale Flow Simulation of Shear-Thinning Fluids in a Rough Fracture, Transport in Porous Media 128 (1) (2019) 243–269.

[92] R. E. Hayes, A. Afacan, B. Boulanger, A. V. Shenoy, Modelling the flow of power law fluids in a packed bed using a volume-averaged equation of motion, Transport in Porous Media 23 (2) (1996) 175–196.

[93] N. Zamani, I. Bondino, R. Kaufmann, A. Skauge, Computation of polymer in-situ rheology using direct numerical simulation, Journal of Petroleum Science and Engineering 159 (2017) 92–102. doi:10.1016/J.PETROL.2017.09.011.

[94] O. Iliev, A. Mikelic, P. Popov, Fluid structure interaction problems in deformable porous media: Toward permeability of deformable porous media, Tech. rep., Fraunhofer-Institut für Techno- und Wirtschaftsmathematik (2004).

[95] A. Hrouda, L. Capek, M. Vanierschot, K. Denis, Macroscale simulation of the filtration process of porous media based on statistical capturing models, Separation and Purification Technology 266 (7 2021). doi:10.1016/j.seppur.2021.118577.

[96] O. V. Soloveva, S. A. Solovev, S. I. Kharchuk, L. A. Belousova, A. R. Talipova, Determination of the effective porosity of a single filter fiber, in: Journal of Physics: Conference Series, Vol. 2094, IOP Publishing Ltd, 2021, pp. 1–5. doi:10.1088/1742-6596/2094/2/022075.

[97] J. A. Destephen, K.-J. Choi, Modelling of filtration processes of fibrous filter media, ELSEVIER Separations Technology 6 (1996) 55–67.

[98] J. Gong, S. Viswanathan, D. A. Rothamer, D. E. Foster, C. J. Rutland, Dynamic Heterogeneous Multiscale Filtration Model: Probing Micro- and Macroscopic Filtration Characteristics of Gasoline Particulate Filters, Environmental Science and Technology 51 (19) (2017) 11196–11204. doi:10.1021/acs.est.7b02535.

[99] K. Schmidt, S. Rief, Simulation of DPF Media, Soot Deposition and Pressure Drop Evolution, Tech. rep., Fraunhofer ITWM (2009).

[100] A. Tsuda, F. S. Henry, J. P. Butler, Particle transport and deposition: Basic physics of particle kinetics, Comprehensive Physiology 3 (4) (2013) 1437–1471. doi:10.1002/cphy.c100085.

[101] A. Wiegmann, S. Rief, A. Latz, Soot Filtration Simulation-Generation of Porous Media On The Micro Scale From Soot Deposition On The Nano Scale, Tech. rep., Fraunhofer ITWM (2006).

[102] D. Hoppach, E. Werzner, C. Demuth, E. Löwer, H. Lehmann, L. Ditscherlein, R. Ditscherlein, U. A. Peuker, S. Ray, Experimental Investigations of the Depth Filtration inside Open-Cell Foam Filters Supported by High-Resolution Computed Tomography Scanning and Pore-Scale Numerical Simulations, Advanced Engineering Materials 22 (2) (2020) 1900761. doi:10.1002/ADEM.201900761.

[103] S. Fotovati, H. V. Tafreshi, B. Pourdeyhimi, A macroscale model for simulating pressure drop and collection efficiency of pleated filters over time, Separation and Purification Technology 98 (2012) 344–355. doi:10.1016/j.seppur.2012.07.009.

[104] A. M. Saleh, S. Fotovati, H. Vahedi Tafreshi, B. Pourdeyhimi, Modeling service life of pleated filters exposed to poly-dispersed aerosols, Powder Technology 266 (2014) 79–89. doi:10.1016/j.powtec.2014.06.011.

[105] A. Costa, Permeability-porosity relationship: A reexamination of the Kozeny-Carman equation based on a fractal pore-space geometry assumption, Geophysical Research Letters 33 (2) (1 2006). doi:10.1029/2005GL025134.

[106] N. Basha, L. Cochrane, F. Hamad, Macroscale modelling of pressure drop for a moulded cylindrical filter within a vacuum pump to predict aerosol loading, Asia-Pacific Journal of Chemical Engineering 15 (3) (5 2020). doi:10.1002/apj.2431.

[107] K. Liu, Y. Zhao, L. Jia, R. Hao, D. Fu, A novel CFD-based method for predicting pressure drop and dust cake distribution of ceramic filter during filtration process at macro-scale, Powder Technology 353 (2019) 27–40. doi:10.1016/J.POWTEC.2019.05.014.

[108] K. Lee, Y. W. Jung, H. Park, D. Kim, J. Kim, Sequential Multiscale Simulation of a Filtering Facepiece for Prediction of Filtration Efficiency and Resistance in Varied

Particulate Scenarios, ACS Applied Materials and Interfaces 13 (48) (2021) 57908–57920. doi:10.1021/acsami.1c16850.

[109] J. Gong, C. J. Rutland, PDF-based heterogeneous multiscale filtration model, Environmental Science and Technology 49 (8) (2015) 4963–4970. doi:10.1021/acs.est.5b00329.

[110] H. Li, J. Sansalone, Multi-scale physical model simulation of particle filtration using computational fluid dynamics, Journal of Environmental Management 271 (2020) 111021. doi:10.1016/J.JENVMAN.2020.111021.

[111] K. Lee, D. Kim, J. Kim, Computational Modeling of Multiscale Air Filter Media Consisting of Nano- and Microfibers, ACS Applied Nano Materials 6 (11) (2023) 9415–9425. doi:10.1021/acsanm.3c01139.

[112] B. Liedl, C. Burgstaller, Influence of selected contaminations and melt filtration on the properties of ABS and ABS recyclate, Polymer Engineering & Science 64 (7) (2024) 3025–3035. doi:10.1002/PEN.26743.

[113] K. Koller, C. Paulik, C. Burgstaller, Influence of material contamination on polypropylene melt filtration using assembled and fused screens, SPE Polymers 3 (1) (2022) 12–24. doi:10.1002/PLS2.10061.

[114] V. Schöppner, P. Meilwes, Modelling the contamination behaviour of polymer melt filters, AIP Conference Proceedings 2139 (1) (8 2019).

[115] Gommes, Cedric J, J. Tharakan, The Peclet number of a casino: Diffusion and convection in a gambling context, American Journal of Physics 88 (6) (2020) 439–447.

[116] L. Costigliola, D. M. Heyes, T. B. Schrøder, J. C. Dyre, Revisiting the Stokes-Einstein relation without a hydrodynamic diameter, Journal of Chemical Physics 150 (2) (1 2019). doi:10.1063/1.5080662.

[117] M. A. Mujeebu, M. Z. Abdullah, M. Z. Bakar, A. A. Mohamad, M. K. Abdullah, A review of investigations on liquid fuel combustion in porous inert media, Progress in

Energy and Combustion Science 35 (2) (2009) 216–230. doi:10.1016/J.PECS.2008.11.001.

[118] C. E. Brennen, Fundamentals of multiphase flow, Fundamentals of Multiphase Flow 9780521848046 (2013) 1–345. doi:10.1017/CBO9780511807169.

[119] Porvair Filtration Group Ltd., World Class Filtration Solutions Polymer Filtration Candles, capsules, needles, spinpacks and disposable cartridges, Tech. rep. (2021).

[120] ANSYS Inc., ANSYS Workbench Documentation, Tech. rep., ANSYS Inc., Canonsburg, PA (2005).

[121] SolidWorks Corporation, 3DEXPERIENCE SOLIDWORKS.
URL https://www.solidworks.com/

[122] F. Durst, S. Ray, B. Ünsal, O. A. Bayoumi, The development lengths of laminar pipe and channel flows, Journal of Fluids Engineering, Transactions of the ASME 127 (6) (2005) 1154–1160. doi:10.1115/1.2063088.

[123] R. J. Poole, B. S. Ridley, Development-length requirements for fully developed laminar pipe flow of inelastic non-Newtonian liquids, Journal of Fluids Engineering, Transactions of the ASME 129 (10) (2007) 1281–1287. doi:10.1115/1.2776969.

[124] ANSYS Inc., ANSYS FLUENT 12.0 User's Guide - 7.2.3 Porous Media Conditions (2012).

[125] P. Diwu, T. Liu, Z. You, B. Jiang, J. Zhou, Effect of low velocity non-Darcy flow on pressure response in shale and tight oil reservoirs, Fuel 216 (2018) 398–406.

[126] Y. Teng, Z. Li, C. Chen, A Comprehensive Review of Pre-Darcy Flows in Low-Permeability Porous Media (1 2024).

[127] W. Abou-Hweij, F. Azizi, CFD simulation of wall-bounded laminar flow through screens. Part I: Hydrodynamic characterization, European Journal of Mechanics, B/Fluids 84 (2020) 207–232. doi:10.1016/j.euromechflu.2020.06.008.

[128] J. Pfitzner, Poiseuille and his law, Anaesthesia 3 (1) (1976) 273–275.

[129] ANSYS Inc., ANSYS FLUENT UDF Manual, Vol. 14.0, ANSYS Inc., Southpointe, Canonsburg PA, 2011.

Appendix A

CFD Mesh Details

This Appendix gives more detailed descriptions of each mesh used for each CFD model of the screen filter system, the single candle filter pack and seven candle filter pack.

A.1 Screen filter system meshes

In total, twelve separate geometries representing the screen filter system were created. There were four grades of screen filters used, all with different geometrical properties, and 3 different porous zone configurations were tested. In the interest of completeness, the mesh details for the medium mesh of each of these configurations is detailed.

Table A.1 shows general meshing details for each filter grade for the full length model. Figure A.1 shows an example of a mesh for a particular filter grade. Sweep meshing was used on the inlet and outlet pipe for each filter grade, with a bias of 10 selected and the number of divisions set to 100. Edge sizing was specified on the edge of the inlet face, with the number of divisions set to 40. Patch conforming method was selected upstream of the filter. The method was set as tetrahedrons. Mesh density varied based on thickness of each filter grade.

The density increased with decreasing filter thickness.

Table A.1: General meshing parameters for generation of each filter grade medium mesh for the full length model.

Filter grade [μm]	80	60	40	23
Element size [m]	0.001	0.001	0.001	0.001
Mesh defeaturing [m]	0.00001	0.00001	0.00001	0.00001
Curvature min size [m]	0.00001	0.00001	0.00001	0.00001
Proximity gap factor	3	3	3	3
Mesh nodes	1311260	1368715	1250271	1233089
Mesh elements	4645692	4977995	4300035	4200252

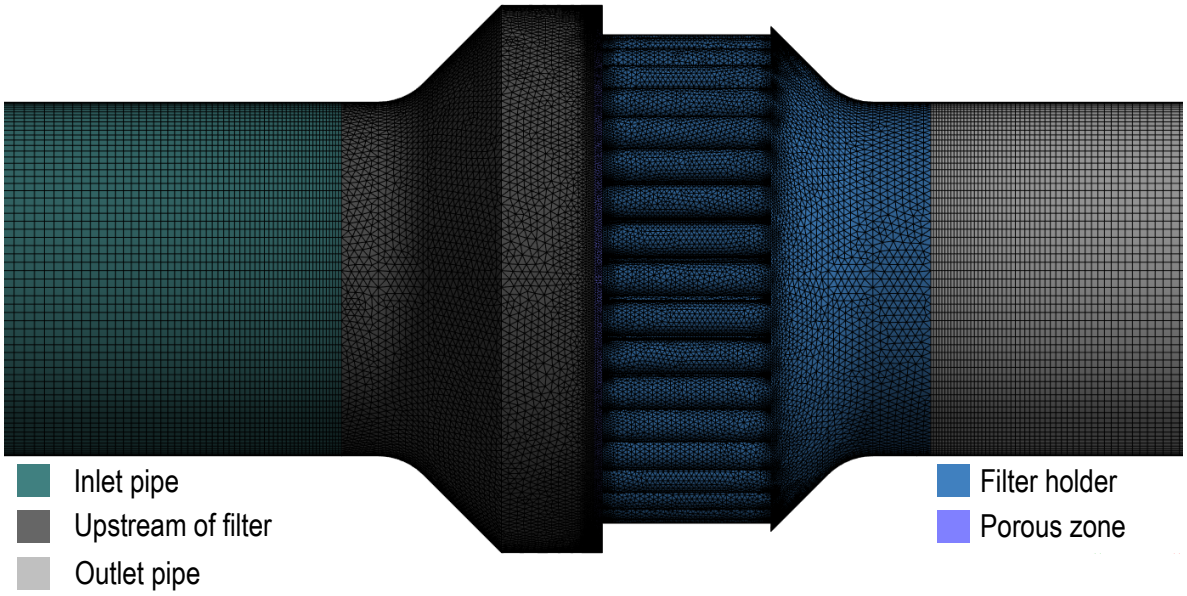

Figure A.1: The full length 80 micron screen filter medium mesh.

Table A.2 shows general meshing details for each filter grade for the filter by holder model. Figure A.2 shows an example of a mesh for a particular filter grade. Sweep meshing was used on the inlet and outlet pipe for each filter grade, with a bias of 10 selected and the number of divisions set to 55. Edge sizing was specified on the edge of the inlet face, with the number of divisions set to 30. Patch conforming method was selected upstream of the filter. The method was set as tetrahedrons. The reduced thickness of the porous zone compared to the

full length model greatly increased mesh density.

Table A.2: General meshing parameters for generation of each filter grade medium mesh for the filter by holder model.

Filter grade [μm]	80	60	40	23
Element size [m]	0.01	0.01	0.01	0.01
Mesh defeaturing [m]	0.0001	0.0001	0.0001	0.0001
Curvature min size [m]	0.0001	0.0001	0.0001	0.0001
Proximity gap factor	3	3	3	3
Mesh nodes	3612982	3355353	3244327	3993529
Mesh elements	20137224	18629579	18141197	22427251

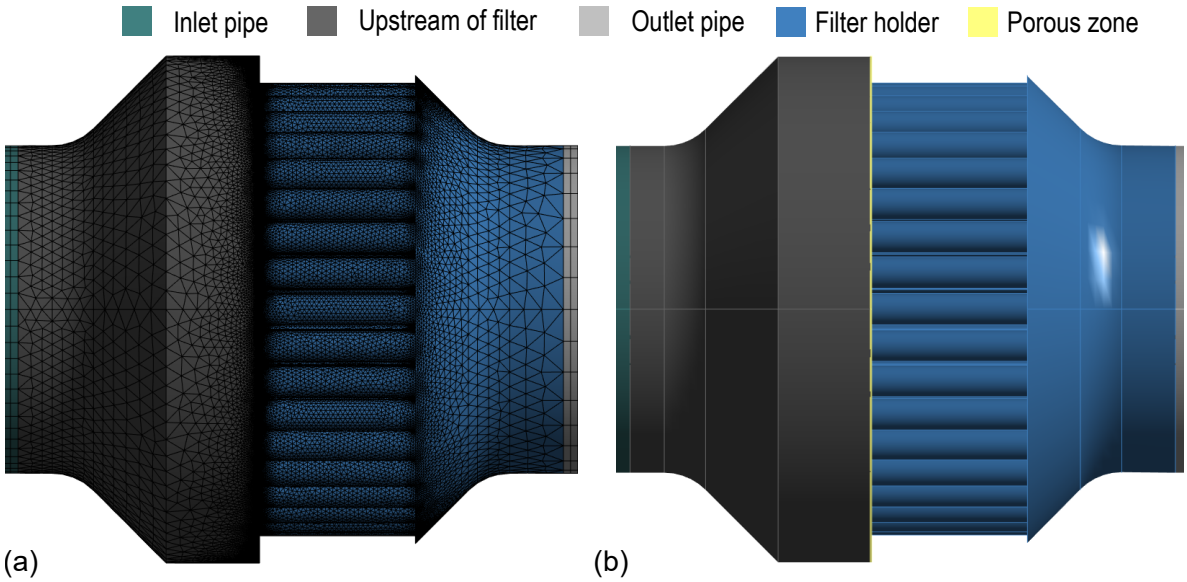

Figure A.2: (a) The filter by holder 80 micron screen filter medium mesh. (b) The geometry, included to highlight the porous zone.

Table A.3 shows general meshing details for each filter grade for the filter away from holder model. Figure A.3 shows an example of a mesh for a particular filter grade. Sweep meshing was used on the inlet and outlet pipe for each filter grade, with a bias of 10 selected and the number of divisions set to 55. Edge sizing was specified on the edge of the inlet face, with the number of divisions set to 30. Patch conforming method was selected upstream of the filter. The method was set as tetrahedrons.

Table A.3: General meshing parameters for generation of each filter grade medium mesh for the filter away from holder model.

Filter grade [μm]	80	60	40	23
Element size [m]	0.01	0.01	0.01	0.01
Mesh defeaturing [m]	0.0001	0.0001	0.0001	0.0001
Curvature min size [m]	0.0001	0.0001	0.0001	0.0001
Proximity gap factor	3	3	3	3
Mesh nodes	4560205	4161300	3823747	4540352
Mesh elements	21772132	21255294	17187652	21685221

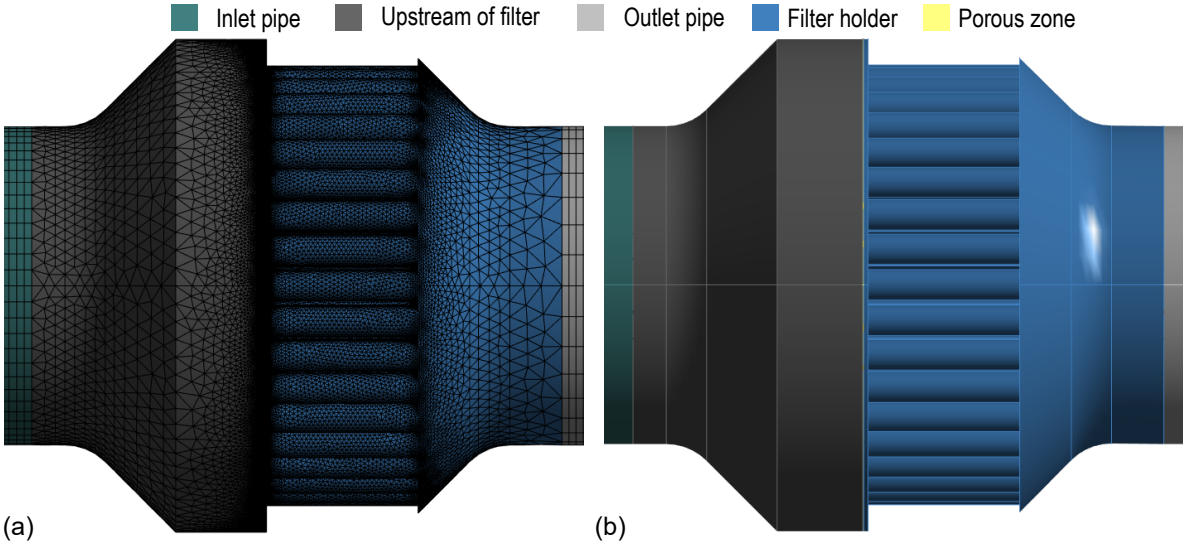

Figure A.3: (a) The filter away from holder 80 micron screen filter medium mesh. (b) The geometry, included to highlight the porous zone.

A.2 Single candle pack meshes

A one-sixth geometry of the single candle filter pack was created and used for processing results; it was designed to exploit the symmetry of the pack. A full model of the pack was designed to verify that the geometrical symmetry of a single candle filter pack resulted in exploitable flow symmetry. A simplified, axisymmetric version of the single candle filter pack was created by exploiting the axisymmetry of flow in the core of the pack. This allowed

quicker testing and processing of the developed filter blocking model in Chapter 7.

Table A.4 shows general meshing details for the original one-sixth single candle filter pack geometry, which was presented in Section 6.4. The mesh was shown in Figure 6.11. The controls described here are for the original geometry. As described in Section 6.4, the mesh was adapted in regions of high pressure gradients to ensure mesh independence. As shown in Figure 6.11, the mesh was made up of several sections. Sweep meshing was utilized on the inlet pipe, outlet pipe and porous zone. The number of divisions was set to 100 and a sweep bias of 5 was specified at the inlet pipe and outlet pipe. The number of divisions was set to 1000 for the porous zone sweep. Edge sizing was specified with number of divisions set to 10 on the inlet boundary face.

Table A.4: General meshing parameters for generation of the original one-sixth single candle filter pack mesh.

Element size [m]	0.013
Mesh defeaturing [m]	0.000065
Curvature min size [m]	0.00013
Proximity gap factor	8.0
Mesh nodes	480770
Mesh elements	1165021

Table A.5 shows general meshing details for the full single candle filter pack geometry, which was presented in Subsection 6.4.2. Figure A.4 shows the medium mesh. Sweep meshing was utilized on the inlet pipe, outlet pipe and porous zone. The number of divisions was set to 100 and a sweep bias of 5 was specified at the inlet pipe and outlet pipe. The number of divisions was set to 1000 for the porous zone sweep. Edge sizing was specified with the number of divisions set to 30 on the inlet boundary face.

Table A.5: General meshing parameters for generation of the full single candle filter pack medium mesh.

Element size [m]	0.013
Mesh defeaturing [m]	0.000065
Curvature min size [m]	0.00013
Proximity gap factor	8.0
Mesh nodes	3544436
Mesh elements	7353068

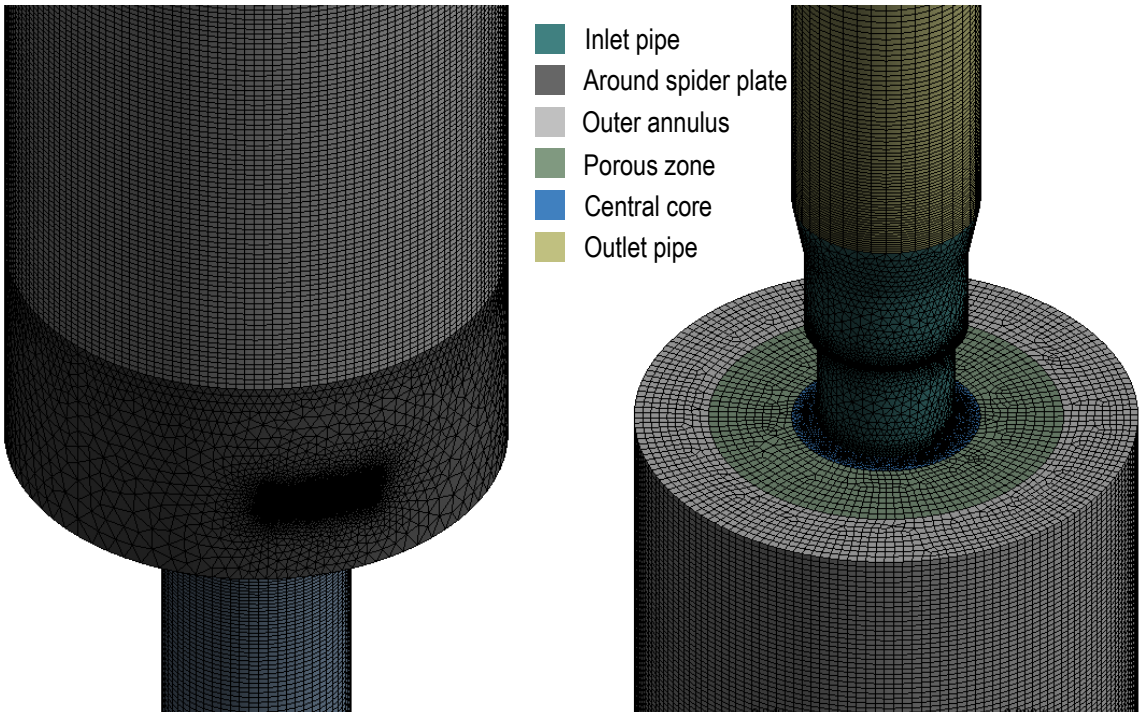

Figure A.4: Full single candle pack medium mesh.

Table A.6 shows general meshing details for the original axisymmetric single candle filter pack geometry, which was presented in Section 7.4. The mesh was shown in Figure 7.5. The controls described here are for the original geometry. As described in Section 7.4, the mesh was adapted in regions of high pressure gradients to ensure mesh independence.

Table A.6: General meshing parameters for generation of the axisymmetric single candle filter pack medium mesh.

Element size [m]	0.0004
Mesh defeaturing [m]	0.000002
Curvature min size [m]	0.000004
Proximity gap factor	11.0
Mesh nodes	249338
Mesh elements	246627

A.3 Seven candle filter pack meshes

A one-twelfth geometry of the seven candle filter pack was created and used for processing results; it was designed to exploit the symmetry of the pack. An inlet section geometry was also made, designed to verify that the geometrical symmetry of a seven candle filter pack resulted in exploitable flow symmetry. A multiple outlet geometry was created to help understand the influence of outlet geometry on flow patterns inside the filter. A modified geometry was created to improve pack performance.

Table A.7 shows general meshing details for the original one-twelfth seven candle filter pack geometry, which was presented in Section 6.7. The mesh was shown in Figure 6.21. The controls described here are for the original geometry. As described in Section 6.7, the mesh was adapted in regions of high pressure gradients to ensure mesh independence. Sweep meshing was specified at the outlet pipe, inlet pipe and porous zones. At the outlet and inlet pipe, the number of divisions was set to 25 and a bias of 5 was specified. At the porous zones, the number of divisions was set to 1000.

Table A.7: General meshing parameters for generation of the original one-twelfth seven candle filter pack mesh.

Element size [m]	0.025
Mesh defeaturing [m]	0.0001
Curvature min size [m]	0.0002
Proximity gap factor	3.0
Mesh nodes	459928
Mesh elements	1753368

Table A.8 shows general meshing details for the medium mesh generated for the seven candle inlet geometry, which was presented in Section 6.7.2. In addition to the general controls, sweep meshing was used on the inlet pipe and outlet section of the geometry. Figure A.5 shows the mesh. For the outlet section, a bias of 5.0 was used and a number of divisions of 60 was specified. At the inlet, a bias of 5 was again specified with a number of divisions of 50 chosen. Face sizing was applied on the inlet boundary face, with an element size of 0.0012 m and proximity gap factor of 20 specified.

Table A.8: A table to show the general meshing parameters for generation of the medium seven candle inlet mesh.

Element size [m]	0.01
Mesh defeaturing [m]	0.0001
Curvature min size [m]	0.0001
Proximity gap factor	4.0
Mesh nodes	585609
Mesh elements	2183726

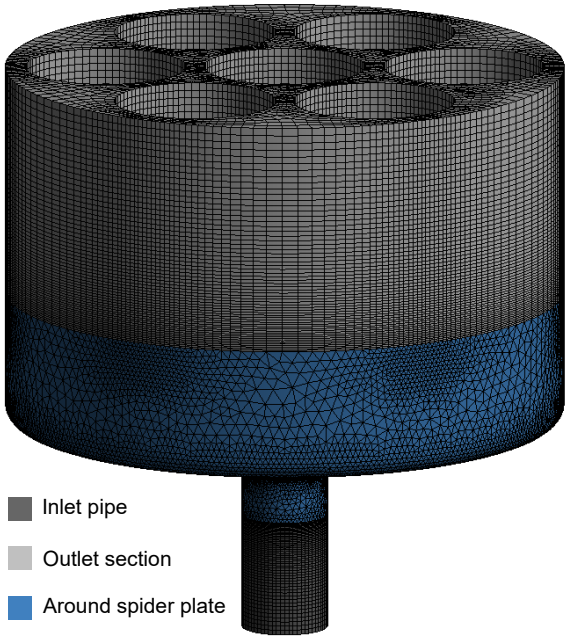

Figure A.5: Seven candle inlet medium mesh.

Table A.9 shows general meshing details for the original one-twelfth multiple outlets seven candle filter pack geometry, which was presented in Subsection 6.10.2. Figure A.6 shows the mesh. The controls described here are for the original geometry. As described in Subsection 6.10.2, the mesh was adapted in regions of high pressure gradients to ensure mesh independence. Sweep meshing was specified at the inlet pipe and porous zones. At the inlet pipe, the number of divisions was set to 25 and a bias of 5 was specified. At the porous zones, the number of divisions was set to 1000.

Table A.9: General meshing parameters for generation of the original multiple outlet seven candle filter pack mesh.

Element size [m]	0.025
Mesh defeaturing [m]	0.0001
Curvature min size [m]	0.0002
Proximity gap factor	3.0
Mesh nodes	450869
Mesh elements	1739189

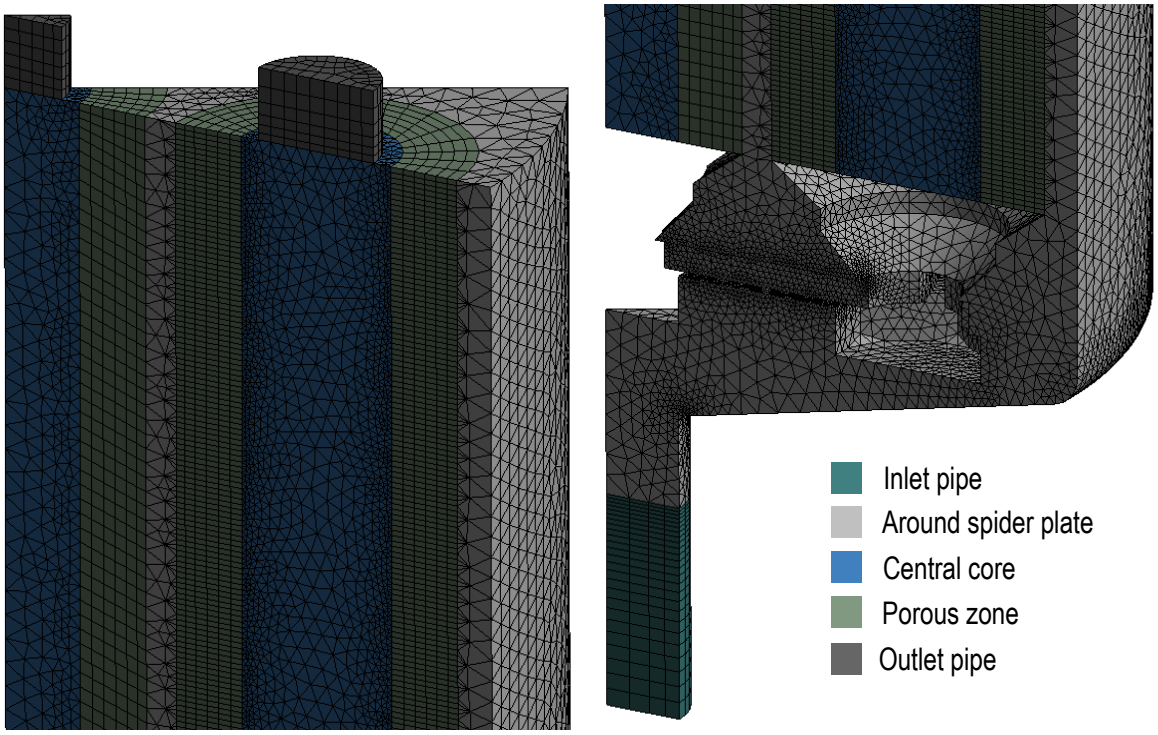

Figure A.6: Original multiple outlet seven candle filter pack mesh.

Table A.10 shows general meshing details for the original one-twelfth modified outlet seven candle filter pack geometry, which was presented in Section 7.10. Figure A.7 shows the mesh. The controls described here are for the original geometry. As described in Subsection 7.10, the mesh was adapted in regions of high pressure gradients to ensure mesh independence. Sweep meshing was specified at the outlet pipe, inlet pipe and porous zones. At the inlet and outlet pipes, the number of divisions was set to 25 and a bias of 5 was specified. At the porous zones, the number of divisions was set to 1000.

Table A.10: General meshing parameters for generation of the original one-twelfth modified outlet seven candle filter pack.

Element size [m]	0.01
Mesh defeaturing [m]	0.0001
Curvature min size [m]	0.0002
Proximity gap factor	7.0
Mesh nodes	1554729
Mesh elements	5873759

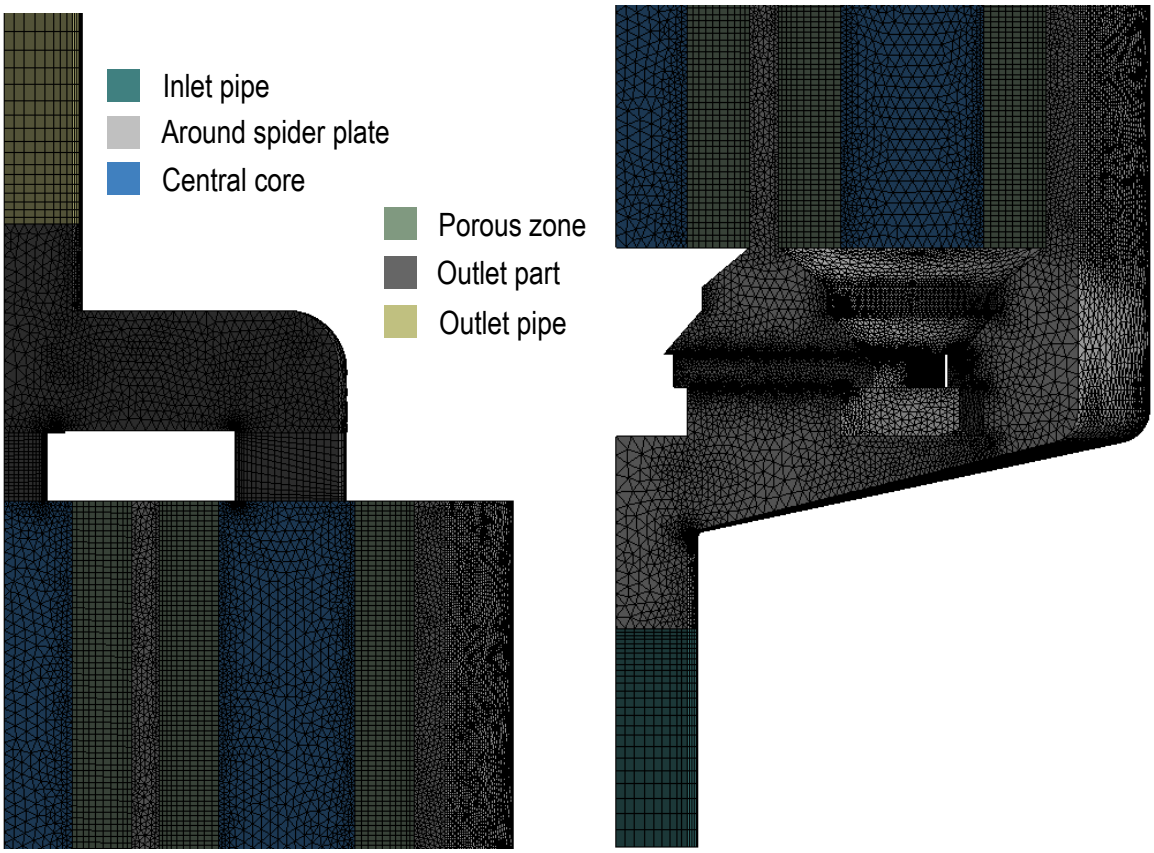

Figure A.7: Original one-twelfth modified outlet seven candle filter pack mesh.

Appendix B

Filter Blocking Model UDFs

This appendix gives example source files, written using C programming, which are interpreted into Fluent for use with the standard blocking model with a 10 hour time step. For the axisymmetric model, the source file used is titled `axis_standard.c` and is given below:

```
/* Enables definition of macros and functions*/
#include "udf.h"
/* Allow Fluent user to manually save radial velocity at every
   cell centroid to a UDM */
DEFINE_ON_DEMAND(dod)
{
  Domain *d;
  Thread *t;
  cell_t c;
  d = Get_Domain(1);
  thread_loop_c(t,d)
    {
        /* Loop over all cells */
```

```
    begin_c_loop(c,t)
           {
               C_UDMI(c,t,0) = C_V(c,t);
           }
    end_c_loop(c,t)
    }
}
/* Defines the profile, from the standard model, to be hooked to the
   porous zone for the quasi-steady state 10 hour time step*/
DEFINE_PROFILE(vis_res_10,t,i)
{
  real x[ND_ND];
  real a;
  real r_vel;
  cell_t c;
  begin_c_loop(c,t)
  {
    r_vel = C_UDMI(c,t,0);
    C_CENTROID(x,c,t);
    a = 1.25e9*pow((1-(0.0358 * M_PI * x[1] * 1225\
    * 0.9575 * -r_vel * 10)),-2);
    F_PROFILE(c,t,i) = a;
    F_UDMI(c,t,1) = a;
  }
  end_c_loop(c,t)
}
/* Defines the profile, from the standard model, to be hooked to the
   porous zone for the quasi-steady state 20 hour time step*/
DEFINE_PROFILE(vis_res_20,t,i)
```

```
{
  real x[ND_ND];
  real a;
  real r_vel;
  cell_t c;
  begin_c_loop(c,t)
  {
    r_vel = C_UDMI(c,t,0);
    C_CENTROID(x,c,t);
    a = 1.25e9*pow((1-(0.0358 * M_PI * x[1] * 1225\
    * 0.9575 * -r_vel * 20)),-2);
    F_PROFILE(c,t,i) = a;
    F_UDMI(c,t,1) = a;
  }
  end_c_loop(c,t)
}
```

The source file continues to repeat the `DEFINE_PROFILE` macro for each time step up until the desired maximum time. The workflow for the implementation and execution of this source file for a blocking simulation is described in Subsection 7.3.2. As this is hooked onto an axisymmetric CFD model, the radial velocity is already defined and called by `C_V(c,t)` in the `DEFINE_ON_DEMAND` macro.

For the single candle model, the source file used is titled `single_standard.c` and is given below:

```
/* Enables definition of macros and functions*/
#include "udf.h"
/* Allow Fluent user to manually save radial velocity at every
   cell centroid to a UDM */
```

```
DEFINE_ON_DEMAND(dod)
{
  real x[ND_ND];
  real r_vel;
  Domain *d;
  Thread *t;
  cell_t c;
  d = Get_Domain(1);
  thread_loop_c(t,d)
    {
        /* Loop over all cells */
    begin_c_loop(c,t)
           {
           C_CENTROID(x,c,t);
           r_vel =  ( (x[0]*C_U(c,t) + x[2]*C_W(c,t))\
           /sqrt(x[0]*x[0] + x[2]*x[2]));
           C_UDMI(c,t,0)=r_vel;
           }
    end_c_loop(c,t)

    }
}
/* Defines the profile, from the standard model, to be hooked to the
   porous zone for the quasi-steady state 10 hour time step*/
DEFINE_PROFILE(vis_res_10,t,i)
{
  real x[ND_ND];
  real a;
  real r_vel;
```

```
  cell_t c;
  begin_c_loop(c,t)
  {
    r_vel = C_UDMI(c,t,0);
    C_CENTROID(x,c,t);
    a = 1.25e9*pow((1-(0.0358 * M_PI * sqrt(x[0]*x[0] + x[2]*x[2])\
    *0.9575* 1225 *-r_vel * 10)),-2);
    F_PROFILE(c,t,i) = a;
    F_UDMI(c,t,1) = a;
  }
  end_c_loop(c,t)
}
/* Defines the profile, from the standard model, to be hooked to the
   porous zone for the quasi-steady state 20 hour time step*/
DEFINE_PROFILE(vis_res_20,t,i)
{
  real x[ND_ND];
  real a;
  real r_vel;
  cell_t c;
  begin_c_loop(c,t)
  {
    r_vel = C_UDMI(c,t,0);
    C_CENTROID(x,c,t);
    a = 1.25e9*pow((1-(0.0358 * M_PI * sqrt(x[0]*x[0] + x[2]*x[2])\
    *0.9575* 1225 *-r_vel * 20)),-2);
    F_PROFILE(c,t,i) = a;
    F_UDMI(c,t,1) = a;
  }
```

```
  end_c_loop(c,t)
}
```

Again, the source file continues to repeat the `DEFINE_PROFILE` macro for each time step up until the desired maximum time. The workflow for the implementation and execution of this source file for a blocking simulation is described in Subsection 7.3.2. As this is hooked onto an 3D CFD model, the radial velocity is calculated using (6.2) in the `DEFINE_ON_DEMAND` macro.

For the seven candle model, the source file used is titled `seven_standard.c` and is given below:

```
#include "udf.h"
/* Allow Fluent user to manually save central radial velocity at every
   cell centroid to a UDM */
DEFINE_ON_DEMAND(central_rvel)
{
  real x[ND_ND];
  real r_vel;
  Domain *d;
  Thread *t;
  cell_t c;
  d = Get_Domain(1);
  thread_loop_c(t,d)
    {
        /* Loop over all cells */
    begin_c_loop(c,t)
          {
          C_CENTROID(x,c,t);
          r_vel =  ( (x[0]*C_U(c,t) + x[2]*C_W(c,t)) /sqrt(x[0]*x[0] +\
    x[2]*x[2]));
```

```
            C_UDMI(c,t,0)=r_vel;
            }
    end_c_loop(c,t)
    }
}
/* Allow Fluent user to manually save outer radial velocity at every
   cell centroid to a UDM */
DEFINE_ON_DEMAND(outer_rvel)
{
  real x[ND_ND];
  real r_vel;
  Domain *d;
  Thread *t;
  cell_t c;
  d = Get_Domain(1);
  thread_loop_c(t,d)
    {
        /* Loop over all cells */
    begin_c_loop(c,t)
            {
            C_CENTROID(x,c,t);
            r_vel =  ( ((x[0]-0.054127)*C_U(c,t) + (x[2]-0.03125)*C_W(c,t))\
            /sqrt((x[0]-0.054127)*(x[0]-0.054127) + \
            (x[2]-0.03125)*(x[2]-0.03125)));
            C_UDMI(c,t,1)=r_vel;
            }
    end_c_loop(c,t)
    }
}
```

```
/* Defines the profile, from the standard model, to be hooked to the
   central porous zone for the quasi-steady state 10 hour time step*/
DEFINE_PROFILE(c_10,t,i)
{
  real x[ND_ND];
  real a;
  real r_vel;
  cell_t c;
  begin_c_loop(c,t)
  {
    r_vel = C_UDMI(c,t,0);
    C_CENTROID(x,c,t);
    a = 1.25e9*pow((1-(0.038 * M_PI * sqrt(x[0]*x[0] + x[2]*x[2]) * 1400.1 *\
    0.9575 *-r_vel  * 10)),-2);
    F_PROFILE(c,t,i) = a;
    F_UDMI(c,t,2) = a;
  }
  end_c_loop(c,t)
}
/* Defines the profile, from the standard model, to be hooked to the
   outer porous zone for the quasi-steady state 10 hour time step*/
DEFINE_PROFILE(o_10,t,i)
{
  real x[ND_ND];
  real a;
  real r_vel;
  cell_t c;
  begin_c_loop(c,t)
  {
```

```
    r_vel = C_UDMI(c,t,1);
    C_CENTROID(x,c,t);
    a = 1.25e9*pow((1-(0.038 * M_PI * sqrt((x[0]-0.054127)*(x[0]-0.054127) +\
    (x[2]-0.03125)*(x[2]-0.03125)) * 0.9575 * 1400.1 *-r_vel * 10)),-2);
    F_PROFILE(c,t,i) = a;
    F_UDMI(c,t,3) = a;
  }
  end_c_loop(c,t)
}
/* Defines the profile, from the standard model, to be hooked to the
   central porous zone for the quasi-steady state 20 hour time step*/
DEFINE_PROFILE(c_20,t,i)
{
  real x[ND_ND];
  real a;
  real r_vel;
  cell_t c;
  begin_c_loop(c,t)
  {
    r_vel = C_UDMI(c,t,0);
    C_CENTROID(x,c,t);
    a = 1.25e9*pow((1-(0.038 * M_PI * sqrt(x[0]*x[0] + x[2]*x[2]) * 1400.1 *\
    0.9575 *-r_vel  * 20)),-2);
    F_PROFILE(c,t,i) = a;
    F_UDMI(c,t,2) = a;
  }
  end_c_loop(c,t)
}
/* Defines the profile, from the standard model, to be hooked to the
```

```
   outer porous zone for the quasi-steady state 20 hour time step*/
DEFINE_PROFILE(o_20,t,i)
{
  real x[ND_ND];
  real a;
  real r_vel;
  cell_t c;
  begin_c_loop(c,t)
  {
    r_vel = C_UDMI(c,t,1);
    C_CENTROID(x,c,t);
    a = 1.25e9*pow((1-(0.038 * M_PI * sqrt((x[0]-0.054127)*(x[0]-0.054127) +\
    (x[2]-0.03125)*(x[2]-0.03125)) * 0.9575 * 1400.1 *-r_vel * 20)),-2);
    F_PROFILE(c,t,i) = a;
    F_UDMI(c,t,3) = a;
  }
  end_c_loop(c,t)
}
```

The source file continues to repeat the DEFINE_PROFILE macros for each candle for each time step up until the desired maximum time. The workflow for the implementation and execution of this source file for a blocking simulation is described in Subsection 7.3.2. The equations for the viscous resistance profiles for each filter are described in Section 7.7. As this source file is hooked onto an 3D CFD model with a central and outer porous zone, the central radial velocity is calculated using (6.2) and the outer radial velocity is calculated using (6.8) in the two DEFINE_ON_DEMAND macros.